

THE UNIVERSITY OF CALGARY

FIELD MODELLING WITH RELUCTANCE WAVES

by

Cecil Edgar Gordon

A THESIS

SUBMITTED TO THE FACULTY OF GRADUATE STUDIES
IN PARTIAL FULFILLMENT OF THE REQUIREMENTS FOR THE
DEGREE OF MASTER OF SCIENCE

DEPARTMENT OF ELECTRICAL AND COMPUTER ENGINEERING

CALGARY, ALBERTA

JUNE, 1992

© Cecil Edgar Gordon 1992



National Library
of Canada

Acquisitions and
Bibliographic Services Branch

395 Wellington Street
Ottawa, Ontario
K1A 0N4

Bibliothèque nationale
du Canada

Direction des acquisitions et
des services bibliographiques

395, rue Wellington
Ottawa (Ontario)
K1A 0N4

Your file *Votre référence*

Our file *Notre référence*

The author has granted an irrevocable non-exclusive licence allowing the National Library of Canada to reproduce, loan, distribute or sell copies of his/her thesis by any means and in any form or format, making this thesis available to interested persons.

L'auteur a accordé une licence irrévocable et non exclusive permettant à la Bibliothèque nationale du Canada de reproduire, prêter, distribuer ou vendre des copies de sa thèse de quelque manière et sous quelque forme que ce soit pour mettre des exemplaires de cette thèse à la disposition des personnes intéressées.

The author retains ownership of the copyright in his/her thesis. Neither the thesis nor substantial extracts from it may be printed or otherwise reproduced without his/her permission.

L'auteur conserve la propriété du droit d'auteur qui protège sa thèse. Ni la thèse ni des extraits substantiels de celle-ci ne doivent être imprimés ou autrement reproduits sans son autorisation.

ISBN 0-315-79162-4

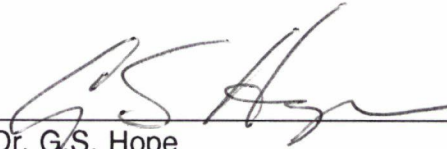
Canada 

THE UNIVERSITY OF CALGARY
FACULTY OF GRADUATE STUDIES

The undersigned certify that they have read, and recommend to the Faculty of Graduate Studies for acceptance, a thesis entitled *Field Modelling With Reluctance Waves*, submitted by Cecil Edgar Gordon in partial fulfillment of the requirements for the degree of Master of Science.



Supervisor, Dr. T.H. Barton
Department of Electrical and Computer
Engineering



Dr. G.S. Hope
Department of Electrical and Computer
Engineering



Dr. O.P. Malik
Department of Electrical and Computer
Engineering



Dr. R.D. Rowe
Department of Mechanical Engineering

24 June 1992
Date

ABSTRACT

Existing methods for determining magnetic field distributions in saturated synchronous machines are either inaccurate or very complex and computer intensive.

This research models the field distribution as a function of a position dependent, MMF independent reluctance in series with a position independent, MMF dependent reluctance.

A flux density model is developed using field data collected from a specially modified synchronous machine. Computed fields from this model are used to compute steady state torque and operating curves.

Reasonable results are obtained, given the simplicity of the model. Average error in computed torque is 8% for all excitation conditions. The error in computed torque for any excitation condition can be compensated for.

Because of its simplicity and minimal computing requirements this model can be used in synchronous machine simulations where very high accuracy is not required.

ACKNOWLEDGEMENTS

I wish to thank Dr. T.H. Barton for faithfully guiding and encouraging me throughout this research. It has been a privilege to work with a man who has such depth of experience and insight.

Thanks also to Ed Evanik who devoted his time, energy, and talent to assisting me with my equipment problems.

Thanks to the Natural Sciences and Engineering Research Council whose financial support made this research possible.

Thank you, Rosalee, for always being there to correct my perspective and keep me going. You are God's most tangible expression of His love for me.

TABLE OF CONTENTS

Item	Page
APPROVAL PAGE	ii
ABSTRACT	iii
ACKNOWLEDGEMENTS	iv
TABLE OF CONTENTS	v
LIST OF TABLES	viii
LIST OF FIGURES	ix
LIST OF SYMBOLS	xi
1. INTRODUCTION	1
1.0 CHAPTER OBJECTIVES	1
1.1 TRANSIENT ANALYSIS OF SYNCHRONOUS MACHINES	1
1.2 RESEARCH SCOPE	2
1.3 MAGNETIC DESIGN AND MODELLING METHODS	3
1.3.1 The Magnetic Circuit Concept	3
1.3.2 Applying the Magnetic Circuit Concept	5
1.3.3 Graphical Methods	8
1.3.4 Permeance Distributions	12
1.3.5 Integral Methods	15
1.3.6 Finite Difference Methods	15
1.3.7 Finite Element Methods	18
1.4 PROBLEM STATEMENT, RESEARCH GOAL, INITIAL PROPOSAL, AND OUTLINE	23
2. EQUIPMENT AND MEASUREMENT SYSTEM	28
2.0 CHAPTER OBJECTIVES	28
2.1 MEASUREMENT REQUIREMENTS	28
2.1.1 The Proposal's Requirements	28
2.1.2 Available Methods for Determining B Distributions	31
2.1.3 Suitability of the Experimental Equipment for Developing and Testing the B Distribution Model	33
2.2 EXPERIMENTAL MOTOR, INSTRUMENTATION, AND MEASUREMENT CONDITIONS	37
2.2.1 Experimental Motor	37
2.2.2 Instrumentation and Auxiliary Systems	37

2.2.3 Using Static Measurements	39
2.3 THE DATA ACQUISITION SYSTEM	43
2.3.1 General Description	43
2.3.2 Application of the Data Acquisition System	44
2.3.3 Advantages of Using Data Acquisition	46
2.4 TYPICAL DATA RUNS	46
3. RELUCTANCE WAVE CHARACTERIZATION	51
3.0 CHAPTER OBJECTIVES	51
3.1 STRATEGY FOR FINDING R_{base} AND R_{sat}	51
3.2 DEVELOPMENT OF THE RELUCTANCE WAVE MODEL	53
3.2.1 Using Averaged Flux Density Distributions	53
3.2.2 Using Averaged MMF Distributions	54
3.2.3 Characterizing R_{base}	62
3.2.4 Determining and Using the Experimental Armature MMF Wave	69
3.2.5 Determination of Field MMF	81
3.2.6 Characterizing R_{sat}	88
4. THE AIR GAP FLUX DENSITY MODEL	97
4.0 CHAPTER OBJECTIVES	97
4.1 DESCRIPTION OF THE B DISTRIBUTION PROGRAM	97
4.1.1 The B Distribution Model	97
4.1.2 Static Versus Steady State Conditions	98
4.1.3 Program Structure	98
4.2 B DISTRIBUTION PROGRAM RESULTS	99
4.2.1 Field Excitation Only	99
4.2.2 Armature Excitation Only	99
4.2.3 Compound Excitation	99
4.3 POTENTIAL IMPROVEMENTS AND MODIFICATIONS	110
5. THE TORQUE MODEL	111
5.0 CHAPTER OBJECTIVES	111
5.1 TORQUE COMPUTATION METHODS	111
5.1.1 Coenergy Derivations	111
5.1.2 Torque from Circuit Models	112
5.1.3 Direct Force Computation Using the Maxwell Stress Method	116
5.1.4 The Flux Linkage Method	117
5.2 THE TORQUE COMPUTATION ALGORITHM	118
5.3 MEASURED VS. COMPUTED TORQUE RESULTS	119
6. THE VOLTAGE MODEL	125
6.0 CHAPTER OBJECTIVES	125
6.1 FLUX LINKAGE VOLTAGE COMPUTATION	125
6.2 COMPUTED VOLTAGE WAVEFORMS	128

6.3 MODELLED STEADY STATE CONDITIONS	131
7. CONCLUSIONS AND FUTURE WORK	135
7.0 CHAPTER OBJECTIVES	135
7.1 CONCLUSIONS	135
7.2 FUTURE WORK	139
REFERENCES	141
APPENDIX A: EXPERIMENTAL INACCURACIES	144
APPENDIX B: FLUX LINKAGE, TORQUE, AND VOLTAGE CALCULATION	147
APPENDIX C: APPLICATION OF D-Q AXIS THEORY TO THE COMPUTER MODEL	164

LIST OF TABLES

Table No.	Title	Page
Table 6.1	Normalized Harmonic Content of Flux Density and Voltage Distributions from Figure 6.1	130
Table A.1	Summary of Experimental Inaccuracies	144
Table B.1	Effect of Skewing on Flux Linkage	161
Table B.2	Comparison of Measured Flux Density Harmonics	163
Table C.1	Sample Trial and Error Steady State Computation of a Point on the No-Load V-Curve	174

LIST OF FIGURES

Figure No.	Title	Page
Figure 1.1	Magnetic Field Distribution Around a Current Carrying Conductor	9
Figure 2.1	Cross-Section of Specially Modified Synchronous Motor	32
Figure 2.2	Experimental Armature Winding Connections	41
Figure 2.3	Block Diagram of Data Acquisition System	45
Figure 2.4	Flux Density Data, Constant Field Current, Different Probe Depths	47
Figure 2.5	Effects of Rotor Slot Skewing on Flux Density Distributions, Constant Field Current, Different Probe Depths	49
Figure 2.6	Effects of Saturation on Flux Density Distributions	50
Figure 3.1	Comparison of Unaveraged to Averaged Flux Density Data	55
Figure 3.2	Effects of Saturation Upon Averaged Flux Density Data	56
Figure 3.3	Theoretical Computation of MMF Distributions	57
Figure 3.4	Theoretical Centre Contour and Averaged MMF Distributions	60
Figure 3.5	Effect of 15° Mechanical Segment Width on R_{base} Calculation	63
Figure 3.6	Effect of 20° Mechanical Segment Width on R_{base} Calculation	64
Figure 3.7	Comparison of R_{base} Waves for Different Magnetic Histories	66
Figure 3.8	Comparison of Typical Overlapping Reluctance Segments	67
Figure 3.9	Completed R_{base} Distribution	70
Figure 3.10	Comparison of Back Calculated A and -B MMF Waves	71
Figure 3.11	Comparison of Averaged Theoretical and Spliced Measured MMF Waves	73
Figure 3.12	Comparison of R_{base} Computed Using Different Segment Widths	75
Figure 3.13	Comparison of MMF from Different Excitations	77
Figure 3.14	Single Phase Spliced MMF Wave	78
Figure 3.15	Comparison of Summed and Spliced MMF	79
Figure 3.16	Comparison of Armature MMF	80
Figure 3.17	Trapezoidal and \sin^2 Approximations to Flux Distributions	82
Figure 3.18	Comparison of Flux Distributions for Field and Armature Excitations	83
Figure 3.19	Comparison of Field MMF Waves for Different Field Currents	84
Figure 3.20	Integration Path for Determining N	86
Figure 3.21	Harmonic Content of Field MMF Wave	87
Figure 3.22	Comparison of R Waves for Different Armature Currents	89
Figure 3.23	Variation of R with Armature Current Levels	90
Figure 3.24	Typical B-H Curve Shape for Iron	91
Figure 3.25	Comparison of R Waves for Different Field Currents	92
Figure 3.26	Comparison of R Waves for Field and Armature Currents	93
Figure 3.27	Plots of R_{sat} vs. MMF and Angular Position	94
Figure 3.28	Scatter Plot of R_{sat} vs. MMF	95

Figure 4.1	Measured vs. Computed B Distributions, Field Excitation	100
Figure 4.2	Measured vs. Computed B Distributions, Armature Excitation on Direct Axis	101
Figure 4.3	Measured vs. Computed B Distributions, Armature Excitation on Quadrature Axis	102
Figure 4.4a	Measured vs. Computed B Distributions, Compound Excitation, $\psi = 90^\circ$ electrical	103
Figure 4.4b	Measured vs. Computed B Distributions, Compound Excitation, $\psi = 45^\circ$ electrical	104
Figure 4.4c	Measured vs. Computed B Distributions, Compound Excitation, $\psi = 0^\circ$ electrical	105
Figure 4.4d	Measured vs. Computed B Distributions, Compound Excitation, $\psi = -45^\circ$ electrical	106
Figure 4.4e	Measured vs. Computed B Distributions, Compound Excitation, $\psi = -90^\circ$ electrical	107
Figure 5.1	Cylindrical, Reluctance, and Total Torque vs. Torque Angle	115
Figure 5.2	Comparison of Linear Modelled, Saturation Modelled, and Measured Torques	120
Figure 5.3	Measured and Computed Torques vs. Power Factor Angle	121
Figure 6.1	Computed Induced Voltage Waveforms from Modelled and Measured Flux Data	129
Figure 6.2	Open Circuit Line to Neutral Voltage	132
Figure 6.3	Constant Power Factor Curve and No Load V-Curve	133
Figure B.1	Rotor Flux Integration Surface	147
Figure B.2	Definition of Time Varying Angular Coordinates	150
Figure B.3	Cross-Section of Rotor Surfaces Showing Integration Regions	158
Figure C.1	Magnetic Field Conditions, Phasor Diagram, and Circuit Diagram for a Two Pole, Salient Pole Motor	165
Figure C.2	Magnetic Field Conditions, Phasor Diagram, and Circuit Diagram for a Two Pole, Salient Pole Generator	171

LIST OF SYMBOLS

Symbol	Description
a	distance between successive flux lines (m)
\mathbf{A}	magnetic vector potential (Wb/m), three phase MMF axis space vector (A-turns)
A_c	magnetic core area (m ²)
A_z	magnitude of the z component of magnetic vector potential (Wb/m)
α	phase angle between phase a load current and induced phase a voltage (electrical degrees or radians)
\mathbf{B}	magnetic flux density vector (Wb/m ²)
B_c	magnetic flux density magnitude in core (Wb/m ²)
\mathbf{B}_{net}	space vector for the peak of the fundamental of the net flux density distribution (Wb/m ²)
B_r	magnitude of radial component of magnetic flux density vector (Wb/m ²)
δ	internal torque or power angle (electrical degrees or radians)
\mathbf{E}	induced voltage phasor (V)
E	magnitude of induced voltage (V)
\mathbf{E}_a	induced winding voltage under load (phasor) (V)
E_a	induced winding voltage under load (magnitude) (V)
\mathbf{E}_f	induced winding voltage for no load conditions (phasor) (V)
E_f	induced winding voltage for no load conditions (magnitude) (V)
e	instantaneous induced voltage (V)
\mathbf{F}	force vector (N), field MMF axis vector (A-turns)
\mathcal{F}	magnetomotive force (A-turns)
\mathcal{F}_n	n^{th} order space harmonic of mmf distribution (A-turns)
g	radial length of air gap (m)
g_{eqv}	equivalent air gap for a salient pole machine (m)
g_{min}	minimum air gap dimension for a salient pole machine (m)
\mathbf{H}	magnetic field intensity vector (A-turns/metre)
H	magnetic field intensity magnitude (A-turns/metre)
H_c	magnetic field intensity in core (A-turns/metre)

h	rotor height or length (m)
I_a	phase a rms load current (A)
I_d	component of load current in quadrature with no load induced voltage (phasor) (A)
I_d	component of load current in quadrature with no load induced voltage (magnitude) (A)
I_{rms}	AC rms current magnitude (A)
I_{DC}	DC current magnitude (A)
I_q	component of load current in phase with no load induced voltage (phasor) (A)
I_q	component of load current in phase with no load induced voltage (magnitude) (A)
i	current (A)
\mathbf{J}	current density vector (A/m^2)
J_z	current density in z direction (A/m^2)
j	index variable
K_b	breadth factor
K_p	pitch factor
K_w	winding factor
k	index variable
$\mathcal{L}[A_z]$	energy functional of magnetic vector potential (J)
ℓ	length of flux tube between successive equipotentials (m)
ℓ	length unit vector (metres)
ℓ_c	mean core length (metres)
m	number of coils in a phase winding (index)
μ	permeability (H/m)
μ_c	core permeability (H/m)
μ_{copper}	permeability of copper (H/m)
μ_{iron}	permeability of iron (H/m)
μ_o	permeability of free space ($4\pi \times 10^{-7}$ H/m)
μ_r	relative permeability (unitless)
n	harmonic order index, number of contour intervals

N	number of conductor turns, or number of conductors per coil side (turns)
Ω	scalar magnetic potential (Wb/m)
Ω_{ab}	scalar magnetic potential difference from points a to b (Wb/m)
ω	angular frequency (rad/s)
P	permeance (Wb/m ² /A-turn), number of poles, power (watts)
P_n	permeance distribution for n^{th} order mmf (Wb/m ² /A-turn)
Φ	magnetic flux lines (Wb)
Φ_c	magnetic flux lines in core (Wb)
ϕ	time varying angular position of rotor w.r.t. the stator (mechanical degrees or radians)
φ	power factor angle between phase a current and phase a terminal voltage (electrical degrees or radians)
ψ	skewing angle of rotor teeth (mechanical degrees or radians), internal power factor angle (electrical degrees or radians)
q	particle charge (C), number of machine phases
R	general limits of area integral, reluctance of total magnetic circuit of a machine (A-turns/Wb)
R_a	armature winding resistance (ohms)
R_{air}	magnetic circuit reluctance of machine air gap (A-turns/Wb)
R_{base}	linear portion of total machine magnetic circuit reluctance (A-turns/Wb)
R_c	core reluctance (A-turns/Wb)
R_{iron}	iron portion of total machine magnetic circuit reluctance (A-turns/Wb)
R_{lin}	linear portion of magnetic circuit reluctance of machine iron (A-turns/Wb)
R_{sat}	saturable portion of magnetic circuit reluctance of machine iron (A-turns/Wb)
r	distance from point current source to point of interest, outside radius of rotor (m)
<i>rotorg</i>	rotor gauge reading in mechanical degrees
S	general limits of surface integral
T	torque, instantaneous or average (N-m)
t	time (s)
τ	fundamental pole pitch (m)

θ	general angular polar coordinate (degrees or radians)
\mathbf{u}	coil side velocity (m/s)
\mathbf{u}_x	unit vector in x direction
\mathbf{u}_y	unit vector in y direction
V	region of integration for a volume integral
\mathbf{V}_a	phase a line to neutral terminal voltage (phasor) (V)
V_a	phase a line to neutral terminal voltage (magnitude) (V)
V_{DC}	DC voltage (V)
\mathbf{v}	velocity vector (m/s)
W'_{fld}	magnetic coenergy (J)
X_a	winding leakage reactance (ohms)
X_{bus}	bus reactance (ohms)
X_{dT}	total direct axis reactance (ohms)
X_{qT}	total quadrature axis reactance (ohms)
X_{rd}	direct axis magnetizing reactance (ohms)
X_{rq}	quadrature axis magnetizing reactance (ohms)
x	general Cartesian coordinate
y	general Cartesian coordinate
z	general Cartesian coordinate

CHAPTER 1

INTRODUCTION

1.0 CHAPTER OBJECTIVES

- i) *Describe the importance and difficulties of transient analysis of synchronous machines, and the scope of my research in this area.*
- ii) *Describe the nature and limitations of several magnetic design and modelling methods used for rotating machines.*
- iii) *Define the problem statement, research goal, and the initial solution proposal.*
- iv) *Outline the remainder of this document.*

1.1 TRANSIENT ANALYSIS OF SYNCHRONOUS MACHINES

No-one can argue with the very important role which synchronous machines play in our society by providing electrical power which sustains our way of life, and by driving very large mechanical loads (typically 5000 HP and above). In order to properly predict and analyze their use, we must not only be able to determine their steady state operation, but also their behaviour under electrical and mechanical transient conditions (start-up, fault conditions, sudden load changes, etc.). Given the high cost of these installations, and the key role they play in the power distribution systems and industrial processes they serve, we must ensure that they can endure these transient conditions to avoid facing potential life threatening and/or economically severe consequences. As an example of the importance of transient analysis, Ojo/Lipo [1] describe the potential for mechanical failure in a synchronous motor drive application:

" During the starting interval, the transient currents generate double slip frequency pulsating torques. In a complex mechanical drive application, the mechanical system can have numerous resonance frequencies lying between zero and twice the supply frequency. If these resonance frequencies coincide with the pulsating torque frequency of the motor, severe torsional oscillations can result which can lead to coupling shearing and shaft breakage. "

Numerous authors have incorporated the effects of saturation into machine models. Some examples include Slemon [2] in 1971 who modified existing circuit models by introducing nonlinear shunt inductors to the basic synchronous reactance model and then successfully applied this model to predict steady state operating conditions; and

Piriou/Abdel-Razek [3], in 1983, who used finite element analysis to precalculate inductance elements (expressing them as functions of rotor position, armature reaction, and field current) in the steady state equations for a salient pole synchronous machine under saturated conditions. Ramshaw/Xie [4,5], from 1984 to 1986, modified Kron's matrix formulations to account for magnetic saturation under steady state and transient conditions by using "static" and "dynamic" permeances.

Recent developments in the area of transient analysis of synchronous machines depend heavily on finite element analysis techniques to predict magnetic field distributions.

Krefta/Wasynczuk [6] developed a state model representation which predicts elements of the state equation coefficient matrix using finite element field modelling. Under linear, non-salient conditions, these elements are constant throughout a transient simulation. The full transient solution is found by performing a finite element solution once to find the elements, then time-stepping through an integration algorithm subject to the initial and boundary conditions of the problem. Under salient and/or saturation conditions, the elements must be recomputed at each time step due to changes in conductivity and reluctivity in many of the nodes. This method is elegant and powerful due to the versatility of the state model, but requires lots of computing time and advanced integration algorithms which take advantage of the sparsity of some of the matrices.

In 1989, Ojo/Lipo [1] developed new circuit models (similar to Slemon's [2]) which used finite element modelled parameters. This technique was quite successful in obtaining accurate results with less computational effort than the state model approach. This is because parameter characteristic curves are precomputed for a given machine using finite element modelling, and once computed are then useful for all types of transient studies - the circuit models accounting for the different operating and boundary conditions for each study.

1.2 RESEARCH SCOPE

This research primarily addresses one aspect of the overall transient analysis problem for salient pole synchronous machines: **predicting air gap magnetic flux density distributions under all possible operating conditions**, which basically amounts to varying levels of saturation in different regions of the machine. Although I developed and tested the air gap flux density distribution model to provide an alternative to the finite element methods now used in transient studies, due to time constraints I was unable to

carry the work past steady state torque and voltage predictions. The results are very promising at this point, and I hope that myself or others will be able to extend the model's development to its full potential: a fast, simple, and accurate replacement for finite element modelling within transient solution techniques such as those used in references [1] and [6].

1.3 MAGNETIC DESIGN AND MODELLING METHODS

This section briefly describes the techniques used to predict machine fields and account for non-idealities such as fringing (due to salient poles or teeth) and iron saturation. These techniques are applicable to all of the major machine categories (AC induction, DC, and synchronous), since all possess similar magnetic structures. The objective of this section is to provide background information for the justification of the problem statement at the start of section 1.4.

1.3.1 The Magnetic Circuit Concept

The magnetic circuit concept is described in practically all basic electric machine textbooks, an example being Fitzgerald [7].

Ampere's Circuital Law,

$$\oint \mathbf{H} \cdot d\boldsymbol{\ell} = Ni = \mathcal{F} \quad (1.1),$$

can be reduced for a simple iron geometry to

$$H_c \ell_c = Ni = \mathcal{F} \quad (1.2),$$

where ℓ_c is the mean path length in the iron, and H_c is the field intensity in the iron path. The relationship

$$\Phi = \int_S \mathbf{B} \cdot d\mathbf{A} \quad (1.3)$$

reduces to

$$\Phi_c = B_c A_c \quad (1.4),$$

when all of the flux lines are assumed normal to, and contained in, the iron path's cross-section. Here A_c is the cross-sectional area of the iron path, B_c is the flux density, and

Φ_c is the total flux in the iron path.

For linear conditions in the iron, $\mu_c = \mu_r \mu_o = \text{constant}$ (μ_c = core permeability, μ_r = relative permeability, and μ_o is the permeability of free space), and the relation

$$\mathbf{B} = \mu \mathbf{H} \quad (1.5)$$

reduces to

$$B_c = \mu_c H_c \quad (1.6).$$

Equations (1.2), (1.4), and (1.6) can be solved to give

$$\mathcal{F} = Ni = \Phi_c R_c \quad (1.7),$$

where $R_c = \ell_c / \mu_c A_c$ is the core reluctance, analogous to resistance in an electric circuit. For iron and iron-air geometries which may be sectioned into volumes of uniform length, cross-section, and permeability, series and parallel circuits can be drawn with a reluctance assigned to each volume. Flux, Φ_c , is analogous to current, and Ni or \mathcal{F} (the mmf in A-turns) is analogous to a voltage source. The magnetic circuit equations can then be solved in the same fashion as electric circuit equations to find the unknown variables.

Because of the analogy between the magnetic field equations and basic electric circuit equations, the engineer can readily understand and apply this method. However, it has inherent limitations due to the simplifying assumptions which were made to get equations (1.2), (1.4), (1.6), and (1.7). Flux fringing occurs when flux travels from one iron surface through an air gap to another iron surface (as in the case of armature teeth, or a salient pole structure) and it is difficult to define what A_c to use. μ_c is never really constant, even in low mmf regions of the B - H saturation curve. Its deviation from a constant value increases as mmf levels increase and the iron enters saturation (to economically use the iron in a machine, saturation occurs in some regions of the magnetic circuit even during normal operating conditions). A further problem proceeds from the rotating machine designer's need for accurate, detailed knowledge of the field distribution in the airgap in order to predict the torque and induced emf of the machine. This method not only has difficulty with fringing and saturation, but does not provide high resolution or accuracy since it depends on relatively coarse sectioning of the iron structure.

Despite these major drawbacks, the magnetic circuit approach gives a great deal of qualitative insight into the magnetic behaviour of a structure, and serves as a helpful tool in the area of machine design and analysis.

1.3.2 Applying the Magnetic Circuit Concept

Many references describe rotating machine design as being a very complex task. The designer must optimize the electrical, magnetic, mechanical, and thermal aspects of the design while meeting performance specifications, minimizing costs, and satisfying manufacturing constraints. Frequently, all of this work needs to be done under time pressure. My focus, of course, is upon the magnetic aspects of the design, but it is important to note that the final magnetic design is optimized by considering all of the above factors.

Until recently, a primary method for performing magnetic design involved using subjective estimates of saturation effects, flux leakage, and fringing (around salient poles, teeth, etc.) in conjunction with the magnetic circuit approach. These estimates were based on past measurements, empirical correlations, rules-of-thumb, the designer's personal experience, and theoretical approximations from the work of F.W. Carter [8] and others. Without these estimates it would have been impossible to reasonably predict the performance of the finished machine. It has only been within the last few years, with the proliferation of finite element analysis programs, that reliance upon these estimates has been reduced. However, this does not render these estimates obsolete, rather, they now provide a means of checking and interpreting the results of finite element solutions. The aim of this section is to briefly outline some of these estimates.

Detailed descriptions of magnetic designs using some of the above estimates may be found in Moullin [9] (estimate of field amp-turns required for a DC machine design), Walker [10] (estimate of field amp-turns for a salient pole synchronous generator), and Alger [11] (estimate of magnetizing current for an induction motor).

In 1900, Carter first published a paper using a geometrical transformation technique known as Schwarz's Transformation to solve the two dimensional Laplace equation in the air gap of a magnetic circuit

$$\frac{\partial^2 \Omega}{\partial x^2} + \frac{\partial^2 \Omega}{\partial y^2} = 0 \quad (1.8),$$

where Ω is the scalar magnetic potential (defined only at points where there is no current density), and x and y are Cartesian coordinates (see Hayt [12]).

Basically, Schwartz's Transform permits us to simplify the geometry of the iron structure of the magnetic circuit before we attempt to solve the airgap magnetic field. For example, a scalar equipotential pole face can be mapped onto a scalar equipotential line. Regions of the transformed structure are assigned scalar magnetic potentials corresponding to their scalar magnetic potentials in the original iron structure. The flux and scalar potential distributions are then solved, in general form, subject to these scalar potentials. The general flux distribution is then inverse transformed, and its constants are determined in order to give a scalar equipotential curve which fits, as closely as possible, the outline of the original scalar equipotential boundary (in this case, the outline of the pole face). This procedure is quite lengthy, and is also recursive since the transforming equation needs to be selected in a trial and error fashion to get the best fitting scalar equipotential solution for the original scalar equipotential boundaries in the problem.

There are two major problems with using this method for routine design and analysis:

- i) lengthy, complex, trial and error mathematical manipulations are required, even for very simplified iron structures, and
- ii) saturation effects are not considered, scalar equipotential surfaces are assumed to be on the surface of the iron. This assumption requires infinite iron permeability. Under saturated conditions the scalar equipotential surfaces will not necessarily coincide with the iron boundary.

However, for very simple situations, assuming infinite iron permeability, Carter was able to present the results of his work in a form suitable for direct inclusion in the magnetic circuit method. He did this by creating factors, known as Carter coefficients, which adjust air gap widths under salient pole faces, over teeth, etc., to account for flux fringing. The adjusted width for the air gap is then used to compute the reluctance of the air gap. In most machine structures fringing is a result of several non-idealities (eg: salient poles, teeth, and ventilation ducts) and the coefficient for each non-ideality

multiplies the previous one(s). Each coefficient is computed using a formula which contains constants corresponding to iron structure dimensions, and a factor which is determined from a chart where the factor is plotted as a function of iron structure dimensions. Formulas exist for many different structures, some introducing non-idealities such as a wider pole shoe than pole core, rounded pole corners, and chamfered pole faces. Refer to [9] for a more thorough treatment.

In addition to Carter's coefficients, designers have other rules-of-thumb which allow them to make their magnetic circuit calculation more accurate. A couple of examples are listed below:

- i) For teeth on the rotor, if the slots are rectangular, then the top of the tooth is wider than its root. Rather than using the width of the tooth at its middle to estimate the total cross-sectional area of iron in the teeth, the width about two-thirds of the way down the tooth is used. This rule reduces the net tooth area, increases its reluctance, and increases its mmf drop. This gives a better approximation of tooth saturation than taking the tooth width mid-way. The reason for this is that it compensates for the effects of slot leakage flux and the high degree of saturation at the root of the tooth.
- ii) To account for leakage flux in the pole windings (assuming the poles are on the stator), the ratio $(\text{air gap flux} + \text{leakage flux})/(\text{air gap flux})$ is set equal to 1.2. This increases the mmf drop in the yoke and pole cores, which carry both the air gap and the leakage fluxes.

In order to estimate the amp-turns for the field windings, an air gap flux/pole level is assumed which will produce rated winding induced voltage at rated speed. A reluctance is defined for each distinct cross-section of the main magnetic flux path. Distinct cross-sections typically include the yoke, pole cores, pole shoes, air gap, teeth, and rotor core. As required, each reluctance is modified using the methods mentioned above, and the flux in each reluctance is assigned. The total mmf is then computed using the magnetic circuit approach.

Moullin [9] suggests that errors with this method are +/-10%. Uncertainty exists in the estimated mmf due to a number of reasons:

- i) The dimensions of the actual air gap may not be accurate, especially in small machines. These may be due to an eccentric rotor, or gaps between the

machined surfaces of the yoke and pole core at their joint.

- ii) An inaccurate knowledge of the iron properties, effects of laminations, or inhomogeneities in the steel due to casting.
- iii) Manufacturing defects, or errors in workmanship.
- iv) The magnetic history of the iron (hysteresis effects).

Some errors in the assumptions of the magnetic circuit model are present, but most of these will be negligible since they are a small percentage error in a small percentage of the total mmf drop (the mmf drops in the air gap and saturated teeth dominate).

The most significant region of saturation is in the teeth. In the example worked out in Moullin [9], for a 300 kW DC generator on open circuit with rated speed and 1.13 p.u. voltage, the mmf drops in the air gap and the teeth were 38% and 36%, respectively, of the total mmf. The significance of this, in terms of my research into machine saturation, is that my first priority for saturation modelling is to address the saturation in the teeth.

1.3.3 Graphical Methods

Numerous authors have developed methods of sketching magnetic field distributions by hand. Many have developed methods for use in air gap regions where the current density is zero, but fewer address the problem of regions, such as within field pole windings, where the current density is not zero.

Stevenson/Park [13] developed a method for hand plotting magnetic flux lines in both current and non-current carrying regions using "lines of no work" in current carrying regions, and "scalar magnetic equipotential" lines in non-current carrying regions. In order to understand the method they used, it is helpful to define some of their key terms: "scalar magnetic equipotential lines", "lines of no work", "kernels", and "flux tubes".

"Scalar magnetic equipotentials", or "scalar magnetic equipotential lines", were terms already used in the previous discussion of Carter's method. These are simply contours along which the scalar magnetic potential, Ω , remains constant. In regions where the current density $J \neq 0$, the scalar magnetic potential is not defined (see Hayt [12] p. 271), so in these regions the concept Stevenson and Park used in place of scalar equipotential lines was "lines of no work".

What is the difference between a line of no work and a scalar magnetic equipotential line? Moving from a to b along a line of no work in the current carrying region of Figure 1.1, the integral

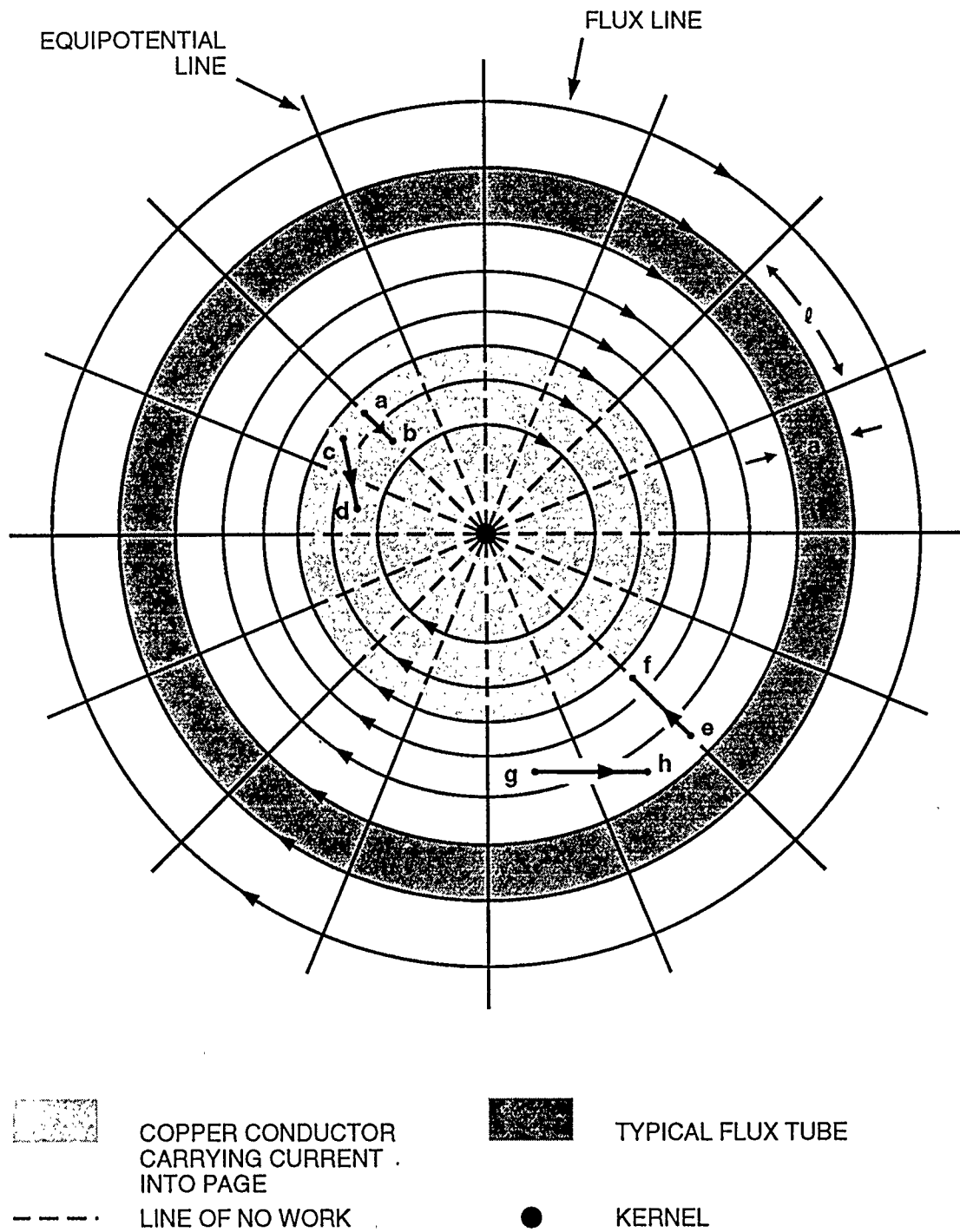


Figure 1.1: Magnetic Field Distribution Around a Current Carrying Conductor

$$\int_a^b \mathbf{H} \cdot d\ell \quad (1.9),$$

equals 0. This is because $\mathbf{H} \cdot d\ell$ equals 0 at all points along the integration path since \mathbf{H} , and therefore Φ , is normal to the integration path at all points between a and b . The name "line of no work" is coined because this integral is equal to the work done against the magnetic field in transporting a unit pole from point a to point b , which in this case equals 0. However, if we move from point c to point d , the integral does not equal 0 and this path is not a line of no work. Consider evaluating the integral along the path from point e to point f in the non-current carrying region (air). In this case, the above integral is defined as Ω_{ef} (the scalar magnetic potential between e and f). Ω_{ef} will equal zero since the integration path is along an equipotential line, and the flux is normal to every point along that line. Similar to the path from points c and d in the current carrying region, the path from points g to h is not an equipotential. Both scalar magnetic equipotential lines and lines of no work intersect flux lines at right angles within their respective regions. At the conductor-air interface, the scalar magnetic equipotential line becomes a line of no work.

Stevenson and Park also identified a "kernel" or "point of indifference" existing somewhere within the current carrying region. At this point, all of the lines of no work converge. The total current carried by the region is divided into equal portions by this kernel, the lines of no work, and the physical boundary of the current carrying region. Refer to the current carrying conductor of circular cross-section shown in Figure 1.1. All of the lines of flux are concentric with the centre of the conductor, and all of the lines of no work (within the conductor) and equipotentials (outside the conductor) are radially directed out from the centre of the conductor (therefore they intersect the flux lines at right angles). In this situation, the kernel coincides with the centre of the conductor, and the total current is divided up into equal portions. Each portion is bounded by the kernel, the lines of no work, and the outer surface of the conductor. For field coils around a field pole, the kernel normally does not coincide with the geometric centre of the coils.

As identified in Figure 1.1, a "flux tube" is the region enclosed between two successive sketched flux lines, with an assumed depth of 1.0 unit. Therefore, the area of a flux tube is equal to its sketched width. Formulas for computing Φ , \mathbf{B} , \mathbf{H} , etc. are found in reference

[13].

With these terms defined, let us look at the method itself. In short, the graphical method of plotting the field is done by trial and error, but experience with the method and knowledge of the expected solution can greatly accelerate the process, especially near the beginning. The outline of the iron structure is drawn, and scalar magnetic equipotentials are assigned to the outline of each of the identifiable boundaries. Major scalar equipotential contours and flux lines are drawn in regions where the field shape is well known, for example, in the centre of the air gap. Then, scalar magnetic equipotentials, lines of no work, and flux lines are drawn in all regions subject to the following criteria (refer to [13] for full details and some time-saving rules-of-thumb):

- i) all flux lines must cross scalar magnetic equipotentials and lines of no work at right angles,
- ii) flux lines enter the iron at right angles (for infinite permeability),
- iii) all rectangles in air are curvilinear squares, $(\ell/a) = 1.0$, where ℓ is the length of the flux tube between successive scalar magnetic equipotentials, and a is the distance between successive flux lines (the width of a flux tube), and
- iv) inside the current carrying region, $\ell/a < 1.0$ and ℓ/a equals the ratio of current enclosed by the flux tube, the two successive lines of no work, and the kernel; to the current enclosed by the border of the region, the two successive lines of no work, and the kernel.

If the sketch does not meet these conditions, the violating sections are resketched. The correct final solution is the one where the reluctance of the structure is minimized (i.e., the flux/pole is maximized). In Figure 1.1, the equipotentials are not drawn to meet the conditions in rules iii and iv in order to avoid cluttering the figure. About 41 radial equipotentials/lines of no work would be required to do this.

Stevenson/Park [13] provide full details of the theoretical development of this graphical method. They also use it to establish boundary conditions for analytical solutions for some simple problems. In order to do this, they represent the hand sketched solution obtained for a difficult boundary of the problem region as a Fourier series function. This Fourier series can then be manipulated algebraically when solving the total solution analytically.

Wieseman [14] wrote a supplementary paper to [13], where he applied the graphical

method to various situations of practical interest for a salient pole synchronous machine. For example, the effects of slots were determined, and the results presented in the same form as the results from Carter's method (see section 1.3.2). The two methods gave practically the same results. One of the main advantages of the graphical method over Carter's method is that fairly complex geometries can be tackled (under the assumption of infinite iron permeability) without mathematical complexity. Wieseman also computed pole fluxes for a salient field pole, and determined the first and third flux harmonics, similar to some of the work I have done in my research.

The advantages of this method are that it can provide a high level of detail, and it provides a good picture of the overall field distribution in the air and within the copper regions. The difficulties are:

- i) the process is subject to human error: it is unlikely the designer can properly check the entire solution region, and the hand measurements required to do the checking are subject to error;
- ii) to obtain higher accuracy, more man-hours and therefore more money are required, the accuracy is limited by the size of the sketch and the skill of the designer;
- iii) finite permeability and saturation are not considered; and
- iv) the method is not automatable for use in transient studies.

1.3.4 Permeance Distributions

Doherty/Nickle [15] used permeance distributions ($P(\theta)$'s) to compute radial flux density distributions ($B_r(\theta)$'s) from armature reaction mmf distributions ($\mathcal{F}(\theta)$'s) using the formula

$$B_r(\theta) = P(\theta)\mathcal{F}(\theta) \quad (1.10),$$

where θ is the angular position in the air gap. Permeance distributions were derived from graphically determined $B_r(\theta)$'s and assumed $\mathcal{F}(\theta)$'s using equation (1.10) (the assumed $\mathcal{F}(\theta)$'s are required to graphically determine the $B_r(\theta)$'s). Doherty and Nickle then used Fourier components of these permeance distributions, combined with Fourier components of armature reaction mmf, to compute Fourier components of air gap flux density, which they then used to determine the Fourier components of air gap winding voltages.

For an arbitrary salient pole iron structure and winding distribution the following

method can be used to predict $B_r(\theta)$ in the air gap, for different mmf conditions, based on only one field plot:

- i) using graphical sketching (section 1.3.3), or some other method, determine $B_{r,0}(\theta)$ (the radial flux density distribution corresponding to the zero order mmf harmonic) under infinite iron permeability conditions with a constant valued mmf distribution around the air gap ($\mathcal{F}_0(\theta) = \text{the zero order mmf harmonic} = \text{constant}$).
- ii) Compute $P_0(\theta) = B_{r,0}(\theta)/\mathcal{F}_0(\theta)$ where $P_0(\theta)$ is the permeance distribution for the zero order mmf harmonic.
- iii) For a uniform air gap machine, Doherty and Nickle derived the following formula:

$$P_n(\theta) = \frac{n\pi}{\tau} \coth\left(\frac{n\pi g}{\tau}\right) \quad (1.11),$$

where $P_n(\theta)$ is the permeance distribution of the n^{th} order mmf harmonic ($P_n(\theta) = \text{a constant for a uniform air gap machine}$), n is the order of the space harmonic of the mmf distribution on the armature surface ($n > 0$), g is the radial length of the air gap which is constant for a uniform air gap machine, and τ is the fundamental pole pitch.

The significance of this formula, which was derived analytically, is that the permeance distribution is different for each mmf harmonic order. Therefore, under linear conditions, the total $B_r(\theta)$ is the sum of the $B_{r,n}(\theta)$'s for each mmf harmonic, each of which, in turn, is the product $P_n(\theta)\mathcal{F}_n(\theta)$. In general, the $P_n(\theta)$'s determined from cosine and sine mmf distributions of the same order are different, but Doherty and Nickle demonstrated that for practical purposes they may be considered equal.

To extend this formula to a salient pole structure, Doherty and Nickle introduced the concept of an equivalent air gap. The equivalent air gap of a salient pole machine is computed from its $P_0(\theta)$ (determined in step ii above) according to the following formula:

$$g_{\text{eqv}}(\theta) = \frac{[P_0(\theta)]_{\text{max}}}{P_0(\theta)} g_{\text{min}}(\theta) \quad (1.12),$$

where $g_{\text{eqv}}(\theta)$ is the equivalent air gap at any point for a salient pole machine,

$g_{\min}(\theta)$ is the minimum air gap of the machine, which is at the same position as $[P_0(\theta)]_{\max}$ which is the maximum value of $P_0(\theta)$. $g_{\text{eqv}}(\theta)$ is then substituted into equation (1.11) to give:

$$P_n(\theta) \approx \frac{n\pi}{\tau} \coth\left(\frac{n\pi g_{\text{eqv}}(\theta)}{\tau}\right) \quad (1.13).$$

Equation (1.13) will then give the permeance distribution for any mmf harmonic for a salient pole machine. $P_n(\theta)$'s derived using this method, when compared with those determined directly from graphic plots done for each different mmf harmonic, were found to be in good agreement.

- iv) Assuming linearity, $B_r(\theta)$ is then found from the sum of all n harmonics of $B_{r,n}(\theta)$ where $B_{r,n}(\theta) = P_n(\theta)\mathcal{F}_n(\theta)$ as follows:

$$B_r(\theta) \approx P_0(\theta)\mathcal{F}_0(\theta) + P_1(\theta)\mathcal{F}_1(\theta) + P_2(\theta)\mathcal{F}_2(\theta) + \dots \quad (1.14).$$

In this equation, $P_0(\theta), P_1(\theta), P_2(\theta)$, etc. are each representable as a Fourier series since these functions are periodic. $\mathcal{F}_0(\theta), \mathcal{F}_1(\theta), \mathcal{F}_2(\theta)$, etc. are the coefficients of the mmf distribution's Fourier series (there will, in general, be both cosine and sine coefficients, but the permeance coefficient will be approximately the same for each of the cosine and sine coefficients of the same order). The mmf distribution's Fourier series is determined from the winding cross-section.

In [15], Doherty and Nickle did not provide any quantitative experimental confirmation of the accuracy of the above method for $B_r(\theta)$ determination, but only provided pictures of analogous iron filing distributions.

The advantages of this method are:

- i) the permeance distributions are readily expressed with Fourier series, therefore lending themselves easily to computer calculation (an advantage which, unfortunately, Doherty and Nickle were unable to exploit back in 1926). However, with Fourier series, they were able to generalize Blondel's two reaction salient pole synchronous machine theory, and obtain valuable insights into the relative importance of the different mmf harmonics during steady state operation.
- ii) it is mathematically simple to understand and implement.

The problems associated with this method are:

- i) finite permeability and saturation is neglected, and
- ii) we must do at least one flux plot under infinite permeability conditions in order to determine $P_o(\theta)$.

1.3.5 Integral Methods

Computerized implementation of the two dimensional Biot-Savart Law can be used to solve magnetic fields. The Biot-Savart Law is given below:

$$\mathbf{B} = \frac{\mu}{2\pi} \iint_R \frac{[y\mathbf{u}_x - x\mathbf{u}_y] J_z}{r^2} dR \quad (1.15),$$

where r is the distance from a current carrying point to the point of interest, \mathbf{u}_x is the unit vector in the x direction, \mathbf{u}_y is the unit vector in the y direction, J_z is the z component of current density, R defines the region of integration (usually the current carrying conductor cross-section), and dR is a differential element of that region. The Biot-Savart Law expresses the magnetic flux density at one point in space as the sum of the flux contributions of all of the current carrying elements in the solution region. This integral is discretized and evaluated at each point in the solution region independently. Hoole [16, pp. 111-135] gives a complete discussion of this approach.

The advantage of this method is that, for simple problems of high symmetry and uniform permeability, closed-form solutions can be obtained.

The problems with this method are as follows:

- i) special consideration must be given to points within the conductors where r drops to 0.
- ii) Modifications must be made to the Biot-Savart Law for inhomogeneous regions. These techniques, known as the "magnetization vector" and "boundary integral" methods are elaborated on in [16]. Matrix inversions in these methods are time consuming since the matrices are generally not symmetric or sparse.
- iii) It is difficult to make general purpose computer programs which can handle complicated and/or detailed structures (eg: a salient pole machine with teeth).

1.3.6 Finite Difference Methods

In general, for long machine lengths where flux variations in the axial (z) direction can be neglected, the two-dimensional steady state magnetic field is governed by the following

quasi-Poissonian equation in rectangular coordinates:

$$\frac{\partial}{\partial x} \left(\frac{1}{\mu} \frac{\partial A_z}{\partial x} \right) + \frac{\partial}{\partial y} \left(\frac{1}{\mu} \frac{\partial A_z}{\partial y} \right) = -J_z \quad (1.16),$$

where $\mu = \mu_o$ in air, $\mu = \mu_{\text{copper}} \cong \mu_o$ in the windings, $\mu = \mu_{\text{iron}}$ in the iron (μ_{iron} is subject to saturation and is therefore a function of A_z), A_z is the z component of the vector magnetic potential \mathbf{A} , and J_z is the z component of the current density vector \mathbf{J} (J_z is equal to 0 everywhere except in the windings). Equation 1.16 is valid in all regions of the machine, both in air and in iron, in saturated and non-saturated conditions, and in current carrying and non-current carrying regions.

For practical machine structures we cannot analytically solve this equation. The finite difference method is a numerical solution method which solves for A_z at a large number of points. A full discussion of this method is found in Hoole [16, pp. 73-109, 135-158] and Trutt/Erdelyi/Jackson [17]. The basic method is as follows:

- i) divide up the entire solution region with rectangular grids. Finer grids are required near material interfaces and small or irregular features. Areas where the flux distribution is not expected to be drastically changing may use a coarser grid. Use symmetry to limit the size of the region and reduce the grid size. Material interfaces should coincide with grid lines.
- ii) Define the boundary conditions (Neumann, where the normal derivative of the magnetic vector potential with respect to the boundary is zero; and Dirichlet, where the magnetic vector potential is known and is usually a constant).
- iii) Use algebraic interpolating equations to approximate the partial derivatives of equation 1.16 at each node (a node is the junction of two grid lines). Nodes where boundary conditions are defined and/or material interfaces exist require different approximating equations than nodes in the middle of homogeneous regions.
- iv) Solve the complete set of approximating equations simultaneously, in a fashion analogous to a circuit network solution, for the magnetic vector potential at each node. If the problem is small and linear, routine matrix inversion may be done (for example, Gaussian row reduction). If the problem is large, and/or saturation is occurring at some of the nodes, special non-linear matrix inversion procedures

must be used. References [16] and [17] use a technique known as "alternating successive overrelaxation", where an initial guess must be input at each node and the program recursively computes magnetic vector potentials and node permeabilities. If the initial guess is close enough, the difference between solutions for successive iterations will converge to within an acceptable error. This process is speeded up by using properly chosen acceleration and deceleration factors.

Burtness/Ahamed/Erdelyi [18] used the finite difference method to predict detailed magnetic fields in a saturated DC machine at no load. The finite difference method was the first to provide a full picture of the magnetic flux distribution in both the air gap and machine iron.

Coleman/Sarma/Erdelyi [19] used the finite difference method to model a saturated salient pole alternator. This machine had only 8 poles, so, to avoid errors due to curvature, the authors used rectangular coordinate grids for some sections of the machine, polar coordinate grids for others, and tied the different grids together with interpolating functions.

Fuchs/Erdelyi [20] used the finite difference method to model a large hydrogenerator, and used the computer generated field solution to compute the steady state direct and quadrature axis magnetizing reactances. This work bridged the gap between the finite difference model and steady state circuit models.

The advantages of the finite difference method are as follows:

- i) the approximation equations and solution method, though algebraically involved, are straightforward to derive and implement.
- ii) The solution process is fully computerized, and output plots can be computer generated.
- iii) Greater accuracy and detail can be obtained with this method than with any other method I have described so far. The ultimate limit of accuracy is dependent upon the available computing resources, the designer's available time and ability to properly define the grid system, and the program efficiency. The designer has full knowledge of the field and saturation conditions in all regions of the machine structure.

The problems with the finite difference method are as follows:

- i) large variations in permeability from region to region (as in an iron-air interface)

- slows convergence and reduces accuracy (see [18,19] and Chari/Silvester [21]).
- ii) Sometimes oscillation or divergence occurs in the matrix solution if the initial guess is poor, or if errors are made in the selection of acceleration or deceleration factors.
 - iii) Complicated programming is required to handle boundary conditions, material interfaces, regions of high field gradient, and small or rounded parts. Even with advanced procedures, such as graded meshes and false boundaries, accuracy is lower than in simple, homogeneous regions. Also, these programming requirements make it difficult to write general purpose software.
 - iv) Computing effort is high since, typically, several thousand nodes must be solved. Efficient memory storage algorithms that take advantage of symmetry and sparsity are required.

1.3.7 Finite Element Methods

Currently, finite element analysis is the most widely used method for computing two dimensional magnetic fields in rotating machines. According to Hoole [16, pp. 237-286] the concept of finite elements was first used in 1941, in the area of structural analysis, where a continuum of material was replaced with a lattice-work of steel struts. By 1956, this method was developed to a degree where it would be recognized as finite element analysis by today's standards. Finite element analysis was introduced into the electrical engineering area in 1967 by Winslow, under the name "finite differences for triangles"; but Silvester, starting in 1969, pioneered its use by applying it to many different electrical engineering magnetic field problems.

The following is a general description of the basics of the finite element approach:

- i) divide the solution region into elements. These elements can be of any size or orientation, but they should be properly fitted so that all elements contain only one type of material and the outline of the material interfaces is accurately traced out by the edges and corners of the elements. Finer elements may be used in regions of high field gradient, or where more accuracy or detail is required. The completed network of elements is known as a "mesh". In most electrical engineering applications triangular element shapes are used since they can be arranged with great flexibility, and simple expressions can be derived for their trial functions (see ii below).

Computational effort is reduced by choosing the smallest solution region possible by considering the symmetry and boundary conditions of the problem.

- ii) Postulate a trial function. A trial function is a function which represents the variable being solved for (in this case A_z) in the quasi-Poissonian equation (1.16). A separate trial function is defined for each element. As a simple example, for a triangular element shape, the selected trial function may be a first order polynomial with two free parameters. These free parameters are coefficients that are selected through some optimization criterion (see iii below) or boundary conditions (see iv below) to cause the trial function in each element to optimally approximate the actual A_z within each element. The variables and parameters of the trial function must be expressed in terms of coordinates uniquely defined by the nodes, dimensions, and shape of the element (eg: Cartesian coordinates are replaced with triangular coordinates for a triangular element).

There is a trade-off between the simplicity of the trial functions and the size and layout of the elements, and this trade-off becomes apparent when fine detail is required. If finer elements are used, simpler trial functions may be used. In order to tell if the trial functions and element layout are correct, we can look at the "roughness" of the field solution in a detailed area. In the correct solution, there should not be any large changes of slope (or kinks) in the field lines when crossing the border between successive elements (except at those material interfaces where a drastic change of permeability occurs). In the finite element solution, if these kinks do occur between elements of the same or similar permeability (giving the appearance of "roughness" in the plotted flux line), then the trial functions and/or the element sizes need to be changed until the roughness is smoothed out, bringing the approximated solution into better agreement with the actual solution.

The reason why using a different trial function may help is as follows: the free parameters of the trial functions in each of the elements are optimally chosen to match the actual field solution. If the element size is large, but the trial function's shape is similar to the shape of the actual field solution in that element, then the optimization procedure will adjust the free parameters to give the trial function a good fit within that element. If the permeability of successive elements changes little and the trial functions in all of these elements are the same, then the trial

functions in the successive elements will all have good fits, and the flux plot will be smooth and accurate.

The reason why using a smaller element size may help is as follows: if we have a relatively large element with a very simple trial function (eg: a straight line), and if the actual field has a significant curvature within this element, then the simple trial function does not have enough free parameters which can be adjusted to give a good approximation to the actual field. If, however, several small elements are used in place of this large one, then the simple trial function can give a better fit because it spans a smaller interval. In other words, a large number of short, straight lines can better approximate a twisting curve than a small number of long, straight lines.

- iii) Select an Optimization Criterion. This is necessary to determine the free parameters of the trial functions in all of the elements. As an example, a commonly used approach is the variational optimization technique, based on the principles of calculus of variations. The stored energy in the magnetic field is minimized by extremizing the energy functional of the magnetic vector potential, as given below:

$$\mathcal{L}[A_z] = \iint_R \left\{ \frac{1}{2} \frac{1}{\mu} [\nabla A_z]^2 - J_z A_z \right\} dR \quad (1.17),$$

where $\mathcal{L}[A_z]$ is the energy functional of the magnetic vector potential A_z . Other optimization methods exist, such as the least-square error criterion. See Hoole [16, pp. 287-311] for more detail.

- iv) Solve the matrix equations derived using the optimization criterion. To use the energy functional to solve a two dimensional field problem, (1.17) must first be expressed in terms of triangular coordinates and matrices. Then, in order to minimize the energy functional, the matrix derivative of the functional is set equal to zero, and the resulting matrix equation is solved. Boundary conditions are also introduced during this process: Dirichlet conditions are specified, but Neumann conditions can be neglected since the optimization procedure naturally satisfies them. Refer to Hoole [16] for details of this procedure.

The derivations and matrix manipulation of sections iii and iv are lengthy and complex; but, if properly programmed, are versatile. The complexity of the derivations largely depends on the selection of trial functions and optimization criteria. Additional complication is encountered when dealing with saturation phenomena in the iron, requiring recursive procedures. The $B-H$ curve can be modelled using one or more of several different formulas. Many other advanced topics are covered in Hoole [16].

One of the earliest references to using the finite element method for machine field analysis was Chari/Silvester [21], in 1971. Here the authors applied first order triangular finite elements (first order polynomial trial functions with triangular elements) to a round rotor turboalternator. A complete set of factory tests was predicted with an error, in all cases, of less than 1% from actual test values. In order to model saturation, a Newton-Raphson iteration technique was used which converged in 6 to 8 passes. The initial estimate for the Newton-Raphson technique was determined using a less sophisticated convergence technique known as the chord method.

The authors claimed that, for comparable results, the finite element method required about a tenth of the computing time required for a finite difference solution, largely due to the much smaller number of elements required with the finite element method than nodes required in the finite difference method. Since that early paper, Silvester has gone on to develop many more advanced techniques.

Hybrid finite elements can also be used, an example of which is Abdel-Razek [22], in 1981. An air gap "macro-element", in which an analytical field calculation was conducted, was used in place of finite elements in the air gap. Conventional elements were used in the rotor and stator iron, and these elements were spliced to the air gap macro-element through interpolating functions. This procedure was developed to improve computing times and accuracy for transient analysis studies. The problem they were addressing was that, as time elapsed, the rotation of the rotor with respect to the stator distorted the air gap elements, causing inaccurate field solutions. Until this work was done, this problem was normally handled by having the program frequently redraw the air gap mesh. This greatly increased the computing time.

Piriou/Abdel-Razek [3] used finite element analysis to precalculate inductance values in the steady state equations for a saturated salient pole machine.

Jian-She [23] used finite element analysis to determine the effects of saturation on

Blondel's two reaction circuit model parameters.

Krefta/Wasynczuk [6] derived a finite element based state model to predict transient operating conditions.

The advantages of the finite element method are as follows:

- i) modern PC based finite element programs have sophisticated pre- and post-processing capabilities, graphics, and user interfaces which keep the user from getting bogged down in mathematical and programming complexities, and automates the tedious finite element mesh preparation procedures needed to handle detailed rotating machine problems. These simple (to use) and accurate computer simulation programs give the machine designer more opportunity to eliminate design flaws before the expensive and time consuming prototype stage. This means reduced cost and product development time. Some packages' output is compatible with CAD and computer controlled manufacturing systems, which further improves the quality of the finished product and shortens development and production schedules [24].
- ii) Saturation in the machine iron can be accounted for.
- iii) No restriction is imposed on the density of mesh elements, so areas requiring detailed solution (such as air gaps or teeth) can have finer resolution, while areas of less interest (such as the stator backiron) can have coarser elements. This makes efficient use of the computing resources.
- iv) Boundary conditions are easily introduced without affecting the accuracy of the solution.
- v) Gives the full field solution in all regions of the machine.
- vi) Accuracy is limited only by mesh construction and computing resources.

The problems with the finite element method are as follows:

- i) derivation and programming of the finite element equations is complex and lengthy, requiring advanced mathematical and computer programming skills in order to develop a simple, fast, and accurate software package. This is, of course, reflected in the price of the software.
- ii) Computing times and memory storage must be reduced through sophisticated data storage and computational algorithms (see Hoole [16, pp.195-235]). Hardware platforms must be reasonably powerful: a fast 386 PC, or SUN Workstation is

required for many of the simplest packages [24]. The most complex ones require supercomputing facilities.

- iii) Using the finite element method in transient studies is accurate, but since a complete field solution is required at every time step, computing a full transient response for a saturated salient pole synchronous machine can be a slow process due to its computational intensity. This justifies the development of a faster process for computing the fields for transient analysis.

1.4 PROBLEM STATEMENT, RESEARCH GOAL, INITIAL PROPOSAL, AND OUTLINE

Based on the background information provided in section 1.3, we are now in a position to write our problem statement. The magnetic circuit approach, Carter's coefficients, rules of thumb, and graphical methods mentioned in section 1.3 are very useful for manual design and provide qualitative insight, but they are neither very accurate (especially when saturation is present), nor computerized. Therefore, they cannot play a significant role in transient analysis in machines. Analytical methods are generally not able to handle complex geometries, however, the boundary integral method is emerging as a competitor of finite element analysis for three dimensional problems, since the boundary integral method permits us to reduce the dimensionality of the problem by one (Hoole [16, pp. 6-7]). The finite difference method was largely ignored after the success of finite element methods became apparent. It is too computationally intensive, general purpose software cannot be written using it, and it is less accurate in some regions than the finite element method. The finite element method is the most accurate and best developed method we have, but it is slow in transient studies since it is computationally intensive and performs a complete solution at each time step. We need a simpler and faster method.

Therefore, the problem statement for this research is as follows:

PROBLEM STATEMENT

The existing method for performing transient analysis on rotating machines is unsatisfactory since it uses a finite element solution at each time step. This is computationally intensive and therefore involves long computation times and/or high cost.

The goal of this research, addressing the above problem statement, is as follows:

RESEARCH GOAL

To develop an alternative magnetic field solution method which will be much less computationally intensive than a finite element solution, but will still provide acceptable accuracy under all foreseeable steady state and transient conditions, including magnetic saturation.

My supervisor, Dr. T.H. Barton, felt that the classical field modelling work which had been published in the 1920's and 1930's (in references such as Stevenson/Park [13]) had the potential, if combined with today's personal computing power and his following initial proposal, to help me fulfill this research goal.

INITIAL PROPOSAL

Model the air gap magnetic flux distribution as a function of a position dependent, mmf independent reluctance in series with a position independent, mmf dependent reluctance.

The reasoning behind this proposal can be seen from the results mentioned at the end of section 1.3.2. Moullin (see reference [9]) used the magnetic circuit approach, Carter's coefficients, and rules of thumb to determine that at 1.13 p.u. open circuit voltage, the mmf drop due to saturation in the teeth of a 300 kW DC generator was 36% of the total, while that of the air gap was 38%. The mmf drop in the teeth is mostly due to saturation, since at 0.38 p.u. voltage, the mmf drop in the teeth is only 0.4% of the total. Tooth saturation effects were found to be the most significant of the saturation effects, since other regions of the machine iron did not have nearly the same increase in mmf drop: the second most saturated region was in the poles, whose portion of the total mmf drop goes from 1.5% at 0.38 p.u. voltage to 14.8% at 1.13 p.u. voltage.

If we wanted to characterize this type of magnetic behaviour with discrete reluctance components (using the magnetic circuit concept), we could approximate the reluctance of the entire magnetic circuit, R , with two reluctances in series.

The first of the two reluctances in series, R_{base} , would be constant valued, and would, itself, be the sum of the reluctances of the air gap, R_{air} , which is not subject to saturation; plus the constant reluctance of the machine iron, R_{lin} , which represents the iron in its linear region of operation. R_{base} , by definition, will not change even when the machine iron is in saturation.

The second of the two reluctances in series, R_{sat} , would represent the increase in the

total reluctance of the magnetic circuit due to saturation (primarily in the teeth; but also, to some degree, in the other iron parts).

Looking at it another way, if the total reluctance of the machine iron, R_{iron} , were defined in the normal way, it would increase as the saturation in the iron increases; but what I have done is split R_{iron} into two parts: the linear (constant) portion, R_{lin} (which is added to the air gap reluctance, R_{air}); and the difference between R_{iron} and R_{lin} , R_{sat} , being left to be characterized independently.

The equations below summarize this:

$$\begin{aligned} R &= R_{\text{air}} + R_{\text{iron}} \\ &= R_{\text{air}} + R_{\text{lin}} + R_{\text{sat}} \\ &= R_{\text{base}} + R_{\text{sat}} \end{aligned} \tag{1.18},$$

where $R_{\text{iron}} = R_{\text{lin}} + R_{\text{sat}}$ (1.19),

and $R_{\text{base}} = R_{\text{air}} + R_{\text{lin}}$ (1.20).

One of the weaknesses with the magnetic circuit approach, however, is that R_{base} and R_{sat} are gross parameters, not giving any information at all about the details of the radial flux density distribution ($B_r(\theta)$) in the air gap. θ is the angular position in the air gap. Detailed knowledge of the flux density distribution is necessary to determine all of the torque and induced voltages in the machine.

In order to obtain this distribution, R_{base} must be defined in terms of its distribution around the air gap of the machine, $R_{\text{base}}(\theta)$. $R_{\text{base}}(\theta)$ will be strongly affected by saliency and the shape of the pole face. The effect of armature teeth on $B_r(\theta)$ and $R_{\text{base}}(\theta)$ will be apparent if we consider their distributions around the air gap at different cross-sections along the length of the rotor. However, since armature teeth are normally skewed, $B_r(\theta)$'s harmonics due to the teeth (say, the 15th and higher) are largely smoothed out and their effects upon torque and induced voltage are negligible (see Moullin [9, p. 267]).

R_{sat} is expected to be a function of the applied mmf in the magnetic circuit because

of the saturation characteristic of the iron (the applied mmf, itself, is current and position dependent). R_{sat} will also be position dependent due to pole saliency and the damper bar slots in the pole faces. Therefore $R_{\text{sat}} = R_{\text{sat}}(\mathcal{F}, \theta)$, where \mathcal{F} is the position dependent mmf applied by the currents in the windings.

A major part of this research concerns characterizing $R_{\text{base}}(\theta)$ and $R_{\text{sat}}(\mathcal{F}, \theta)$ for use in the field prediction model, and determining if it is valid to consider $R_{\text{sat}}(\mathcal{F}, \theta)$ to be independent of position. In other words, is $R_{\text{sat}}(\mathcal{F}, \theta) = R_{\text{sat}}(\mathcal{F})$?

OUTLINE

The remainder of this document can be broken down in the following manner:

Chapter 2:

This chapter describes the equipment and procedures used to gather the experimental data:

- i) the measurement requirements for developing and testing the flux density distribution model;
- ii) the specially modified salient pole synchronous motor, and the instrumentation systems used to measure magnetic field distributions;
- iii) the PC based data acquisition system, and the measurement procedures used to collect and store the magnetic field distributions; and
- iv) some typical measurement results.

Chapter 3:

This chapter describes how $R_{\text{base}}(\theta)$ and $R_{\text{sat}}(\mathcal{F})$ are characterized:

- i) details of the strategy for finding $R_{\text{base}}(\theta)$ and $R_{\text{sat}}(\mathcal{F})$,
- ii) averaging of $B_r(\theta)$ distributions,
- iii) determining armature mmf distributions and $R_{\text{base}}(\theta)$, and
- iv) determining field mmf distributions and $R_{\text{sat}}(\mathcal{F})$.

Chapter 4:

This chapter describes development and testing of the $B_r(\theta)$ distribution program:

- i) assumptions used in the program,
- ii) comparison of program results to measured $B_r(\theta)$ distributions, and
- iii) potential modifications.

Chapter 5:

This chapter describes how the $B_r(\theta)$ distribution program is used to predict steady state torque, and evaluates its performance:

- i) summary of torque calculation methods and selection of the flux linkage approach,
- ii) integration of torque calculation into the $B_r(\theta)$ distribution program, and
- iii) comparison of computed and measured steady state torques.

Chapter 6:

This chapter describes how the $B_r(\theta)$ distribution program is used to predict steady state phase voltages:

- i) using the flux linkage voltage calculation in conjunction with D-Q axis theory,
- ii) comparison of computed voltage distributions from measured and modelled $B_r(\theta)$ distributions, and
- iii) results of computer prediction of steady state operating characteristics.

Chapter 7:

This chapter draws conclusions and identifies possible future work:

- i) effectiveness of the $B_r(\theta)$ distribution program for steady state analysis, and
- ii) extension of the $B_r(\theta)$ distribution program to transient analysis.

CHAPTER 2

EQUIPMENT AND MEASUREMENT SYSTEM

2.0 CHAPTER OBJECTIVES

- i) *Describe the measurement requirements for developing and testing the flux density distribution model, and how the equipment and measurement system satisfies these requirements.*
- ii) *Describe the specially modified synchronous motor, and its instrumentation.*
- iii) *Describe the personal computer (PC) based data acquisition system, and the measurement procedures used to collect and process radial flux density distribution data.*
- iv) *Present data from actual measurement runs and comment on its main features.*

2.1 MEASUREMENT REQUIREMENTS

2.1.1 The Proposal's Requirements

In Chapter 1, we saw that we will need to find $R_{\text{base}}(\theta)$ and $R_{\text{sat}}(\mathcal{F}, \theta)$. In order to characterize them from experiments, we need to have a basic mathematical definition for them which relates them to quantities we can measure experimentally. We can attempt a simplistic derivation based on the Ohm's Law analogy used in the magnetic circuit approach (see section 1.3.1). The equation

$$R = \frac{\mathcal{F}}{\Phi} \quad (2.1);$$

is valid for a magnetic field path having uniform cross-section, and large, constant, and uniform permeability (which permits us to neglect leakage flux).

In an actual salient pole machine, all of these assumptions are violated. Further, equation 2.1 does not provide any detail of the distribution of magnetic flux density, B , which is critical for predicting the machine's behaviour. In an actual machine B is a function of angular position due to saliency, chamfered pole faces, and teeth. B will also vary with radial position. Due to the saturation characteristic of the iron, B is also a function of the applied mmf, \mathcal{F} , in the magnetic circuit (the applied mmf is also a function of position). Due to the effects of slot skewing in the armature, the teeth are in a different

angular position at each axial position (contour) along the armature surface, therefore B is also a function of the axial depth z . End effects also cause a variation with axial depth. As a result of all these factors affecting B , in terms of functional notation B may be expressed as $B(\theta, r, z, \mathcal{F})$.

Since $B(\theta, r, z, \mathcal{F})$ is a function of so many variables, a model using a single, constant magnetic circuit reluctance value is insufficient to determine $B(\theta, r, z, \mathcal{F})$. However, if we approximate the actual machine magnetic circuit with a large number of narrow cross-section parallel magnetic circuits, we can expect to get a better prediction of $B(\theta, r, z, \mathcal{F})$. If we take an infinite number of parallel circuits, we can express equation 2.1 in continuous form as:

$$R(\theta, r, z, \mathcal{F}) = \frac{\mathcal{F}(\theta, r, z)}{B(\theta, r, z, \mathcal{F})} \quad (2.2).$$

Equation 2.2 suggests that $R(\theta, r, z, \mathcal{F})$ can be determined from:

- i) a knowledge of the mmf distribution (in equation 2.2 it is expressed explicitly in terms of its position dependence). The mmf distribution can be determined from the winding distributions and magnetic structure of the machine.
- ii) The flux density distribution in the magnetic circuit, which is available from measurements.

The original definition of reluctance given in equation 1.18 can be expanded as follows:

$$R(\theta, r, z, \mathcal{F}) = R_{\text{base}}(\theta, r, z) + R_{\text{sat}}(\theta, r, z, \mathcal{F}) \quad (2.3).$$

In equation 2.3, R is expressed in terms of R_{base} and R_{sat} . Since R will be determined from steps i and ii above, R_{base} and R_{sat} can then be characterized. In order to use the proposed method of Chapter 1, R_{base} must be characterized as a function of θ only. In order to do this, we will always work with a constant radius, r , just above the surface of the rotor in the air gap; and we will use averaged data runs along the length of the rotor to eliminate variation with z . This automatically eliminates dependence upon r and z in R_{sat} . The proposal calls for R_{sat} to be dependent only upon mmf. Therefore, R_{sat} 's dependence upon θ is neglected and R_{sat} is characterized as a function of \mathcal{F} only. Chapter 3 discusses the characterization of R_{base} and R_{sat} in detail.

The continuous form of the magnetic circuit equation, equation 2.2, provides the mathematical basis for my flux density distribution model. My approach to developing it can be summarized in the following two steps (note that all of the functional notation has been dropped for simplicity):

- i) with known \mathcal{F} 's and B 's, R is found for different operating conditions using equation 2.2. R_{base} and R_{sat} are characterized from R using equation 2.3.
- ii) With known \mathcal{F} 's and a characterized R_{base} and R_{sat} , R is determined for different operating conditions using equation 2.3. B 's for these conditions are calculated using equation 2.4 below:

$$B(\theta, r, z, \mathcal{F}) = \frac{\mathcal{F}(\theta, r, z)}{R(\theta, r, z, \mathcal{F})} \quad (2.4).$$

Step ii is merely the reverse of step i, and equation 2.4 is simply equation 2.2 rearranged.

This chapter and Chapter 3 deal with step i, the remaining chapters with step ii. The effects of neglecting various parameters in R_{base} and R_{sat} are examined in Chapter 3. The validity of using equation 2.4 to predict magnetic field distributions from known \mathcal{F} 's and the characterized R_{base} and R_{sat} under variable operating conditions are demonstrated in chapters 4 and 5. Since there is no rigorous mathematical proof for equations 2.2 or 2.4 (both having been derived from approximate equations in the first place), I depend entirely on measurements to determine their validity and accuracy. Measured B distribution and torque data will be compared to modelled data for the same conditions.

In equations 2.2 and 2.4, B is used instead of Φ , so that the units of R are no longer amp-turns/Wb, but rather amp-turns/Wb/m². This means that R is not the same as the "reluctance" of the conventional magnetic circuit method, but could instead be called a "reluctance density distribution", a "reluctance distribution" or a "reluctance wave". From this point on, in this document, any of these terms will mean the continuous distribution of reluctance as a function of angular position, as defined by equation 2.2, unless I indicate otherwise. The reasons I changed this definition are to simplify the computation of R and simplify the comparison of modelled and experimental results. My experimental equipment determines B data directly, so the conversion from B data to Φ for computing R , and converting modelled Φ 's back to B 's for comparison with experimental data give no additional insights and increase computing requirements.

Based upon the previous description of how the proposed flux density distribution model will be developed and tested, it is obvious that being able to determine B distributions is necessary to both development and testing.

2.1.2 Available Methods for Determining B Distributions

In Chapter 1, we found that analytical methods such as Schwarz's transformation were very mathematically involved, and were restricted to infinite permeabilities and very simple geometries. Application of the Biot-Savart Law was subject to similar restrictions, although by using some elaborate techniques it can handle regions of finite permeability. To practically simulate real machines with complicating factors such as teeth, damper bar slots, salient poles, and saturation, a finite element analysis program is required. This method provides complete field solutions for all points within the machine structure, which helps us to identify local regions of saturation within the teeth or in parts having narrow cross-sections. Unfortunately a finite element package was not available during the course of my research. If it had been, it would have provided me with all the B distributions I needed to conduct my research. However, I would still need to make experimental verification. Instead I used a specially modified salient pole synchronous motor with a radial flux density measurement probe and a torque transducer. All of the measurements made on this motor were under static conditions (no rotation). DC currents were circulated in the windings to simulate balanced steady state conditions. This equipment allowed me to develop and test the B distribution model. Details of the motor, its instrumentation, and its measurement conditions are provided in section 2.2, and details of the PC based data acquisition system are provided in section 2.3.

This experimental set-up (see Figure 2.1) allowed me to collect data for the radial component of magnetic flux density in the air gap. I obtained this data using a Hall effect flux density probe which was attached to a rotating disk. The disk's axis was concentric with the shaft of the motor, which was mounted vertically with its top end bell removed. The probe was at the end of a long, narrow shaft which descended from the disk into the air gap of the motor. As the disk rotates, the instrumentation and data acquisition system collect data for all angular positions, θ 's, in the air gap. The vertical position of the probe can be adjusted to any contour depth, z , along the length of the rotor (armature). However, the radial position, r , of the probe in the air gap cannot be adjusted. This is because the probe shaft holder is set at a fixed radius on the disk. The radial position of

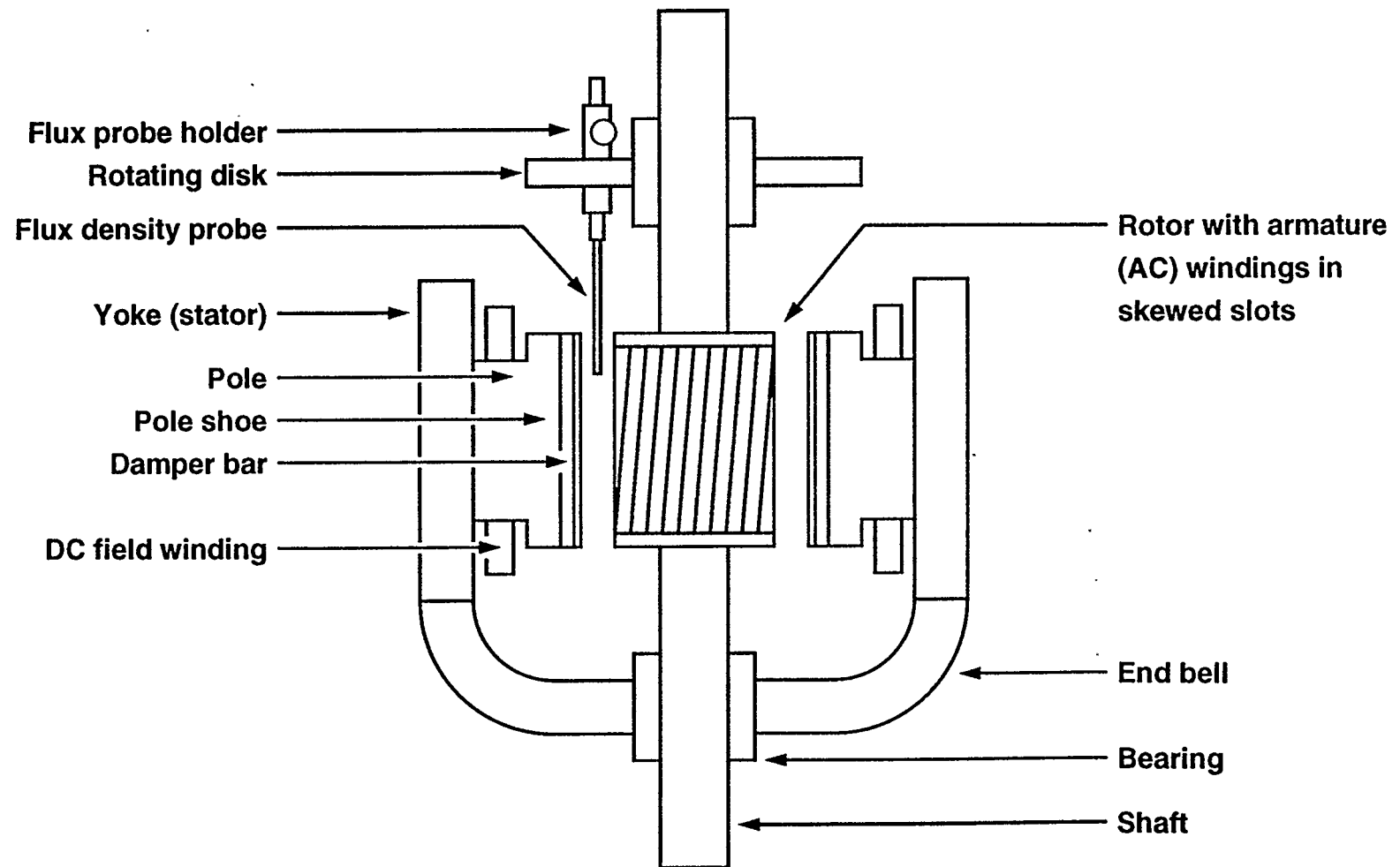


Figure 2.1: Cross-Section of Specially Modified Synchronous Motor

the probe was set to keep the probe as close as possible to the rotor surface to ensure that the magnetic flux lines were normal to the Hall effect crystal's surface.

2.1.3 Suitability of the Experimental Equipment for Developing and Testing the B Distribution Model

In this section I will show that the air gap radial flux density data collected by my experimental equipment is suitable for developing and testing the B distribution model.

A major restriction in using the magnetic circuit approach, equations 2.2 and 2.4, comes from the fact that the magnetic flux is a vector quantity, \mathbf{B} . The magnetic circuit approach assumes that the direction of \mathbf{B} is always normal to the cross-section of the magnetic circuit. Therefore, in order for the magnetic circuit approach to predict the correct B (the magnitude of \mathbf{B}), the cross-section of the magnetic circuit must always be normal to the direction of \mathbf{B} . If I extend the magnetic circuit idea to model a complex geometry, I require a large number of parallel magnetic circuits. However, the requirement for \mathbf{B} to be normal to each magnetic circuit's cross-section still holds. When I extend this approach to the continuous case (as defined by equations 2.2 and 2.4), \mathbf{B} must be normal, at every point, to the cross-section on which I want to define B , R , and \mathcal{F} .

Only a small subset of all possible cross-sections in the magnetic field region satisfy this normality condition. Even fewer satisfy this normality condition and also permit us to define B , R , and \mathcal{F} over their entire length. The air gap region of the machine is one place where this can be done. Chapter 3 discusses the mmf distribution in the air gap, so I will now describe the conditions under which normality can be assumed in the air gap, and show that my Hall effect probe always measures this normal (radial) field.

It is vital that the probe is always normal to the air gap field. When collecting data using the Hall effect probe, it is rotated around the air gap of the motor at a constant depth. If \mathbf{B} is normal to the traced path at all points, then B_r (the radial component of \mathbf{B}) is equal to the magnitude of \mathbf{B} at all points as well. If the Hall effect probe is oriented to measure B_r data directly, this measured data can be used in equations 2.2 and 2.4 directly.

For \mathbf{B} to be approximately normal to the traced path at all points along its length, the flux density probe must rotate around the air gap in close proximity to the surface of the armature. This restriction can be readily seen by examining the boundary conditions at

an iron-air interface (see Hoole [16, p. 11]). For interfaces free of current densities,

$$B_{r,1} = B_{r,2} \quad (2.5),$$

and

$$H_{\theta,1} = H_{\theta,2} \quad (2.6);$$

where $B_{r,1}$ and $B_{r,2}$ are the radial components of magnetic flux density in materials 1 and 2 respectively; and $H_{\theta,1}$ and $H_{\theta,2}$ are the tangential components of magnetic field intensity in those materials. For linear conditions, equation 2.6 may be expressed as

$$\frac{B_{\theta,1}}{\mu_1} = \frac{B_{\theta,2}}{\mu_2} \quad (2.7),$$

where $B_{\theta,1}$ and $B_{\theta,2}$ are the tangential components of magnetic flux density, and μ_1 and μ_2 are the permeabilities. Let material 1 be air and material 2 be iron, and let the permeability of the iron go to infinity. Equation 2.7 then says that $B_{\theta,1}$ goes to zero, and that the magnetic flux density in the air possesses only a radial component (which is normal to the iron-air interface). For typical machine steel operating in the linear region, μ_2 may be about 300 times that of air (Hayt [12, p. 509]). Therefore, $B_{\theta,1}$ will be about $1/300^{\text{th}}$ of $B_{\theta,2}$, which is still a very small quantity. Under heavy saturation conditions, the effect upon the tangential components of the field is the same as if μ_2 decreases. $B_{\theta,1}$ may be around $1/100^{\text{th}}$ of $B_{\theta,2}$, depending upon the shape of the saturation curve (see reference [17, p. 16] for an example curve). Special irons can make the normality assumption even more valid. Silicon iron has a μ which is about 3500 times that of air, making the value of $B_{\theta,1}$ vanishingly small (Hayt [12, p. 509]).

These interface conditions are only valid at the interface, but since the flux lines are smooth curves in air, normality or near normality extends some distance into the air gap. With my experimental salient pole machine, for angular positions beneath the pole faces, normality may be assumed at any point in the air gap between the pole face and the armature face. In regions close to the neutral axis (where lines of flux are forced to curve the most), the normality condition is probably still valid at distances up to an air gap width from the armature surface (the air gap width is defined as the minimum radial clearance

between the pole face and the armature face). See reference [20] for some typical plots. Slots can cause a deviation from normality since the lines of flux spread apart above the slot in order to enter the tops and sides of the teeth. However, the angular deviation from normality is small, say within 5° to 10° mechanical, until you get right beside the teeth (see reference [20]). If the angular deviation of the Hall effect crystal surface's normal from the field vector is even as high as 10° mechanical, then the error is only about 1.5% due to the dot product relationship between the normal and the field. My measurement equipment keeps the probe within 1 mm of the armature surface, yet still above the tooth tops. Since the air gap width (as previously defined) is 3.2 mm, and since the deviation from normality over the slots is small where the probe is measuring, then the collected data will meet the normality requirement. It will then be suitable for direct use in equations 2.2 and 2.4. Figure 2.4 in Section 2.4 is an example of a measured data run.

Another factor affecting the measurements, which I will address in Chapter 3 and Appendix B, is slot skewing. In my machine, the armature slots do not run parallel to the axis of the machine, but are skewed by a small angle. This results in a different flux density distribution at every axial position, z , along the machine length since the angular position of all of the tooth tops is shifted by a small amount with every small change in z . Figure 2.5 in Section 2.4 shows this effect.

Using B_r to determine the air gap torque and the induced winding emf in rotating machines is part of the classic approach. To predict these quantities, Moullin [9, pp. 5-15, 38-39] and other authors use B_r in the air gap, and the general flux linkage torque and voltage equations. These equations are given below as :

$$T = -i \frac{\partial \Phi}{\partial \theta} \quad (2.8),$$

and

$$E = - \frac{\partial \Phi}{\partial t} \quad (2.9).$$

Here T is the induced torque and E is the induced emf for a single turn coil. Φ is the flux linking the coil, and i is the current flowing in the coil. See Appendix B for the derivation of the expanded forms of these equations which I used for the multiple turn windings in my machine.

In order to make the mathematics tractable linearity is normally assumed in the references, and the effects of saturation upon B_r are neglected. Equations 2.8 and 2.9 (and their expanded forms) are valid under both linear and saturation conditions because they require only B_r 's actual values in the air gap. In other words, saturation effects may complicate how we determine B_r , but once we have it, equations 2.8 and 2.9 can be used in exactly the same way as if no saturation were present. Therefore, in order to model the effects of saturation in the machine, all I need to do is properly characterize the effects of saturation upon B_r , and the correct torque and voltage quantities will be found using equations 2.8 and 2.9.

Intuitively, since all of the torque that the machine produces is transmitted from the stator, through the magnetic field, and into the rotor; it would seem reasonable that this torque could be determined from a knowledge of the magnetic field in the air gap. Equation 2.8, as well as other formulations such as Maxwell's Tensor (see reference [22] and equation 5.6), are means of determining rotor torque from this information. In order to satisfy the power balance in the windings, the electrical power entering the windings has to equal the mechanical power exerted by the windings on the machine iron, or vice versa. Equations 2.8 and 2.9 satisfy this power balance condition when applied to the same winding under the same time varying field conditions (caused by rotational motion of the winding through the field).

In summary, the experimental equipment I have will permit me to develop and test the B distribution model as follows:

- i) I will be able to characterize the F distributions by using the experimental data in equation 2.2. This will permit me to use the reverse process, equation 2.4, to develop the B distribution model.
- ii) I will be able to check the shape of the B distributions computed using my model with the experimental data for the same conditions.
- iii) Since my experimental equipment can measure the stationary shaft torque of the machine, I can use these torque measurements to check the calculated torque from my B distribution model and equation 2.8.

2.2 EXPERIMENTAL MOTOR, INSTRUMENTATION, AND MEASUREMENT CONDITIONS

2.2.1 Experimental Motor

Figure 2.1, back in section 2.1.2, is a schematic cross-section of the specially modified salient pole synchronous motor used for data collection.

One end bell was removed from the motor, and it was mounted vertically onto a frame. On the top end there is a rotating disk, concentric with the motor shaft, which supports the flux probe. This disk is rotated using a small auxiliary single-phase synchronous (constant speed) motor. On the bottom end, the shaft is coupled to a torque transducer, and the other end of the torque transducer is coupled to a disk/worm gear combination. This gear configuration permits a small auxiliary DC motor to rotate the rotor to any desired angular position, but prevents the rotor from rotating because of induced electromagnetic torques.

The ratings for the machine are found in Fahmy/Browne/Silvester/Barton [25]. It is a three phase, four pole synchronous motor rated at 440 volts, 14.5 amps, 10 HP, 0.8 pf lead, 1800 rpm. The salient poles are on the stator, and each has a 1068 turn field excitation winding. Each pole face has 5 copper damper bars, connected as a squirrel cage. The three-phase armature windings are embedded in a 48 slot rotor, and the slots are skewed by one slot pitch over the length of the rotor. The armature core length is 17.3 cm, the rotor diameter is 20.85 cm, and the stator bore is 21.49 cm. The minimum air gap is 3.2 mm. The face of the pole shoe is chamfered, starting at 39° electrical from the pole centre-line and increasing linearly until the air gap is 7.94 mm, at which point there is a rounded corner.

2.2.2 Instrumentation and Auxiliary Systems

The Hall effect probe is key to measuring the radial distribution of magnetic flux density, B_r . It consists of a Hall effect crystal at the tip of a 45.7 cm long aluminum shaft of thin, rectangular cross-section. Electrical output from this probe is fed into a gaussmeter, which provides an analog gauge reading and 0 to 1 volt analog voltage output proportional to B_r . The active crystal area is about 1.8 mm in diameter, and the measured B_r is averaged over this area. The basic principle behind the Hall effect probe (see reference [26]) is that with a current flowing in the crystal, a force will be exerted on the moving charges if magnetic flux density is applied at right angles to the current flow.

The equation governing this force is:

$$\mathbf{F} = q\mathbf{v} \times \mathbf{B} \quad (2.10),$$

where \mathbf{F} is the force exerted on a particle, q is the particle charge, \mathbf{v} is the particle velocity, and \mathbf{B} is the magnetic flux density vector normal to the Hall effect crystal. The average magnitude of this vector on the crystal surface is B_r , which I use in my measurements.

\mathbf{F} will cause the moving charges to be deflected in a direction normal to both the current flow and \mathbf{B} , causing charge separation in the crystal. Electrostatic forces act in a direction which opposes this charge separation. The two forces eventually balance each other and a stable voltage difference can be measured across the crystal. This voltage difference is detected, amplified, and scaled by the gaussmeter. During probe rotation, the measured B_r distribution is slowly changing, but the response time of the measurement system is fast enough that no dynamic error is introduced.

The Hall effect probe is very fragile, which eliminates the possibility of using it in the air gap of an actual rotating machine. This is the reason why the experimental machine has been specially mounted and only static measurements can be collected.

Two potentiometers are available which give output voltages proportional to the probe position and the rotor position. The only potentiometer I used in my research was the one for probe position, since my flux density readings were always taken with the rotor fixed and the probe slowly rotating around the air gap under the power of its drive motor. While the probe travelled, the probe position potentiometer output voltage was sampled simultaneously with the flux density reading at a rate of about 10.0 Hz. Visual gauges are also present on the equipment which give these positions in mechanical degrees. Both visual gauges were extensively used to correlate data runs.

The torque transducer/torque meter provided an analog voltage output proportional to torque on the machine shaft. This data was especially useful for Chapter 5. A 60 Hz AC signal is applied to the windings of a primary coil. The core of the coil is a thin walled steel tube (about 1 mm wall thickness) which transmits the full torque of the rotor to the fixed frame. If there is no torque on the tube, then the voltage of a secondary coil (also wrapped around the tube) will be in phase with the voltage of the primary coil. The two voltages are compared using a phase detector, and a 0 torque reference voltage is given. As electromagnetic torque is applied to the rotor, it is transmitted through the torque tube,

the phase of the secondary coil changes with respect to the primary, and the phase detector output voltage changes in proportion to the rotor torque.

A description of the inaccuracies in these instrument systems, and how they were handled, is given in Appendix A.

2.2.3 Using Static Measurements

Although the motor is no longer operable, the static field measurements we can obtain from it still represent the field conditions present under steady state operating conditions. Under balanced steady state conditions the fundamental armature mmf distribution, caused by the time fundamentals of the three phase currents, remains fixed with respect to the field poles (see references [7, pp. 146-150], Langsdorf [27, pp. 199-218], and Appendix C).

The higher harmonics of armature mmf, caused by both the winding shape (space harmonics) and the time harmonics of current, rotate at various speeds with respect to the field poles. However, the magnitude of these harmonics is inversely proportional to their harmonic order, and the armature reaction mmf's magnitude is small relative to the field mmf's magnitude under normal operating conditions. Therefore, unless very high accuracy is required, the higher order space and time harmonics are normally neglected and only the fundamental is considered. This assumption will be checked and confirmed in Chapter 3.

Since the armature windings' fundamental mmf distribution remains fixed in space (relative to the field poles) under steady state conditions, I can easily establish static field measurement conditions which closely resemble the magnetic fields present under balanced steady state operating conditions. Terminations for the windings of each of the three armature phases and the field are accessible, so I can connect and energize them to simulate different operating conditions.

For no load conditions, steady state conditions are simulated by simply exciting the field windings with DC current. No armature current flows. The no load terminal voltage for the machine would be induced in the windings if the machine were actually rotating.

Under load conditions, balanced three phase currents exist in the armature windings. Space superposition of the individual phase winding mmf's caused by the phase currents, combined with the armature's rotation with respect to the field poles, creates the resultant armature mmf wave. For balanced steady state operation, the resultant mmf distribution

(neglecting harmonics) has a constant magnitude and angular position relative to the field poles. In order to create a flux distribution corresponding to this situation, I can pass DC currents through both the armature windings and the field windings. The experimental DC current level in the field windings can be whatever the operating conditions require. However, in order to choose the proper current levels in the armature phases, the experimental DC current magnitudes in the armature phases must be set equal to the instantaneous current values which occur in a balanced three phase winding set for some point in time during the AC cycle. Neglecting the effects of harmonics, the armature mmf distribution is constant in time and space (relative to the field poles) during the entire cycle, and I can select a point in the cycle which makes connecting and energizing the windings as simple as possible.

For most points in the cycle, because each instantaneous phase current has a different value, it is impossible to obtain the proper experimental DC currents in all three phases without using a separate DC voltage source to energize each phase (I did not have enough equipment to do this). If we consider the point in time when the phase a current is equal to twice the phase b and c currents, it would be possible to use just one voltage source by connecting the phase a winding in series with the phase b and c windings in parallel. Unfortunately, since the resistances of the windings are not exactly equal, the currents in the phase b and c windings are not equal, which is required to simulate balanced conditions.

However, consider the point in time when the instantaneous current in one phase, say phase c, is zero. Then, since Kirchoff's current law specifies that the sum of the three phase currents entering the neutral equals zero, the phase currents in phases a and b must be equal in magnitude and opposite in direction. This point in the cycle can be easily simulated by connecting phases a and b in series and letting phase c remain unconnected, as shown in Figure 2.2. A single voltage source can be used, and the difference between phase resistances is inconsequential since no parallel connections are involved. This is the connection I used for simulating all loaded conditions.

It is necessary to define a relation between the AC rms phase currents and the experimental DC currents in order to know what experimental DC current to pass through the windings when simulating the actual loaded machine. Let a balanced three phase circuit have instantaneous phase currents defined by:

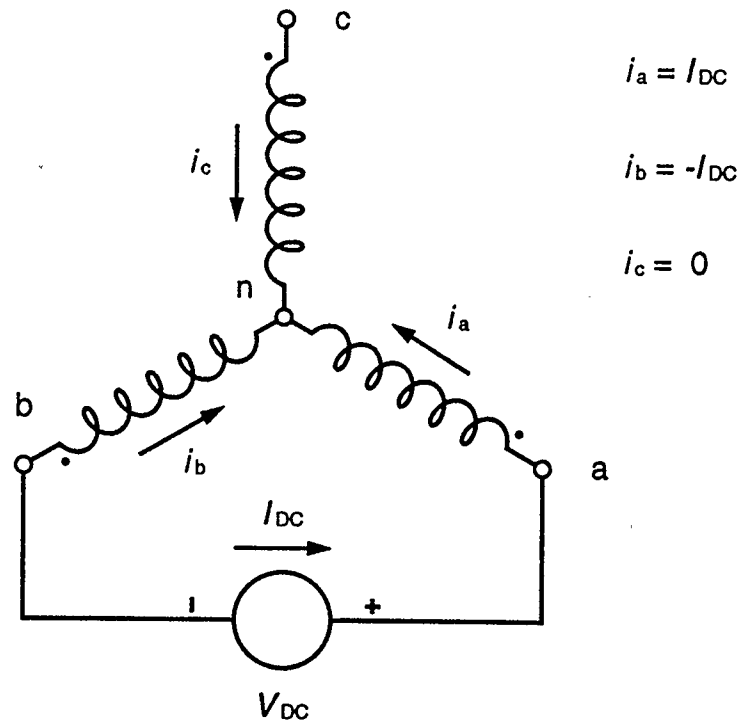


Figure 2.2: Experimental Armature Winding Connections

$$\begin{aligned}
 i_a &= \sqrt{2} I_{rms} \cos(\omega t) \\
 i_b &= \sqrt{2} I_{rms} \cos\left(\omega t - \frac{2\pi}{3}\right) \\
 i_c &= \sqrt{2} I_{rms} \cos\left(\omega t - \frac{4\pi}{3}\right)
 \end{aligned}
 \tag{2.11},$$

where i_a , i_b , and i_c are the three instantaneous phase currents, I_{rms} is the AC rms magnitude of the current, and ω is the angular frequency. If we select the point in time when $\omega t = -\pi/6$, then

$$\begin{aligned}
 i_a &= \sqrt{2} \frac{\sqrt{3}}{2} I_{\text{rms}} \\
 i_b &= -\sqrt{2} \frac{\sqrt{3}}{2} I_{\text{rms}} \\
 i_c &= 0
 \end{aligned}
 \tag{2.12}.$$

Since the instantaneous magnitude at this point in time equals the experimental DC current magnitude in the windings (I_{DC}), then

$$I_{\text{DC}} = \sqrt{2} \frac{\sqrt{3}}{2} I_{\text{rms}}
 \tag{2.13}.$$

The windings must be connected so that current flows in the positive direction for phase a, and in the negative direction for phase b as shown in Figure 2.2. The DC voltage source shown in Figure 2.2, V_{DC} , has a variable magnitude so that the current level in the windings can be changed. It was implemented using an autotransformer, full wave diode rectifier, and resistive load bank, all connected in series.

By exciting the a and b field windings as shown in Figure 2.2, and by manually positioning the armature reaction mmf axis at some angular position relative to the centres of the field poles, a constant torque is induced in the rotor. This constant torque, measured under static conditions, is equal to the steady state developed (air gap) torque since the flux distribution in the machine, neglecting harmonics, is the same in both cases (see Moullin [9, pp. 5-6]). If this were a cylindrical stator machine, this static torque would be proportional to the sine of the angular difference between the field pole axis and the armature reaction mmf axis, and would reach a maximum when this angle is about 90° electrical. See equation 5.3. For a salient-pole machine the maximum torque is slightly higher than that of a cylindrical stator machine (all other factors being equal) due to the effects of the salient poles on the flux distribution, but this maximum torque occurs at a somewhat smaller angular difference (see Figure 5.2 and equation 5.4). Chapter 5 discusses the torque characteristic of the experimental machine in more detail. The net shaft torque delivered to the load from the rotating motor would be slightly less than the air gap torque due to hysteresis, eddy current, bearing friction, and windage losses.

Finite element analysis methods, which are successfully used in both steady state and transient simulations, also use static field solutions (see [21] and [6]). For the transient case, a static field solution is performed at each time step. The success of this approach argues the acceptability of using static field and torque measurements in steady state (as well as transient) simulations.

The measurements I can obtain from my experimental machine can just as easily be computed using finite elements. Therefore, the procedure I am developing to obtain a flux density prediction model using this measured data could also be followed using finite element generated data. Similarly, the torque measurements I obtain from my machine can be obtained from finite element simulation. In a sense, I am using measurements from an actual machine in place of a finite element computer program. If my modelling procedure is successful using experimental data, it should be successful with finite element generated data.

The machine I am using has features common to synchronous machines of all sizes, such as salient poles, chamfered pole faces, damper windings, and tooth skewing. If I am successful with modelling this machine, other machines of similar or less complexity can probably be handled as well.

In conclusion then, the experimental data I can collect with this machine and its associated instrumentation should be satisfactory for developing and testing my flux distribution model. Using a static machine in place of a rotating machine is not a drawback when simulating steady state machines, and the model developed to predict the static or steady state field conditions can also be applied to transient studies.

2.3 THE DATA ACQUISITION SYSTEM

2.3.1 General Description

Large volumes of data needed to be collected, stored, analyzed, and displayed during the course of this research. For every operating condition under investigation, 10 contours, each consisting of 1600 flux density vs. position points were collected and averaged to smooth out the effects of teeth and skewing. In order to do this in a reasonable period of time, I used a commercial personal computer (PC) based data acquisition system. The system consists of a general purpose I/O board which plugs into an expansion slot of my PC, a terminal block, and data acquisition program development software. This software consisted of a collection of drivers for running the I/O board, disk

drives, and monitor of the PC. These drivers are used by calling Quickbasic or C language subroutines.

2.3.2 Application of the Data Acquisition System

Figure 2.3 is a block diagram which describes how I applied the commercial PC based data acquisition system in my research.

The procedure for collecting data for a given contour is as follows:

- i) Set up the rotor angular position, probe depth, field current, armature winding connections and current levels appropriate for the operating condition under study. All instrument ranges are set to the most sensitive range possible without overranging.
- ii) The probe's initial starting angle, number of points to be sampled, instrument range setting data (scaling factors), and probe temperature conditions are entered into the program from the keyboard. This information is represented by the arrow numbered "1" in Figure 2.3.
- iii) The signal to start sampling data (probe angular position and flux density readings) is entered on the keyboard, a few seconds later the probe drive motor is manually switched on. The probe rotates slightly more than 360° mechanical around the air gap in about 150 seconds, after which it is stopped by limit switches. The computer stops sampling a few seconds after the probe stops rotating. The extra data collected at the start and stop is removed from the data later by the averaging program referred to in Chapter 3. The commands from the PC to the I/O board are represented by the arrow numbered "2" in Figure 2.3.
- iv) Sampled data is sent from the I/O board to computer memory during the sampling process. This stored data is handled as binary data arrays in the user written data acquisition program. Once sampling is completed, the binary arrays are converted to decimal format, and scaled using the range data entered in step ii. After this is done, the data is displayed on the monitor. If it is acceptable, then it is written to a standard DOS compatible ASCII file for use in other programs. This process is represented by the arrows numbered "3" in Figure 2.3.
- v) If the data is acceptable then the probe depth, or any other variable, is changed and the next run is started. If not, then the error is corrected and the run is repeated.

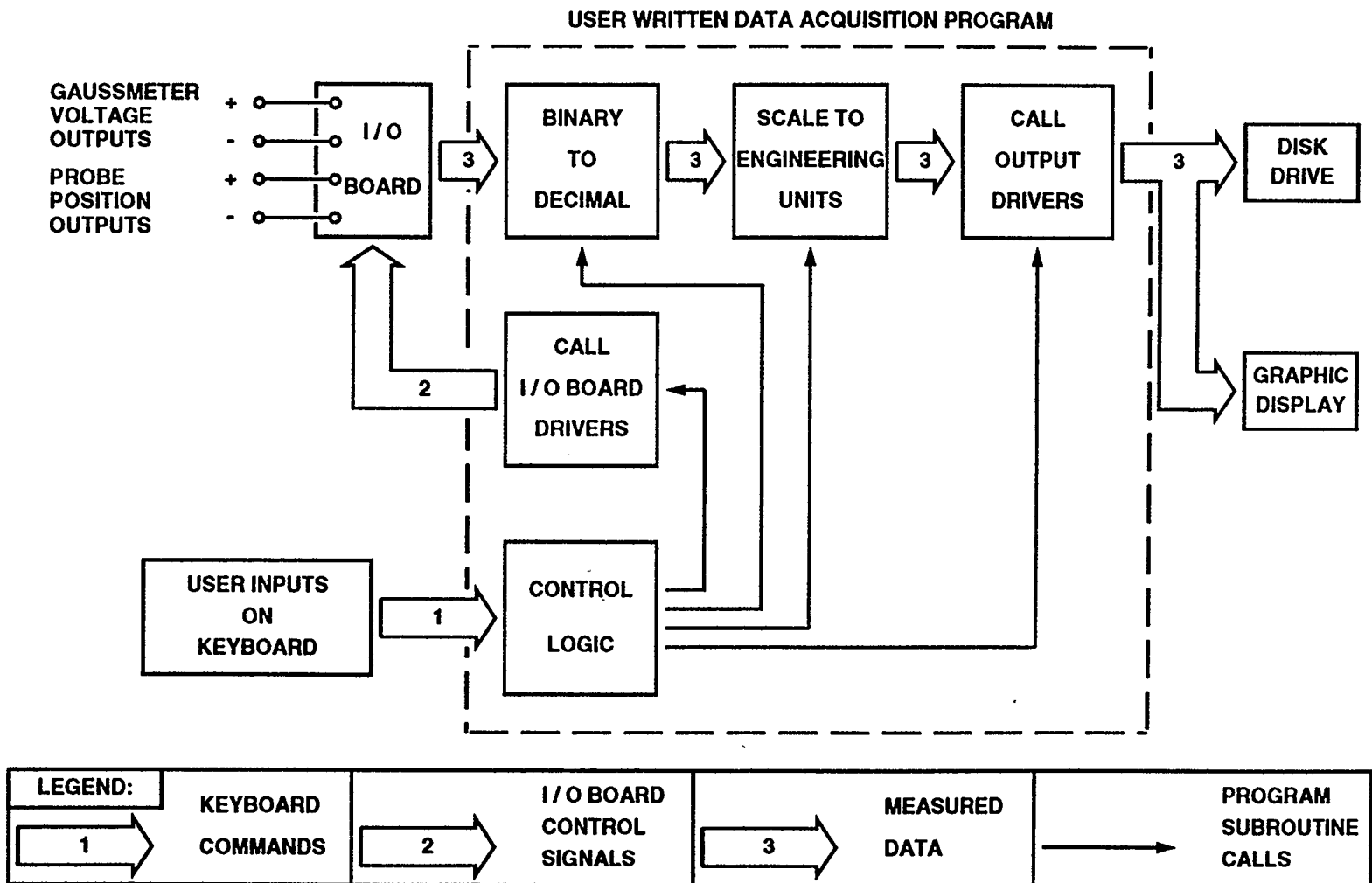


Figure 2.3: Block Diagram of Data Acquisition System

2.3.3 Advantages of Using Data Acquisition

I required large numbers of data points for accurate field resolution, and for numerical integration in my Fourier analysis program. This data acquisition system easily sampled at a high enough rate to give me that accuracy. It also allowed me to zoom in on fine details in the field (see Figure 2.5 as an example). By immediately producing ASCII files, the inaccurate and time consuming process of digitizing flux plots, say from an analog chart recorder, is eliminated. Further, any analysis program which can access data files can access this data. Routinely, I used this data in my own Fortran 77 programs and in a simple spreadsheet program. By using a simple indexing system, I retrieved data quickly from among hundreds of different data runs.

2.4 TYPICAL DATA RUNS

Figure 2.4 shows two typical raw data runs at different probe depths (z 's). The 18.8 cm probe depth is about half way down the rotor length, the 12.0 cm probe depth is near one end of the rotor. The main features of interest are listed below:

- i) For the 18.8 cm case, the flux density wave is periodic, repeating itself every 360° electrical or every 180° mechanical. Therefore, it is suitable for Fourier series representation. Fourier analysis results will be shown in Chapter 3.
- ii) For the 18.8 cm case, the shape of the positive half-wave is identical to the shape of the negative half-wave, except for the sign change. This means that there are no even order harmonics present in its Fourier series.
- iii) For the 12.0 cm case, the symmetries that were present in the 18.8 cm case are lost. This is because of end effects. In this machine, the total rotor length is 17.3 cm. End effects disappear at distances greater than about 1.7 cm from each end of the rotor, therefore the air gap field may be simplified to a two dimensional problem along about 80% of the rotor's length.
- iv) The rotor teeth and slots have a pronounced effect upon the flux density distribution. The flux density is higher, of course, where a tooth is present, and lower where a slot is present. Reference [25] shows results from finite element analysis simulation of the fields in this machine. The computer produced flux density plots for similar excitation conditions show the dips corresponding to slots to be much deeper than those plotted here (two to three times as deep in some cases). The simulations show that for decreasing r 's (as you get closer to the

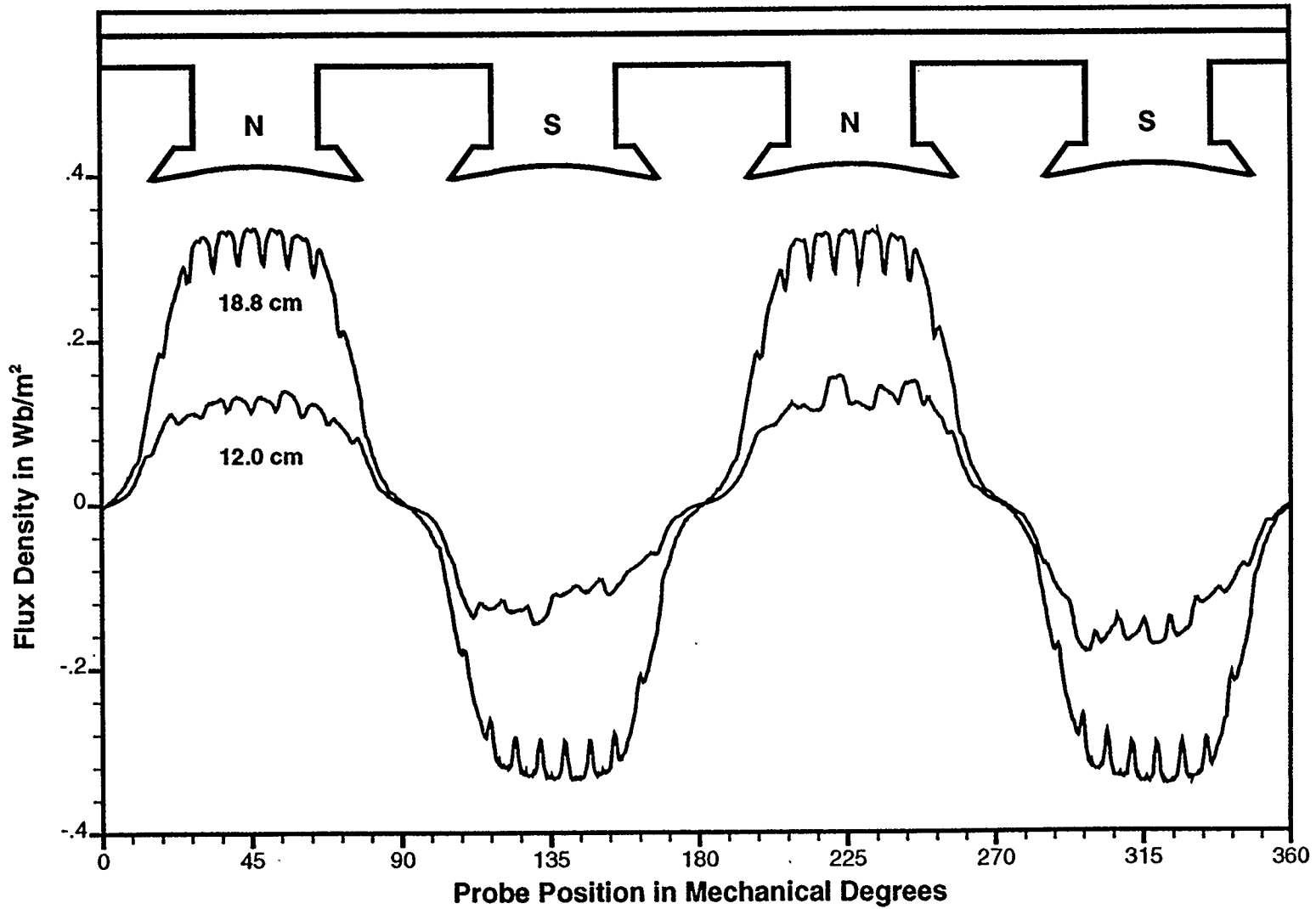


Figure 2.4: Flux Density Data, Field Current = 1 A, Probe Depth = 12.0 cm and 18.8 cm

rotor surface) the radial flux density distribution increases over the teeth and decreases over the slots. This is because as you approach the rotor surface, the lines of flux crowd toward the tops of the teeth. Once the radius is less than the tops of the rotor teeth, the radial flux density in the slots gets very small since most of the flux lines which have made it into the slot head toward the sides of the teeth. It is impossible to exactly control the radial position of the probe in the air gap, so similar data cannot be obtained experimentally. The averaging effect caused by the finite width of the Hall effect crystal also reduces the depth of the dips.

- v) Tiny perturbations exist in the measured field data. These are especially obvious in regions above the teeth. Sharp "glitches" result from noise in the measurement channel, and the number of glitches varies from data run to data run. Small, rounded bumps, however, are faithful to the actual field shape (and are confirmed in the computer simulations). In the interpolar regions where the field slope is changing rapidly, the noise effects are still present, but less visible in the plot. The error level caused by noise depends on the quantization levels, analog voltage ranges, and noise characteristics of the instrumentation and I/O board. Appendix A discusses this problem in more detail. These noise errors are not significant since, as we will see in Chapter 3, most of my work will use averaged data runs, therefore the random effects of noise are smoothed out.
- vi) The shape of the wave form deviates considerably from a pure sinusoid. It will be shown that, due to the effects of slot skewing (see Appendix B) and the armature winding space distribution (see Chapter 6), the induced voltage in the windings is much more sinusoidal.

Figure 2.5 is an enlarged view of the flux density distribution directly beneath the centre of the first pole for three different probe depths. The rotor position is constant for all three data runs. The flux density over the same tooth is indicated by an 'A' in each of the three runs. Due to the skewing of the rotor teeth, this tooth's flux changes angular position by 7.5° mechanical over the length of the rotor (the difference between depths of 13.7 and 23.9 cm is only about 5° since the distance between these two depths is only about 0.667 of the rotor length, the actual end depths (12.0 cm and 27.3 cm) are not shown because they are subject to end effects).

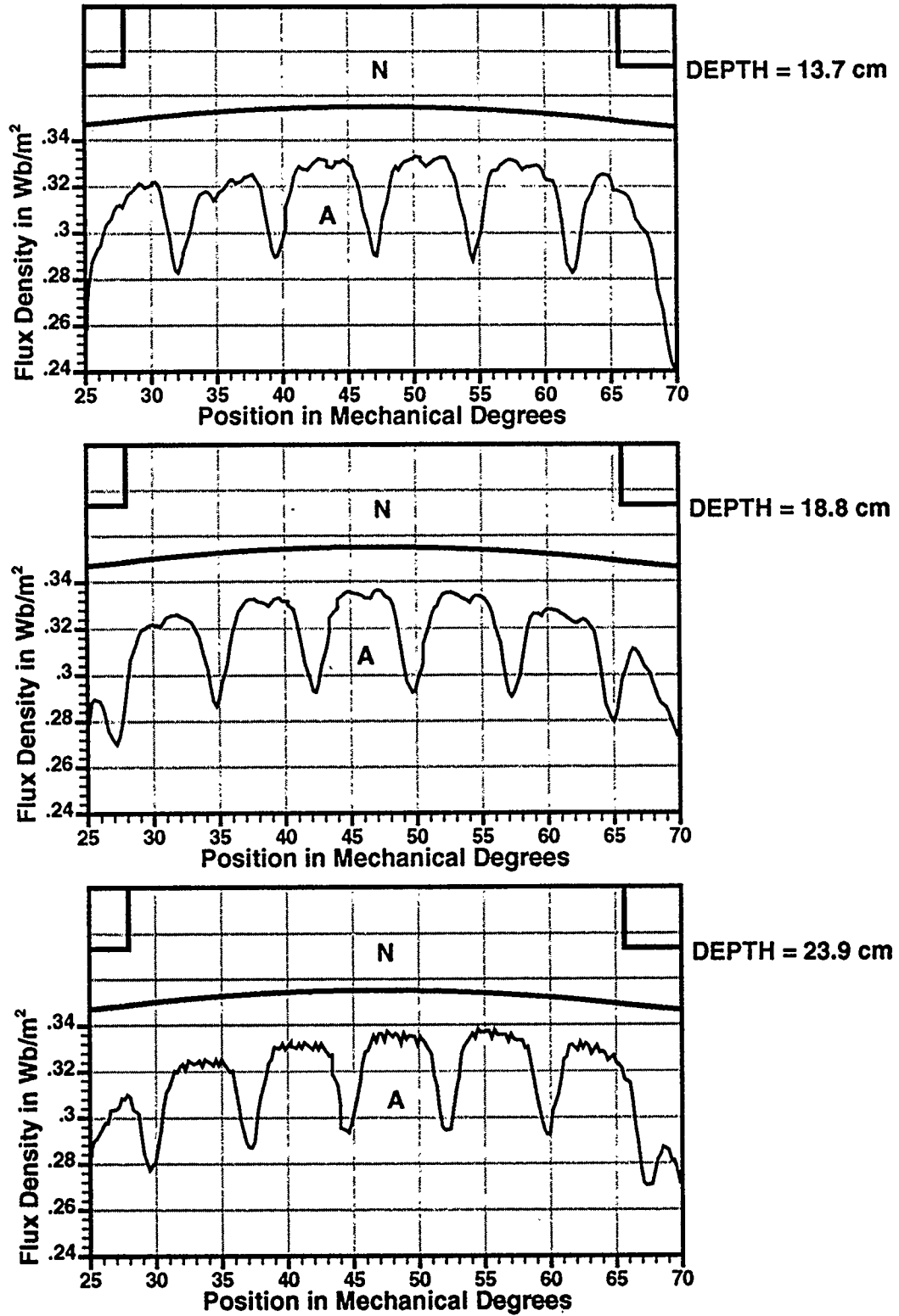


Figure 2.5: Effects of Rotor Slot Skewing on Flux Density Distributions, Field Current = 1 A, Probe Depth = 13.7, 18.8, and 23.9 cm

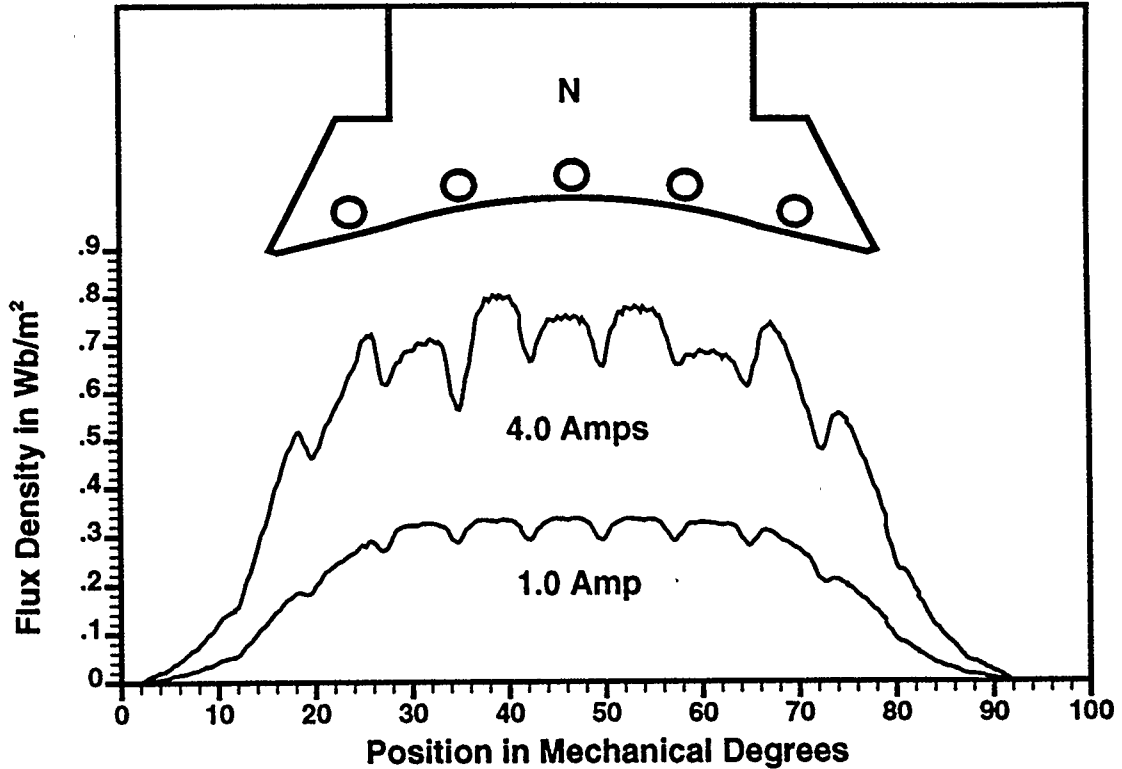


Figure 2.6: Effects of Saturation on Flux Density Distributions, Field Current = 1 A and 4 A, Probe Depth = 18.8 cm

Figure 2.6 shows the flux density distribution under one pole. The rotor position and the probe depth are constant for both runs, but one data run has a field current of 1.0 Amp (0.5 p.u.), and the other has a field current of 4.0 Amps (2.0 p.u.). I have also shown the positions of the damper bars in the pole shoe. Due to the saturation characteristic of the machine iron, if we quadruple the field current, as shown here, we do not get four times the original flux per pole, but somewhere around 2.25 times. The assumption of linearity is clearly not true. Also, due to the geometry of the iron structure, saturation effects are not uniformly distributed. This is obvious from the varying flux levels over the teeth.

CHAPTER 3

RELUCTANCE WAVE CHARACTERIZATION

3.0 CHAPTER OBJECTIVES

- i) Outline the strategy for characterizing R_{base} and R_{sat} for use in the flux density distribution model.
- ii) Determine the justification for, and limitations of, using the averaged flux density, B , distributions.
- iii) Determine the theoretical averaged armature magnetomotive force (MMF or \mathcal{F}) wave, and check it against experimental results.
- iv) Determine R_{base} under linear conditions.
- v) Determine the field MMF wave.
- vi) Determine R_{sat} from saturated conditions.

3.1 STRATEGY FOR FINDING R_{base} AND R_{sat}

Using equations 2.2 and 2.3, the R_{base} and R_{sat} distributions can be characterized if the \mathcal{F} and B distributions are known. From equation 1.20, R_{base} may be found under linear conditions in the iron. From equation 1.18, R_{sat} is the difference between R and R_{base} under saturated conditions. Saturation occurs as the MMF increases, so it is natural to try to describe R_{sat} as a function of MMF. The following is an outline of the strategy used to characterize R_{base} and R_{sat} :

- i) Determine what B and \mathcal{F} to use. B will be shown to be the averaged flux density, B_{avg} , over the length of the rotor, and \mathcal{F} will be the equivalent rotor MMF that produces B_{avg} . The \mathcal{F} distribution in the air gap can be determined for the armature (rotor) conductor distribution from theory, but will need to be checked. \mathcal{F} is a function of the coil distributions, the number of conductors in each coil, and the current in the phase windings. \mathcal{F} cannot be determined theoretically for the field windings for three reasons. First, they are set back on the field poles; second, the field pole shape affects the distribution of flux (and therefore the distribution of MMF); and third, there is an MMF drop in the pole iron between the windings and the air gap. \mathcal{F} for the armature windings is known, but since large currents are needed in the armature windings in order to produce a substantial

MMF in the air gap, the armature MMF can only be used to excite the machine iron for linear conditions. Since large numbers of data runs are required, and a long cooling time between runs is necessary for high armature currents, using armature MMF to create heavily saturated conditions is not practical. Therefore, armature MMF can be used to determine R_{base} directly, but not R_{sat} . The field MMF drives the machine into saturation with much lower currents, so once it is determined it can be used to find R_{sat} .

- ii) Determine R_{base} . Under armature MMF excitation only, measure B_{avg} . The theoretical MMF distribution for the machine is flat-topped for a 22.5° mechanical span centred on the positive and negative peaks (axes) of the wave (this is for the a and -b winding excitation conditions referred to in section 2.2.3). To be cautious, a 10° mechanical span ("segment") was used. 10° mechanical is slightly greater than one slot pitch for this machine, which is 7.5° mechanical. The rotor angular position was varied through 90° mechanical (180° electrical) in 7.5° mechanical increments so that there would be overlap from segment to segment. The armature current level is held constant for all segments. For each segment B_{avg} was determined, and R_{base} was found using equation 2.3 (R_{sat} is 0 since these measurements were for linear conditions). R_{base} for the entire air gap was thus obtained. In the overlapping portions of successive segments, the computed R_{base} data was averaged. Continuity from segment to segment was checked, and will be discussed later in this chapter.

The R_{base} distribution determined in this fashion is the inverse of the zero order MMF's permeance distribution (see section 1.3.4) used by Doherty and Nickle [15]. Both distributions are found for constant MMF conditions.

Once R_{base} is found, then the armature a and -b MMF wave can be "back calculated" using equation 2.2, and compared with the theoretical. Phase superposition of three phases can be checked, and the effects of time and space harmonics on armature MMF can be determined.

- iii) With R_{base} known, field MMF only can be applied at a level which gives approximately the same peak B_{avg} as for the measurements in step ii (to give approximately the same linear conditions as in step ii). B_{avg} is then measured, and the field MMF wave can be back calculated using equation 2.2. This field MMF wave is assumed to retain its shape, but be proportional to field current.

- iv) With a known field MMF, increase the field current so that various levels of saturation occur in the machine iron. R_{sat} may then be found using equation 2.3 since the field MMF, B_{avg} , R , and R_{base} are known. R_{sat} may be characterized as a function of MMF. Since R_{sat} is also a function of position, error will be introduced by neglecting this position dependence.
- v) With R_{base} , R_{sat} , the armature MMF, and the field MMF known, the B model is ready to be implemented (Chapter 4). All the waves are periodic so they may be expressed as Fourier series in the computer program. The armature and field MMF waves will be added at each angular position in the air gap to produce a total air gap MMF.

3.2 DEVELOPMENT OF THE RELUCTANCE WAVE MODEL

3.2.1 Using Averaged Flux Density Distributions

In order to compute reluctances, equation 2.2 requires known B and \mathcal{R} distributions in the air gap. This section examines what B to use.

Appendix B discusses the assumptions made in using averaged B distributions. An averaged B distribution is found by measuring the radial air gap flux density distribution, as a function of angular position, at a number of different depths. The radial position of the probe is the same at all depths. The rotor position is the same for all depths. The averaged B distribution is then found by computing the average B value across all ten depths for the same angular position. The formula for this computation, implicit to equation B.13, is stated explicitly as

$$[B_r(\theta)]_{\text{avg}} = \frac{1}{n} \sum_{i=1}^n B_r(\theta, z_i) \quad (3.1),$$

where θ is used in place of ϕ since $\omega t = 0$ for static measurements. n is the number of contours and equals 10 in my research. z_i is the depth or axial position of contour i . Equation 3.1 is computed using an averaging program. For each averaged B distribution ten 1600 point files are averaged.

Appendix B describes the errors introduced by using averaged B distributions. Essentially, we are neglecting the effects of the skewing of the coil sides upon flux linkage, torque, and voltage computations. This error is neglected because of the complexity that would be introduced by accounting for skewing, the diminishing importance

of flux density harmonics with increasing order, and the smoothing effect of the Hall effect crystal. Every contour would have to be modelled individually if the general equation (equation B.3) were used, resulting in a ten-fold increase in characterization work and computing time. Smoothing from the Hall effect crystal eliminates sharp features and the higher order harmonics in the measured B distribution data before it is averaged (see section 2.4).

By averaging over the full rotor length we also incorporate the end effects into the averaged B distribution.

Based on the findings of Appendix B, and the reasons just mentioned, the averaged B distribution defined by equation 3.1 should be adequate for all of my research needs. Further investigation is outside of the scope of this research.

As an example of the results of averaging, consider Figure 3.1. This plot compares the unaveraged (raw) data for a contour depth of 18.8 cm (midway along the rotor length) with the averaged data for all ten contours. Both are for a field current of 0.5 p.u. (1.0 A). By averaging, the effects of teeth and measurement noise are largely removed (Appendix B contains a detailed Fourier analysis comparing these two waveforms).

As the field current is increased, position dependent saturation effects cause distortion of the field shape which becomes apparent when averaging is performed. In Figure 2.6, the effects of saturation are apparent, but variations in the flux distribution due to the teeth make it difficult to see how saturation varies with angular position. Averaging allows this to be determined. Figure 3.2 shows how the positionally dependent saturation effects (caused by the pole shape and damper bar slots) cause increased distortion of the field shape as field MMF increases. The field current varies from 0.25 p.u. (0.5 A) to 3.0 p.u. (6.0 A). Also readily apparent is the non-linearity of the machine iron since at high current levels the flux increase is no longer proportional to the current increase.

3.2.2 Using Averaged MMF Distributions

Equation 2.2 also requires a known MMF (\mathcal{F}) distribution, which will be effective at all points for which we have defined B . Since we measure B in the air gap at a radius just outside of the rotor surface, the MMF distribution must be defined there as well. This section determines the averaged theoretical MMF distribution for the armature conductors.

Defining \mathcal{F} for the armature windings on the rotor may be done using equation 1.1, repeated here

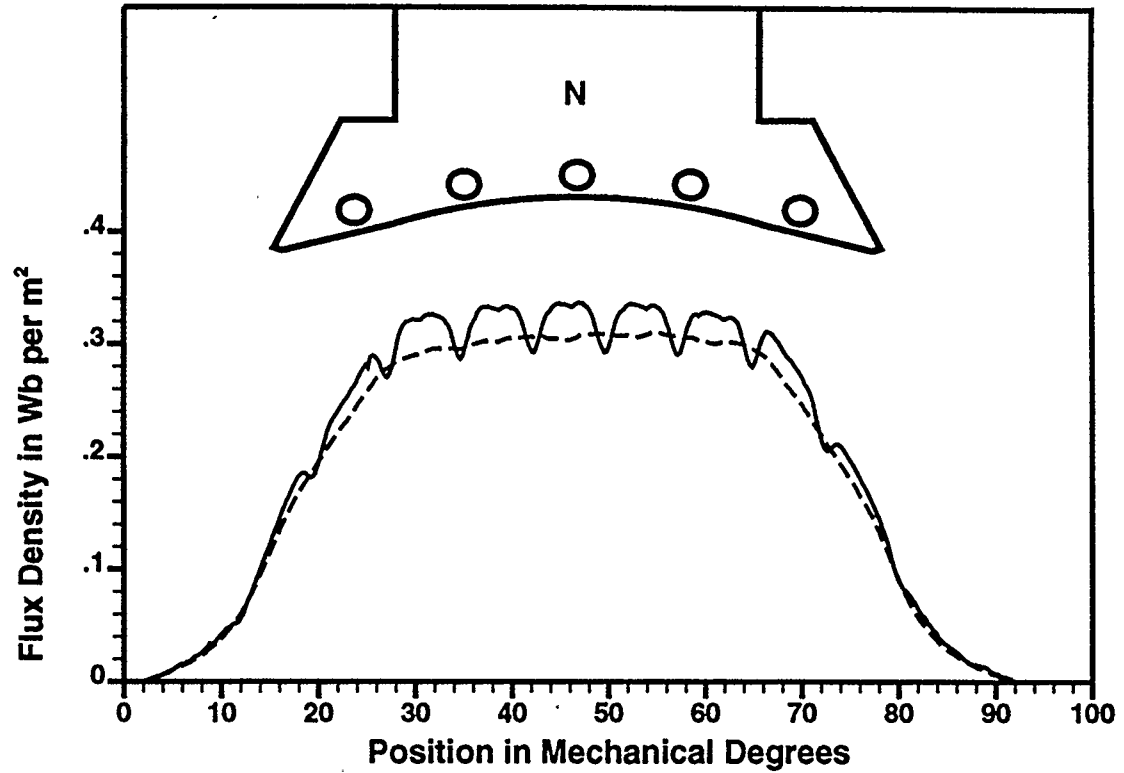


Figure 3.1: Comparison of Unaveraged Flux Density Data (Depth = 18.8 cm, solid) to Averaged Data (dashed), Field Current = 0.5 p.u.

$$\oint H \cdot d\ell = Ni = \mathcal{F} \quad (3.2).$$

This is the approach used in Fitzgerald [7, pp. 131-133] and Langsdorf [27, pp. 171-172].

Under the assumption of negligible MMF drop in the iron, the MMF in the air gap may be calculated using equation 3.2. If a cross-section of the machine in Figure 3.3a is considered, the MMF distribution of the rotor may be considered to be equal to the current

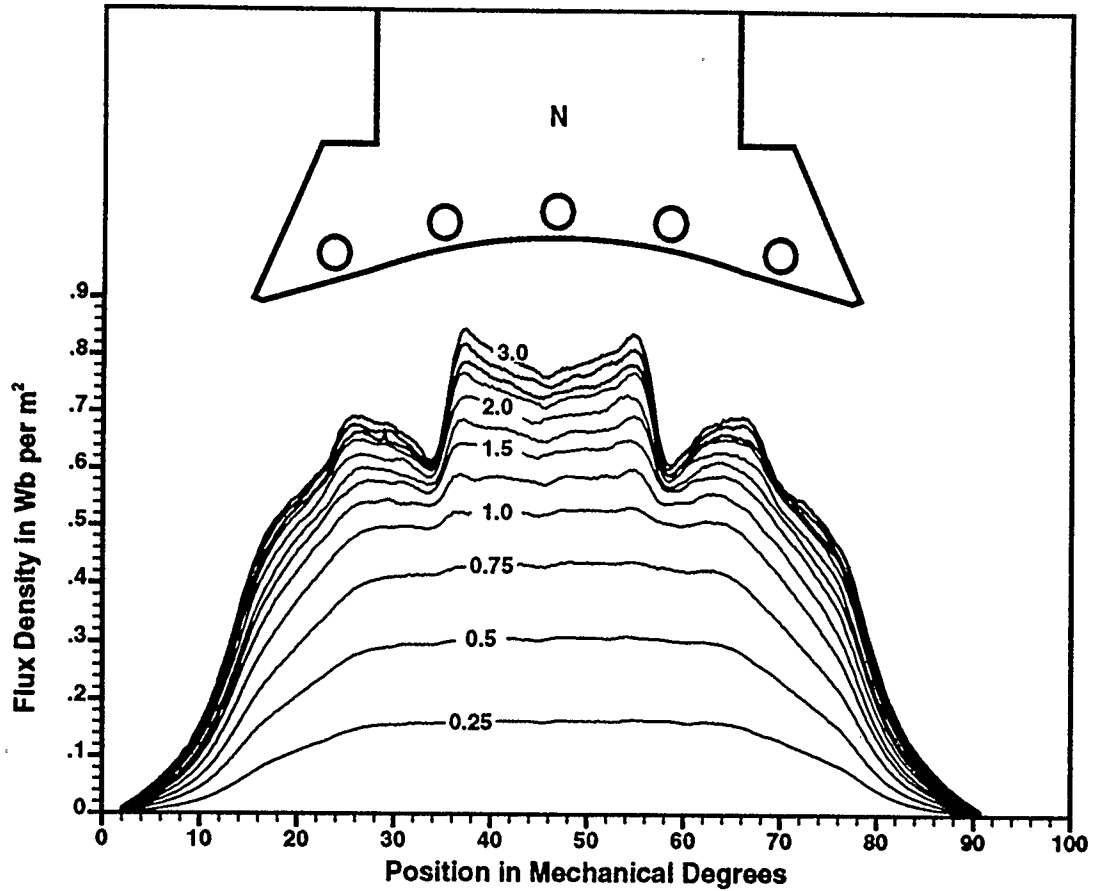


Figure 3.2: Effects of Saturation Upon Averaged Flux Density Data, Field Current = 0.25 to 3.0 p.u.

enclosed within a closed path which goes across the air gap twice. When using the magnetic circuit concept, this closed path should coincide with actual lines of flux. The integration path, like the lines of flux in the air gap, should be drawn straight across the air gap when the air gap is small (or at least normal to both the rotor and stator surfaces if not).

Each coil side in Figure 3.3a contains N conductors, and each conductor has i amperes flowing in it. For path a-b-c-a the enclosed current is $0Ni$ amp-turns, for path

Figure 3.3a:
Integration Paths and
Coil Side Distributions

- ⊙ Coil Side in Slot,
Current Out of Page
 - ⊗ Coil Side in Slot,
Current Into Page
- (Note: Slots Not Shown)

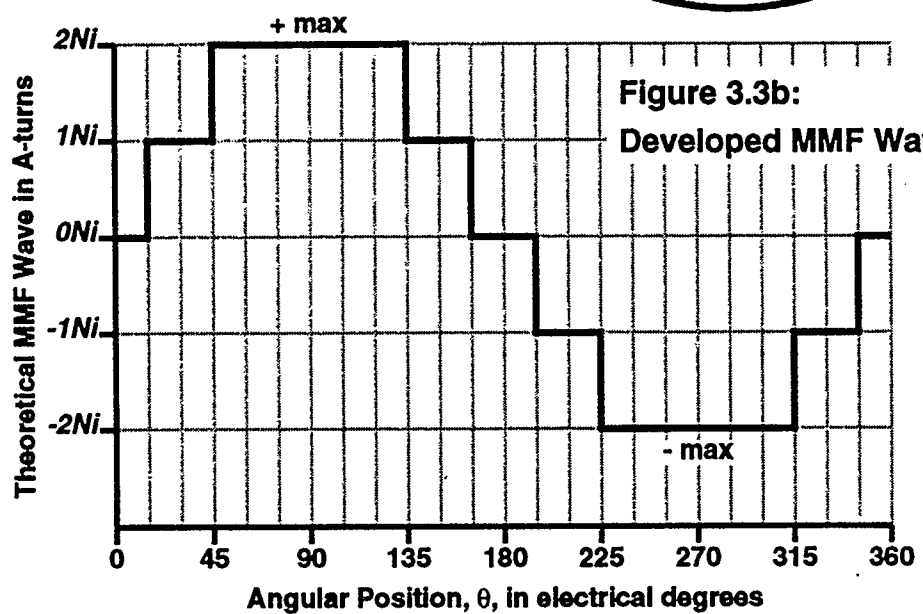
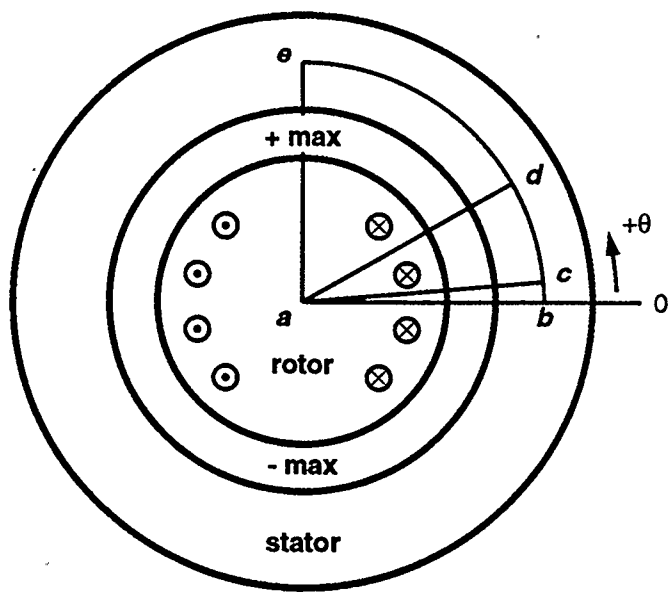


Figure 3.3b:
Developed MMF Wave

Figure 3.3: Theoretical Computation of MMF Distributions

a-b-d-a it is $1Ni$ amp-turns, and for path a-b-e-a it is $2Ni$ amp-turns (which is the maximum value of the MMF wave). This theoretical MMF wave is shown in developed form in Figure 3.3b. As the angular position, θ , passes every current carrying coil side there is a step in the theoretical MMF wave. The height of each step is equal to the current carried by the coil side. As θ increases, the paths start enclosing coil sides with current in the opposite sense, the steps become negative, and the net enclosed amp-turns reduces. As we make a complete revolution, we see that the MMF wave is periodic. Zero crossings occur at the mid-points of each phase band (a group of coil sides, all from the

same phase, in successive slots). The maximum positive and negative values occur 90° electrical from the zero crossings.

The theoretical armature MMF distribution for this machine is directly proportional to the number of conductors per coil and the current in each conductor. The MMF waves for more complex coil distributions are developed in the same fashion as in Figure 3.3. Generally the number of steps is greater, there are two coil sides per slot, and the number of coil sides of the same phase in each slot can be different due to partial pitch windings.

For the rotor of my machine, the armature coil sides are separated by 7.5° mechanical. There are two coil sides per slot and 48 slots on the rotor. No further information was available on this machine, but the following assumptions and conventions were made when developing the theoretical MMF wave for my machine:

- i) The coil pitch is 11/12. Normally the coil pitch should be easily seen from the end turns, but the experimental machine's end turns were encapsulated in a thick resin coating, the surface of which was darkened and partially coated with old insulating tape fibres. This made it impossible to trace the paths of individual end turns without physically penetrating the resin and risking damage to the coils.

A partial coil pitch is commonly used to make the armature MMF wave more sinusoidal. My machine is 4 pole, three phase, and has 48 slots. If the coil pitch were full, then each phase band would occupy 4 slots with 2 coil sides per slot. By using a partial coil pitch, the phase band is distributed over 5 slots. The middle three slots each contain two coil sides from, say, phase a only. One of the end slots will have one coil side from phase a and one from phase b, and the other end slot will have one coil side from phase a and one from phase c.

- ii) The number of conductors per coil side, N , will be set equal to one for now. Later in this chapter N will be found to be about 9. As long as N retains the same value, the determination of reluctance and MMF waves are all normalized with respect to N . The reluctance and MMF waves plotted in this chapter and Chapter 4 are all for N equal to 1, the actual numerical values of these waves can be found by multiplying the plotted results by 9. N had to be determined in order to properly compute torque in Chapter 5 and voltage in Chapter 6.
- iii) The polarity of the armature MMF wave is reversed to that assigned by the right hand rule (as shown in figures 3.3a and 3.3b). This is in order to be

consistent with the field MMF wave (to be found later in this chapter). The armature and field MMF waves will need to be added numerically in the air gap when the model is developed, so a positive armature MMF value should produce flux density in the same direction as a positive field MMF value. This positive MMF direction causes flux to pass from the stator into the rotor.

- iv) For the armature current conditions mentioned in section 2.2.3 the magnitudes of current in the a and b phases are the same, but phase c current is zero. The phase b current is also negative at that point in time. By having positive current in phase a and negative current in phase b in combination with the spatial distributions of the coil sides of the two phases, the MMF waves of the phase a and b windings acting alone superimpose to give a single, larger MMF wave than for one phase alone. For simplicity, I will refer to this resultant wave as the a and -b MMF wave. I performed many of my experimental measurements with the a and -b MMF wave.

The theoretical a and -b MMF wave for a contour mid-way along the rotor length is shown by the stepped distribution in Figure 3.4.

Appendix B states that when we use averaged B distributions and neglect skewing we should use an averaged or equivalent MMF distribution for the rotor. The dashed, smooth waveform shown in Figure 3.4 is the averaged MMF distribution taken from 10 waveforms like the one shown by the stepped distribution in Figure 3.4. Each stepped waveform is shifted to the appropriate angular position for its contour depth along the rotor, then all ten shifted waveforms are averaged. The smoothed waveform has substantially smaller harmonics than the stepped waveform for orders above 13.

Experimentally, the angular coordinate of the centre of the a and -b MMF axis was found as follows:

- i) The a and -b windings were excited with a current which was small enough to ensure linearity (1.0 p.u.).
- ii) The average B distribution was determined for some rotor angular position, and the fundamental of this B distribution was determined.
- iii) If the fundamental of the a and -b MMF distribution's B distribution coincided with the centre line of a pole face, then the angular position of the rotor was such as to cause the a and -b MMF distribution's axis to be on the centre line of the

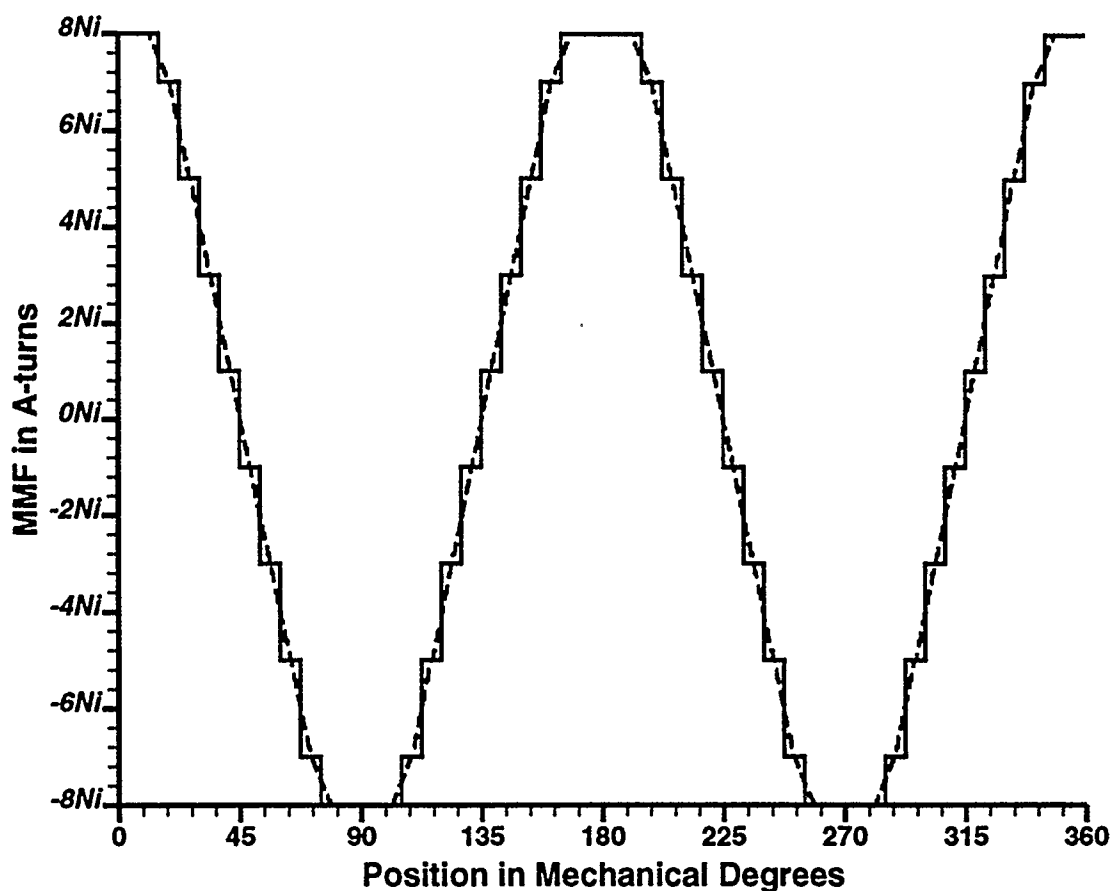


Figure 3.4: Theoretical Centre Contour (solid) and Averaged Theoretical MMF (dashed) Distributions for Phases A and -B Excited

pole face. If not, a new rotor angular position was tried.

For my machine, the rotor gauge reading which satisfied step iii was 35° mechanical. Therefore, the position of the a and -b armature mmf wave with respect to the centreline of my reference field pole, θ_r , was always $\theta_r = \text{rotorg} - 35$, where *rotorg* is the rotor position gauge reading in mechanical degrees.

Because the coil pitch is assumed, the stepped distribution shown in Figure 3.4 may not be exact. If the coil pitch is full, the sloping sides of the averaged distribution will be

steeper and the constant portions at the top and bottom will be wider. The averaged distribution for the 11/12 pitch case has a constant portion which is 22.5° mechanical wide. By considering a range less than 22.5° mechanical (at first I used 15° , and later I used 10° mechanical) centred on the axis of the MMF wave, the value of MMF over this range can be assumed constant.

By using the averaged B distribution over this range, found using an MMF level that ensures linear conditions in the machine iron (1.0 p.u. armature current), equation 2.2 can be used to compute R . For linear conditions, R is equal to R_{base} . Once the R_{base} distribution for the entire air gap has been found, then the experimental a and -b MMF wave can be found by multiplying the experimental B and R_{base} . Then the theoretical a and -b MMF wave can be compared to the experimental one.

In Figure 3.3 the MMF wave is drawn for a cylindrical stator, and negligible MMF drop in the iron. This is not valid for saturated conditions. Why not? \mathbf{H} and $d\ell$ vary at all positions in the machine iron and in the air gap, especially under saturation, even though the integral of their dot product on any closed path always satisfies the right hand side of equation 3.2. For simplicity, select an integration path where $d\ell$ always coincides with \mathbf{H} (by following a flux line) and assume this path does not change with changing MMF. Under linear conditions, as current increases, H (the magnitude of \mathbf{H}) will increase proportionally at all points along the integration path. However, since B and H are related by the non-linear saturation curve in the iron, B will not increase linearly due to the iron saturation. Therefore, as we try to increase B by increasing the current, H in the iron increases faster than H in the air gap, and the fraction of the right hand side of equation 3.2 that goes toward producing B in the iron increases. An MMF drop will occur between the coils and the air gap. Therefore, if we have defined an MMF wave in the air gap under linear conditions, and we assume the air gap permeability to remain constant, under saturated conditions the air gap MMF wave will be less than proportional to winding current since B in the air gap will be less than proportional to winding current. The assumption of linearity (and superposition) of the MMF wave in the air gap (where we are doing our modelling), key to the magnetic circuit approach, is therefore invalid under saturation conditions. However, we can define the MMF wave in the air gap to be linear if we account for the saturation effects upon B by using an MMF dependent air gap permeability or reluctance instead of a constant air gap reluctance.

By assuming that linearity (as well as superposition) is valid for the MMF waves, we transfer the responsibility of characterizing how salient poles and saturation affect the B distribution entirely to R_{base} and R_{sat} . A general test of these assumptions will come in Chapter 4, when compound excitation (both the field and armature windings being excited at the same time) is modelled. Since all we can measure is B , it will be difficult to prove if errors in the computed field distributions are caused by errors in the MMF linearity assumptions, or from the reluctance characterizations, or both. However, potential sources of error will be identified as we characterize R_{base} and R_{sat} which appear to explain the errors in the computed field distributions. This will leave the linearity and superposition assumptions for MMF unchallenged.

3.2.3 Characterizing R_{base}

Under linear conditions, equation 2.3 reduces to

$$R = R_{\text{base}} \quad (3.3)$$

since R_{sat} is assumed to be zero. R_{base} will be an unchanging distribution which incorporates the effects of the air gap and the machine iron (including salient poles) for linear conditions. From Figure 3.2, we can estimate what flux density levels we can go to before we get into non-linear conditions. For flux density levels corresponding to a field current of less than 0.75 p.u. (1.5 A), the machine iron should be linear. Since we must use armature MMF to characterize R_{base} , we must use an armature current which ensures linearity. In this machine, 1.0 p.u. (18 A) of a and -b excitation current gives approximately the same peak B (under the centre of the field pole) as 0.5 p.u. (1 A) field current, which is known to be in the linear region. Therefore, 1.0 p.u. armature current was passed through the a and -b windings when characterizing R_{base} .

A series of averaged B distributions was collected with the a and -b MMF axis rotated by successive 7.5° mechanical steps. For each B distribution, the MMF was assumed constant over the middle 15° mechanical of the MMF half-wave (each of these 15° mechanical wide regions is called a segment). Equation 2.2, $R = \mathcal{F}/B$, was computed for each segment. Since the successive segments were rotated by 7.5° mechanical, there was a 50% overlap from segment to segment. This allowed me to compare the reluctances from successive segments for the same angular position.

The first characteristic which was tested was whether or not the segments' 15°

mechanical width was too large. I expected R_{base} to be constant under the central portion of the pole face where the pole face's cross-section was circular, the air gap width was constant, and there are no fringing effects due to saliency. Since the MMF wave is assumed to be constant over the segment, the reluctance wave is directly proportional to the inverse of the B wave.

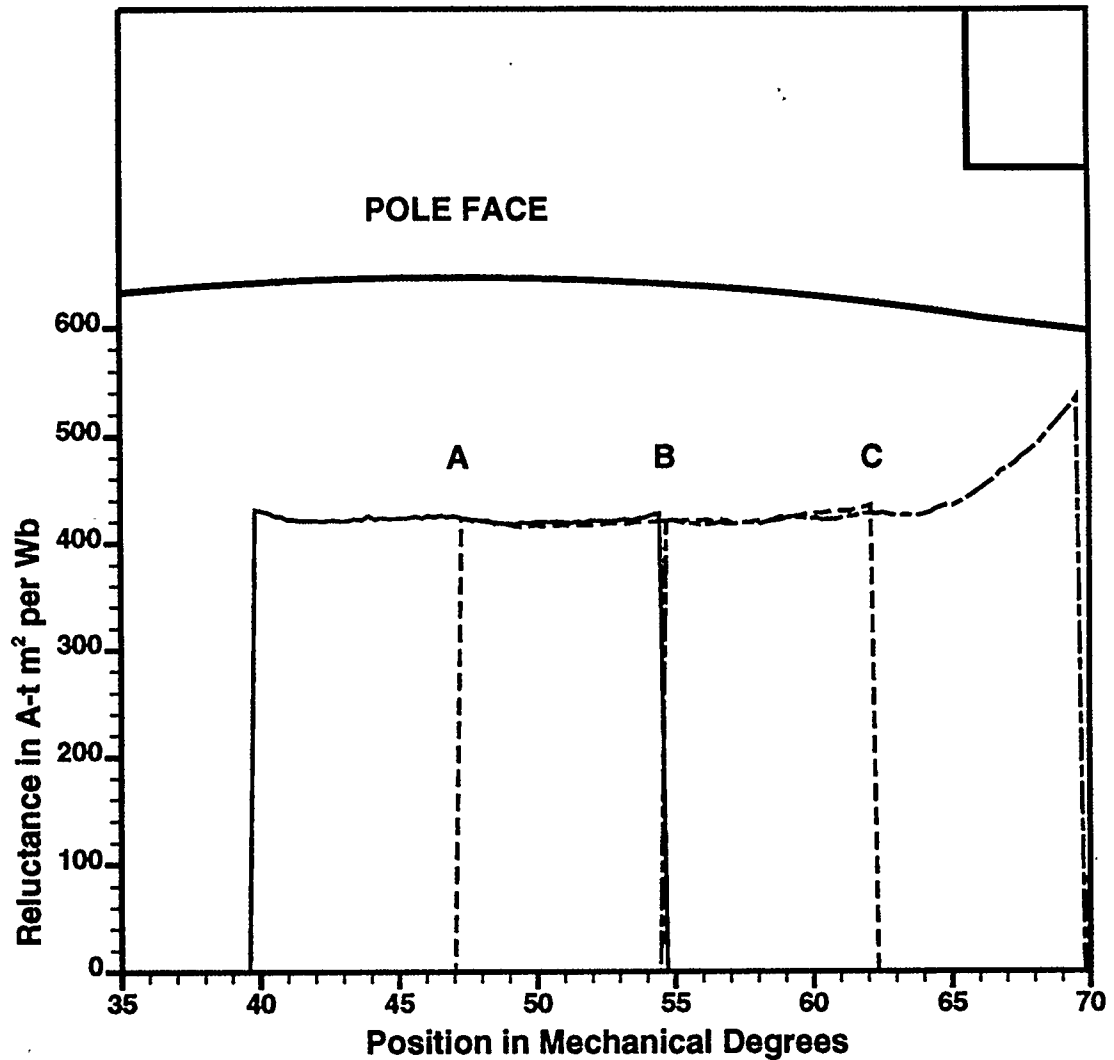


Figure 3.5: Effect of 15 Mechanical Degree Segment Width Upon R_{base} Calculation

Figures 3.5 and 3.6 compare the results from using 15° mechanical and 20° mechanical segments. Each figure has three successive reluctance segments, the leftmost range (indicated by an A) is centred on the field pole axis, the second (B) is

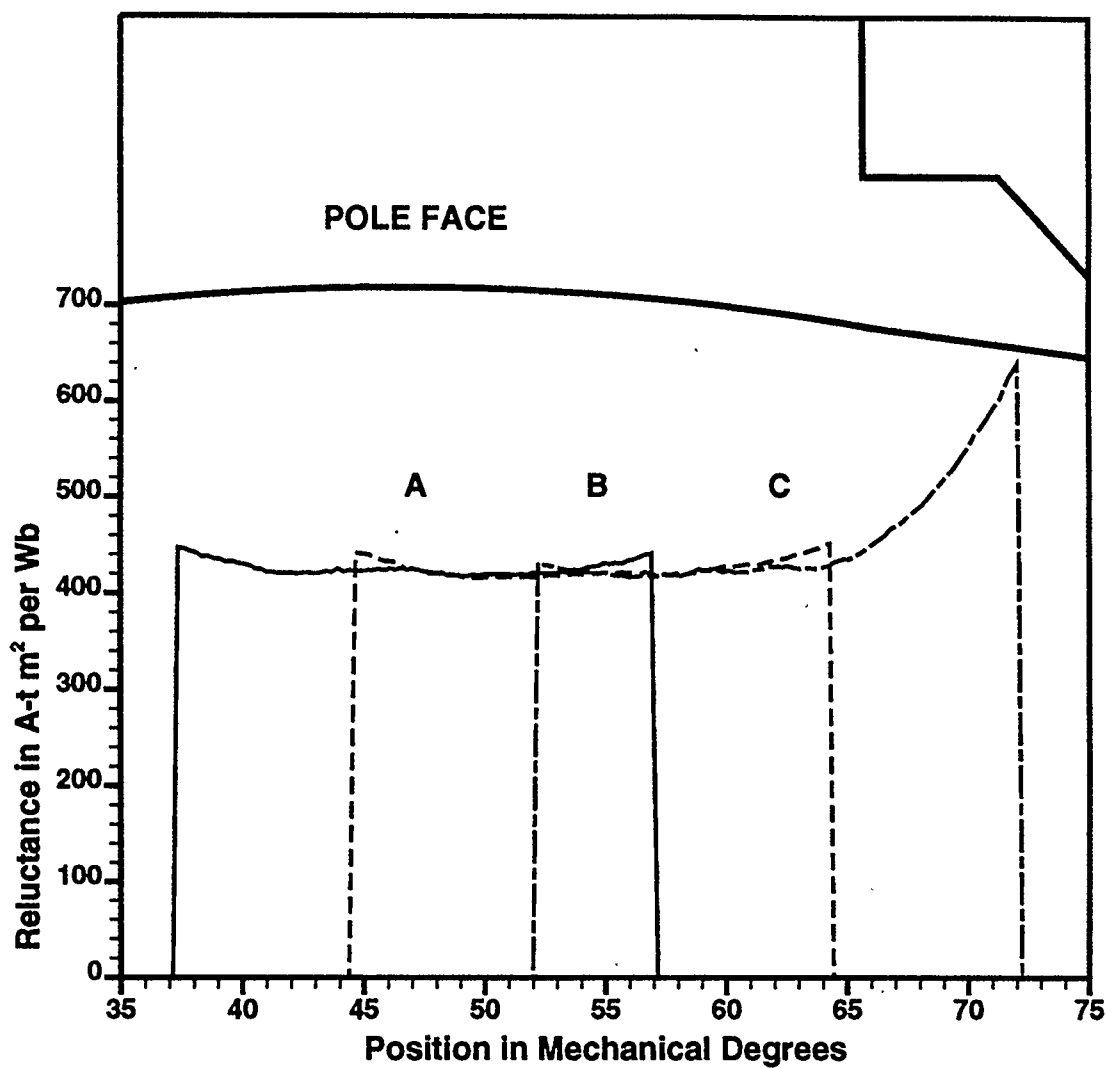


Figure 3.6: Effect of 20 Mechanical Degree Segment Width Upon R_{base} Calculation

centred 7.5° mechanical from the field pole axis, and the third (C) is centred 15° mechanical from the field pole axis. The vertical lines which drop to zero are simply the limits of each segment, and are put there for clarity.

In Figure 3.5 the 15° mechanical acceptance range has a nearly constant R wave for both segments A and B, and over the left half of segment C. Only at the very ends of each segment is there deviation from a constant value. The point on segment C where the R wave starts steadily increasing is exactly where the chamfer starts on the pole shoe.

In Figure 3.6, the 20° mechanical segment is too wide because the ends of all of the

segments curve upward. Consequently, the centre position of segment B gives a different R value than the right end of segment A at the same angular position. If the segment widths are made smaller, this error will not result. In order to avoid any error whatsoever, a 10° mechanical segment width was used to define R_{base} .

The second characteristic which was investigated was the sensitivity of R_{base} to the magnetic history of the iron. This effect is apparent when working at low excitation levels, and results from the hysteresis characteristic of the iron. The first series of reluctance segments covered a range of rotor angles from 0° to 180° electrical or 0° to 90° mechanical (from the +D axis to the -D axis, where the +D axis is the centreline of my reference North field pole and the -D axis is the centreline of the next South field pole in a clockwise direction). Figure 3.10 shows the mechanical angular positions of the +D, -D, +Q, and -Q axes. While covering a 90° mechanical span my reluctance program calculated R_{base} for all 360° mechanical of the air gap since it computed the R_{base} for four constant valued MMF segments at once. However, the reluctance waves of the first and last segments in the series were not the same, even though they were for the same angular positions. The reluctance for the last segment was higher than the reluctance of the first segment over the entire segment width. Apparently, the field poles were used to being magnetized in one direction, and to reverse magnetize them using the armature MMF (which was done with the last segment in the series) gave higher R_{base} results.

In order to eliminate this hysteresis effect I started the reluctance segment series at the -Q axis (a point 90° electrical or 45° mechanical counterclockwise from the reference North field pole) and ended at the +Q axis (a point 90° electrical or 45° mechanical clockwise from the reference North field pole). Over this span I used the a and -b MMF wave of the same polarity as the field pole between the -Q and +Q axes. This produced more consistent results.

A comparison of the R_{base} values from the -Q to the -D axis is shown in Figure 3.7. Case A is the R_{base} distribution determined by taking segments from pole centre (+D axis) to pole centre (-D axis). This was the first series that was taken and it was here that the hysteresis effect was detected. Case B is determined by taking them from the +Q interpolar axis to the -Q interpolar axis with the armature MMF magnetizing the field poles in their normal sense. Case C is the same as Case B, but a large DC current was manually applied to the field windings, first in one direction, then in the opposite direction several times. The final DC current was in the normal operating sense. This process,

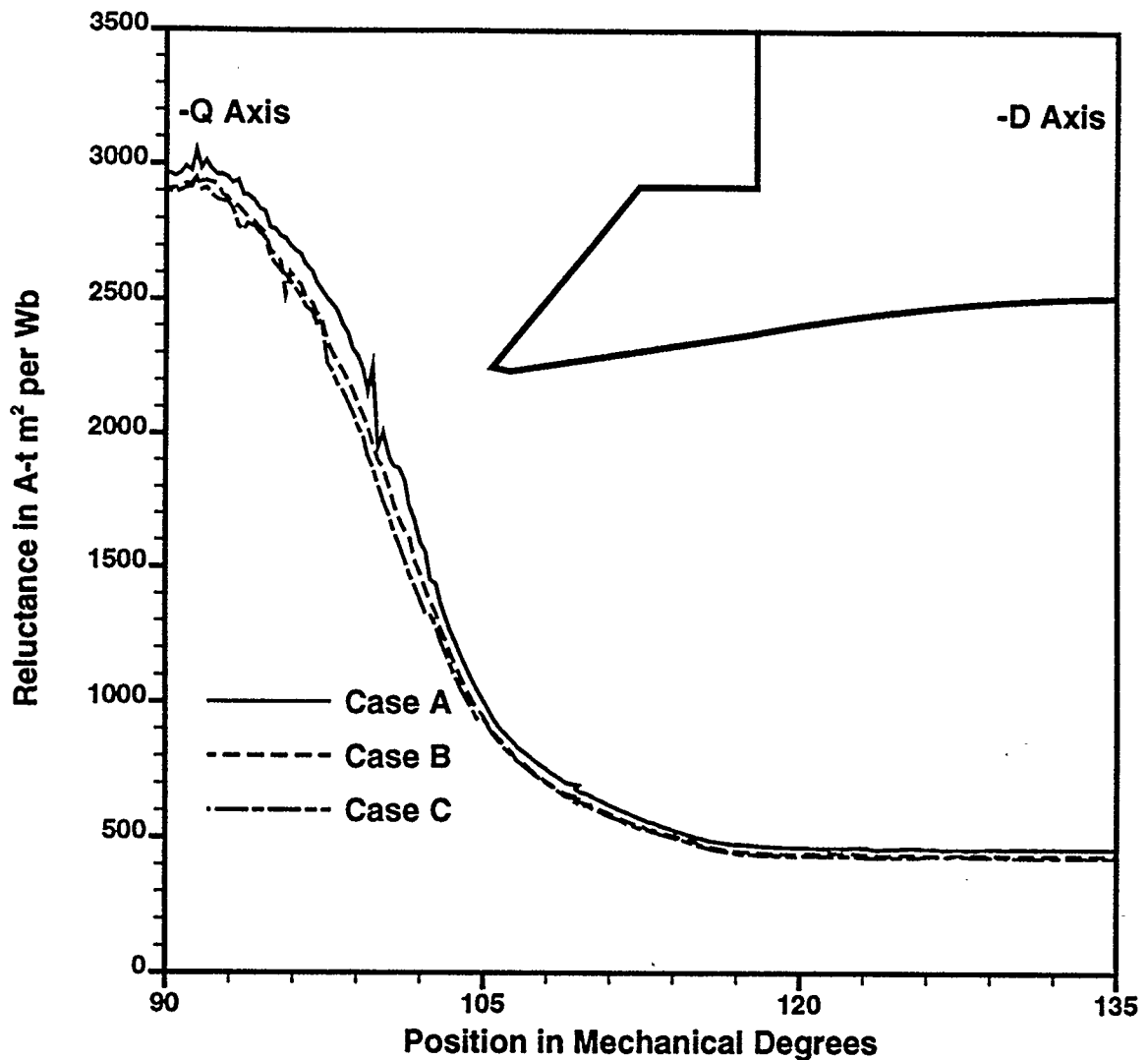


Figure 3.7: Comparison of R_{base} Waves for Different Magnetic Histories

which I called "magnetic resetting" ensured that there were no hysteresis anomalies in the magnetic circuit from previous experiments. It was with the machine magnetically reset that R_{base} was finally characterized. The hysteresis effects are noticeable, with Case A being about 7% higher than Case C below the field pole, and 14% higher in some spots in the quadrature axis region.

Even at these low excitation levels, the linearity assumption is not totally correct. The assumption of μ being constant for iron is only an approximation and should be used with discretion.

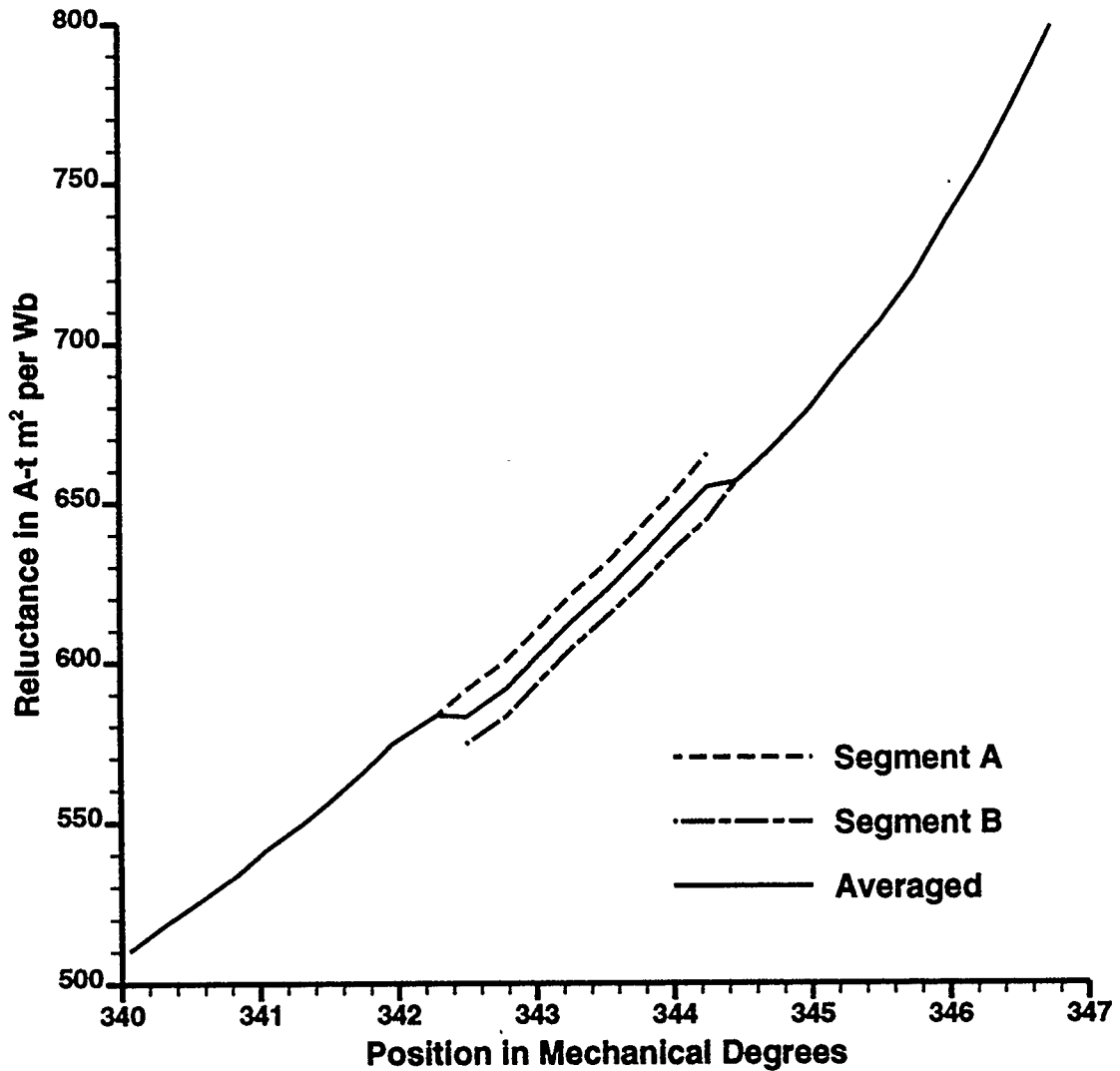


Figure 3.8: Comparison of Typical Overlapping Reluctance Segments

The third characteristic which was investigated was the difference in reluctances in the overlap between consecutive segments. Below the pole face, the average error between the overlapping portions is about 1.7% and is fairly consistent. In the interpolar regions the error can vary from 4 to 9% with higher errors occurring in later segments in the series. Detail of the typical overlap between consecutive segments is shown in Figure 3.8.

These errors are from three sources:

- i) Less smoothing effect is present in the interpolar regions' averaged B data. This

results in a rougher reluctance wave in the interpolar regions. There is less smoothing here because the unaveraged B distribution in the interpolar regions has a high slope, and where there is a slot there is a wide dip in the distribution followed by a flat region. When averaging over a tooth pitch, these wide dips and flat spots, being on a sloping distribution, do not smooth out as readily as the dips under the pole faces. The averaged B distribution then has some roughness left in it.

- ii) Higher percentage error occurs for later segments in the series. The effects of hysteresis caused by partial reverse excitation of the field poles (when the MMF axes are centred on the quadrature axes) lead to increased error (about 4% more) in the overlapping sections of successive segments on one side of the pole, relative to the other side. This can be partially corrected by magnetically resetting the machine iron between measurements for successive segments, but dissymmetry still exists in the B distributions.
- iii) Another source of error between successive, overlapping R_{base} segments is from fringing in the B distribution. Regardless of which side of the pole you are on, when the overlap between successive segments is compared, the segment with the higher reluctance (for the same angular position) is the one whose MMF axis is closer to the pole centre line. Figure 3.8 is an example: segment A is higher than segment B in the overlapping region. The MMF distribution is constant over the segment width, and remains the same in the overlapping regions for both segments. However, in order for the R_{base} values to differ for the same position, the B distribution must have a different magnitude for the same angular position from one segment to the next. The magnetic circuit modelling approach proposal in this research simply offers no means of modelling this behaviour. Under linear conditions, it would say that since you have the same MMF values at the same angular position then you should have the same B value and the same R_{base} value. Therefore, in order to predict this fringing behaviour, the entire field region (or symmetrical portions of it) should be modelled using finite element analysis. This error is most significant in the interpolar regions (about 4%). Some of the flux that would have gone from the rotor into the field pole is going into the stator backiron directly thus complicating the field solution. When successive segments are

compared under the field poles this error drops to about 1.7% implying that these fringing effects are not as significant here.

By averaging the two successive segments where they overlap (as shown by the averaged segment in Figure 3.8), a reasonably continuous R_{base} waveform can be assembled as shown in Figure 3.9. R_{base} can be expressed by using a Fourier series. By truncating the series after 30 terms, any remaining glitches are smoothed out. The R_{base} distribution contains both odd and even harmonics since there is no half-wave symmetry. R_{base} has minimum constant reluctance below the constant air gap portions of the pole faces, and this reluctance starts increasing below the chamfered portions of the pole faces. It then increases significantly in the interpolar regions.

R_{base} has now been determined. It will be assumed to be constant, regardless of MMF level. It essentially models the effects of the pole face and pole saliency under linear conditions.

The shape of R_{base} is similar to the inverse of the zero order MMF's permeance distribution shown in Doherty/Nickle [15, p. 916]. Differences between the two may be because Doherty/Nickle did not include finite iron permeability, and differing pole shapes. Doherty/Nickle also considered the permeance distributions for each specific MMF harmonic separately.

3.2.4 Determining and Using the Experimental Armature MMF Wave

Now that R_{base} has been found, equation 2.2 can be used to back calculate the full a and -b MMF wave under linear conditions for comparison with the theoretical one.

Figure 3.10 shows results for back calculated MMF waves. These MMF waves are superimposed upon the R_{base} wave. Three cases are considered. Case A is for the a and -b MMF axis centred on the direct axis. Case B is when it is centred on the +Q axis, and Case C is when it is centred on the -Q axis. The magnitude of the MMF waves are all normalized with $N = 1$, and the armature current is 1.0 p.u. (18 A). The B data used is the same B data for those cases that were used in determining R_{base} , so all we have done is use equation 2.2 in reverse to find MMF.

Concentrating on Case A first, we can see that beneath the pole, the MMF shape is smooth, and very much like the theoretical averaged one shown in Figure 3.4 (a more detailed comparison shall be made later). In the quadrature axis regions (on the flanks of the MMF wave), the MMF wave has a step-like characteristic. This is because the

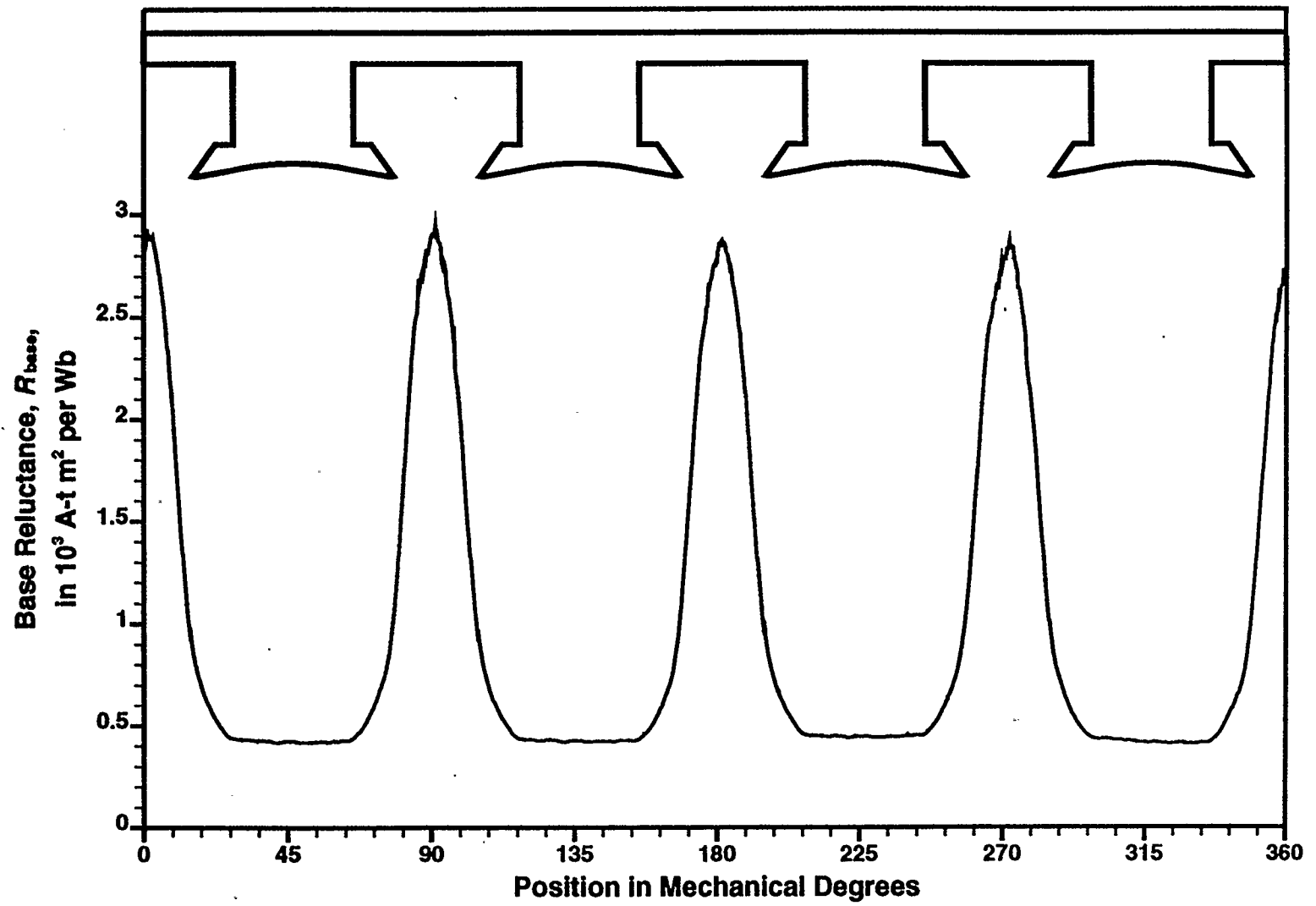


Figure 3.9: Completed R_{base} Distribution, Armature Current = 1.0 p.u.

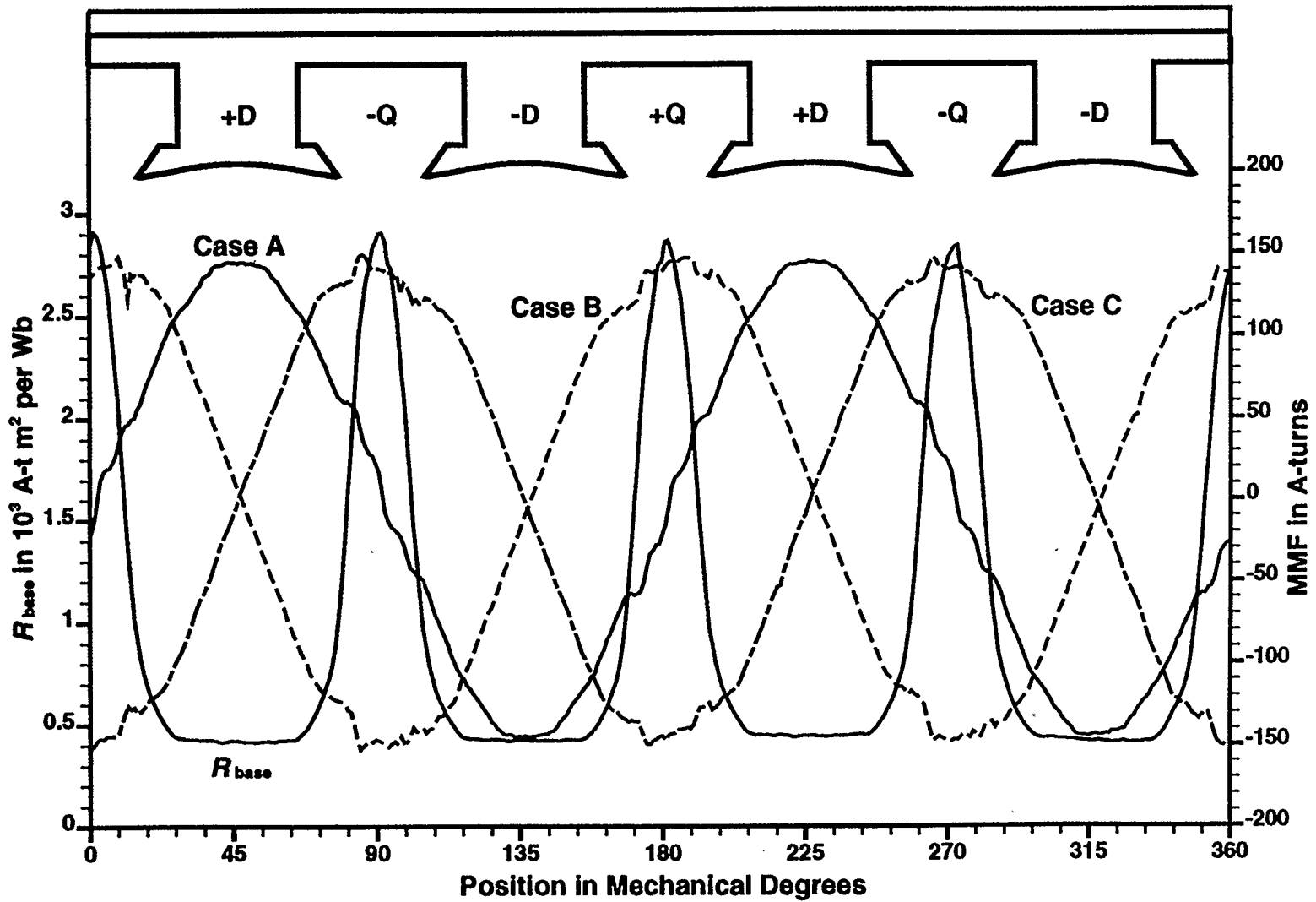


Figure 3.10: Comparison of Back Calculated A and -B MMF Waves, Armature Current = 1.0 p.u., $N = 1$

averaged B distribution is rougher in the quadrature axis regions, and R_{base} possesses small bumps at the joints between consecutive segments. In reality, this stepped part should be a straight line.

Cases B and C confirm the effect of quadrature axis roughness in the averaged B and R_{base} distributions, since they also have rough peaks in the same angular positions as the rough flanks of Case A. Under the poles, however, the MMF waves have very smooth sides, in agreement with the theoretical averaged MMF wave in Figure 3.4. In both cases B and C, the sides of the armature MMF wave beneath field poles which have the same field MMF polarity as the armature MMF wave are higher than the sides where the armature MMF wave's polarity is opposed to the field MMF's polarity. This is evidently due to hysteresis effects, as mentioned in section 3.2.3.

In order to obtain a better picture of what the actual MMF wave is like, the quadrature axis roughness and hysteresis effects need to be removed. Two approaches were tried. The first was to shift the two quadrature axis MMF waves onto the direct axis and average them. The second was to take the well defined portion of the Case A MMF wave (under the poles) and splice it to the position shifted smooth sides of the case B and C MMF waves (these were also, originally, from positions under the poles). The second approach, splicing, was better than the first since the averaging approach still left the roughness in the axis region of the MMF wave. The resulting spliced MMF wave is compared with the averaged theoretical MMF wave (of Figure 3.4) in Figure 3.11.

The spliced MMF distribution appears to be closer to a sinusoid than the theoretical one. Fourier analysis shows that the theoretical one has a fundamental which is 3.86% higher than the spliced case, and all of the spliced case's higher harmonics are much smaller. The highest one for the theoretical case is the 5th with a magnitude about 3% of its fundamental. The highest harmonic for the spliced case is the 5th, with a magnitude about 1.08% of its fundamental. In much of the literature the simplifying assumption of a sinusoidal MMF wave is used. Apparently, based on my measurements, this is not a bad assumption.

In order to use the spliced a and -b MMF distribution for modelling purposes, it can be expressed in terms of Fourier components. The total a and -b MMF is simply the sum of these components. The general formula for computing the a and -b armature MMF at any point is

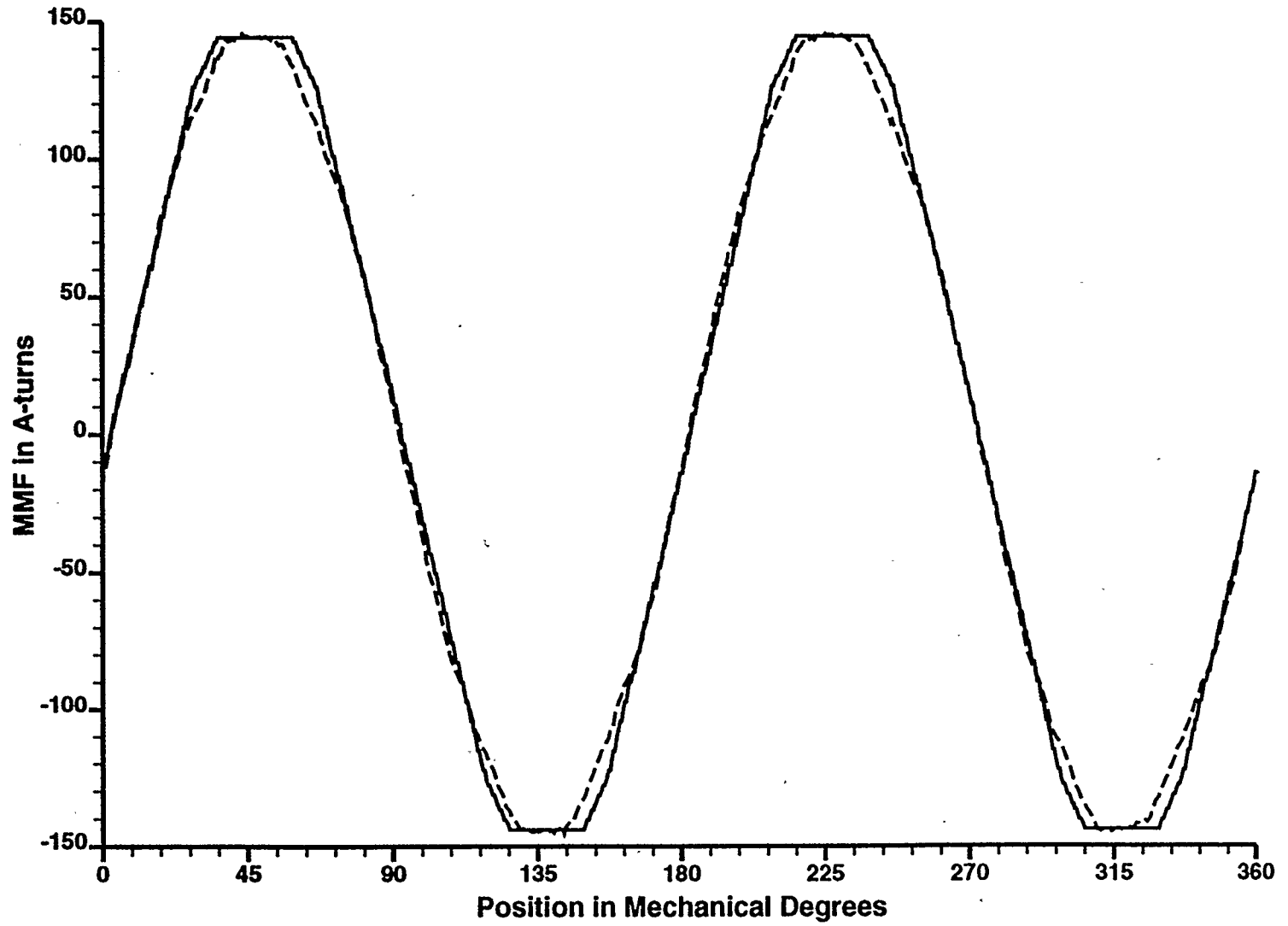


Figure 3.11: Comparison of Averaged Theoretical (solid) and Spliced Measured (dashed) MMF Waves, Armature Current = 1.0 p.u., $N = 1$

$$\mathcal{F}(statorg) = \sum_{j=1}^m \mathcal{F}_j \times i \times \sin [(2 \times j \times statorg) + \theta_j + (2 \times j \times (rotorg - 35))] \quad (3.4),$$

where $\mathcal{F}(statorg)$ is the a and -b armature MMF distribution at angular location *statorg*. *statorg* is the stator gauge reading on the experimental machine in mechanical degrees (or radians). This is the angular position coordinate present on the horizontal axes of all of the figures so far (for example, see Figure 3.11). *statorg* ranges from 0° to 360° mechanical. Each term in the sine function is in electrical degrees, so $(2 \times j \times statorg)$ goes through 720° electrical, or 2 full cycles, as the rotor physically rotates 360° mechanical. *j* is the harmonic order, *m* is the maximum order used in the approximation (for modelling purposes *m* only needed to be 15). θ_j is the phase angle (in electrical degrees or radians) and \mathcal{F}_j is the magnitude of each component. These are output from my Fourier analysis program. *rotorg* is the rotor gauge reading on the experimental machine in mechanical degrees or radians. As mentioned earlier, *rotorg* - 35 (in mechanical degrees) is the angular position of the a and -b MMF axis with respect to the centre line of the reference North pole (+D axis). *i* is the experimentally applied DC current flowing through the a and -b windings.

With the spliced a and -b MMF wave now known, and expressible using equation 3.4, R_{base} can be determined from fewer *B* distributions by making the segment width greater. Rather than using 12 averaged runs of 10° mechanical segment width stepped by 7.5° mechanical, I was able to fully characterize R_{base} using only three. This greatly speeded up the process of determining the effects of saturation upon *R* since several reluctance waves had to be computed for different current levels.

A number of trials with varying acceptance widths and varying MMF wave orientations were performed. If the acceptance widths were too wide, divide by zero problems started to occur as the *B* distribution approached zero. The best solution was to use three segments, one centred on the +D axis with a width of 55° mechanical, one centred on the +Q axis with a width of 40° mechanical, and one centred on the -Q axis with a width of 40° mechanical. Both quadrature axis reluctance waves were averaged to eliminate roughness and hysteresis effects. The rms error in the R_{base} wave computed this way, as compared to the one computed using twelve 10° mechanical segments, is 2.8%. The

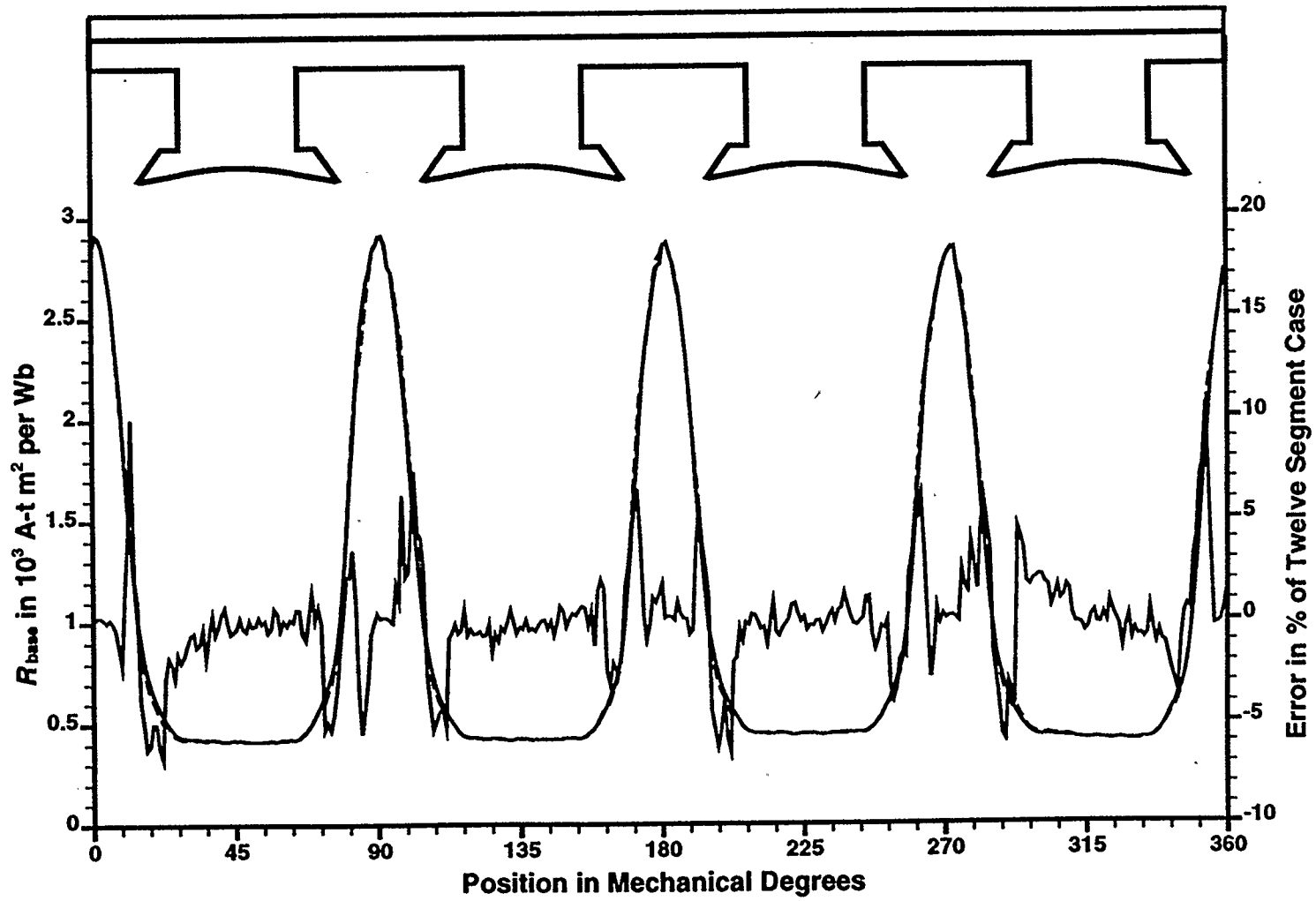


Figure 3.12: Comparison of R_{base} Computed Using Twelve 10° Mechanical Segments (solid) vs. Three Wider Segments (dashed), Error Also Plotted

results are shown in Figure 3.12.

Success in determining R_{base} with the experimental armature MMF wave shows that if the armature MMF wave is known, R_{base} can be determined with fewer data runs by using wider segments. Direct use of the theoretical armature MMF wave, or even just a sinusoid, could also be attempted. Since the harmonics in the armature MMF wave are small relative to the fundamental, little error should be present in an R_{base} wave determined using the theoretical armature MMF wave or just the fundamental of the armature MMF wave.

Superposition of the MMF waves of the rotor windings for linear conditions can also be checked. Refer to Figure 3.13. With the a and -b MMF wave centred on the +D axis, and 1.0 p.u. armature current, the resulting MMF wave is determined using equation 2.2. Next, with the rotor in the same position, 1.0 p.u. armature current is passed through the a winding only. The same is then done for the -b winding only. When the MMF waves for a alone and -b alone are numerically added, the result is practically identical to the case when a and -b are excited simultaneously. The principle of superposition appears to hold.

I constructed a spliced single phase MMF wave in the same manner as for the spliced a and -b MMF wave of Figure 3.11. The resulting single phase MMF wave is shown in Figure 3.14.

The harmonics of the single phase MMF wave are substantially higher than for the a and -b MMF wave. However, when the a only and -b only single phase MMF's are added, the harmonic level becomes similar to that for the a and -b MMF wave. The third harmonic, present in the single phase MMF wave, goes to zero when the two single phase MMF's are added. This is due to the spatial arrangement of the single phase windings.

With the single phase MMF's now determined they can be used in the model along with three phase currents. We are no longer restricted to the experimental a and -b MMF wave for one instant in time. All of our static experiments must use the a and -b MMF wave because of equipment limitations, however.

The a only and -b only single phase spliced MMF waves are added and compared to the a and -b spliced MMF wave for the same point in time (armature current is 1.0 p.u.). The result is shown in Figure 3.15.

The summed single phase MMF's in Figure 3.15 are not quite equal to the a and -b

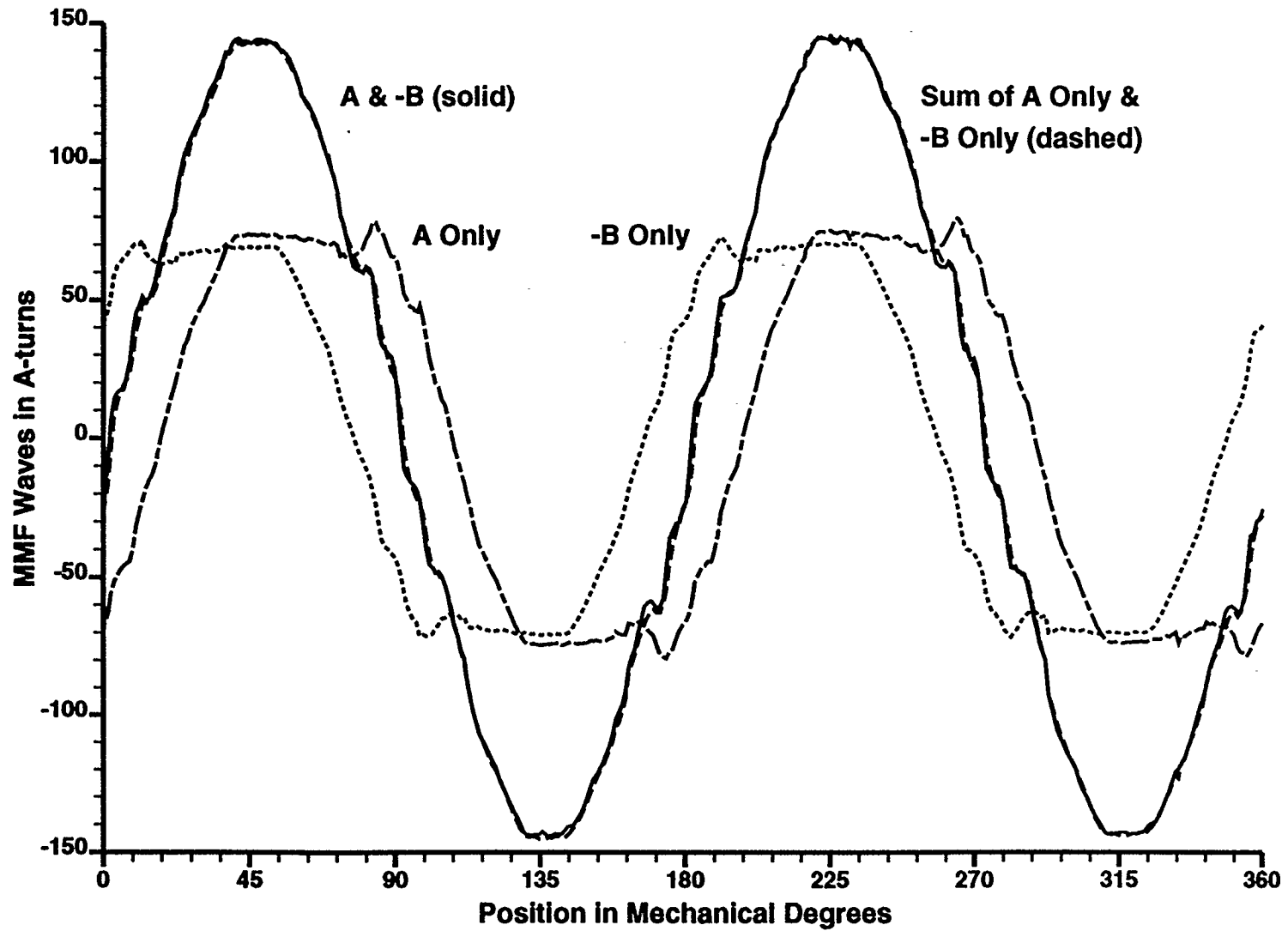


Figure 3.13: MMF Comparison: A and -B Windings, A Alone, -B Alone, Sum of A Alone and -B Alone, Armature Current = 1.0 p.u.

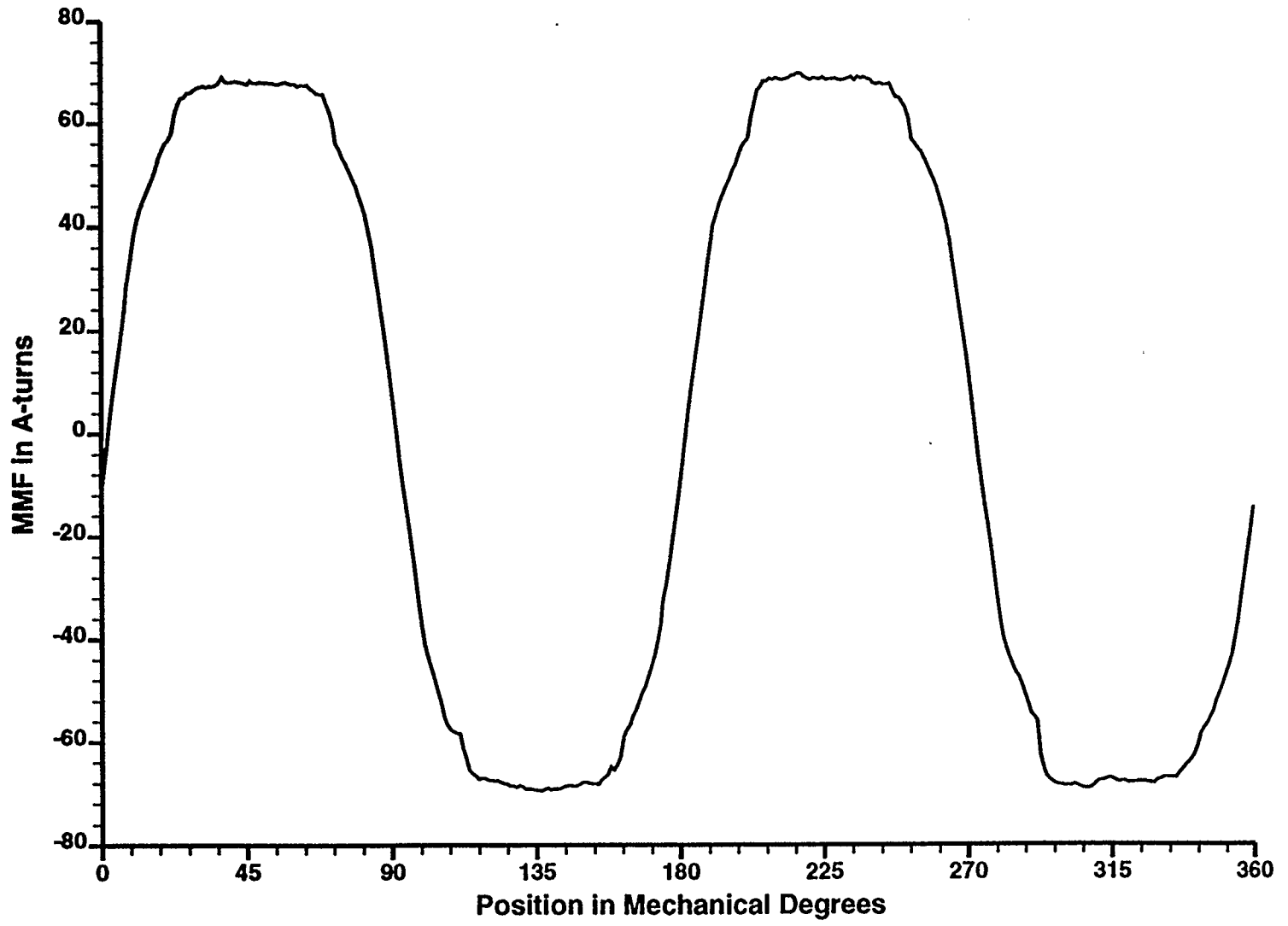


Figure 3.14: Single Phase Spliced MMF Wave

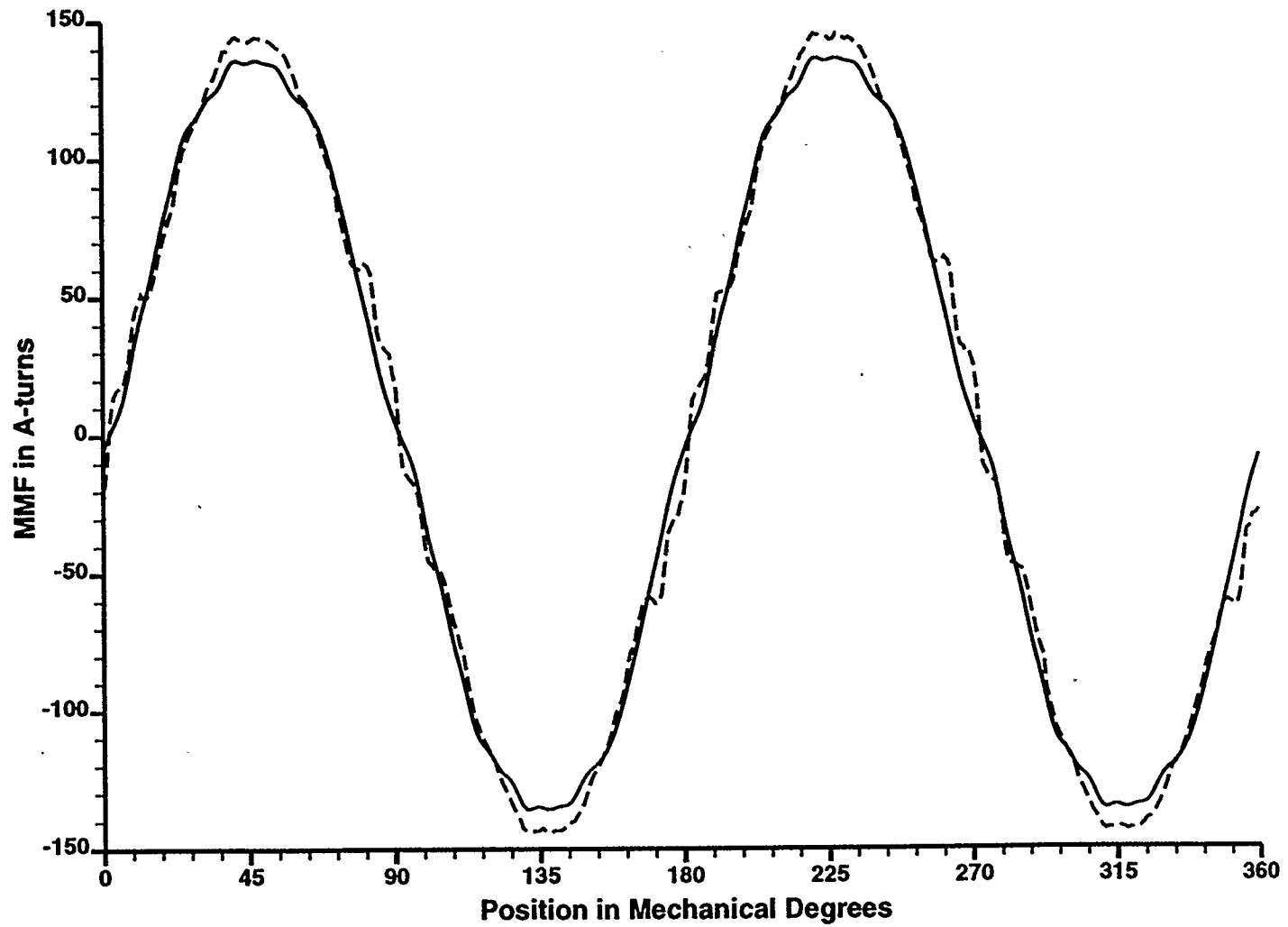


Figure 3.15: Comparison of Summed A Only and -B Only Spliced Single Phase MMF's (solid) and Spliced A and -B MMF (dashed) for the Same Conditions, Armature Current = 1.0 p.u.

MMF. This is due to the nonlinearity of the iron. The single phase MMF's, for the same current, are about half the magnitude of the a and -b MMF. As will be shown later in this chapter, under the lower MMF conditions present when only the single phase windings are excited, R actually increases. When the single phase MMF waves were calculated R was assumed to be constant. Therefore, the lower value of B , caused by a higher R and not a lower MMF, appears to give a lower value of MMF than what linearity would dictate.

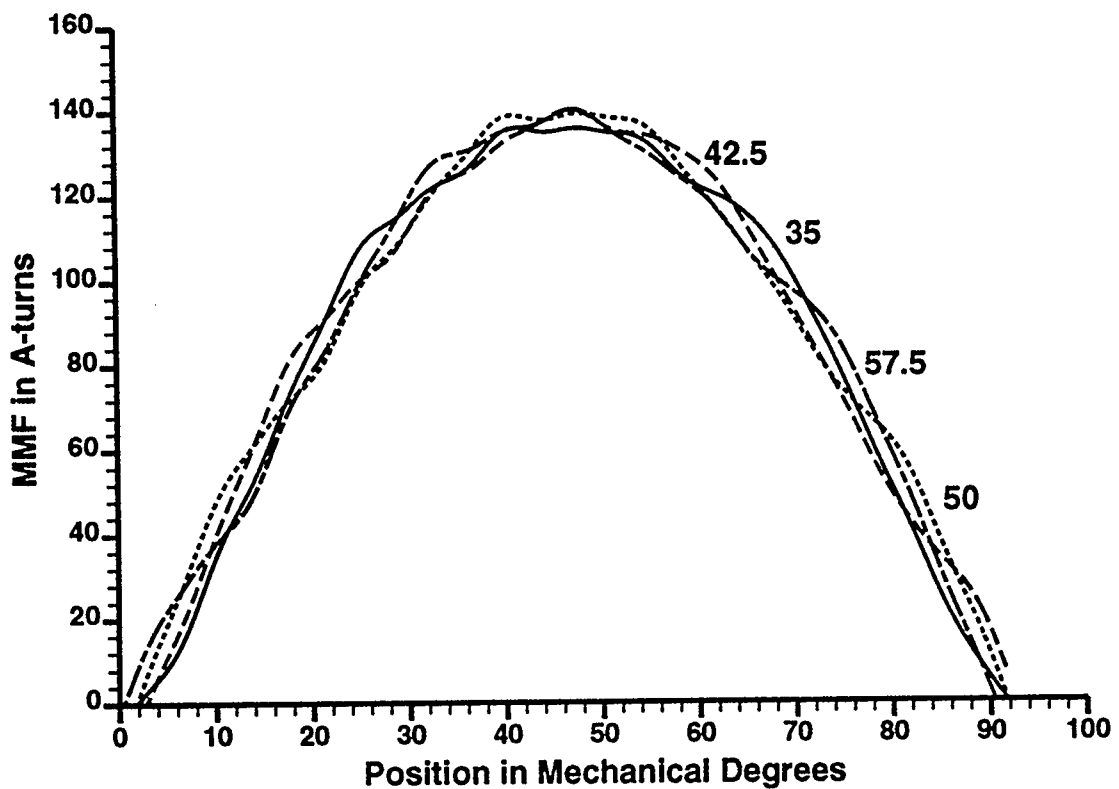


Figure 3.16: Comparison of Armature MMF's, $rotorg = 35^\circ, 42.5^\circ, 50^\circ,$ and 57.5° mechanical

Under steady state conditions, Langsdorf [27, pp. 200-218] demonstrates that the

space harmonics of the phase MMF's, the time harmonics of current, and the rotor rotation combine to create a variety of MMF harmonics rotating both forwards and backwards with respect to the rotor at various fractions of the synchronous speed. By considering only the time fundamental of current, and a three phase balanced system (the rms values of the phase currents are related to the 1.0 p.u. (18 A) experimental DC value by equation 2.13), the effect of the space harmonics of the three phases' MMF's (as time progresses and the rotor rotates) can be calculated. These results for four different rotor positions (four different points in time) are shown in Figure 3.16.

The MMF axis (and the fundamental of MMF) always remains centred on the same angular position, in agreement with the references quoted in section 2.2.3. The variation at any one point over the course of a cycle is ± 5 amp-turns ($\pm 3.6\%$ of the peak). Therefore, the error introduced by using spliced MMF's, or even theoretical MMF waves, is small relative to the harmonic variation. On the other hand, the harmonic variation itself can often be neglected when considering its effects on torque or voltage since the armature MMF wave is normally dwarfed by the field MMF wave. However, for conditions where the armature current becomes very large (for example, under short circuit conditions) the armature MMF wave can become comparable in magnitude to the field MMF wave, in which case harmonics should not be neglected.

In order to limit the scope of this research, the flux distribution, torque, and voltage models will not consider the effects of space and time harmonics, although as just shown here, this can be easily done. Either the a and -b MMF wave or the superimposed a only and -b only MMF wave will be used in the models for consistency with the experimental measurements.

3.2.5 Determination of Field MMF

Moullin [9, p. 254] gives examples of field shapes that can be used to approximate the field shape under a salient pole (see Figure 3.17). One is a trapezoid, and the other is constant in the centre but with a \sin^2 function representing the sides. The latter function has more rounded corners and a smooth curve which approaches the neutral axis tangentially. In Figure 3.17 *B* is the maximum value of the flux density distribution.

Under the conditions of a uniform air gap and infinite permeability, the MMF waves for the salient poles would be proportional to the flux distributions shown in Figure 3.17. However, since we have salient, chamfered poles, we do not have a uniform air gap. Also

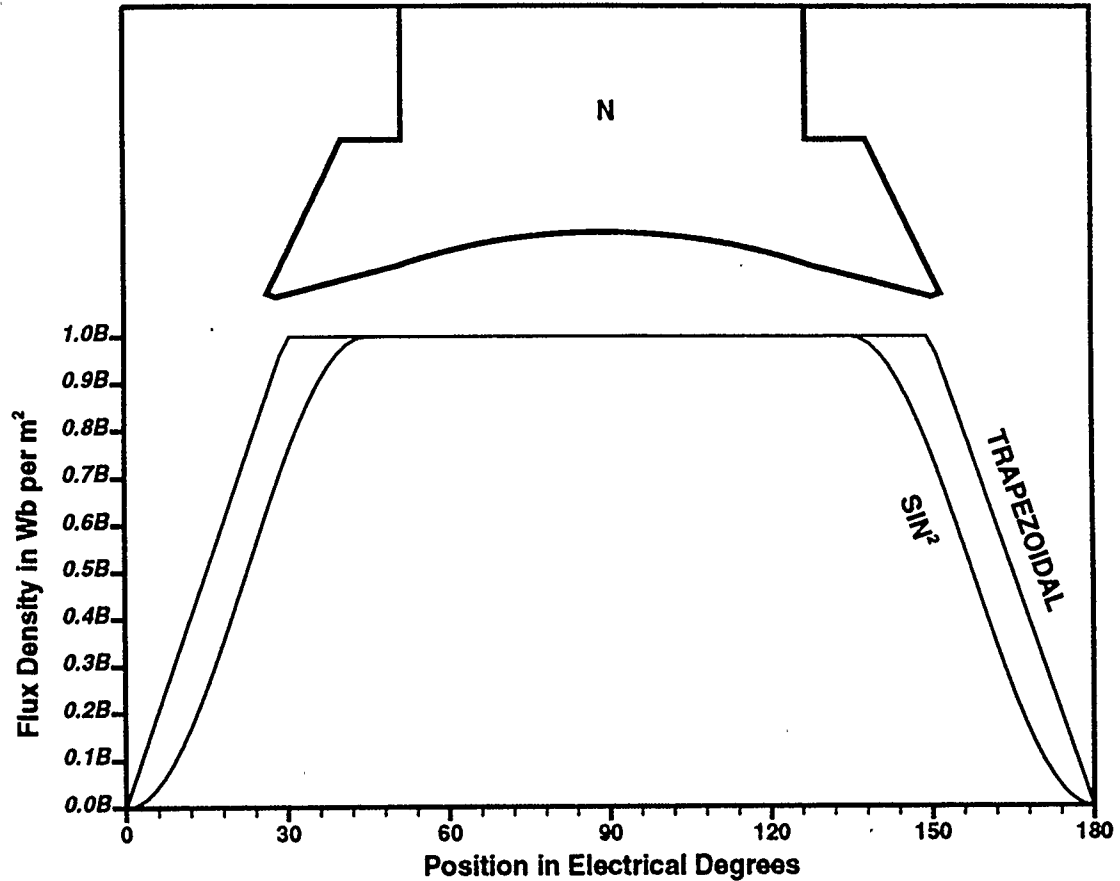


Figure 3.17: Trapezoidal and \sin^2 Approximations to Flux Distributions Under a Salient Pole

infinite permeability is a questionable assumption.

We can compute the field MMF in much the same way as we back calculated the experimental a and -b MMF for the armature, under the assumption that R_{base} remains constant for both the armature and field MMF. R_{base} should be constant if the peak value of the B distribution under field excitation equals the peak value of the B distribution under a and -b armature MMF excitation, the a and -b armature MMF excitation level is the one used to determine R_{base} , and the armature MMF axis is centred on the field pole. Figure 3.18 compares the B distributions for field current levels of 0.5 p.u. (1.0 A) and 0.75 p.u. (1.5 A) with that for 1.0 p.u. (1.8 A) a and -b armature MMF excitation. From Figure 3.18, field B distribution data for a field current level between 0.5 and 0.75 p.u. should be used to compute the field MMF distribution. I will examine both the 0.5 and 0.75 p.u. cases to

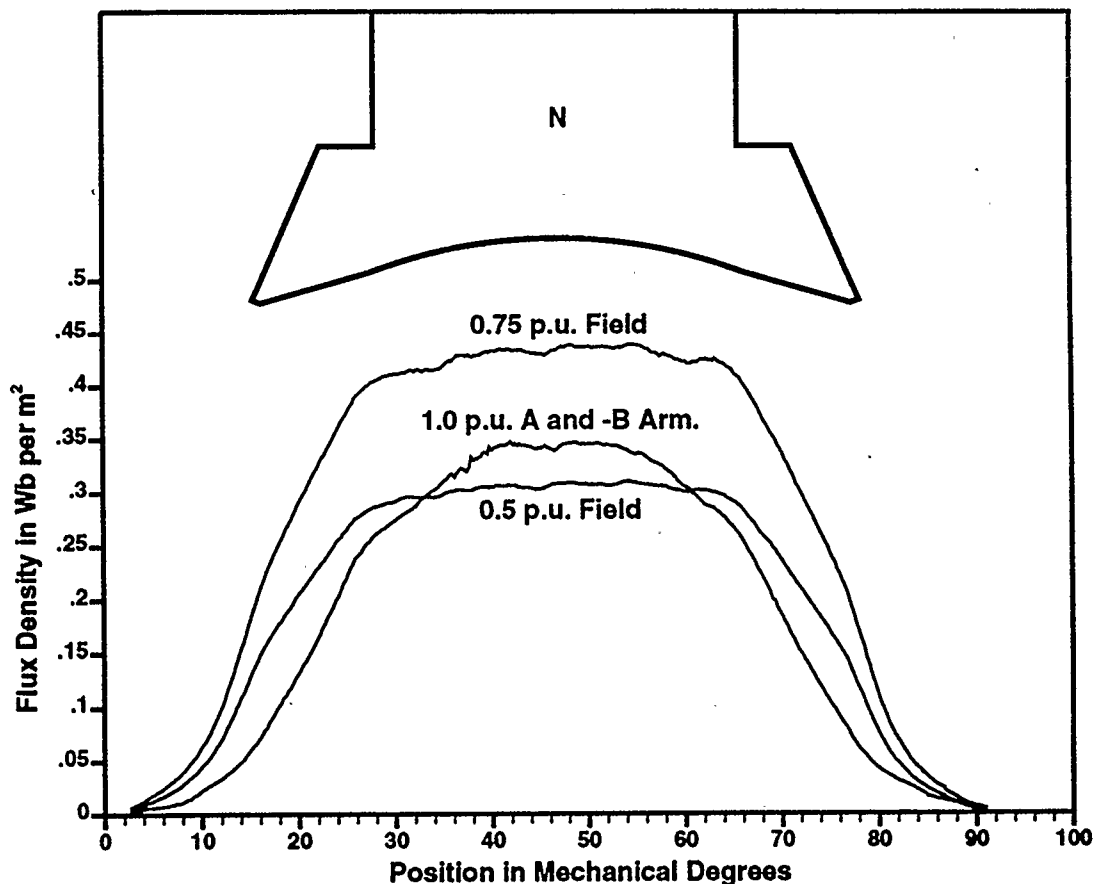


Figure 3.18: Comparison of B Distributions for Field Current Only (0.5 and 0.75 p.u.) and Armature A and -B Only (1 p.u.)

determine how sensitive the field MMF distribution is to the field current level.

In Figure 3.19 I have plotted the resultant field MMF waves for these two cases. Both cases used the R_{base} wave shown in Figure 3.9 and are computed using equation 2.2. In Case A, the field current is 0.75 p.u. (1.5 A). Notice the roughness on the flatter portion of the wave. The roughness is present due to the products of the slight imperfections in R_{base} , and the larger imperfections in B (even though averaging largely removes all of the tooth effects, a small amount is still present). This roughness is also present on the flanks

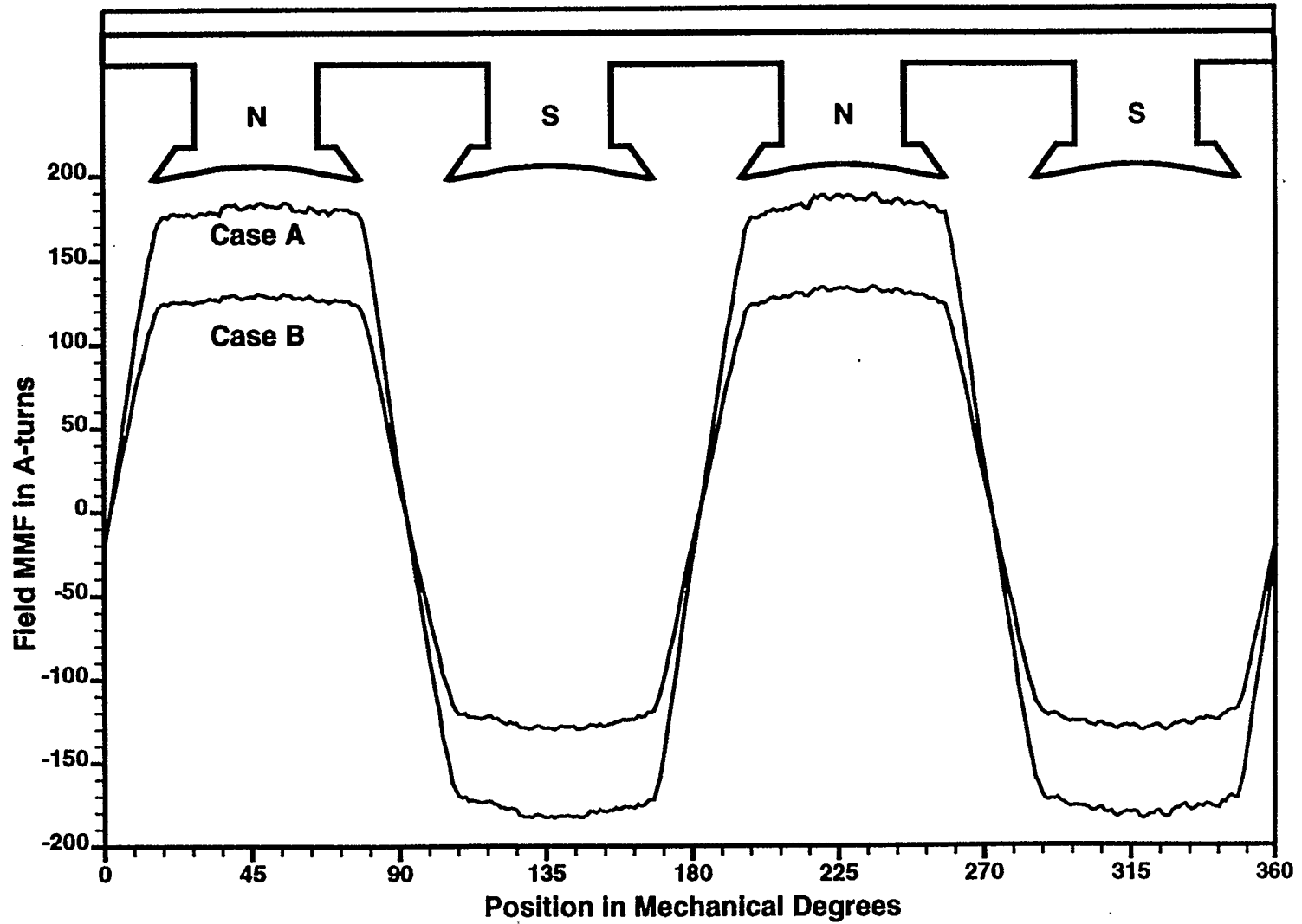


Figure 3.19: Comparison of Field MMF Waves, Case A: Field Current = 0.75 p.u., Case B: Field Current = 0.5 p.u.

of the field MMF wave, although it is less visible due to the wave's steep slope in those regions. Case B is for 0.5 p.u. (1.0 A) field current. Its peak value is 1/1.44 times that of the 0.75 p.u. case. This suggests that the field MMF is directly proportional to current for linear conditions since the small deviation from 1/1.5 is likely due to saturation.

If the air gap were uniform, the field MMF would produce a B distribution similar to the trapezoidal case of Figure 3.17.

The field MMF wave in the air gap is not expected to maintain a constant shape and remain proportional to field current under saturated conditions, but these assumptions will be made for modelling purposes. R_{sat} will take care of any deviation from linearity.

Now that we know the shape of the field MMF wave for linear conditions, we can estimate the number of conductors per coil, N , as mentioned earlier in the armature MMF section. Consider the flux density distributions at the centre of the pole face of Figure 3.18. When the flux density distribution (at the pole centre) for the field winding is equal to the flux density distribution from the armature winding (a and -b excitation) then, since R_{base} is constant and the two MMF waves are nearly flat at the centre of the poles, the peaks of the two MMF waves are numerically equal. Consider the integration path (for equation 3.2) shown in Figure 3.20. The total field current enclosed in the integration path for these conditions equals $(1068)(2)(1.15)(1)$ amps. 1068 is the number of turns in each field coil, the 2 is present because there are 2 field coil sides enclosed, each having 1068 turn sides. The $(1.15)(1)$ is the approximate field current required to give the same B values at the centre of the pole face as the 18 amp a and -b case. The required current in the armature windings for the same B value at the centre of the pole face is $(16)(N)(18)$, where 16 is the total number of armature coil sides enclosed in the integration path (from both the a and -b windings), N is the unknown number of conductors in each coil, and 18 amps is the DC current level in each conductor. Solving for N we get $N = 8.53$. Either 8 or 9 conductors per coil can be used. In Chapter 5 I used 9 because it gave better computed torque results.

By determining N as 9, the absolute magnitude of the a and -b armature MMF wave, R_{base} , R_{sat} , and the field MMF wave will all be increased by a factor of 9 from the $N = 1$ assumed in all of the plots shown in this chapter. The modelled B distributions shown in Chapter 4 used $N = 1$, and are all unaffected by whatever N is used, as long as the MMF and reluctance waves are all based on the same N . Chapters 5 and 6 use $N = 9$, since

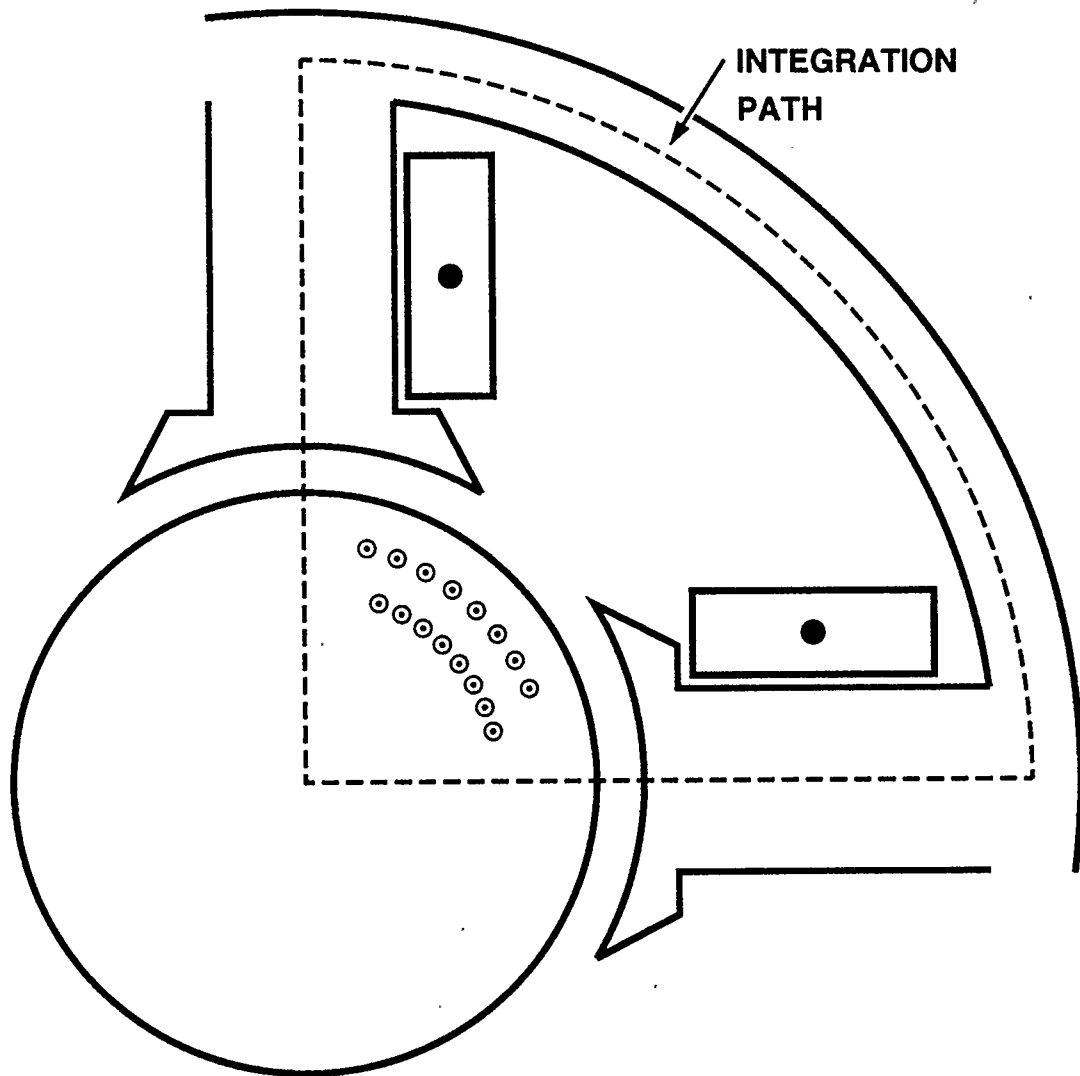


Figure 3.20: Integration Path for Determining N

both the torque and voltage prediction models are directly proportional to N .

Because of its trapezoidal shape, the harmonic content of the field MMF wave is much higher than for the a and -b armature MMF wave. For a field current of 0.5 p.u. (1 A) the harmonic distribution is shown in Figure 3.21. The field MMF's 3rd harmonic is 21.4% and the 5th harmonic is 5.4% of the fundamental. Due to the shape of the reluctance wave, however, the corresponding B distribution's 3rd harmonic is only 2.7% and 5th harmonic is increased to 10.6% of the fundamental.

The pole arc to pole pitch ratio for the trapezoidal field MMF distribution in Figure 3.19

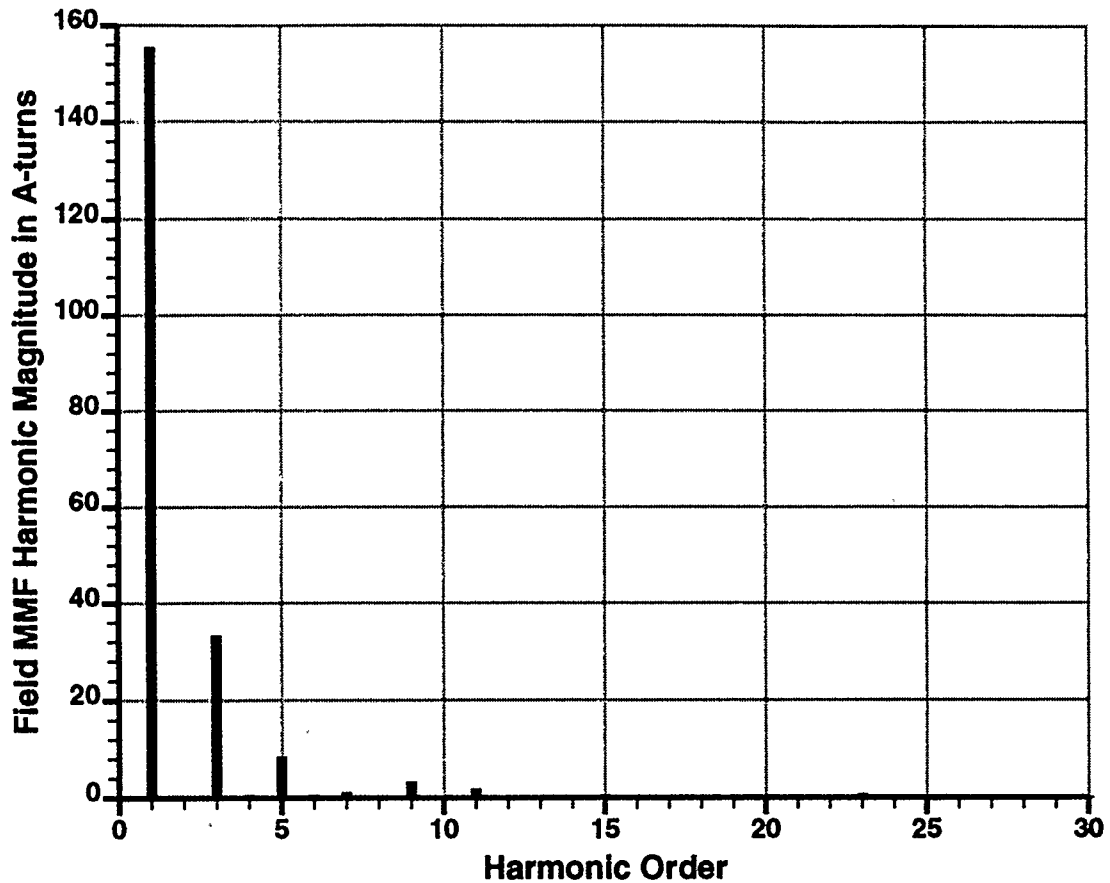


Figure 3.21: Harmonic Content of Field MMF Wave, Field Current = 0.5 p.u.

is 0.7. The physical pole arc to pole pitch ratio of the machine is also 0.7. Walker [10, pp. 82, 117-118] recommends this ratio be 0.7 also. If it is too large (greater than 0.75) then there will be too much leakage flux and too high a flux density in the pole body. If it is too small (less than 0.67) then there is inadequate overhang to support the field coil. Walker also mentions that the curvature of the pole shoe should be less than that of the stator (or, in our case, more than that of the stator) in order to reduce harmonics in the flux density distribution and, in turn, in the induced voltage.

Figure 3.19 suggests that a trapezoid with the width of its constant portion equal to the pole arc width is a good approximation to the field MMF. Its height should be set equal to $(\text{number of field turns})(2)(\text{field current})/2$ where the 2 in the denominator accounts for the integration path crossing two air gaps.

3.2.6 Characterizing R_{sat}

Now that the field MMF distribution is known, we can characterize R 's dependence upon MMF levels. Equation 2.3 is repeated here

$$R = R_{\text{base}} + R_{\text{sat}}$$

Until this point we always worked with a constant MMF level in the armature and field windings. R then equaled R_{base} . Now we will attempt to determine how much R deviates from R_{base} under saturated conditions, and characterize the difference between R and R_{base} with R_{sat} .

Some deviation of R with MMF level can be determined using just the armature MMF wave, but because the armature MMF wave requires about 18 times as much current to equal the magnitude of the field MMF wave, we will concentrate our efforts on using the field MMF to characterize R_{sat} .

Figure 3.22 shows the variation of the R wave in the polar region with different armature current levels. For low MMF's (the 0.5 and 0.75 p.u. cases) R decreases with increasing MMF. A plot of the changing R value under the pole face as a function of armature current is shown in Figure 3.23. This is due to the non-linearity of the B-H characteristic of the iron. R behaves as if it were inversely proportional to μ , the iron permeability. μ is the slope of the B-H curve shown in Figure 3.24 since $B = \mu H$. For low and high H levels μ is small and R is large. When H is in the range for which the B-H curve is considered linear, μ is large and R is small. This is consistent with the shape of the R vs. armature current curve in Figure 3.23.

At high MMF levels R starts to lose its shape due to saturation effects. In the 2.0 p.u. case of Figure 3.22 (roughly the same MMF level as for 1.0 p.u. field current conditions) the effect of damper bar slots is visible. Saturation causes R to vary more at some points than at others. This is why R_{sat} is both a function of MMF level and position. In accordance with the initial proposal, and in order to keep the scope of this research reasonable, we will assume R_{sat} to be a function of MMF only and we will disregard its

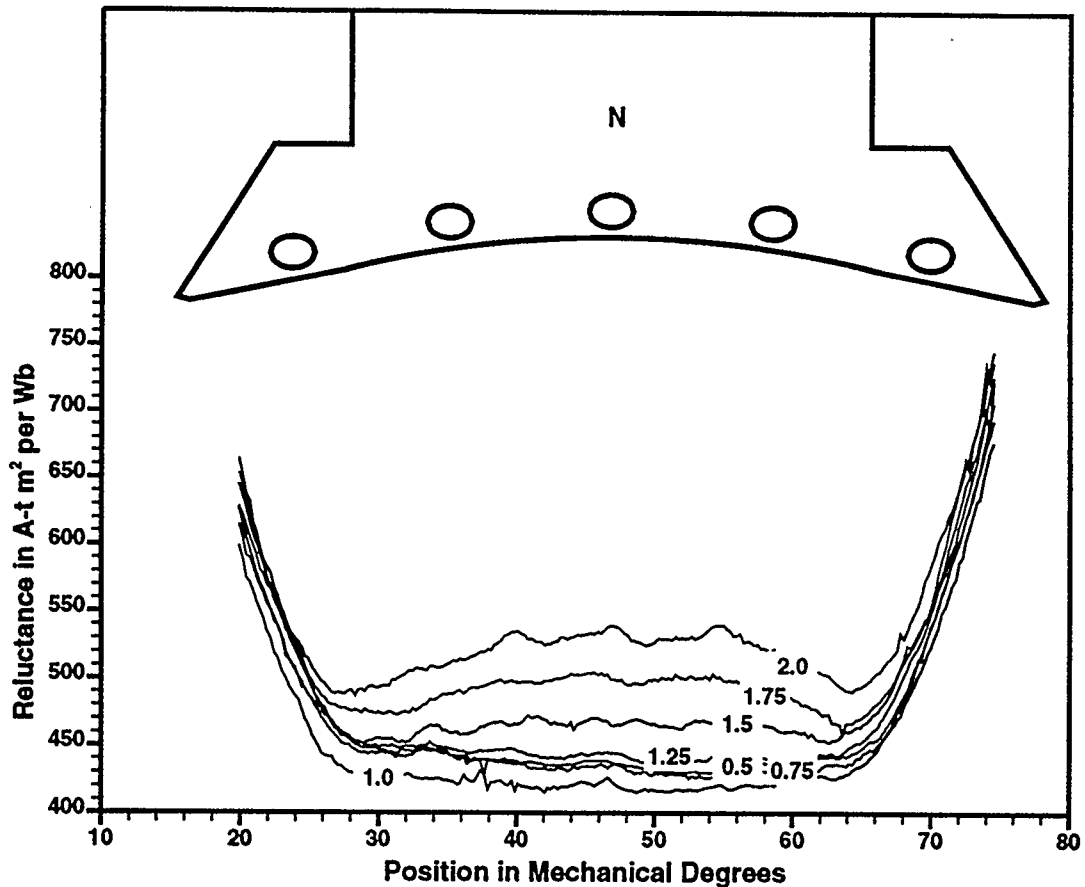


Figure 3.22: Comparison of R Waves for Armature Current from 0.5 to 2.0 p.u.

variation with angular position.

Figure 3.25 shows the variation of R with field current levels from 0.25 to 3 p.u. The R wave is distorted due to saturation.

The R wave for the 2 p.u. armature current case in Figure 3.22 and the R wave for the 1.0 p.u. field current case from Figure 3.25, both for approximately the same peak MMF levels, are compared in Figure 3.26. The effects of saturation upon R are slightly different for the armature and field MMF waves. Under linear conditions, however, R has the same shape for both the armature and field MMF's. For very low field MMF's R does

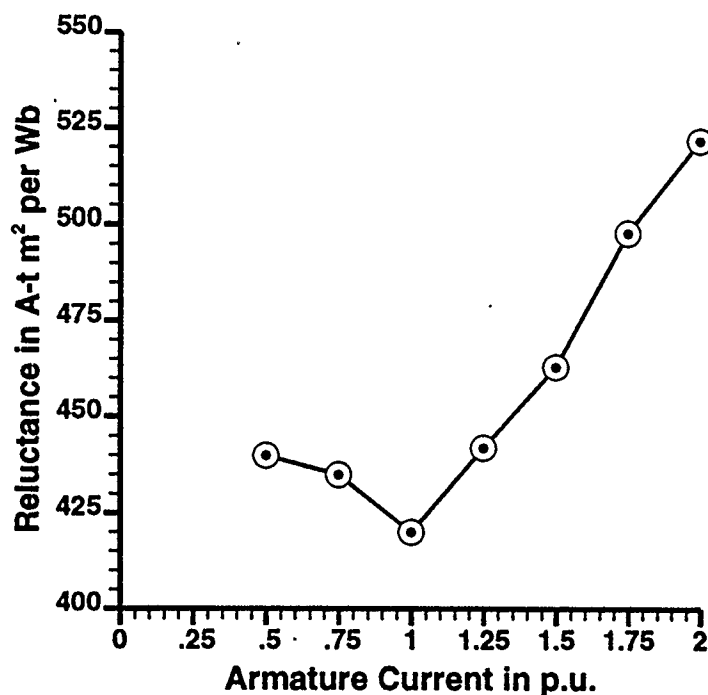


Figure 3.23: Variation of Average R Under the Pole Face with Armature Current Levels

not appear to increase as it does for low armature MMF's. Additional data would have to be collected to see if a point exists where R does start to increase under very low field MMF's. Since I am concentrating on modelling the machine for overexcited conditions, this work is outside of my scope.

By neglecting the position dependence of the saturation effects R_{sat} can be found from the large number of different R vs. MMF values in the curve families shown in Figure 3.25. These R curve families were found using only one averaged B data set for each field current level, but with an 80° mechanical segment width. This substantially reduced the number of data runs which needed to be collected as compared to using only 10° mechanical segment widths. Field excitation was able to give me significantly higher MMF levels than armature excitation given my equipment, voltage level, and heating constraints. Therefore I was able to characterize R_{sat} more extensively than I would be able to with armature excitation alone.

Using a spreadsheet program I made plots of normalized R_{sat} versus MMF for each 2.5° mechanical step over a 39° mechanical range covering half of one peak of the R

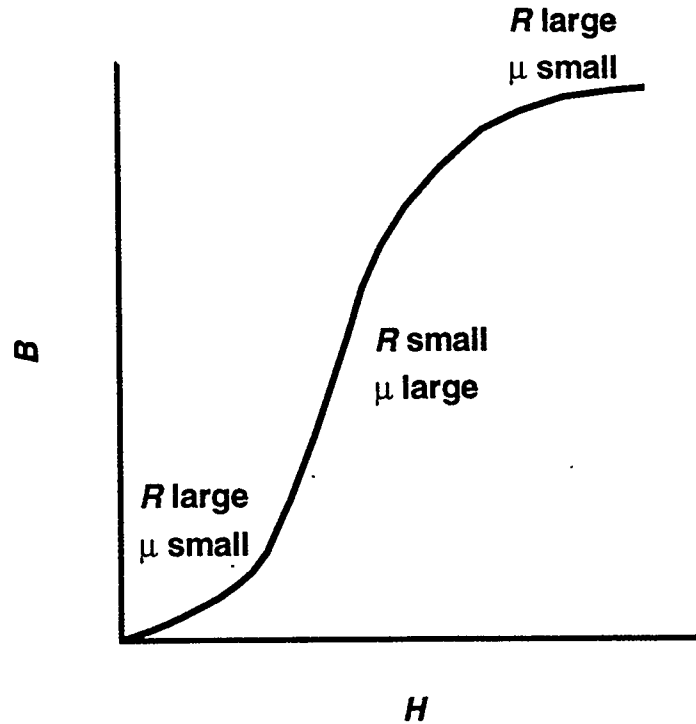


Figure 3.24: Typical B-H Curve Shape for Iron

wave. These are shown in Figures 3.27a, b, and c. The remaining 7 sections of the R wave are symmetric. Normalized R_{sat} was determined by rearranging equation 2.3 to get R_{sat} and then dividing this by R_{base} as shown by

$$R_{\text{sat}}(\theta, \mathcal{F}) = \frac{R(\theta, \mathcal{F}) - R_{\text{base}}(\theta)}{R_{\text{base}}(\theta)} \quad (3.5),$$

where R_{base} is assumed to be unchanging with MMF, and was based on 1.0 p.u. a and -b armature MMF excitation (linear conditions). R_{sat} is assumed to be normalized R_{sat} from this point on, unless mentioned otherwise.

R_{sat} is characterized as a function of the absolute value of MMF since the R versus MMF data, from which R_{sat} is determined, has both positive and negative values of MMF. When R_{sat} is approximated with a polynomial, the absolute value of MMF is used as the independent variable. However, for simplicity I will refer to R_{sat} as a function of MMF.

R_{sat} is negative under very low MMF conditions since the B-H curve is non-linear under these conditions. If the B-H curve were truly linear under low MMF conditions, then R_{sat}

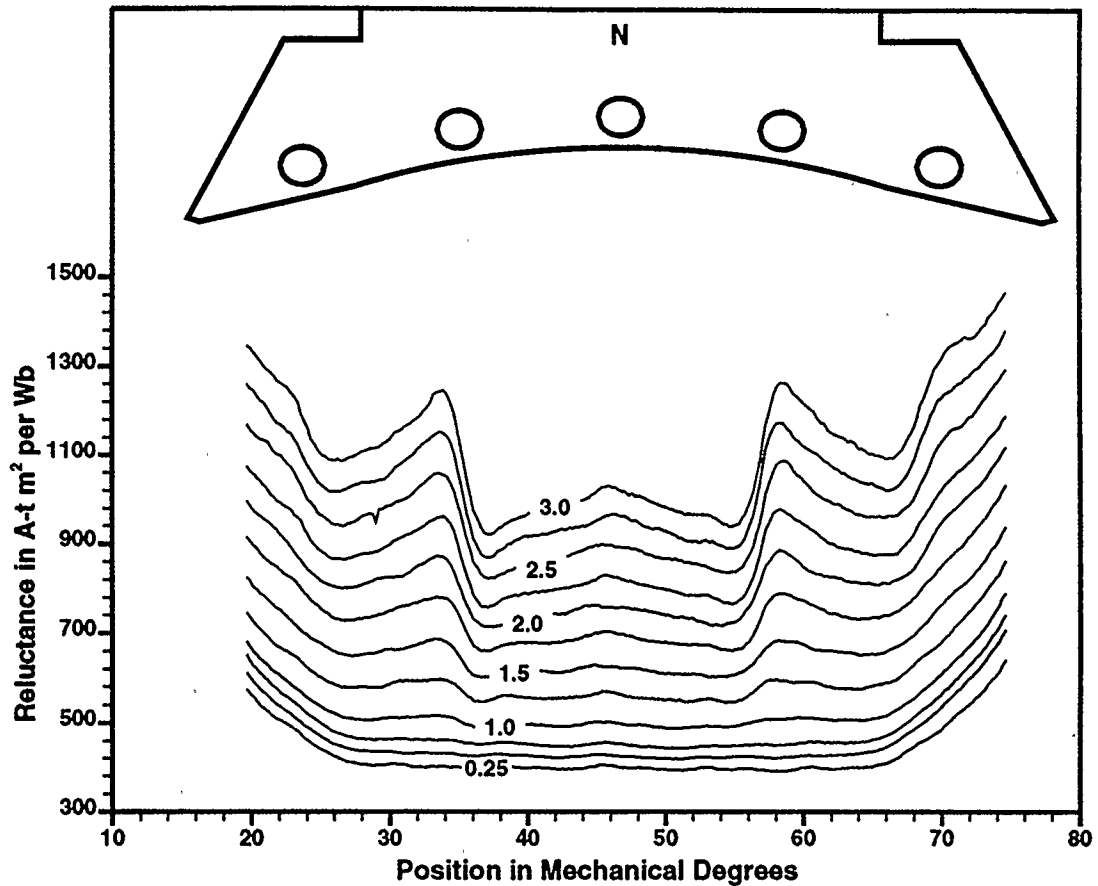


Figure 3.25: Comparison of R Waves for Field Current from 0.25 to 3.0 p.u.

would be constant and equal to 0 throughout the linear region. R_{sat} is 0 when $R = R_{\text{base}}$ since we have defined it this way (when R equals R_{base} , equation 3.5 is zero). R_{sat} increases as MMF increases, and its derivative also increases as MMF increases. This behaviour can be approximated with a second order polynomial.

The plots in Figure 3.27 show the variation of normalized R_{sat} with position. It is possible to maintain the position dependence of R_{sat} by using an approximating polynomial for each curve in Figure 3.27. However, in order to avoid discontinuities at the boundaries between the angular regions where each polynomial is valid, some sort of smoothing

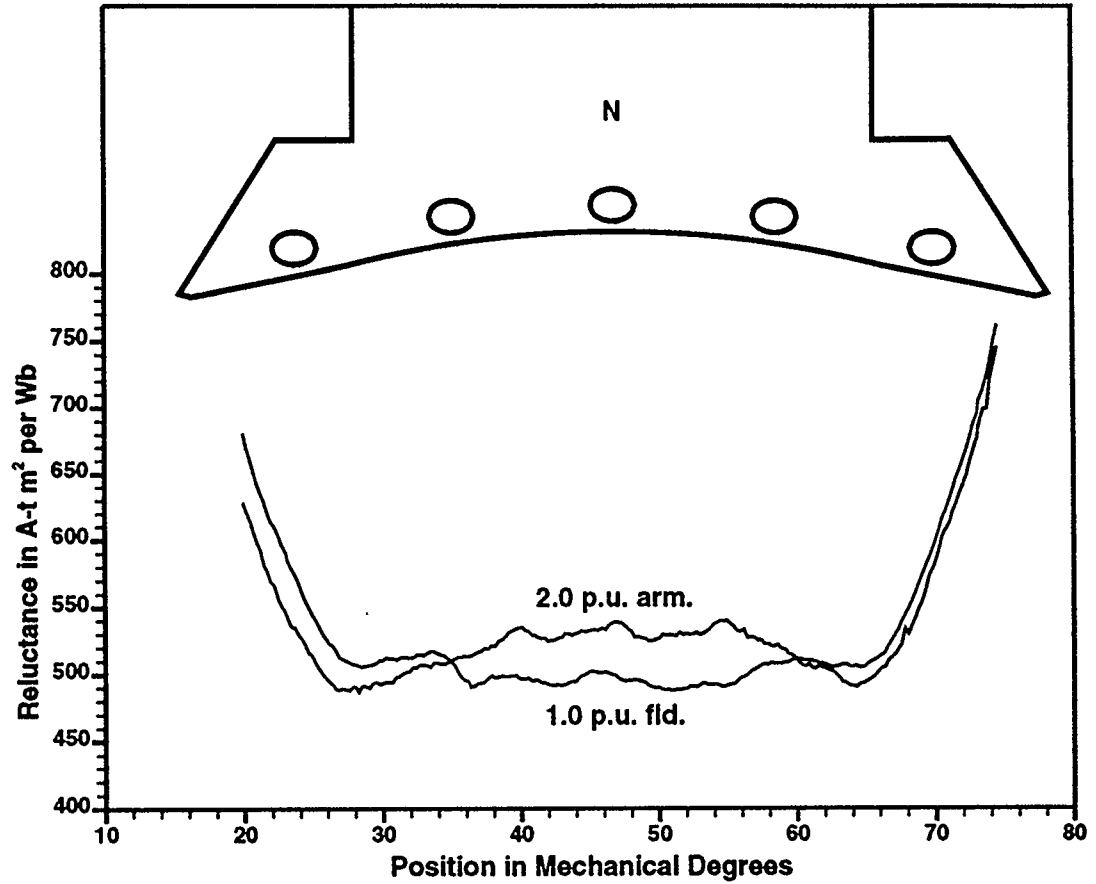


Figure 3.26: Comparison of R Waves for Field Current = 1.0 p.u. and Armature Current = 2.0 p.u.

functions would need to be introduced.

An alternative could be to take the Fourier series of the R waves or of the R_{sat} waveform at each MMF level. Each harmonic magnitude and phase could be plotted as a function of the average half-wave MMF and an approximating function could be used for each magnitude and phase function.

Characterizing R_{sat} as a function of both position and MMF is difficult and outside my research scope. Instead, the position variation of R_{sat} can be ignored and all of the points

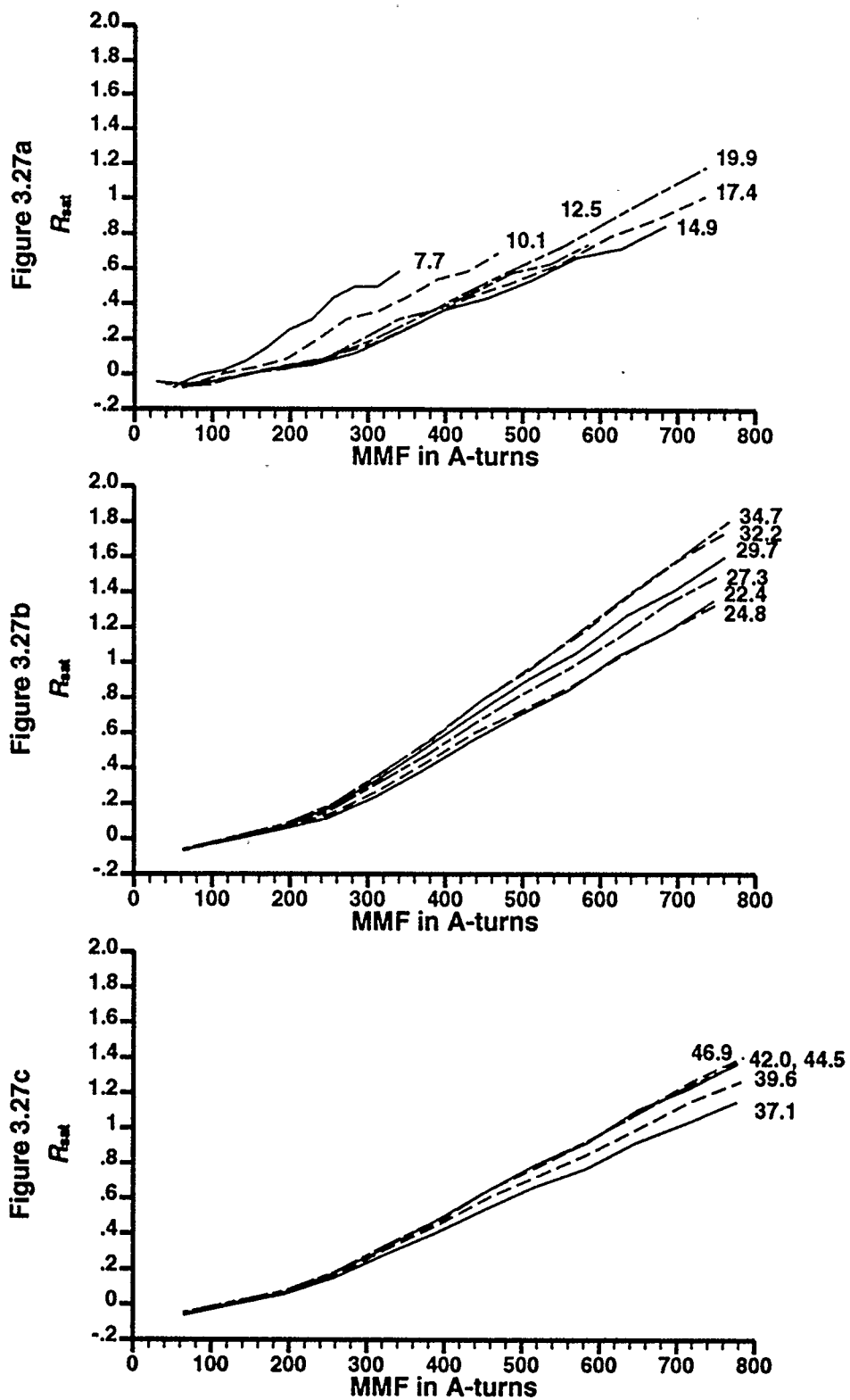


Figure 3.27: Plots of Normalized R_{sst} vs. MMF for Varying Angular Positions in Mechanical Degrees

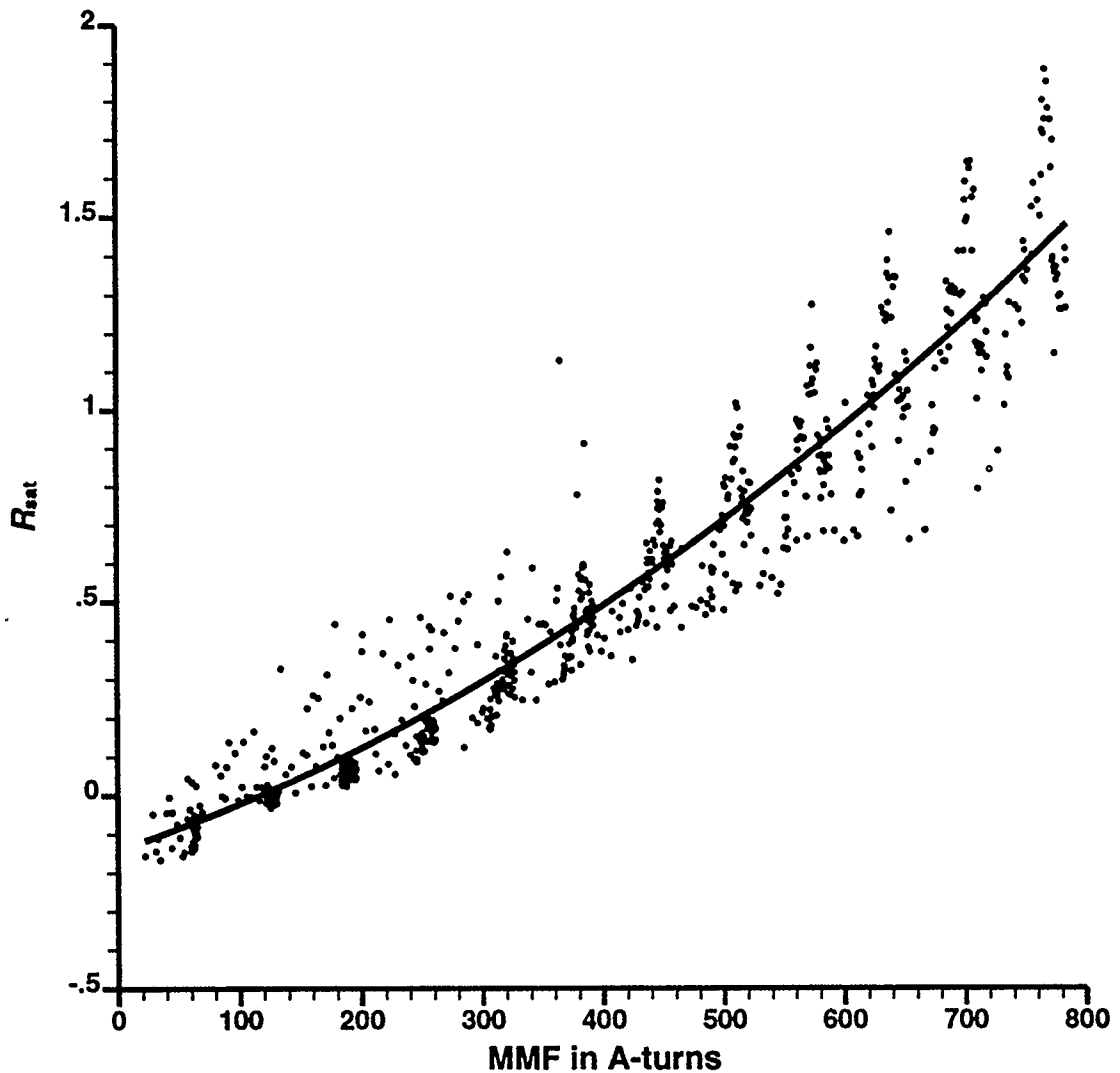


Figure 3.28: Scatter Plot of Normalized R_{sat} as a Function of MMF Only, With Least Squares Approximating Quadratic Equation

in Figure 3.27 can be shown as one scatter plot, as in Figure 3.28. A simple minimum least squares error approximation (Burden, Faires, and Reynolds [29, pp. 323-325]) can be used to fit a quadratic equation to the data. This best fit quadratic is also plotted in Figure 3.28. Even though the direct position dependence of R_{sat} is neglected, the MMF waves themselves are still position dependent, so R_{sat} in the air gap will vary with position since the MMF wave varies with position.

A Fortran program was written which calculated the normalized R_{sat} values, the

corresponding MMF, and the least square error quadratic equation coefficients for all the data at uniform positions throughout the R waves of all different field current levels. The resulting best fit second order polynomial for normalized R_{sat} , which is plotted in Figure 3.28, is

$$R_{\text{sat}}(\mathcal{F}(\theta)) \approx -0.14098 + 0.001056 \mathcal{F}(\theta) + 1.28978e^{-6} (\mathcal{F}(\theta))^2 \quad (3.6),$$

where $\mathcal{F}(\theta)$ is the position dependent MMF. Assuming linearity and superposition holds for the MMF waves, $\mathcal{F}(\theta)$ will be the sum of the armature and field MMF waves in the air gap.

The total reluctance, used in equations 2.2 and 2.3, may be found by rearranging equation 3.5

$$R(\theta, \mathcal{F}) \approx (1 + R_{\text{sat}}(\mathcal{F}(\theta))) R_{\text{base}}(\theta) \quad (3.7).$$

Equation 3.6 may be substituted into equation 3.7. When this is done, R will increase similarly to that shown in Figure 3.25 as the field MMF increases. However, the prominent fluctuations in the experimentally determined R due to the damper bar slots will not be present. Rather than doing this extra work here, these effects will be noticeable when comparing the experimental versus computed B distributions in Chapter 4.

CHAPTER 4

THE AIR GAP FLUX DENSITY MODEL

4.0 CHAPTER OBJECTIVES

- i) Describe the B distribution modelling program.
- ii) Compare experimental and modelled B distributions for field excitation only, armature excitation only, and compound excitation with different rotor positions.
- iii) Describe potential improvements and modifications to the model.

4.1 DESCRIPTION OF THE B DISTRIBUTION PROGRAM

4.1.1 The B Distribution Model

Using equation 2.4 and equation 3.7, the equation for the B distribution in the air gap can be expressed as:

$$B(\theta, \mathcal{F}) = \frac{\mathcal{F}(\theta)}{[1 + R_{\text{sat}}(\mathcal{F}(\theta))] R_{\text{base}}(\theta)} \quad (4.1),$$

where θ is the angular position in the air gap. $\mathcal{F}(\theta)$ is the MMF in the air gap at the angular position θ . If superposition holds, then $\mathcal{F}(\theta)$ will be the sum of the rotor MMF and the field pole MMF at that position. Both of these MMF's can be expressed as Fourier series, as was mentioned in Chapter 3. $R_{\text{base}}(\theta)$ was also determined in Chapter 3, and can be expressed as a Fourier series. $R_{\text{sat}}(\mathcal{F}(\theta))$ was characterized as a quadratic function of $\mathcal{F}(\theta)$, see equation 3.6. Ultimately, since \mathcal{F} is a function of θ , $R_{\text{sat}}(\mathcal{F})$ will also vary with θ . However, R_{sat} also has its own direct dependence upon θ as seen by the effects of the damper bar slots on R in Figure 3.25. This direct dependence is neglected in determining equation 3.6. When equation 3.6 is inserted into equation 4.1 for R_{sat} we get

$$B(\theta, \mathcal{F}) = \frac{\mathcal{F}(\theta)}{[0.85902 + 0.001056(\mathcal{F}(\theta)) + 1.28978e^{-6}(\mathcal{F}(\theta))^2] R_{\text{base}}(\theta)} \quad (4.2).$$

Equation 4.2 is the basis for the B distribution model. Per Chapter 3, $B(\theta, \mathcal{F})$ is the average radial flux density distribution in the air gap.

4.1.2 Static Versus Steady State Conditions

A program was written which computes the flux density using equation 4.2 for static conditions. Static conditions are computed because my measurement equipment can only measure average flux density distributions for static conditions and I want to compare the measured and computed results. All of the space harmonics of MMF and B are present under static conditions, but since all of the currents are DC and there is no rotation, these space harmonics are time invariant.

To extend this B distribution model to the steady state case see the General Torque and Voltage Computation Algorithm in Appendix B. There rotation is introduced, θ becomes ϕ where $\phi = \theta + \omega t$, and provision is made for all the effects of space and time harmonics. Some preliminary comments on extending the model to the transient case are also made there.

In Chapters 5 and 6 I will use this B distribution model to compute steady state torque and voltage under the assumption that the static B distribution is the same as the steady state B distribution. The effects of time and space harmonics are neglected.

4.1.3 Program Structure

Inputs to the program are the DC field current level, the DC armature current level, and the rotor angular position. Fourier series magnitudes and phases, as well as R_{sat} 's coefficients, are preassigned in the program, but could be read in as inputs. These magnitudes and phases are used to represent the field pole MMF, the armature MMF for a and -b windings excited, and R_{base} . Equation 3.4 shows how the armature MMF is computed at each angular point, θ . θ data is computed and stored in an array. The third term in the sine function of equation 3.4 is required since the rotor position can be varied in the experimental machine. The equations for the field MMF and R_{base} are similar, except that the rotor position variation term is not necessary. The MMF waves for the field and armature windings are proportional to the DC field current and the DC armature current respectively. The field and armature MMF's are added together at each angular position to give the $\mathcal{F}(\theta)$ in equation 4.2 (superposition is assumed). Once $\mathcal{F}(\theta)$ and $R_{base}(\theta)$ are calculated, $B(\theta, \mathcal{F})$ is calculated from equation 4.2. θ and B values are written to an output file. Later revisions of the program superimposed single phase a and single phase -b MMF's.

4.2 *B* DISTRIBUTION PROGRAM RESULTS

4.2.1 Field Excitation Only

Figure 4.1 shows two cases of experimental versus computed average *B* distribution results.

Case A compares measured and computed *B*'s for field current of 0.5 p.u., Case B is for 3.0 p.u.. For Case A there is very little error at any point. For Case B the distortion in the measured *B* distribution under the poles is not present in the computed case since the position dependence of R_{sat} is not considered. However, the average flux per pole appears to be close for the measured and computed data. Our R_{sat} model appears to be successfully accounting for the effects of saturation in a "bulk" manner. Precise flux per pole error calculations will be done on the compound excitation cases later in this chapter. There is a small deviation on the flanks of the flux distribution. This will contribute to phase error in computed voltage and magnitude error in computed torque.

4.2.2 Armature Excitation Only

Figure 4.2 shows two cases of experimental versus computed *B* distributions.

Both cases are for the a and -b armature MMF axis lined up on the direct axis. Case A is for 1 p.u. armature current, and Case B is for 2 p.u.. In both cases the measured and computed *B* distributions are in good agreement. In the worst case, the computed *B* distributions have a slightly smaller peak (5.2% low for Case A and 4.1% low for Case B) than the measured *B* distributions. This is likely due to the armature MMF based R being different from the field MMF based R as shown in Figure 3.26. Consequently, our R_{sat} characterization is the source of the error.

Figure 4.3 shows a single case where the armature current is 1 p.u. and the armature a and -b MMF axis is centred on the quadrature axis. The shape seems to be well modelled, and the worst error is where the calculated peak is 9% lower than the measured.

4.2.3 Compound Excitation

Figures 4.4a to e are five cases where both the field and armature a and -b windings are excited. The field winding is carrying 1 p.u. and the armature is carrying 2 p.u. current. In Figure 4.4a, both MMF's are in phase on the direct axis. This would be the approximate field condition for an alternator supplying 90 electrical degree leading current, or a motor drawing 90 electrical degree lagging current. However, the *B* distributions in

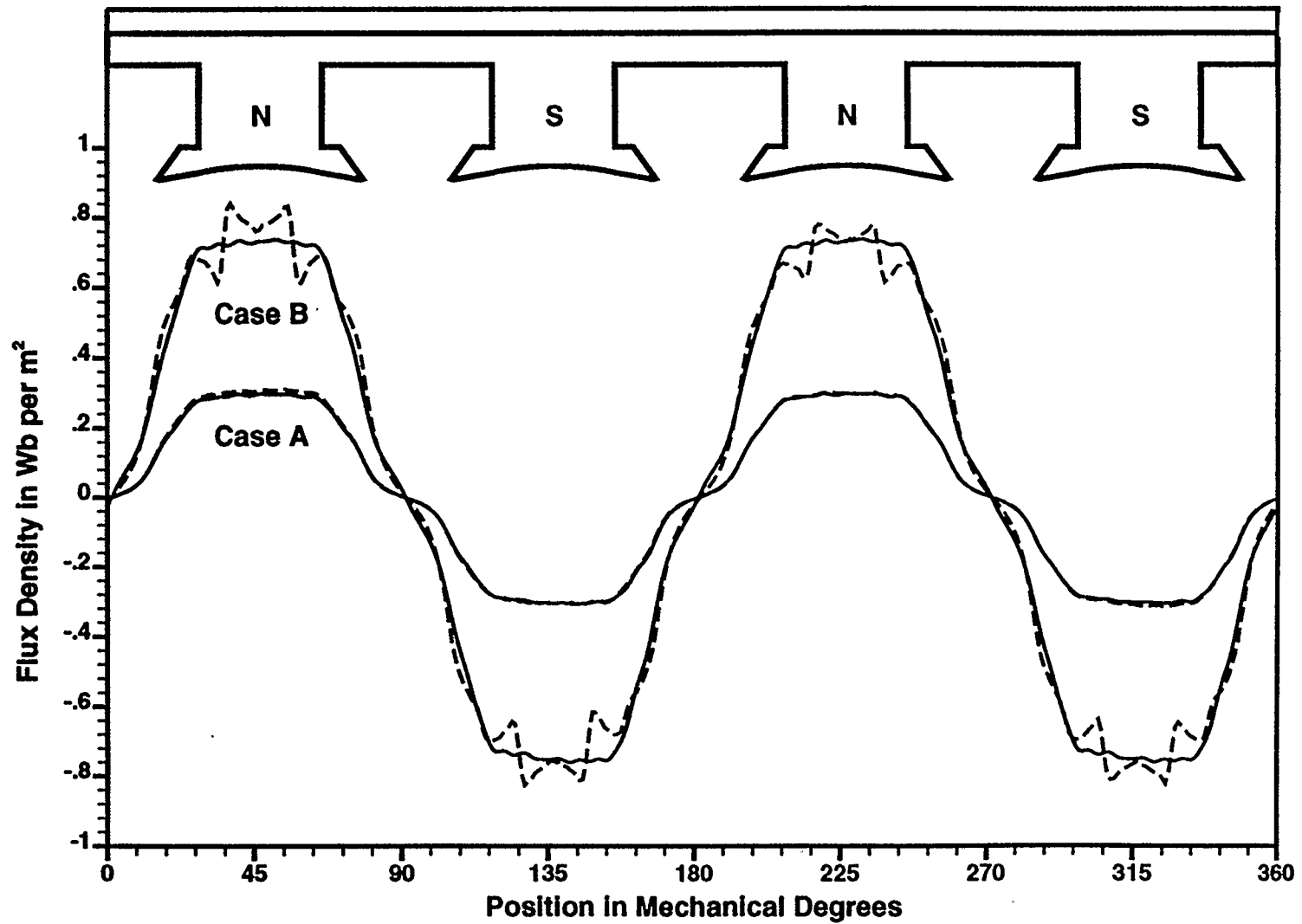


Figure 4.1: Measured (dashed) Versus Computed (solid) B Distributions, Field current = 0.5 and 3.0 p.u.

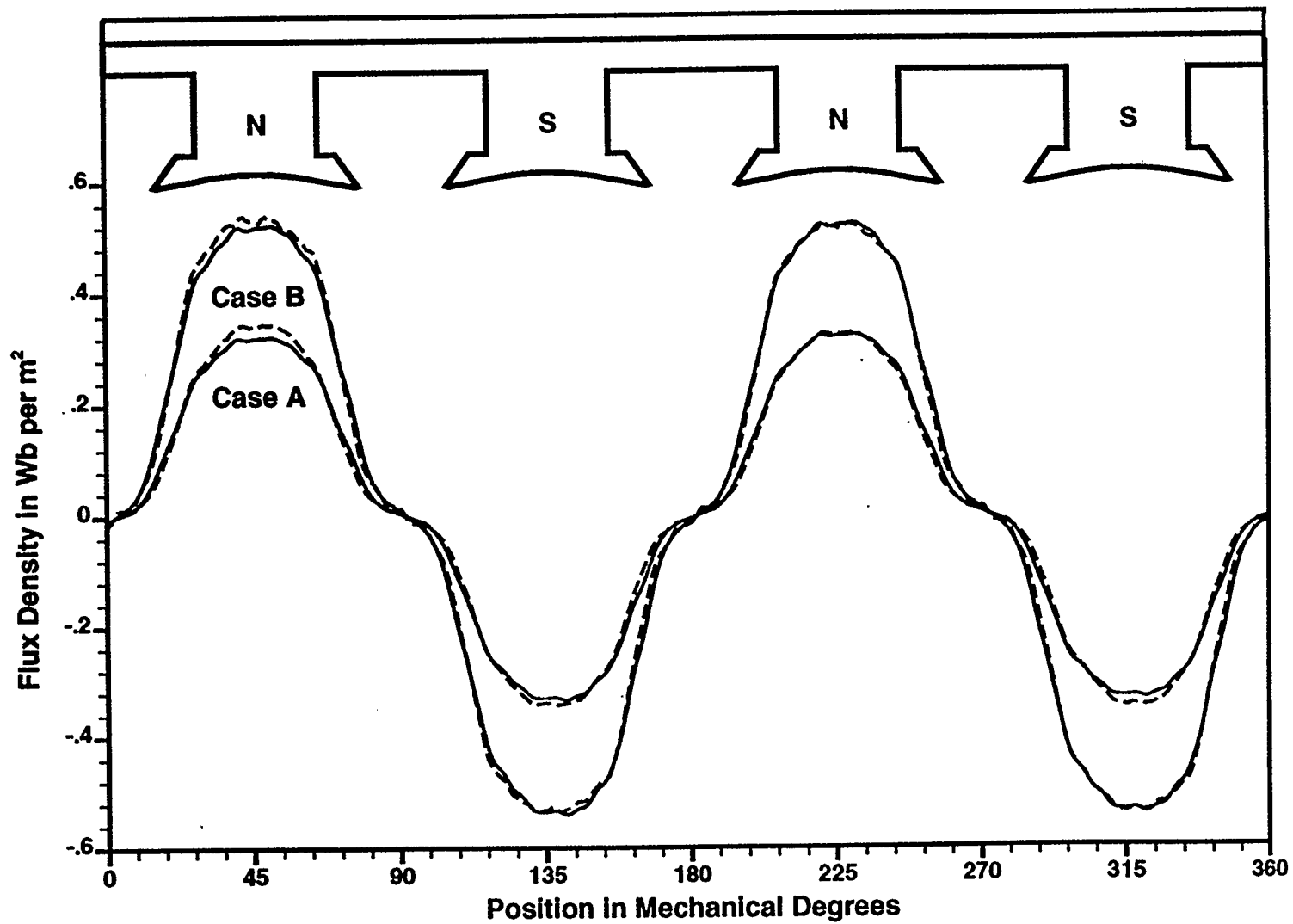


Figure 4.2: Measured (dashed) Versus Computed (solid) B Distributions, Armature Current = 1 and 2 p.u., A & -B MMF on D Axis

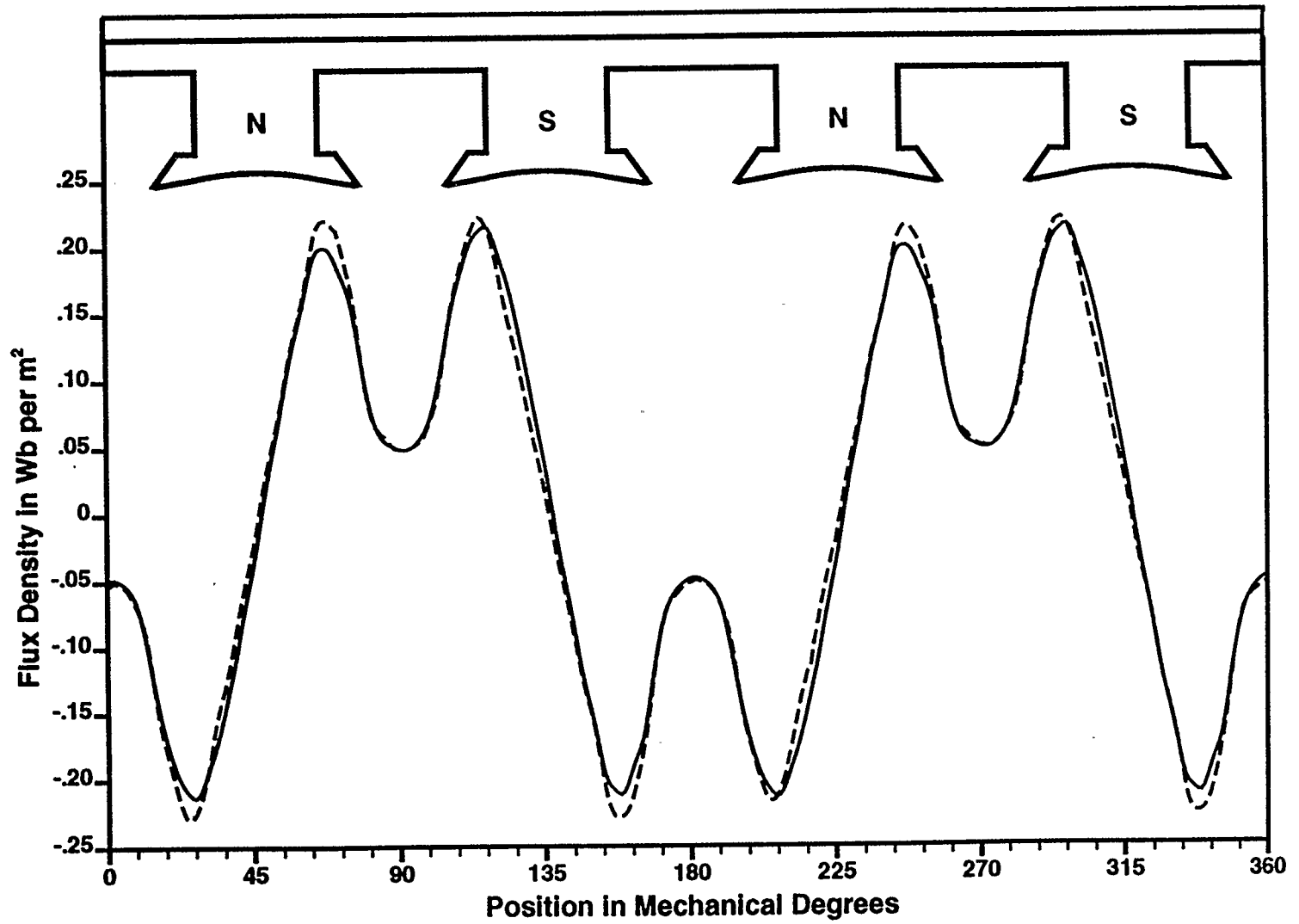


Figure 4.3: Measured (dashed) Versus Computed (solid) B Distributions, Armature Current = 1 p.u., A & -B MMF on Q Axis

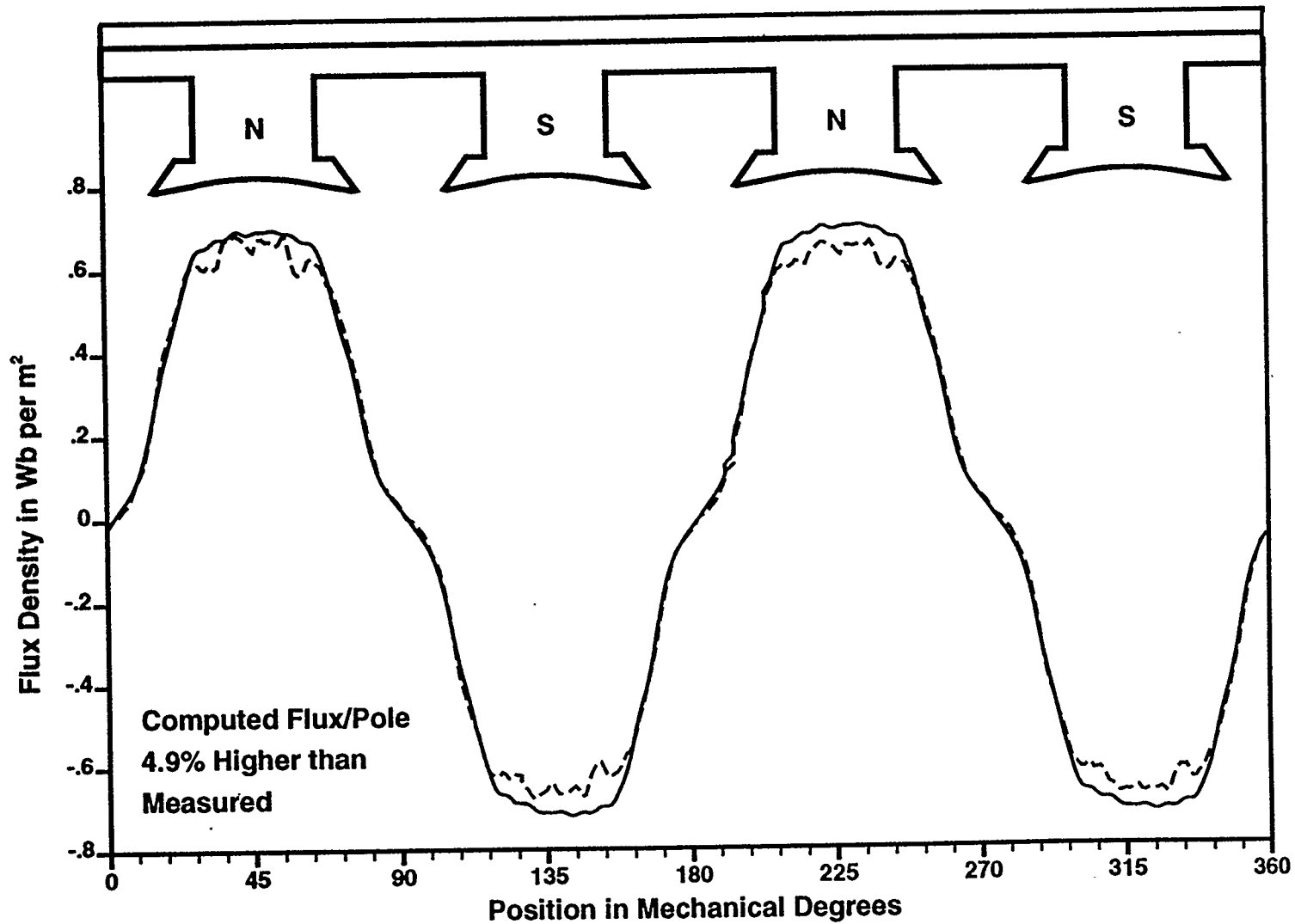


Figure 4.4a: Measured (dashed) vs. Computed (solid) B Distributions, Field = 1 p.u., Arm. = 2 p.u., A & -B MMF Axis on D Axis ($\psi = 90^\circ$ elec.).

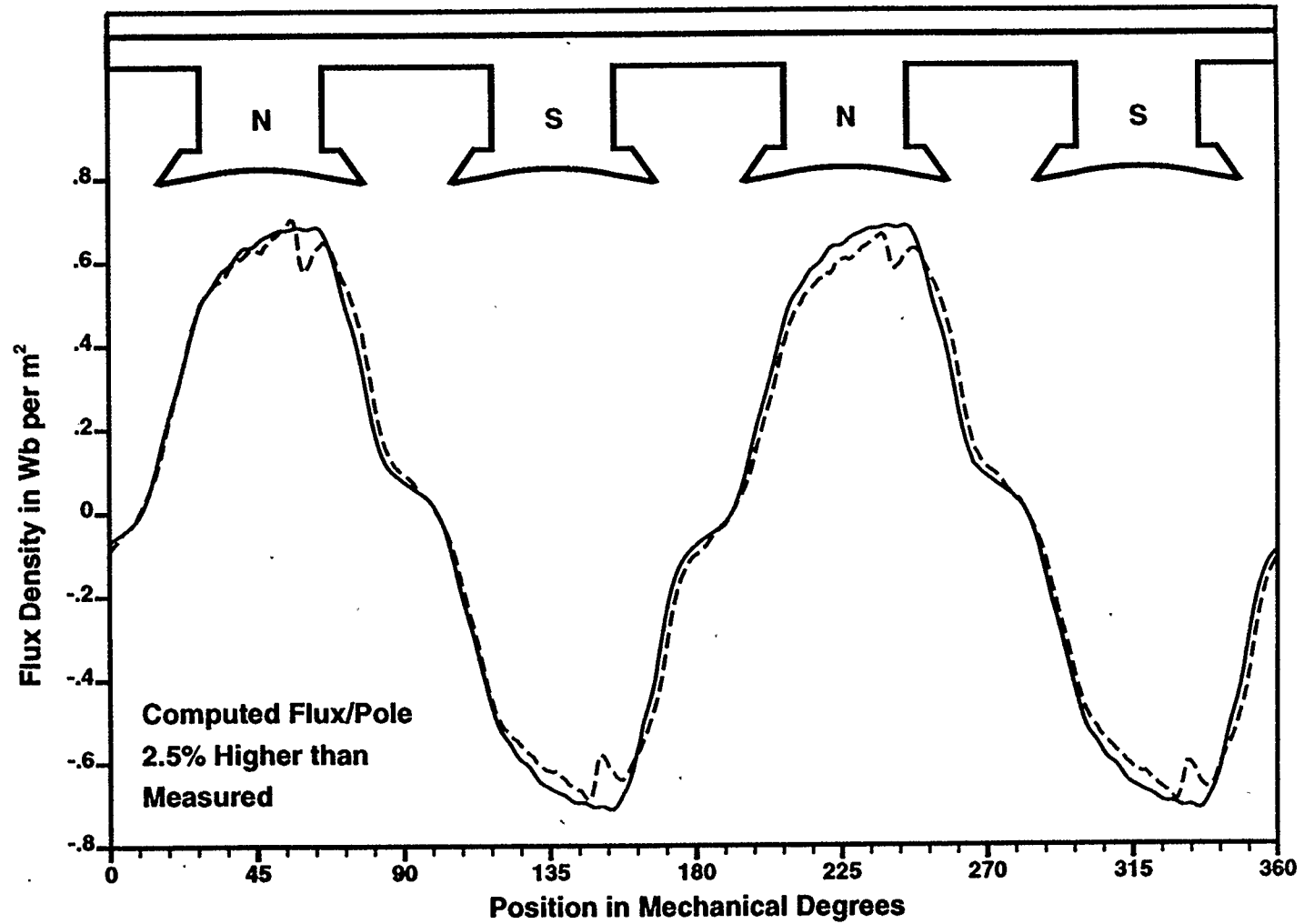


Figure 4.4b: Measured (dashed) vs. Computed (solid) B Distributions, Field = 1 p.u., Arm. = 2 p.u., A & -B MMF 22.5° mech. from D Axis ($\psi = 45^\circ$ elec.).

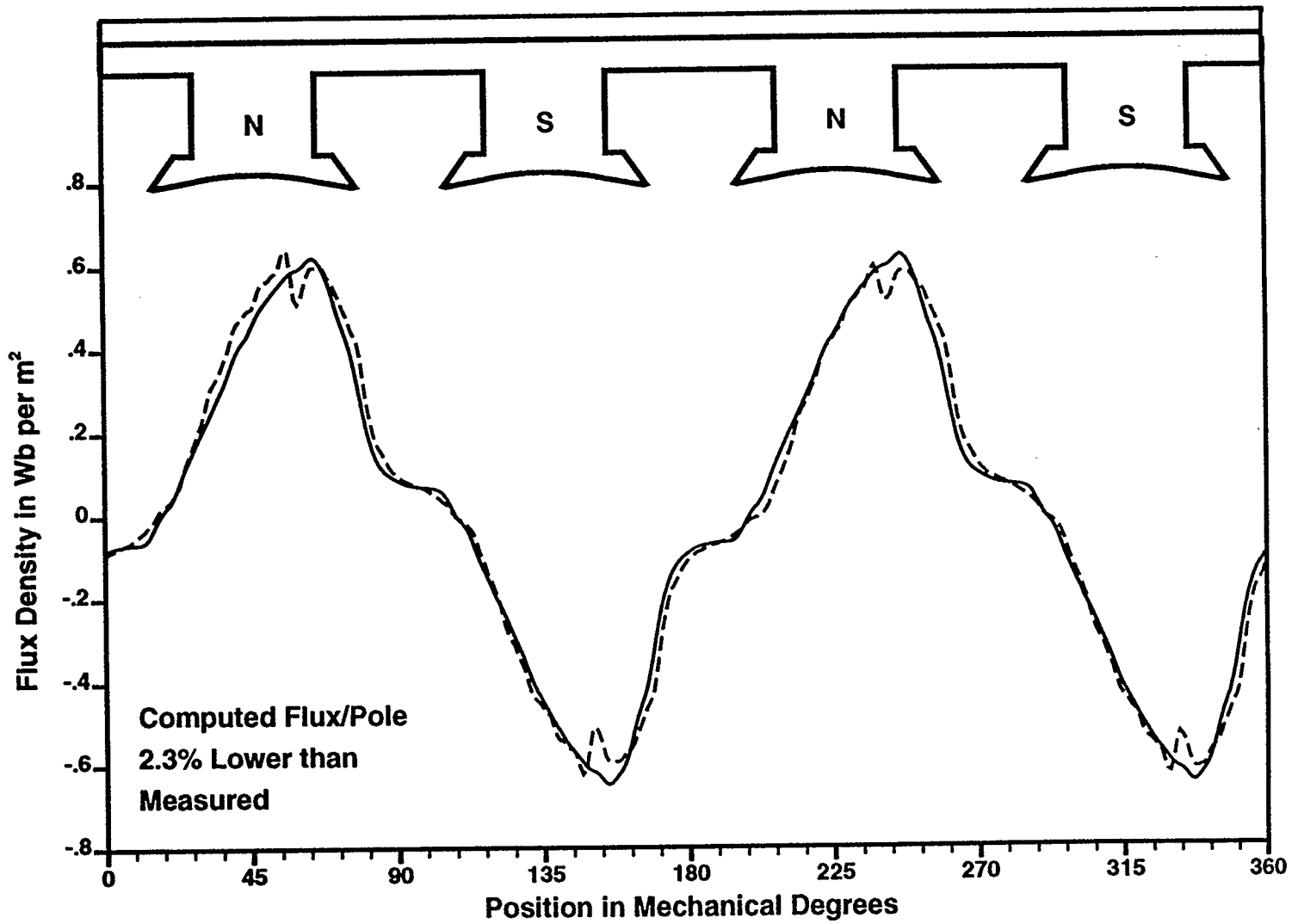


Figure 4.4c: Measured (dashed) vs. Computed (solid) B Distributions, Field = 1 p.u., Arm. = 2 p.u., A & -B MMF Axis on Q Axis ($\psi = 0^\circ$ elec.).

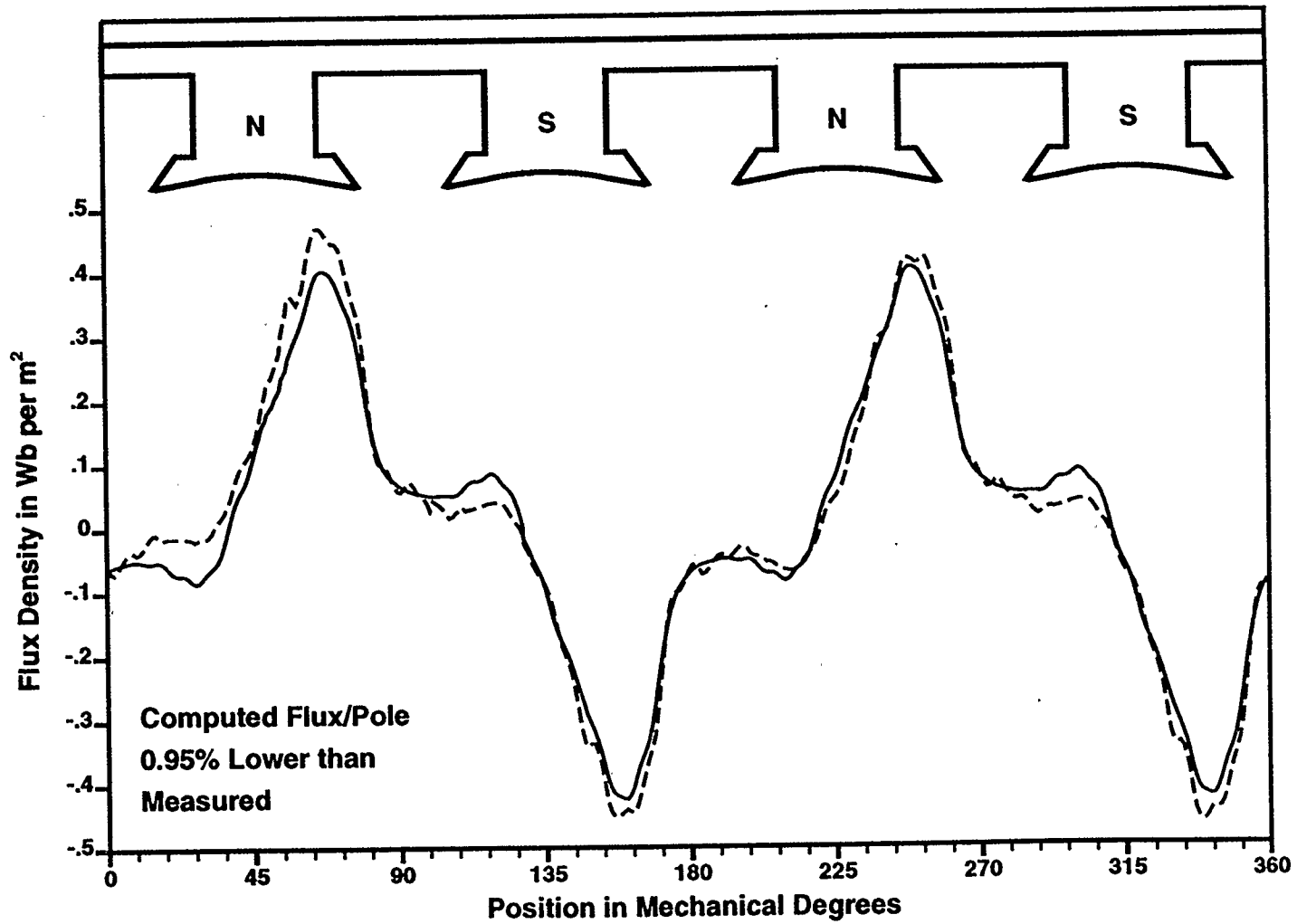


Figure 4.4d: Measured (dashed) vs. Computed (solid) B Distributions, Field = 1 p.u., Arm. = 2 p.u., A & -B MMF 67.5° mech. from D Axis ($\psi = -45^\circ$ elec.).

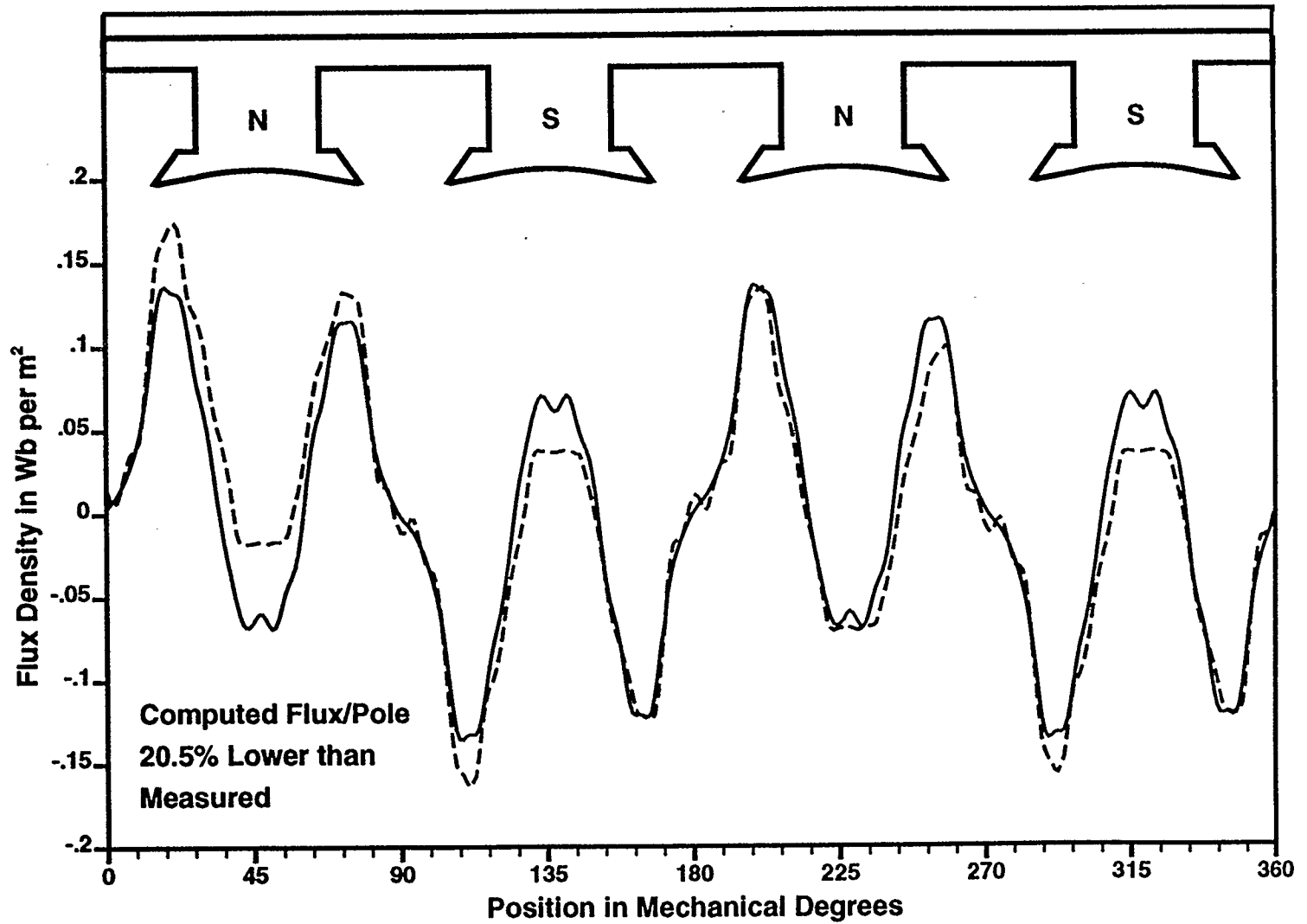


Figure 4.4e: Measured (dashed) vs. Computed (solid) B Distributions, Field = 1 p.u., Arm. = 2 p.u., A & -B MMF Axis on -D Axis ($\psi = -90^\circ$ elec.).

Figures 4.4a to e are not set up to correspond to actual operating conditions. Rather, the rotor position is varied under constant field and armature excitation in order to find weaknesses in the B distribution model. See Appendix C for an explanation of the internal power factor angle ψ .

The error in flux per pole is a good indicator of what error will exist in both the torque and voltage calculated from this B model. In Moullin [9, pp. 7-15], formulas are derived (using the cutting of flux rules mentioned in Appendix B) for torque and voltage which express both of them as being directly proportional to the total flux per pole. The results found in Figure 4.4 will manifest themselves in torque errors in Chapter 5.

Since the general shapes of the modelled and measured waves are consistent, the superposition assumption does not appear to cause any significant error. It is difficult to tell how much error is introduced by this assumption, but it is likely small since errors due to the characterization of R_{sat} appear to account for the error in the predicted fields.

In Figures 4.4a and b, the assumption of R_{sat} being independent of position, and the inconsistency between R_{sat} for field MMF and armature MMF appear to lead to too high of a computed flux per pole.

In Figure 4.4c, we start to underestimate the flux per pole. Error is not only introduced due to the damper bar slots, but also the flanks of the B distribution are in error. Fringing and hysteresis effects in the B distribution which we encountered in section 3.2.3 cannot be accounted for by the magnetic circuit modelling technique proposed in this research. It is likely that this same fringing effect is causing the error in the flanks of the B distribution. A further source of error may be our characterization of R_{sat} . In Figure 3.28, at all MMF levels the actual value of R_{sat} deviates from the approximating quadratic. The amount of this deviation depends upon position however.

In Figures 4.4d and e the armature MMF opposes the field MMF (both are about the same magnitude). The peak flux density level in Figures 4.4a, b, and c are about 0.6 Wb/m² or higher. In Figure 4.4d it is only about 0.4 Wb/m², and in Figure 4.4e it is about 0.15 Wb/m². The computer model underestimates the flux per pole by as much as 20% in Figure 4.4e. The actual magnitude of the error is still the same for these cases as it is for Figure 4.4a. In Figure 4.4a, 5% of 0.6 Wb/m² is 0.03 Wb/m². In Figure 4.4e, 20% of 0.15 Wb/m² is also 0.03 Wb/m². Even though the percentage error in the computed flux per pole is larger, it seems worse in Figure 4.4e because the flux per pole is much

smaller. The negative consequences of a large percentage error in a small quantity are minimized because the quantity is small.

The deviation of the actual position dependent R_{sat} from the approximating quadratic probably contributes to the error. Another possible source of error is the nonlinearity in R at very low MMF's, as discussed in section 3.2.6, which causes the armature MMF based reluctance wave of Figure 3.22 to increase as MMF decreases.

In Figure 4.4e, the field and armature MMF's directly oppose each other, and since they have comparable magnitudes their sum is quite small. If the MMF values are small enough that the R values start to increase, then the B values will start to deviate from what R_{sat} 's approximating quadratic would dictate. R_{sat} was characterized using only field MMF data and no increasing R with decreasing MMF behaviour was noted as in the armature MMF case. This does not mean that this behaviour does not exist for the field MMF wave, but we did not take the field MMF to a low enough level to check.

When we let $\mathcal{F}(\theta)$ become small, equation 4.2 can be reduced to

$$B(\theta, \mathcal{F}) \approx \frac{\mathcal{F}(\theta)}{0.85902 R_{\text{base}}(\theta)} \quad (4.3)$$

since the coefficient in front of $\mathcal{F}(\theta)$ is small, and $(\mathcal{F}(\theta))^2$ is very small. Equation 4.2 becomes linear for low MMF conditions. If the true R deviates from linearity for the reasons described in the preceding paragraph, and our computer model is predicting a linear relationship between B and \mathcal{F} then we will see error between the measured and computed B distributions. In Figure 4.4e, we see that where the net MMF is relatively high (relative to Figure 4.4e's MMF levels) the experimental B distribution is greater than the computed. Where it is lower, the computed values exceed the measured. There is a cross-over point somewhere in between. For total MMF's of 50 A-turns or lower we can expect to see greater errors. This is an arbitrary figure since I have not investigated this low MMF behaviour in detail since that is outside of my scope.

The MMF orientation for Figure 4.4e (the armature MMF directly opposing the field MMF) is the same as for a generator under short circuit conditions (lagging p.f.) or for a motor when it is operating as a synchronous condenser (leading p.f.). But for both situations the control system will boost the field current to a level substantially higher than the 1 p.u. field current used in Figure 4.4e. For a generator under short circuit this will

maintain a high induced winding voltage and a high short circuit current which guarantees breaker activation. For a motor the high induced winding voltage is required to limit the armature current because the applied terminal voltage is constant. Therefore, the high error in flux per pole for Figure 4.4e is normally not encountered in practical machines under short circuit or steady state conditions.

4.3 POTENTIAL IMPROVEMENTS AND MODIFICATIONS

As mentioned earlier, the B model can be extended to the steady state case including space and time harmonics, and eventually to the transient case, per the General Torque and Voltage Algorithm in Appendix B.

Damper windings can be added by determining their MMF wave and adding it to the armature and field MMF waves. This would be essential for accurate transient analysis.

Fourier coefficients and phases for armature MMF, field MMF, and R_{base} can be read in from input files allowing modelling of different machines. The procedure for determining the theoretical MMF waves for the armature or field can be performed by the program based on constructional features of the machine (slot pitch, slot skew, number of conductors per coil side, pole pitch to pole arc ratio, etc.).

Air gap torque and voltage computation will be added in Chapters 5 and 6.

Finite element generated MMF, R_{base} , and R_{sat} data can be used instead of obtaining them from measurements. This would be required in order to simulate designs prior to production, or operational machines. As mentioned in Chapter 2, rather than having to use time consuming finite element analysis in transient analysis programs my model can potentially be used to predict the B distributions in these programs.

CHAPTER 5

THE TORQUE MODEL

5.0 CHAPTER OBJECTIVES

- i) Describe various torque computation methods.
- ii) Justify the selection of the flux linkage method from among these methods.
- iii) Describe the torque computation algorithm.
- iv) Compare measured and computed torques to evaluate the success of the flux density and torque models.

5.1 TORQUE COMPUTATION METHODS

A number of different torque computation methods are found in the literature. This section compares several different methods and shows that the flux linkage torque method is most suited for use with my flux density model.

5.1.1 Coenergy Derivations

Fitzgerald [7, pp. 155-165] computes torque using the coenergy method for linear conditions in a cylindrical rotor machine. The coenergy stored in the magnetic field may be determined using either position dependent inductances or magnetic circuit considerations.

For a material of constant permeability, μ , the coenergy is expressed as

$$W'_{fld} = \int_V \frac{1}{2} \mu H^2 dV \quad (5.1),$$

where W'_{fld} is the magnetic coenergy, and H is the magnetic field strength at each point in the magnetic field volume V .

The coenergy for a linear cylindrical rotor machine can be expressed as a function of the armature (i_a) and field (i_f) currents, and the mechanical angular position in the air gap (θ_m). The torque can be derived from this coenergy function through the relation

$$T = \frac{\partial W'_{fld}(\theta_m, i_s, i_f)}{\partial \theta_m} \quad (5.2).$$

A number of equations for torque can be derived, each being expressed in terms of different combinations of the stator MMF wave magnitude, the rotor MMF wave

magnitude, the vector sum of their magnitudes, or the total flux per pole. An example is

$$T = \frac{\pi}{2} \left(\frac{P}{2} \right)^2 \Phi_{sr} \mathcal{F}_r \sin(\delta_r) \quad (5.3),$$

where P is the number of poles, Φ_{sr} is the total resultant flux per pole, \mathcal{F}_r is the magnitude of the rotor MMF wave, and δ_r is the electrical space angle between the rotor MMF wave axis and the axis of the vector sum of the rotor and stator MMF waves (sinusoidal MMF and flux shapes are assumed).

The essential result for all these equations, however, is that the torque is proportional to the stator and rotor field magnitudes and the sine of the electrical space angle between their magnetic axes.

Hoole [16, p.354] comments on the use of the coenergy approach as well. The coenergy can be computed for the entire solution region (from a finite element solution) for two points in time, where the change in angular position of the rotor over the time increment is small. Equation 5.2 can be approximated and the torque determined.

I cannot use the coenergy method with my flux density model. First, equation 5.3 is only valid for linear conditions in a cylindrical rotor machine. And second, I do not have a full field solution for which I can compute the coenergy. Even if I could assume that only the air gap needs to be modelled, I still have a complex air gap shape in my salient pole machine for which I only know the flux distribution at a radius just outside of the rotor.

5.1.2 Torque from Circuit Models

In section 2.2.3 reference is made to the steady state torque for a salient pole machine under linear conditions. The formulas given in many references (Kingsley [7, pp. 345-349], Doherty/Nickle [15], Langsdorf [27, p.502]) are derived from the D-Q axis model (from the Blondel Two-Reaction Method) discussed in Appendix C. These references express the mechanical power (which is proportional to torque) in the form given below:

$$P = \frac{VE \sin(\delta)}{X_{dT}} + \frac{V^2 (X_{dT} - X_{qT})}{2 X_{dT} X_{qT}} \sin(2\delta)$$

Here V may be the terminal voltage of the machine, or it may be some fixed bus voltage. E is the no load induced voltage in the machine windings. Winding resistance is neglected for simplicity. δ is the electrical phase angle between V and E . X_{qT} is the sum $X_{rd} + X_a + X_{bus}$, where X_{rd} is the direct axis magnetizing reactance and X_a is the winding

leakage reactance as defined in Appendix C. Both of these reactances are characteristics of the machine. X_{bus} is typically the bus reactance between the fixed voltage V and the machine terminals. It is zero if the fixed voltage is assumed to be at the machine terminals. X_{qT} is the sum $X_{rq} + X_a + X_{bus}$, where X_{rq} is the quadrature axis magnetizing reactance as defined in Appendix C. Since my focus is on modelling the machine's internal magnetic field and torque behaviour, X_{bus} can be ignored. X_a is necessary for determining terminal conditions, as mentioned in Appendix C, but for static simulations it can be neglected as well. With these simplifications, and the conventions established in the phasor diagram of Figure C.1, I can rewrite the last equation as follows:

$$P = \frac{E_a E_f \sin(\delta)}{X_{rd}} + \frac{E_a^2 (X_{rd} - X_{rq})}{2 X_{rd} X_{rq}} \sin(2\delta) \quad (5.4),$$

where E_a is the magnitude of the induced phase a winding emf under loaded conditions (created by and in phase with the fundamental of the resulting air gap flux distribution under load). E_f is the magnitude of the induced phase a winding emf under no load conditions (created by and in phase with the fundamental of the air gap flux distribution under unloaded conditions). δ is the electrical phase angle between E_a and E_f . It is also the displacement angle (in electrical degrees) of the axis of the fundamental of the loaded flux distribution from the axis of the fundamental of the unloaded flux distribution. δ is called the internal torque angle or the internal power angle.

If the machine did not have salient poles X_{rd} would equal X_{rq} and the second term of equation 5.4 would disappear. For a constant E_f (under linear conditions this is arranged by holding the field current constant) and a constant E_a , the power and torque would be proportional to $\sin(\delta)$. The peak torque would be at $\delta = 90^\circ$ electrical.

Once saliency is introduced the second term of equation 5.4 comes into effect (for a salient pole machine X_{rd} is greater than X_{rq}). For constant E_a the torque produced by the second term (known as the "reluctance torque") is proportional to $\sin(2\delta)$. The reason why this term is called the reluctance torque is because it represents the magnetic attraction of the rotor to the salient poles when the field is unexcited. Therefore, it is not dependent on the field current at all. The shape of the reluctance torque waveform for varying δ 's around the air gap is the same as if a permanent bar magnet were installed in place of the rotor. This magnet would attempt to align its poles with any of the salient poles (field

current being zero). The torque on the magnet would be zero (and statically stable) when the magnet's axis is aligned with the poles. The torque would increase in magnitude as δ increases until it reaches a maximum when δ is 45° electrical from the pole axis, then it would decrease to 0 when δ was 90° electrical. The torque sense for δ from 0° to 90° electrical was always to draw the magnet back toward the pole axis where δ was 0° electrical. When δ increases past 90° electrical the torque starts to increase again, but this time the torque sense is directed toward the next pole where δ is 180° electrical. In other words, the reluctance torque sense is always in the direction which draws the permanent magnet towards the nearest field pole, regardless of that field pole's magnetic polarity. The angular frequency is twice that of the cylindrical torque. Figure 5.1 shows the cylindrical torque term, the reluctance torque term, and the sum of the two (equation 5.4). This is for linear conditions.

The reluctance torque term is substantially smaller than the cylindrical torque term. The total torque (the sum of the cylindrical and reluctance torque terms) is noticeably skewed relative to the cylindrical torque. It also has a higher peak torque.

The effects of saturation, the space harmonics of flux (caused by distributed windings, teeth, and saliency), and time harmonics of current will cause the machine characteristics to deviate from those of Figure 5.1. Although it is not appropriate to pursue it at this point, the following computations could be done to determine how saturation affects the static torque (T) vs. δ characteristic:

- i) For a constant field current, I_f , of 0.5 p.u. (linear conditions) compute a T vs. δ curve (refer to Appendix C for an example of similar calculations using the models developed in this research). For a fixed terminal voltage (V_a), select the magnitude and phase of the armature current (I_a) for a particular power level. Using the preprocessing program compute the desired magnitude and phase of E_a . The instantaneous phase a current (i_a) can be found using equation 2.13 and I_a . Using the computer model the rotor angular position (*rotorg*) which gives the desired magnitude and phase of E_a can be found through trial and error. Using the same I_f and *rotorg*, and by setting i_a equal to zero, the computer model can be used to determine the magnitude and phase of E_f . The internal torque angle, δ , is the phase difference between E_a and E_f . The torque computed from the computer model when E_a was found is plotted against δ . Change the power level by

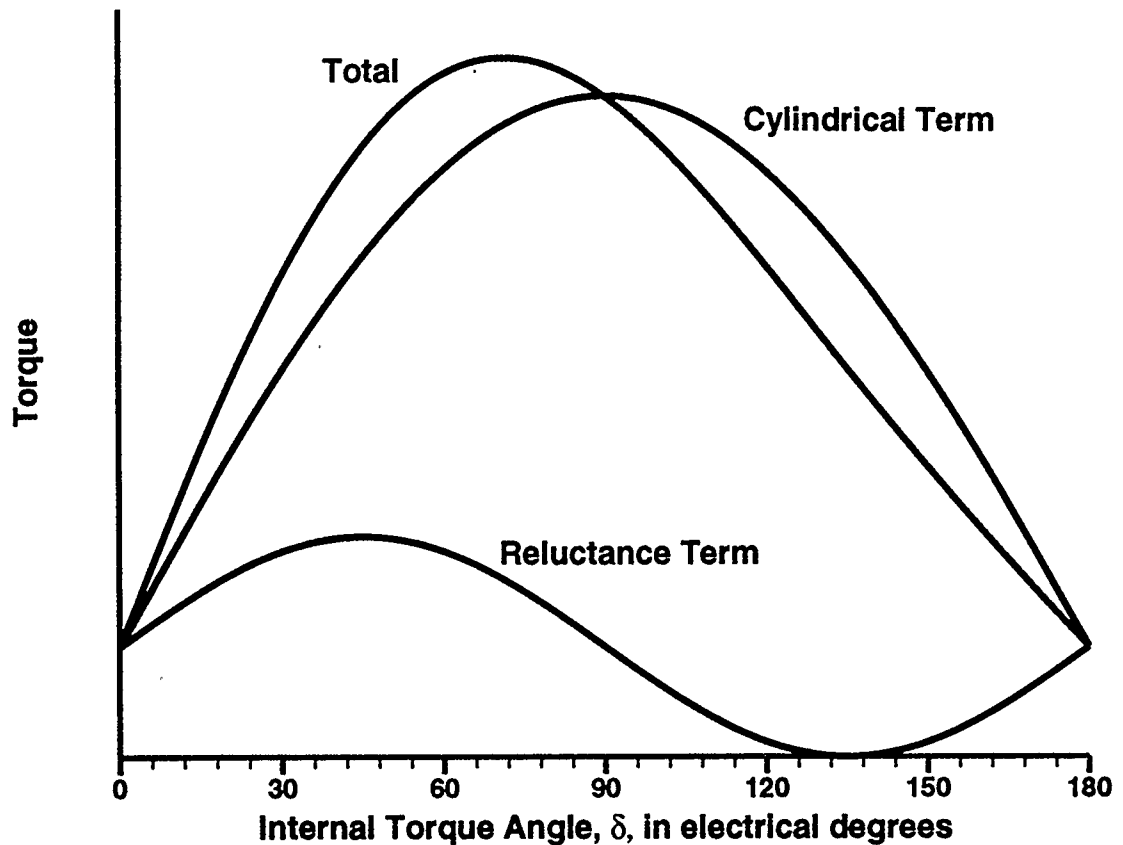


Figure 5.1: Comparison of Cylindrical, Reluctance, and Total Torque vs. Internal Torque Angle, δ . Linear Conditions.

changing I_a and compute the next point. The magnitude of E_a and I_l must be constant from point to point. For linear conditions E_f will be constant if I_l is constant. Continue until the entire T vs. δ curve is defined. If a power level is too high for a constant I_l and any δ , then the power level is above the T vs. δ curve for this I_l and a lower power level will have to be used. The values of X_{rd} and X_{rq} at every point on the T vs. δ curve can be found from the postprocessing program.

- ii) A theoretical T vs. δ curve can be found for the machine using equation 5.4. In

order to do this X_{rd} and X_{rq} will need to be determined for linear conditions. The best magnetization condition to do this is when the field current is low, the armature current is low, and the armature MMF axis is directed onto the quadrature axis. This will ensure that there is no saturation occurring in the iron. Using the linear values of X_{rd} and X_{rq} found in this way, and the constant magnitudes of E_a and E_f from step i, the theoretical T vs. δ curve for the same conditions as step i can be found and compared with the modelled curve of step i.

- iii) Repeat step i with $I_f = 3.0$ p.u..
- iv) Repeat step ii with the same X_{rd} and X_{rq} used in step ii, but use the constant magnitudes of E_a and E_f from step iii.
- v) Plot the four T vs. δ curves from steps i to iv on the same graph for comparison.

5.1.3 Direct Force Computation Using the Maxwell Stress Method

Carpenter [30] and Hoole [16, pp. 352-354] use the following formula for computing the force vector, \mathbf{F} , on a non-current carrying magnetic material in two dimensions:

$$\mathbf{F} = \iint \frac{1}{2} \mu_0 [H_n^2 - H_t^2] \mathbf{u}_n dS + \iint \mu_0 H_n H_t \mathbf{u}_t dS \quad (5.5),$$

where the region of integration is a contour (in air) surrounding the part (in this case a rotor), H_n is the normal component to the contour, H_t is the tangential component to the contour, and \mathbf{u}_n and \mathbf{u}_t are the normal and tangential unit vectors respectively.

When applied to a cylindrical rotor, equation 5.5 can be simplified to give

$$T = \frac{2Pr^2\ell}{\mu_0} \int_0^{2\pi} B_n B_t d\theta \quad (5.6),$$

where P is the number of poles, r is the radius of a circular contour in the air gap surrounding the rotor, ℓ is the rotor length, and B_n and B_t are the normal and tangential components of flux density. Equation 5.6 is known as Maxwell's Tensor (see Abdel-Razek [22]).

Equation 5.6 is readily adapted to finite element methods, but is not suitable for my reluctance model method. The geometry of the contour coincides with that of my model, but B_t is unknown. If the air gap were wide enough beneath the poles, B_t could be measured using the flux probe, but this is not the case. B_t would also have to be

predicted using the reluctance model. The advantage of using equations 5.5 or 5.6 is that they are independent of saturation effects in the iron, depending solely upon the field in the air gap. The field in the air gap, however, is heavily dependent upon the saturation conditions in the machine iron.

5.1.4 The Flux Linkage Method

The flux linkage method, though not providing a detailed picture of the forces and torques acting within the machine iron (important information for mechanical design), is well suited for calculating net air gap torque with my flux density model.

The flux linkage equations originated from Oersted's and Faraday's experiments in the early 1800's (see Langsdorf [31]). They relate the induced torque and voltage to the current and the rate of change of flux linking a coil with respect to angular position or time. Their basic form is given in equations 2.8 and 2.9. Their application to computing torque and voltage in electric machines is discussed in references [9, pp. 38, 88-90] and [31]. In Appendix B I have fully derived the flux linkage torque equation for use with my machine and model. Equation B.16 was implemented in the computer model. Refer to Appendix B for details.

The reasons why the flux linkage approach was used in my model are:

- i) It is simple to implement and understand.
- ii) It can be used to compute the torque and voltage contributions from each coil side or coil independently, and from all of the coils on the rotor cumulatively.
- iii) The same approach, with only a minor change in the formula's constants, can be used to compute both torque and voltage. Air gap power balance on each coil, and for the armature phases as a whole, is assured.
- iv) No simplifying assumptions about coil layouts need to be made since each coil can be treated independently. Breadth factors, pitch factors, and phasor notation are not needed since the computer can rapidly sum the torque and voltage on all of the coils (this is consistent with what is physically happening in the machine). The constructional features of the windings (number of conductors per coil, coil position, etc.) can be easily changed by changing values in various arrays. The algorithm is very flexible.
- v) The flux density distribution data used by the flux linkage equations is directly available from the flux density model and measurements. Saturation needs to be

accounted for only in the flux density distribution model. The flux linkage equations themselves are independent of the machine's magnetic saturation level and can be used for any flux density distribution under any magnetic conditions in the machine. The effects of saturation upon torque and voltage induction is a result of the effects of saturation on the flux distribution only, not because of any direct effect of saturation on the torque or voltage equations themselves.

5.2 THE TORQUE COMPUTATION ALGORITHM

Torque computation for static conditions (see section 2.2.3) has been implemented according to Appendix B. Actual steady state conditions, including the full effects of MMF space harmonics and current time harmonics can be easily implemented according to the General Torque and Voltage Algorithm of Appendix B, but due to time restrictions this was not carried out. This can be done as future work. Simulating static conditions is adequate for evaluating the initial proposal.

The static flux density distribution is computed per Chapter 4, then, since the coil distribution and the armature current levels are known, the static torque may be computed. The static torque is not exactly the same as the steady state torque, except for the one point in time during the AC cycle (twice during each rotor rotation) when $\omega t = -\pi/6$ (neglecting time harmonics of current). At this point in time, all of the superimposed phase winding MMF's combine to give the a and -b armature MMF distribution which is used in the B distribution model and the experimental equipment. All of the space harmonics of field and armature MMF are considered for this one point in time.

The effects of space harmonics were shown to be small relative to the armature MMF wave (see section 3.2.4, Figure 3.16). The armature MMF wave, in turn, is small relative to the field MMF wave under normal operating conditions. If the effects of current harmonics are assumed to be small as well, then, under normal operating conditions, the steady state torque will not vary greatly from the static torque since the armature MMF wave will be substantially fixed in space relative to the field poles. Under short circuit conditions (for a generator), or very high load conditions (for a motor), the armature MMF wave and its harmonics may no longer be small relative to the field MMF wave. This may lead to torque pulsations and shaft damage. Further work should be done in this area to see what harmonics need to be considered when analyzing these conditions.

Appendix B also mentions some potential considerations for implementing a transient

model.

5.3 MEASURED VS. COMPUTED TORQUE RESULTS

The torque measurement approach was already discussed in section 2.2.2. Error estimates are found in Appendix A. The estimated torque measurement error (due to hand calibration) is ± 3 N-m (± 0.076 p.u.).

Field current, armature current, and torque levels for the measurements and their corresponding computer simulations go well beyond rated. This is done to check the model's accuracy in highly saturated conditions. Many of these conditions would not be encountered except during transient behaviour.

As mentioned in section 5.2, the measurements and simulations are for static conditions.

Figure 5.2 compares measured and modelled results for linear and saturated conditions. For high current levels, saturation effects cannot be removed from the measured cases, but they can be removed in the computer model by setting R_{sat} equal to zero. This is done to demonstrate how much error would be present if the torque were predicted with a linear computer model, as compared to the measured torque and the computer model incorporating saturation. In Figure 5.2 the armature a and -b MMF axis is kept on the quadrature axis. Armature current is increased with field current as a parameter. Since the armature MMF is small relative to the field MMF and it is centred on the quadrature axis, saturation effects due to increasing armature current are not significant and each torque vs. armature current curve is nearly a straight line. However, as the field current increases the slope of these curves does not increase as quickly for the measured and modelled (with saturation) cases as it does for the linear modelled case. As a result, the linearity assumption leads to a noticeable torque error for field currents greater than 0.5 p.u.. The curves for the 2.0 p.u. and 3.0 p.u. linear cases go off scale since their error is so large. Beyond 6 p.u. torque they continue to climb with the same slope as their visible portions below 6 p.u. torque. The saturated model appears to give good torque results for all combinations of field and armature current levels when the a and -b MMF wave is centred on the quadrature axis. In Chapter 3 the number of conductors per coil side was estimated to be 9. This appears to be substantially correct, otherwise the slope of the torque vs. armature current curves would not be the same for the measured and computed cases.

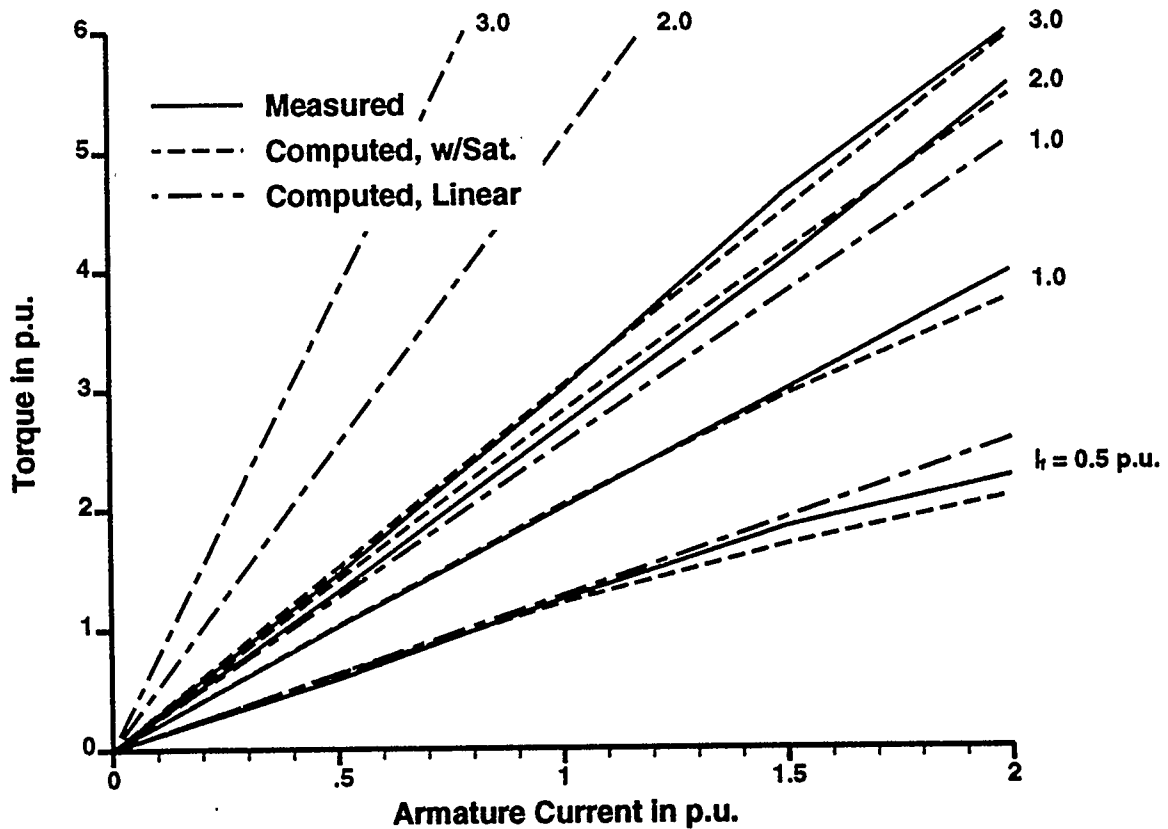


Figure 5.2: Measured, Computed (Linear), and Computed (with Saturation) Torque vs. Armature Current, Field Current as a Parameter. Armature A and -B MMF Axis on Q Axis ($\psi = 0^\circ$ elec.).

The internal power factor angle, ψ , is explained in Appendix C. I am using it in these figures in order to be consistent with the D-Q axis theory of Appendix C. ψ is the location of the centre of the armature MMF axis with respect to the quadrature axis. It is linearly related to the experimental machine's rotor gauge reading, *rotorg*, through equation C.5.

Figures 5.3a to d compare the saturated model's torque results with measured results for all armature a and -b MMF wave orientations (ψ 's). Field and armature currents are given as parameters. In each figure, as armature current increases, so does the T vs. ψ

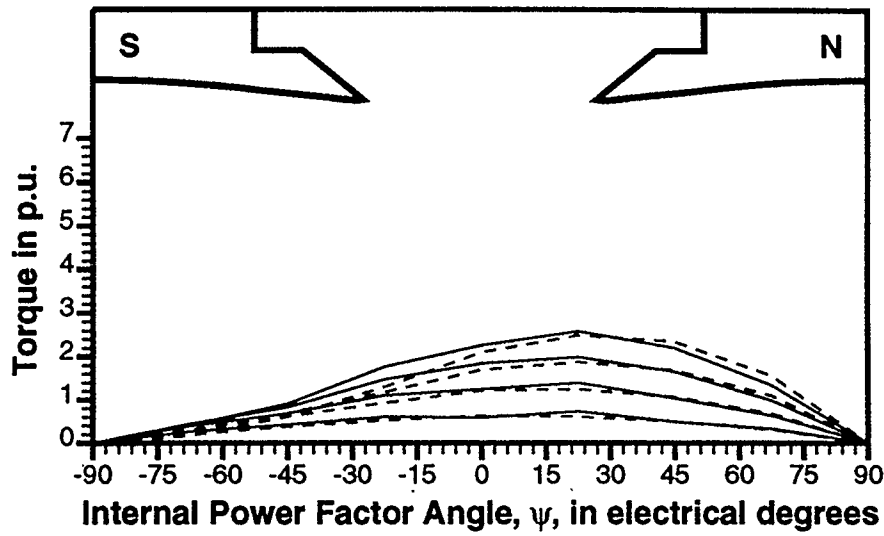


Figure 5.3a:
Field current
= 0.5 p.u.,
Armature current
= 0.5, 1,
1.5, 2.0 p.u.

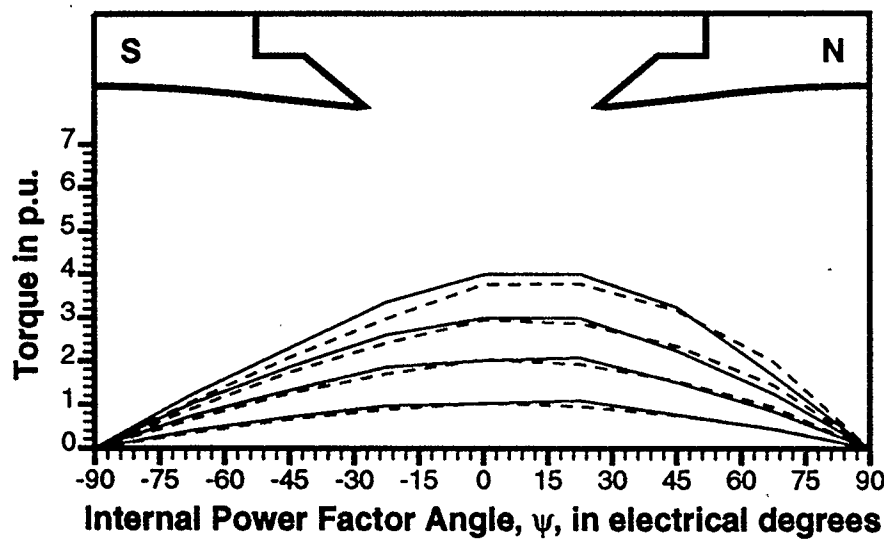


Figure 5.3b:
Field current
= 1.0 p.u.,
Armature current
= 0.5, 1,
1.5, 2.0 p.u.

Figure 5.3: Measured (solid) and Computed (dashed) Torque vs. Internal Power Factor Angle, ψ , with Armature Current and Field Current as Parameters

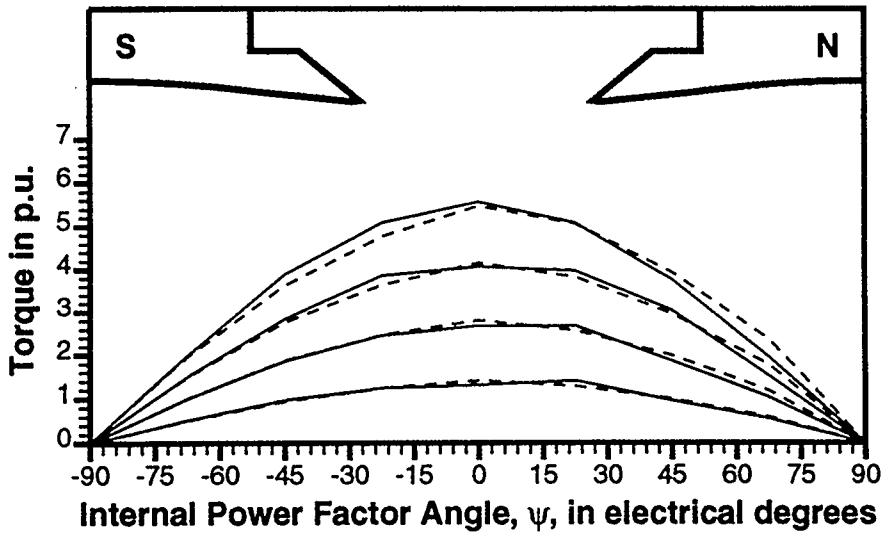


Figure 5.3c:
Field current = 2.0 p.u.,
Armature current = 0.5, 1, 1.5, 2.0 p.u.

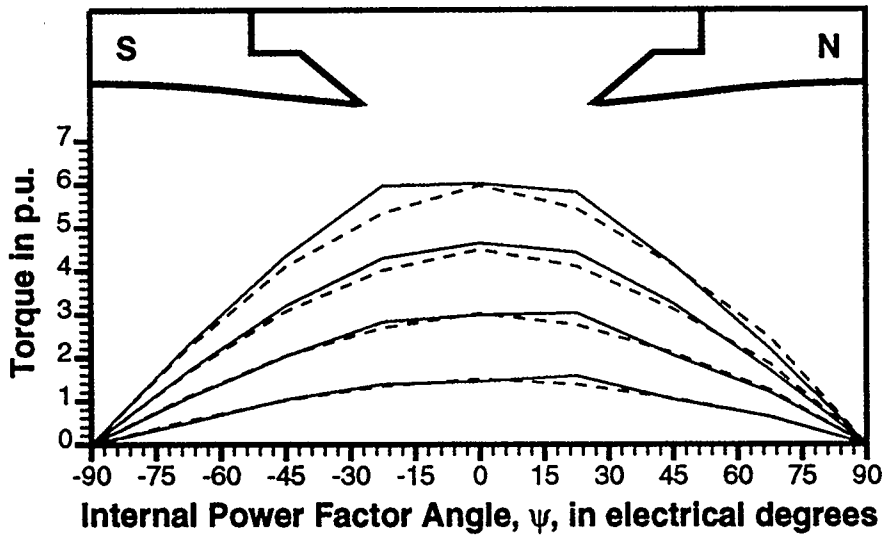


Figure 5.3d:
Field current = 3.0 p.u.,
Armature current = 0.5, 1, 1.5, 2.0 p.u.

Figure 5.3: Measured (solid) and Computed (dashed) Torque vs. Internal Power Factor Angle, ψ , with Armature Current and Field Current as Parameters

curve. As in the compound excitation flux plots shown in Figure 4.4, not all of these combinations of field and armature current levels and ψ 's will be encountered during normal operation. Many will be found only during transient conditions or not at all. The primary purpose of Figure 5.3 is to determine the accuracy of the flux and torque prediction models for static conditions. Accuracy in field, torque, and voltage prediction for steady state or transient conditions should be checked as future work. However, as mentioned in section 2.2.3, static field solutions are already successfully used in transient simulations.

Though the curves shown in Figures 5.3a to d display some reluctance torque effects (as mentioned in section 5.2.2), they are not for the same conditions as the T vs. δ curves shown in Figure 5.1. Those curves are for constant E_a , E_f , X_{rd} , and X_{rq} . All of those assumptions, except for constant E_f when I_f is assumed constant, are violated in Figure 5.3. Perhaps for the 0.5 p.u. field current case we can say that X_{rd} and X_{rq} are constant, but for each T vs. ψ curve I_a is held constant and ψ and E_a are allowed to vary. For a T vs. δ curve E_a is held constant and I_a and ψ are allowed to vary.

The skewing in the T vs. ψ curve due to reluctance torque effects is less visible for 2.0 p.u. and higher field currents (Figures 5.3c and d). In Chapter 6 the constant power factor curves and V-curves were computed. For each operating point on those curves the values of X_{rd} and X_{rq} were computed. For operating points corresponding to points in the T vs. ψ curves for 2.0 p.u. field current and higher the computed values of X_{rd} dropped substantially to values equal to or even lower than X_{rq} . Under such heavily saturated conditions the saturation levels within the poles can become so high that the reluctance torque effects are eliminated and the machine behaves like a cylindrical pole machine. For example, for one point during unity power factor operation the torque is 0.729 p.u., $I_f = 0.655$ p.u., $I_a = 0.5$ p.u., $\psi = -9.4^\circ$ elec., $\delta = 8.6^\circ$ elec., $X_{rd} = 9.88 \Omega$, and $X_{rq} = 5.25 \Omega$. For another point during unity power factor operation the torque is 7.3 p.u., $I_f = 3.3$ p.u., $I_a = 6.07$ p.u., $\psi = -64.8^\circ$ elec., $\delta = 28.07^\circ$ elec., $X_{rd} = 3.43 \Omega$, and $X_{rq} = 3.65 \Omega$. Both X_{rd} and X_{rq} decrease due to saturation, but X_{rd} was affected much more. X_{rq} was not affected as severely because it is dominated by the large interpolar air space.

The major error trends are as follows:

- i) The average error magnitude for all of the computed data points in Figure 5.3 is 7.96% (excluding the 0 torque points).

- ii) At rated conditions ($I_f = 1.0$ p.u., $I_a = 1.0$ p.u., 0.8 pf leading) the computed torque is 6.7% below the measured.
- iii) For $\psi < -45^\circ$ elec. and $I_f \leq 1.0$ p.u. the torque errors are up to 20% low. This is the worst region. Its magnetic field conditions correspond to Figure 4.4e, where the flux per pole was also found to be 20% low. The errors in the computed field result in errors in the computed torque as well. As explained in Chapter 4, R_{sat} characterization, fringing, and hysteresis contribute to this error. Fortunately, as explained in Chapter 4, we do not operate our machines in this excitation state under steady state or transient conditions.
- iv) For $\psi < -45^\circ$ elec. and $I_f > 1.0$ p.u. the torque errors are no more than 5% low.
- v) For $-45 \leq \psi \leq 45^\circ$ elec. (the quadrature axis region) the error is generally less than $\pm 5\%$.
- vi) For $\psi > 45^\circ$ elec. and $I_f \leq 2$ p.u. the torque errors are up to 10% high. This is consistent with the error in computed flux per pole for the similar excitation conditions shown in Figure 4.4a. The primary sources of error in this case are R_{sat} 's inability to account for damper bars, and fringing effects leading to error on the flanks of the flux density distribution.

Considering the simplicity of the modelling approach used, we appear to have done a reasonable job of predicting the fields and torque for all practical operating conditions. Since we have been successful at excitation levels well beyond rated conditions, there is potential for using this modelling approach for transient simulations.

Since the regions and magnitudes of error in flux per pole and torque computation are known, further work can be done to compensate for these errors. Introducing positional variation for R_{sat} , as mentioned in Chapter 4, will help correct for the damper bar errors mentioned in point vi above. For the other errors, a potential correction method may be to adjust the input currents depending upon ψ 's position in order to give the correct torque value at the proper current level (in other words, bending the computed T vs. ψ curves in Figure 5.3 to match the experimental curves).

One application of this torque computation model could be determining torque angle swings under step load changes.

CHAPTER 6

THE VOLTAGE MODEL

6.0 CHAPTER OBJECTIVES

- i) Describe the use of the flux linkage voltage calculation with the flux density model.
- ii) Compare computed voltage distributions based on measured and modelled flux density data.
- iii) Present modelled constant power factor curves and V-curves for steady state conditions.

6.1 FLUX LINKAGE VOLTAGE COMPUTATION

Flux linkage voltage computation (based in equation 2.9) follows easily once flux linkage torque computation has been implemented. This is because the positions of the coil sides and $\partial\Phi/\partial\theta$ are used to determine the torque, and this information is also necessary to compute the voltage. Unlike induced torque, which is produced even under static conditions if current is flowing in the coil sides, induced voltage only exists if $\partial\Phi/\partial t$ is not equal to zero and may exist even if no current flows in the coil (no load conditions).

For simplicity, I assume that $\partial\Phi/\partial t$ can be broken into $\partial\Phi/\partial\theta \times \partial\theta/\partial t$ where $\partial\theta/\partial t$ equals the constant steady state synchronous speed ω . I neglect time variation of flux under steady state conditions due to armature MMF space harmonics and armature current time harmonics by assuming that the static flux distribution which is used to compute torque for one point in time during the AC cycle ($\omega t = -\pi/6$) remains unchanged during the whole AC cycle. In order to compute a voltage waveform for an entire AC cycle, all that my computer model does (assuming an unchanging flux density distribution) is rotate the coil sides through the flux density distribution at synchronous speed and compute the sum of all of the instantaneous voltage contributions for each coil side at each new angular position. Since the rotor's speed is assumed to remain at synchronous speed, the size of the time steps in the AC voltage vs. time waveform and the angular position steps of the rotor are linearly related constants. Since the machine has four poles, the rotor will rotate through 360° mechanical in the same period of time as the voltage goes through 720° electrical.

These assumptions are not necessary if the General Torque and Voltage Algorithm

given in Appendix B is implemented. It would take into account any irregularities in rotor speed, harmonics, etc. As with computed torque, the error introduced by neglecting these complications when computing voltage should be small.

Equation B.17 in Appendix B expresses the general flux linkage voltage equation (equation 2.9) in terms of machine dimensions. Appendix B also describes the voltage computing model in more detail.

Appendix C describes how to apply the voltage computing model under D-Q axis theory. Pre- and postprocessing programs are used to perform phasor computations. An example of trial and error calculations for computing a point on a steady state motor V-curve is given.

The flux density, torque, and voltage models were all combined into one Fortran program. The inputs to this program are the instantaneous value of the armature current, i_a (determined from the rms phase current using equation 2.13); the field current level, I_f , and the angular position of the a and -b armature MMF axis, *rotorg*. *rotorg* is related to the internal power factor angle, ψ , by equation C.5. ψ is the phase delay between the phase a current phasor and the induced no load phase a voltage E_f .

Once i_a , I_f , and *rotorg* are specified, the program computes the air gap field distribution incorporating the effects of armature reaction and saturation. Then the static torque is computed (once *rotorg* is specified then the position of all of the coil sides is known) as shown in Chapter 5. Then two cycles of the phase a voltage are computed by time/position stepping through one complete mechanical revolution assuming the air gap field remains unchanged throughout this time period.

The outputs from the computer program include:

- i) The computed field distribution for $\omega t = -\pi/6$.
- ii) A file giving the position of the coil sides at $\omega t = -\pi/6$. This is the point in the cycle for which the static torque is computed. This point was selected in order to compare computed versus measured field and torque results. This is also the first point on the computed voltage waveform. The remaining points on the voltage waveform are obtained by changing the positions of the coil sides by small steps until the rotor has rotated one complete revolution (two AC supply cycles). Torque is not computed for these points but easily could be.
- iii) The air gap torque at $\omega t = -\pi/6$. For a motor this is greater than the shaft torque

by the amount required to overcome hysteresis, eddy current, windage, and bearing friction losses.

- iv) The rms magnitude and phase of the induced phase a voltage, E_a . Its phase angle, α , is expressed relative to the phase a current fundamental. The phase a current fundamental is used as a reference phasor for the machine model because the phase a current peaks at the point in time when the three phase armature MMF wave axis coincides (in space) with the phase a winding's MMF axis.
- v) The E_a vs. ωt waveform. The range of ωt is 720° electrical.

In order to use the computer program to simulate actual static (or steady state) operating conditions, a preprocessing program computes the desired E_a based on the phase a line to neutral terminal voltage for the motor (V_a), the armature winding resistance (R_a), the armature winding leakage reactance (X_a), the phase a line current (I_a), equation C.1, and the constraints of the type of operating curve to be computed. Through a trial and error process (a good candidate for automation in the future), the model is run with trial values of I_l and *rotorg* until the desired E_a (both in magnitude and phase) is computed by the model. The no load phase a induced emf, E_f , can be computed once the desired E_a is obtained by using the same values of I_l and *rotorg* that gave the desired E_a and letting I_a equal zero. Once the magnitude and phase of both E_a and E_f are known, δ , I_q (the component of load current in phase with E_f), I_d (the component of load current in quadrature with E_f), X_{rq} , and X_{rd} may be found from the D-Q axis theory phasor diagram (Figure C.1.b). This is handled by a postprocessing program. As mentioned earlier, Appendix C contains a detailed example where a point on the zero shaft power V-curve (shown in Figure 6.3) is determined.

Generating conditions can also be handled. See Appendix C.

Since my experimental machine cannot rotate I cannot provide experimental confirmation of the results presented in this chapter. However, by computing steady state results using the computer model and D-Q axis theory, I have laid the foundation for future operating machine simulations. Air gap power balances (where electrical power delivered to the air gap ($3E_a I_a \cos(\alpha)$) should equal mechanical power delivered to the rotor ($T\omega$)) are within 2% for all excitation conditions. Therefore, voltage errors should be consistent with the torque errors described in Chapter 5. The voltage error manifests itself as a magnitude and/or a phase error.

The 2% error is present because only the fundamental of voltage is used in the air gap power balance. If all of the voltage harmonics were considered, there would be much less error. Since this error is so small, the effects of harmonics can be considered to be very small indeed.

6.2 COMPUTED VOLTAGE WAVEFORMS

Figure 6.1 compares computed voltage waveforms based on measured and computed flux density data. The measured and computed flux density distributions from which the voltage is computed are shown in Figure 4.4c.

The following waveforms are shown in Figure 6.1:

- i) The reference phase a current, I_a . I_a is 2 p.u. and it peaks on $\omega t = 0^\circ$ electrical.
- ii) The induced phase a voltage under load (computed from measured flux density data), $E_{a,meas}$. The rms magnitude of $E_{a,meas}$ is 1.333 p.u. (338.65 volts) and it leads I_a by 24.87° electrical ($\alpha = 24.87^\circ$ electrical).
- iii) The induced phase a voltage under load (computed from modelled flux density data), $E_{a,comp}$. The rms magnitude of $E_{a,comp}$ is 1.305 p.u. (331.45 volts) and its α is 18.1° electrical.
- iv) The induced phase a voltage under no load (computed from modelled flux density data), $E_{f,comp}$. The rms magnitude of $E_{f,comp}$ is 1.360 p.u. (345.42 volts), and its α is -2.38° electrical. Under no load conditions, $\alpha = \psi$. The assumed $\psi = 0$ is slightly off as a result of small measurement errors which occurred when *rotorg* was first defined.

The following features are apparent from Figure 6.1:

- i) $E_{a,meas}$ has some roughness which is caused by the effect of damper bar slots on the measured flux density distribution. The normalized 3rd to 9th harmonic components present in the measured flux density distribution are substantially reduced in the corresponding $E_{a,meas}$ distribution. Compare the second and third columns of Table 6.1. After the 9th harmonic, the harmonic levels are very low (due to the smoothing effect of the finite width Hall element) and no trend can be seen. However, if these higher harmonics were present in the data they would be reduced as well. This is one reason why averaged flux density distributions can be used, because higher harmonics of voltage and torque are "filtered out" by the distributed, fractional pitch windings. The $E_{a,meas}$ waveform is much closer in shape

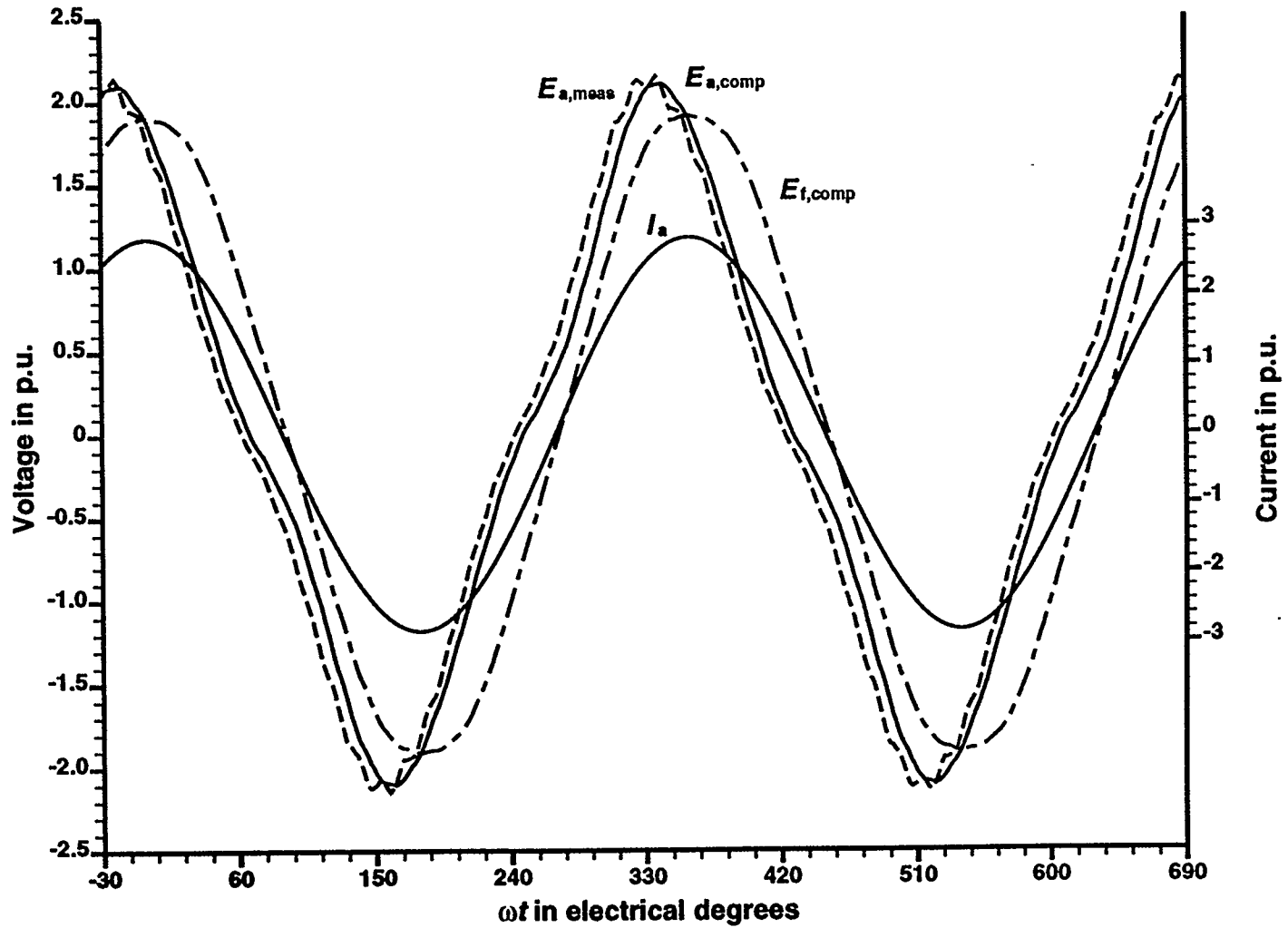


Figure 6.1: Computed Voltage Waveforms from Measured and Computed Flux Density Data. Armature Current = 2 p.u., Field Current = 1 p.u., $\psi = 0^\circ$ electrical.

to a sinusoid than the flux density waveform.

- ii) $E_{a,comp}$ and $E_{f,comp}$ are smoother than $E_{a,meas}$ because their flux density data is smoother. The same filtering effect, caused by the distributed, fractional pitch windings, is present as may be seen by comparing columns 4 and 5 of Table 6.1.

Harmonic Order n	$\frac{B_{a,n,meas}}{B_{a,1,meas}}$	$\frac{E_{a,n,meas}}{E_{a,1,meas}}$	$\frac{B_{a,n,comp}}{B_{a,1,comp}}$	$\frac{E_{a,n,comp}}{E_{a,1,comp}}$	$\frac{B_{f,n,comp}}{B_{f,1,comp}}$	$\frac{E_{f,n,comp}}{E_{f,1,comp}}$
1	1.0000	1.0000	1.0000	1.0000	1.0000	1.0000
3	0.1899	0.1169	0.2113	0.1312	0.0131	0.0073
5	0.0813	0.0161	0.1089	0.0154	0.0988	0.0129
7	0.0335	0.0029	0.0343	0.0077	0.0324	0.0039
9	0.0288	0.0037	0.0096	0.0047	0.0019	0.0044
11	0.0043	0.0056	0.0020	0.0058	0.0012	0.0043
13	0.0078	0.0058	0.0046	0.0055	0.0027	0.0044
15	0.0140	0.0059	0.0121	0.0064	0.0108	0.0054
17	0.0095	0.0055	0.0047	0.0055	0.0033	0.0042
19	0.0080	0.0067	0.0051	0.0055	0.0039	0.0042
21	0.0015	0.0061	0.0038	0.0078	0.0029	0.0060

- iii) $E_{f,comp}$ has a higher fundamental than either $E_{a,meas}$ or $E_{a,comp}$, even though $E_{f,comp}$'s waveform has a smaller peak magnitude. This is because $E_{f,comp}$'s waveform is much wider than $E_{a,meas}$'s or $E_{a,comp}$'s. The significant quadrature axis oriented

armature reaction MMF (which has about the same peak magnitude as the field MMF) causes a drastic change in the shape of the loaded flux density distribution from the no load flux density distribution. The third harmonic of the flux density distribution for the loaded case (column 4) is far greater than for the unloaded case (column 6). The ratio of the absolute magnitude of the unloaded third harmonic to the loaded third harmonic is 6.4%. The corresponding voltage ratio for the third harmonic is 5.8%. It is this much larger third harmonic component in the loaded flux density and voltage waveforms which causes them to be thinner than for unloaded conditions. Harmonics higher than the third are not affected as significantly.

- iv) The electrical power based on the modelled flux density data is 2.54% higher than that based on the measured flux density data. This considers the magnitude and phase (α) of the induced voltage fundamental only. The error in electrical power caused by the difference in α 's (4.8%) is partially offset by the difference in magnitudes (-2.1%). The corresponding torque (mechanical power) is 4.1% higher, which is larger than the electrical power difference of 2.54%. This is because the torque computation considers all of the flux harmonics.

Distributed partial pitch windings reduce the magnitude of higher order harmonics, thus smoothing the voltage waveform and making it closer to a sine wave. A valuable future study would be to compute the voltage using a single, concentrated winding in the computer program, and compare the harmonics from this winding to those of Table 6.1. The reduction in harmonics could be compared to those predicted from breadth (K_b), pitch (K_p), and winding (K_w) factors. See Langsdorf [27, pp. 182-189] and Kingsley [7, pp. 543-550]. As mentioned in Appendix B, the effects of tooth skewing could also be investigated. This could be done in conjunction with the study on K_b and K_p .

6.3 MODELLED STEADY STATE CONDITIONS

Figure 6.2 is the open circuit line to neutral terminal voltage curve for the synchronous machine run as an unloaded generator. The speed is constant at 1.0 p.u. (1800 RPM). The effects of saturation are apparent throughout the curve. The initial slope at the origin is the slope of the air gap line for linear conditions. Saturation effects cause the no load voltage to be much lower than the air gap line. The shape of this curve is consistent with published results. See Kingsley [7, p. 320].

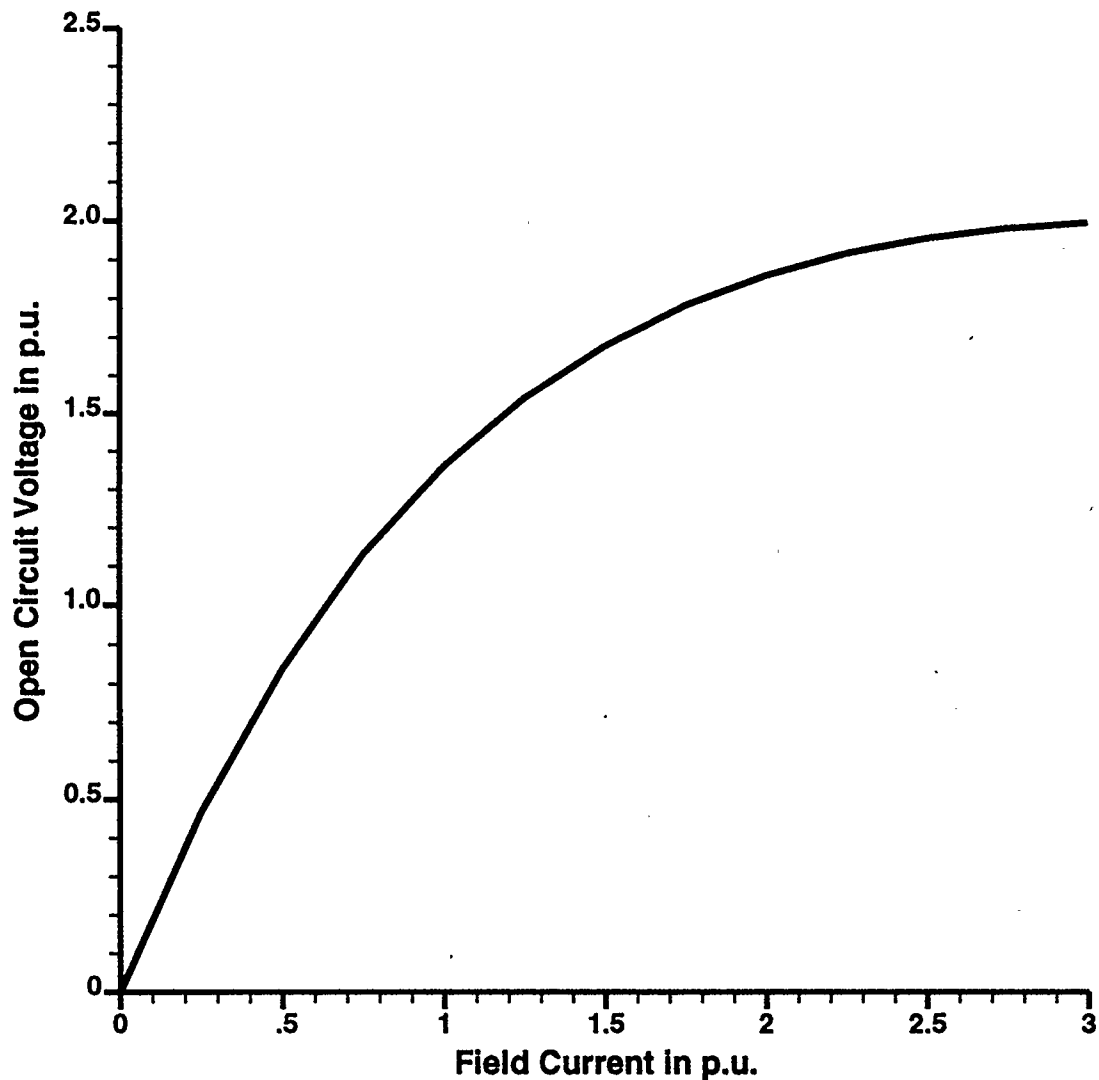


Figure 6.2: Open Circuit Line to Neutral Voltage for 1.0 p.u. Speed

In the computer model, I_f is increased in steps, $i_a = 0$, and *rotor* can be anything. Only the fundamental magnitude is needed. The no load curve is unaffected by the time harmonics of armature current and the space harmonics of the armature MMF wave since there is no armature reaction.

Figure 6.3 compares the motor's constant power factor curves for a power factor of 0.8 lead, 1.0, and 0.8 lag, and the no load V-curve (zero power factor). Detailed computation for a typical point on the no load V-curve is given in Appendix C. Points on the constant power factor curves are computed in a similar manner, but power factor is

held constant instead of developed shaft power.

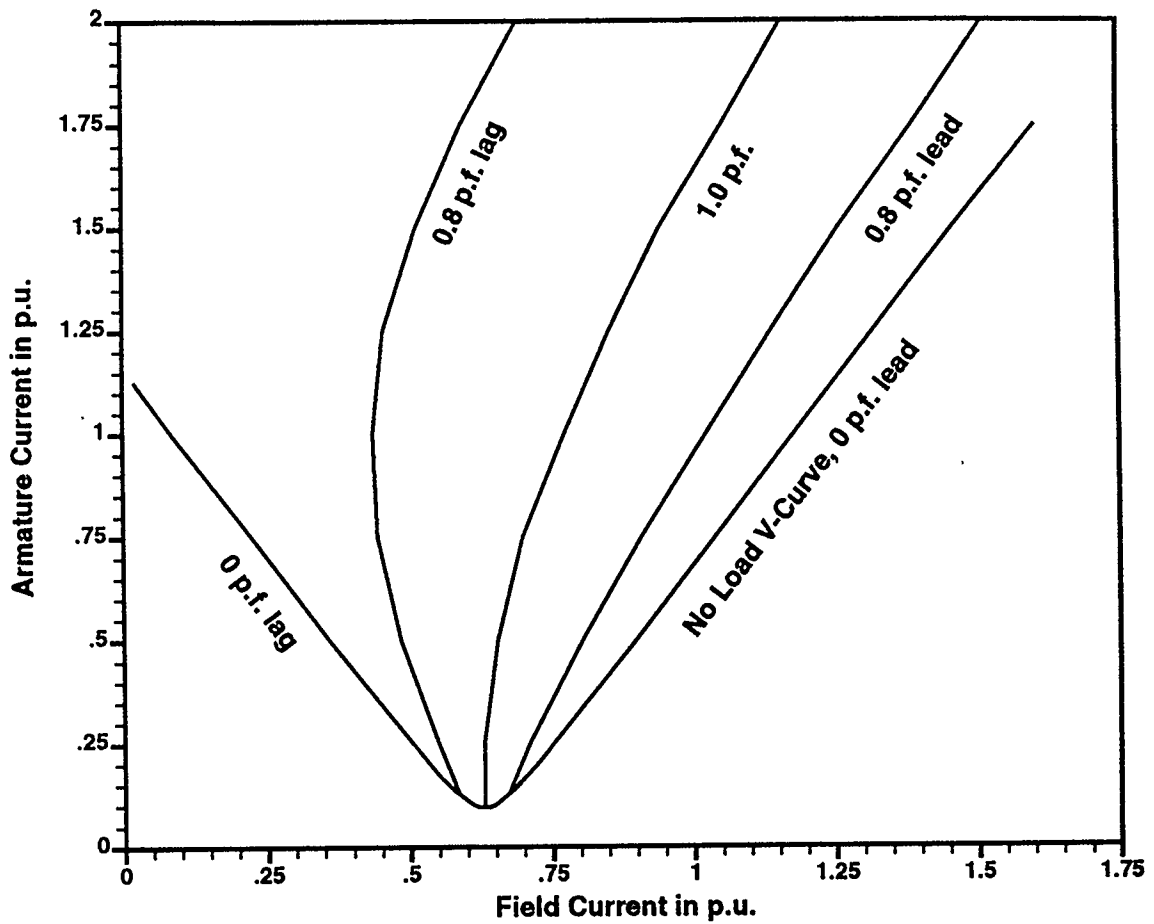


Figure 6.3: Constant Power Factor Curves and No Load V-Curve (Zero Power Factor) for the Motor, Voltage = 1.0 p.u., Speed = 1.0 p.u.

The no load V-curve for zero power factor leading corresponds to a synchronous condenser. High field currents are required to compensate for the armature MMF which opposes the field MMF. If we operated in the leading power factor region with rated field and twice rated armature current (a point which is not obtainable in Figure 6.3), then we would have error in the computed flux per pole of up to 20%. However, this problem is not encountered in a real operating machine because the control system forces the field

current to increase well beyond rated in order to limit the armature current. Under these conditions the torque is very small because the net flux distribution is symmetric on the pole. The net flux is large in order for E_a to have a large enough magnitude to offset V_a and restrict the armature current to a reasonable level. The field solution is expected to be reasonably accurate (and therefore, so should Figure 6.3) under these conditions since the net MMF is large.

For future work, compare these results with ones from a linear model, and an actual operating machine. For an operating machine R_{base} , R_{sat} , and the other parameters of the flux density model could be determined using finite element analysis.

The shape of these curves agrees with published results. See Langsdorf [27, p. 499].

For additional future work, characterize the effects of saturation upon X_{rd} and X_{rq} . I expect that both would decrease as saturation increases. However, as mentioned in Chapter 5, X_{rd} will decrease much faster than X_{rq} due to saturation in the field poles.

CHAPTER 7

CONCLUSIONS AND FUTURE WORK

7.0 CHAPTER OBJECTIVES

- i) *Summarize the major conclusions of this research.*
- ii) *Identify areas of future work.*

7.1 CONCLUSIONS

- i) The significance of synchronous machines and our ability to predict their behaviour under transient conditions is currently an important area of research. Existing methods of determining magnetic fields in synchronous machines have one or more of the following problems:

- inaccurate
- dependent upon infinite permeability in the iron
- mathematically complex
- computationally intensive

The finite element method, the method most widely used today, can provide extensive and accurate magnetic field information for any operating condition, but has heavy computing requirements.

- ii) A new magnetic field model was proposed and developed based on the magnetic circuit approach. Magnetic field data from an experimental machine was successfully used to develop this model. Measurements and corresponding modelled results were for static conditions. Inaccuracies in the flux density measurements were caused by the finite width of the Hall effect crystal which caused smoothing of the measured data (attenuating harmonics in the unaveraged flux density data past the 9th order).
- iii) Averaged flux density distributions were used because they had negligible error and they greatly simplified the modelling process by smoothing out the effects of individual teeth.
- iv) R_{base} was successfully determined for linear conditions. Errors affecting it were roughness in the quadrature axis region of the averaged flux density data, hysteresis, and fringing effects. These errors also complicated the determination

of the MMF wave, and resulted in errors in the computed flux density distribution. R_{base} 's shape was consistent with permeance curves developed by Doherty/Nickle [15]. R_{base} is constant under the middle of the field poles where the air gap is uniform, increases gradually under the chamfered portion, and is substantially higher in the interpolar regions due to the large air gap between the salient poles. R_{base} was approximated using Fourier series in the computer model.

- v) The experimentally determined armature MMF wave is more sinusoidal than the theoretical one.

The variation in the armature MMF due to harmonics is large ($\pm 3.6\%$ of the peak) relative to the difference between the theoretical and experimental armature MMF waves. Therefore, either the theoretical or the experimental armature MMF wave can be used to determine R_{base} over a broad segment width. However, the armature MMF wave is normally small compared to the field MMF wave. Therefore the effects of the armature MMF's space (and time) harmonics can be neglected except for conditions where the armature current is excessively large.

The armature MMF wave is proportional to the armature current and the number of conductors per coil. Its shape was approximated using a Fourier series.

- vi) The experimentally determined field MMF wave is approximately trapezoidal. The width of its constant portion is equal to the pole arc, and its amplitude is equal to the field winding Amp-turns. The field winding MMF wave is proportional to field current and was approximated with a Fourier series.
- vii) Armature and field MMF superposition holds under linear conditions. In order to construct a flux density model, this superposition is assumed to hold in the air gap under saturated conditions as well. Accounting for the effects of saturation then becomes the responsibility of R_{sat} . This assumption did not cause any noticeable error, since the errors in the modelled flux density distribution can be attributed to quadrature axis roughness in the flux density wave, hysteresis, fringing, R_{sat} 's characterization, and ignoring the direct position dependence of R_{sat} (due to damper bar slots and the shape of the pole shoe).
- viii) Normalized R_{sat} was characterized using a best fit quadratic equation. This quadratic is a function of the sum of the armature and field MMF's at each point

in the air gap.

From measurements, R_{sat} was found to be directly position dependent due to saturation effects caused by the damper bar slots and the pole shoe shape. For simplicity this direct dependence was neglected. For high MMF levels under a pole face, the distortion in the measured flux density wave caused by the damper bar slots and pole shoe shape is not present in the computed flux density wave. This causes some error when the torque and voltage are determined from the computed flux density wave.

At very low MMF levels, due to non-linearity in the B-H characteristic which R_{sat} 's quadratic fails to account for, errors occur in the computed flux density wave, torque, and voltage. These conditions are encountered when the armature MMF is large (comparable in magnitude to the field MMF) and directly opposes the field MMF. This corresponds to short circuit conditions for a generator or 90° leading power factor conditions for a motor (synchronous condenser). Fortunately, these conditions are not encountered in operating machines because the field current is boosted in order to maintain the induced winding voltage. In a generator this will sustain the terminal voltage leading to a high short circuit current and ensuring breaker operation. In a motor this limits the armature current to a reasonable level under constant terminal voltage conditions.

R_{sat} is slightly different under armature and field excitation, due to its position dependence. This may also add to the flux density, torque, and voltage errors.

ix) As a result of quadrature axis roughness in the flux density wave, hysteresis, fringing, the neglected position dependence of R_{sat} , and the simple nature of R_{sat} 's characterization, error occurs in the computed flux per pole. These errors are dependent upon the excitation conditions in the machine (orientation of the armature MMF wave axis, field current level, and armature current level). These errors in computed flux per pole can be summarized as follows:

- For $45^\circ < \psi \leq 90^\circ$ elec. (armature MMF on +D axis, additive to field MMF): 5 to 10% high.
- For $-45^\circ \leq \psi \leq 45^\circ$ elec. (armature MMF on Q axis): $\pm 5\%$.
- For $-90^\circ \leq \psi < -45^\circ$ elec. (armature MMF on -D axis, opposed to field MMF): up to 20% low when the armature MMF and the field

MMF are the same magnitude; up to 5% low when the armature MMF magnitude is less than half the field MMF magnitude.

These flux per pole errors cause corresponding torque errors of similar magnitude. The average magnitude of torque error for all conditions is 8%. The 20% low flux per pole and torque errors for the third set of conditions just mentioned are not normally encountered due to the field current being boosted per conclusion viii.

- x) Torque was successfully computed using the flux linkage approach. The effects of saturation and salient poles are apparent in the measured and computed torques. For linear conditions, the T vs. ψ curve is skewed toward the direct axis pole. Under highly saturated conditions this skewing disappears. The saturation in the poles causes X_{rd} to drop more rapidly than X_{rq} until they become comparable in magnitude. Under these conditions the salient machine torque characteristic becomes similar to a cylindrical machine torque characteristic.
- xi) Voltage was successfully computed using the flux linkage approach. Power balance confirms the link between the torque and voltage computation methods. The distributed, partial pitch windings reduce the effects of higher harmonics of flux upon the induced voltage, making the induced voltage more sinusoidal. Steady state operating curves were predicted by combining the developed computer model with D-Q axis theory. The results need experimental verification, but their general shape agrees with the references.
- xii) The flux density, flux linkage torque, and flux linkage voltage models provide a simple, fast, and reasonably accurate means of predicting steady state behaviour, well beyond linear conditions. They also have the potential to replace finite element solutions during the time-stepped transient solution process. However, finite element simulation is still required to initially develop the flux density model for a machine that has not yet been built or from which experimental data cannot be collected. The research goal has been met, and the initial proposal has been shown to provide reasonable results. Its accuracy is not expected to be as high as the finite element approach, but the savings in computing time during long simulations, and its simplicity, are advantages over using finite elements. Since errors in the computed torque have been fully

identified, correcting functions can be developed to compensate for this error, leading to improved accuracy in transient studies.

7.2 FUTURE WORK

- i) Use a finite element package to develop the flux density model instead of measurements. Compare results from the two. The finite element package can compute deep, sharp drops in flux density over the slots which the Hall effect crystal averages over (thus reducing their apparent depth). The nature of the saturation within the pole iron and in other regions of the machine can also be found, leading to a better understanding of the sources and magnitudes of the errors in the flux density model.
- ii) Compare predicted steady state operating curves with and without saturation. Determine the effects of saturation upon X_{rd} and X_{rq} .
- iii) Compare modelled and measured steady state operating curves for an actual machine. The model can be developed using a finite element package.
- iv) Develop correction functions for the torque error. These functions can adjust the input currents to give the correct torque output depending upon ψ and the current levels.
- v) Determine the computed T vs. δ characteristic for my experimental machine using the method described in section 5.1.2. Compare the results from the linear and saturated models.
- vi) Automate the process of determining standard steady state operating curves, such as Figure 6.3.
- vii) Implement the General Torque and Voltage Algorithm in Appendix B. Determine the full effects of space and time harmonics on torque and voltage. Consider normal conditions, and the case where armature reaction is very large. Determine the reduction in accuracy caused by modelling with fewer MMF harmonics.
- viii) Attempt to determine R_{sat} as a function of both MMF and position.
- ix) Per Appendix B, compare the results of flux linkage, torque, and voltage computations done by neglecting skewing and taking a vertical average (as done in this research), and the sum of slices method based on equations B.4 and B.10. The difference is not expected to be great due to the small magnitude of the

higher flux harmonics and the smoothing effects of the tooth skewing and distributed, partial pitch windings.

- x) Investigate the reduction in voltage harmonics due to distributed, partial pitch windings, compare with the classical breadth and pitch factors.
- xi) Extend the General Torque and Voltage Computation Algorithm in Appendix B to transient conditions. Possibly use a state model approach for solving the system equations. Add the MMF waves of the damper windings. Compare the transient model using this method with the finite element based method and actual machine tests. Compare on a time-step by time-step basis, and compare total computing times.
- xii) Combine the flux density, torque, and voltage models with finite element software and state modelling in order to solve for steady state and transient conditions. The whole process of determining MMF waves, R_{base} waves, and R_{sat} can be automated. Inputs to the program would be construction data (machine dimensions, coil locations, etc.). These could even be entered from a CAD package. Armature and field MMF waves would then be computed, a finite element mesh automatically generated, and finite element solutions could be used to determine R_{base} and R_{sat} . Using a state model, the program could then be used to perform standard and specialized steady state and transient studies. The user could select standard studies or curves from a library which the program would then perform or compute automatically.

REFERENCES

- [1] J.O. Ojo and T.A. Lipo, "An Improved Model for Saturated Salient Pole Synchronous Motors", *IEEE Trans. on Energy Conversion*, Vol. 4, No. 1, March 1989, pp. 135-142
- [2] G.R. Slemon, "Analytical Models for Saturated Synchronous Machines", *IEEE Trans. on Power Apparatus and Systems*, Vol. PAS-90, No. 2, March/April 1971, pp. 409-417
- [3] F. Piriou and A. Abdel-Razek, "A Numerical Model for Saturated Inductances in Synchronous Machines", *Electric Machines and Power Systems*, Hemisphere Publishing Corp., 1983, Vol. 8, pp. 215-224
- [4] R.S. Ramshaw and G. Xie, "Nonlinear Model of Nonsalient Synchronous Machines", *IEEE Trans. on Power Apparatus and Systems*, Vol. PAS-103, No. 7, July 1984, pp. 1809-1815
- [5] G. Xie and R.S. Ramshaw, "Nonlinear Model of Synchronous Machines with Saliency", *IEEE Trans. on Energy Conversion*, Vol. EC-1, No. 3, September 1986, pp. 198-203
- [6] M.P. Krefta and O. Wasynczuk, "A Finite Element Based State Model of Solid Rotor Synchronous Machines", *IEEE Trans. on Energy Conversion*, Vol. EC-2, No. 1, March 1987, pp. 21-30
- [7] A.E. Fitzgerald, C. Kingsley Jr., and S.D. Umans, *Electric Machinery*, McGraw-Hill Book Co., 1983, pp. 2-7, 131-133, 146-150, 152, 155-165, 320, 345-349, 543-550
- [8] F.W. Carter, "The Magnetic Field of the Dynamo-Electric Machine", *Journal IEE*, Vol. 64, 1926, pp. 1115-1138
- [9] E.B. Moullin, *Electromagnetic Principles of the Dynamo*, Clarendon Press, Oxford, 1955, pp. 5-15, 28-56, 88-90, 254, 267, 302-311
- [10] J.H. Walker, *Large Synchronous Machines: Design, Manufacture, and Operation*, Clarendon Press, Oxford, 1981, pp. 82, 90-94, 117-118
- [11] P.L. Alger, *Induction Machines: Their Behaviour and Uses*, Gordon and Breach, N.Y., 1970, pp. 181-188
- [12] W.H. Hayt, *Engineering Electromagnetics*, McGraw-Hill, N.Y., 1981, pp. 271-286,

350-352

- [13] A.R. Stevenson, Jr., and R.H. Park, "Graphical Determination of Magnetic Fields: Theoretical Considerations", AIEE, Vol. 46, 1927, pp. 112-135
- [14] R.W. Wieseman, "Graphical Determination of Magnetic Fields", AIEE, Vol. 46, 1927, pp. 141-154
- [15] R.E. Doherty and C.A. Nickle, "Synchronous Machines: I - An Extension of Blondel's Two-Reaction Theory", AIEE, Vol. 45, 1926, pp. 912-947
- [16] S.R.H. Hoole, Computer-Aided Analysis and Design of Electromagnetic Devices, Elsevier, N.Y., 1989, pp. 6-7, 73-109, 111-158, 195-311, 352-354
- [17] F.C. Trutt, R.F. Jackson, and E.A. Erdelyi, "The Non-linear Potential Equation and Its Numerical Solution for Highly Saturated Electrical Machines", IEEE Trans. on Aerospace, Vol. 1, No. 2, 1963, pp. 430-440
- [18] R.D. Burtness, S.V. Ahamed, and E.A. Erdelyi, "Flux Distribution in Saturated DC Machines at No-load", IEEE Trans. on Power Apparatus and Systems, Vol. 84, No. 5, 1965, pp. 375-381
- [19] S.S. Coleman, M.S. Sarma, and E.A. Erdelyi, "Magnetic Fields in Nonlinear Salient Pole Alternators", IEEE Trans. on Power Apparatus and Systems, Vol. 87, No. 10, 1968, pp. 1848-1856
- [20] E.F. Fuchs, and E.A. Erdelyi, "Determination of Waterwheel Alternator Steady-State Reactances from Flux Plots", IEEE Trans. on Power Apparatus and Systems, Vol. 91, No. 6, 1972, pp. 2510-2518
- [21] M.V.K. Chari, and P. Silvester, "Analysis of Turboalternator Magnetic Fields by Finite Elements", IEEE Trans. on Power Apparatus and Systems, Vol. 90, No. 2, 1971, pp. 454-464
- [22] A.A. Abdel-Razek, J.L. Coulomb, M. Feliachi, and J.C. Sabonnadiere, "The Calculation of Electromagnetic Torque in Saturated Electric Machines Within Combined Numerical and Analytical Solutions of the Field Equations", IEEE Trans. on Magnetics, Vol. Mag-17, No. 6, 1981, pp. 3250-3252
- [23] W. Jian-She, "Finite Element Analysis of Saturated Synchronous Reactances of Salient Pole Synchronous Machines", Electric Machines and Power Systems, Hemisphere Publishing Corp., Vol. 11, 1986, pp. 201-213
- [24] D.G. Swanson, Jr., "Simulating EM Fields", IEEE Spectrum, Vol. 28, No. 11, 1991,

pp. 34-37

- [25] S.M. Fahmy, B.T. Browne, P. Silvester, and T.H. Barton, "The Open-Circuit Magnetic Field of a Saturated Synchronous Machine, An Experimental and Computational Study", IEEE Trans. on Power Apparatus and Systems, Vol. 94, 1975, pp. 1584-1588
- [26] F.W. Sears, M.W. Zemansky, H.D. Young, University Physics, Addison-Wesley, MS, 1982, pp. 596-599
- [27] A.S. Langsdorf, Theory of Alternating Current Machinery, McGraw-Hill, Toronto, 1955, pp. 45, 171-172, 182-189, 194-218, 301-303, 419-426, 435-453, 468-470, 499, 502
- [28] E.W. Swokowski, Calculus With Analytic Geometry, PWS, Boston, 1983, p. 252
- [29] R.L. Burden, J.D. Faires, and A.C. Reynolds, Numerical Analysis, PWS, Boston, 1981, pp. 323-325
- [30] C.J. Carpenter, "Surface-Integral Methods of Calculating Forces on Magnetized Iron Parts", Monograph No. 342, IEE, London, 1959, pp. 19-28
- [31] A.S. Langsdorf, "The Development of Torque in Slotted Armatures", IEEE Trans. on Power Apparatus and Systems, Vol. 82, 1963, pp. 82-88
- [32] P.L. Alger, "The Calculation of the Armature Reactance of Synchronous Machines", Trans. AIEE, Vol. 47, 1928, pp. 493-513

APPENDIX A

EXPERIMENTAL INACCURACIES

Table A.1: Summary of Experimental Inaccuracies	
Source and Magnitude of Inaccuracy	Correction
<p>Inaccuracies in flux density measurement instrumentation (per manufacturer's spec.'s): probe: $\pm 1\%$, gaussmeter instrument: $\pm 0.25\%$, gaussmeter internal calibration: $\pm 0.3\%$, gaussmeter internal noise: $\pm 0.00316\%$, A/D converter quantization error: $\pm 0.0488\%$, A/D converter noise: $\pm 0.0488\%$ Total: $\pm 1.65\%$</p>	<p>No improvement possible without replacing equipment.</p>
<p>Inaccuracy due to temperature sensitivity of probe (machine iron and probe heat up due to I^2R losses in windings).</p>	<p>Temperature effects were corrected, when necessary, using the manufacturer's formula. High temperatures were avoided by permitting the motor to cool down for several minutes between data runs. This also prevented the winding insulation from being damaged.</p>
<p>Inaccuracies in probe position potentiometer readings: Visual gauge reading: $\pm 0.137\%$, A/D quantization error: $\pm 0.0488\%$, A/D noise error: $\pm 0.0488\%$, Total: $\pm 0.235\%$</p>	<p>Negligible.</p>
<p>Random spikes in gaussmeter analog voltage output. Suspected cause is elevator motor switching affecting the AC distribution in the building.</p>	<p>Immediately after each data run was finished, the data was displayed on the monitor. If visible spikes were found, the data run was performed again. Small spikes could be detected and/or averaged out using the averaging program from Chapter 3.</p>
<p>The Hall effect element averages the flux density distribution over a width of about 0.07". At a sample rate of 10.0 Hz, this corresponds to 4 sample points. The resolution of the measured distribution is reduced due to the inherent smoothing in the element. Sharp features such as the dips in flux density between the teeth are not as prominent (see reference [25]).</p>	<p>The Hall effect element width cannot be changed. Even though the field is smoothed over 4 data points, the 10.0 Hz sample rate is not reduced in order to keep as much resolution as possible, and provide enough points for numerical integration programs. The reduction in the prominence of the flux density dips between the teeth is not critical since these features are smoothed out by the averaging program of Chapter 3.</p>

Table A.1: Summary of Experimental Inaccuracies	
Source and Magnitude of Inaccuracy	Correction
The Hall effect element is manually adjusted so that its normal is parallel to the radial air gap field. This can introduce a small error.	This manual adjustment is made while the probe is above the centre of a tooth top, and while a field is present. The probe orientation is adjusted so that the flux density reading from the probe is maximized. It was observed that the flux density reading is not very sensitive to the probe orientation, as long as the element normal is within a few degrees of the field direction. The component of field density which is normal to the element is proportional to $\cos(\theta)$, where θ is the angle between the element normal and the flux density vector. $\cos(\theta)$ remains close to 1.0 as θ deviates from 0 degrees by small amounts, and therefore the normal component does not change significantly.
Probe position potentiometer voltage range drifts outside of allowable A/D range due to accidental adjustment of the calibration dial.	The full scale range of the probe position potentiometer was routinely checked and readjusted if necessary.
Resolution of B distribution data depends upon the sampling rate.	The optimum sample rate was 10.0 Hz, yielding 1600 points per file. If the sample rate was lower, then some resolution of the flux density dips between the teeth was lost. If the sample rate is too high, then the change in the quantized probe position potentiometer output voltage is less than 1 LSB, and probe position errors occur. The resulting flux density plot looks ragged since some position data points are less than their predecessors. This suggests that the probe is rotating backwards, which is not the case.
Visual gauge readings were accurate to about 0.5 of their smallest graduation.	No correction possible.
The current would drop in the windings over the course of a single data run, or over several data runs. This was caused by increasing winding resistance due to I^2R heating.	The current value was set immediately before and checked immediately after each data run. For very high current runs, the current was stopped for several minutes between runs to give the motor time to cool down, and avoid insulation failure.

Table A.1: Summary of Experimental Inaccuracies	
Source and Magnitude of Inaccuracy	Correction
Slippage in the worm/disk gear combination resulted in changes in rotor position when magnetic torque was exerted on the rotor. This caused the rotor angular position to deviate from the desired position by up to about 7 mechanical degrees.	When a data run was to be taken where both the field and armature windings were going to be excited, a torque wrench was used to manually "pre-torque" the shaft and eliminate any slippage in the gears. Then, when the magnetic torque was applied to the rotor, there was no slippage in the gears and the rotor stayed in the desired position.
The torque transducer and phase detector were calibrated by manually applying a known torque to the shaft using a dial torque wrench and a custom made extension arm. The estimated error in this procedure is about ± 3 N-m at all torque values.	The average of at least three trials for the same calibration point was used to offset human error.
Under very high magnetic torque conditions, the torque tube was overloaded, causing it to twist. This caused the torque measurement system to become non-linear, and permitted the rotor position to change by up to 1.5 mechanical degrees from the desired position.	Under these conditions, the torque wrench was used to apply a known torque in opposition to the magnetic torque. This permitted the torque measurement system to fall back into linear operation. The total magnetic torque was then taken as the sum of the linear measured torque from the measurement system, plus the known opposing torque applied by the torque wrench. This confirmed the non-linear operation of the torque measurement system, and gave reasonably accurate results. The change in rotor position caused by the twist in the torque tube had a negligible effect on the magnetic torque. Further, any rotor slippage that did exist soon disappeared once an opposing torque was applied using the torque wrench.

APPENDIX B

FLUX LINKAGE, TORQUE, AND VOLTAGE CALCULATION

This appendix derives the flux linkage, torque, and voltage formulas used in Chapters 5 and 6 of this document.

FLUX LINKAGE

Consider the cylindrical surface in the air gap of the machine which coincides with the outer dimensions of the machine rotor, as shown in Figure B.1.

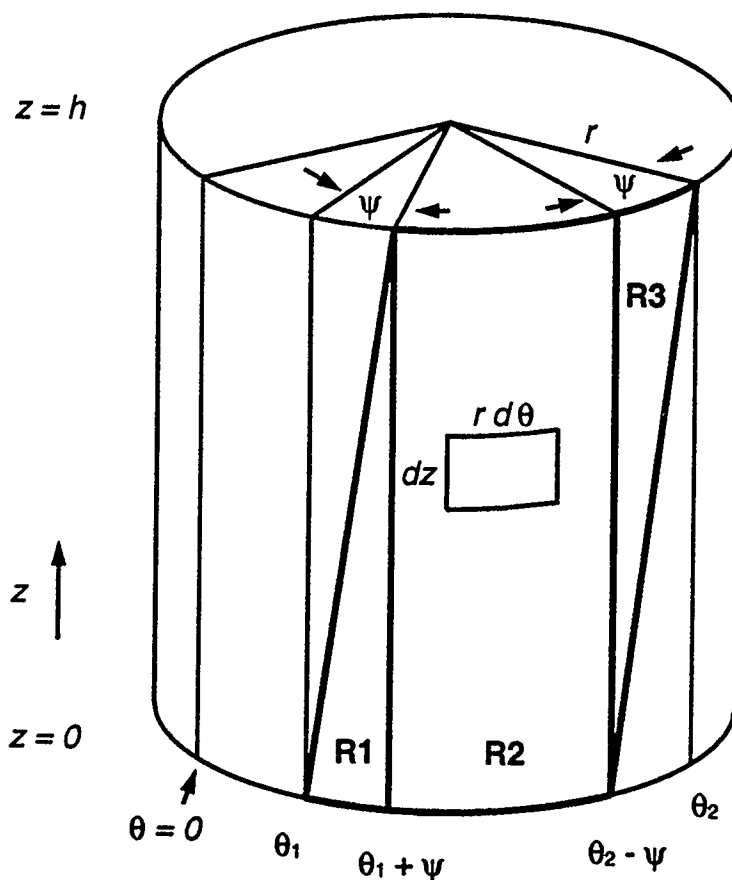


Figure B.1: Rotor Flux Integration Surface

Assuming all of the flux is normal to the sides of the rotor cylinder, the total flux, Φ , entering region R is

$$\Phi = \int_R B_r(\theta, z) r d\theta dz \quad (\text{B.1}),$$

where r is the outside radius of the rotor, θ is the angular position on the rotor surface, and z is the vertical position along the rotor. The flux linking a coil is equal to the net flux entering the rotor surface between the two lines defining the sides of that coil (see Note 1 later in this appendix). For a coil embedded in skewed slots, equation B.1 can be computed over three subregions, $R1$, $R2$, and $R3$, as shown in Figure B.1. The bottom left corner of the coil is defined by the angular position θ_1 , the top right corner by θ_2 , the skewing angle is ψ (in mechanical radians), and the total rotor height is h . Equation B.1 is expressed in terms of these variables as

$$\begin{aligned} \Phi = & \int_{\theta_1}^{(\theta_1 + \psi)} \int_0^{(\frac{h}{\psi}\theta - \frac{h}{\psi}\theta_1)} B_r(\theta, z) r dz d\theta + \\ & \int_{(\theta_1 + \psi)}^{(\theta_2 - \psi)} \int_0^h B_r(\theta, z) r dz d\theta + \\ & \int_{(\theta_2 - \psi)}^{\theta_2} \int_{(\frac{h}{\psi}\theta - \frac{h}{\psi}\theta_2 + h)}^h B_r(\theta, z) r dz d\theta \end{aligned} \quad (\text{B.2}).$$

If no skewing is present, the first and third terms of equation B.2 will disappear. In order to account for the variation of $B_r(\theta, z)$ in the z direction, equation B.2 can be approximated by a summation of short slices in the z direction, where $B_r(\theta, z)$ is assumed to remain constant with z over the height of each slice. Clearly, if a large number of slices (a large n) is used, then this approximation can be very accurate. For the i^{th} slice, equation B.2 becomes

$$\Phi_I = \int_{\theta_{1,l}}^{(\theta_{1,l} + \psi_l)} \int_{h_{1,l}}^{(\frac{\Delta h_l}{\psi_l} \theta - \frac{\Delta h_l}{\psi_l} \theta_{1,l})} B_r(\theta, z_l) r dz d\theta + \int_{(\theta_{1,l} + \psi_l)}^{(\theta_{2,l} - \psi_l)} \int_{h_{1,l}}^{h_{2,l}} B_r(\theta, z_l) r dz d\theta + \quad (B.3),$$

$$\int_{(\theta_{2,l} - \psi_l)}^{\theta_{2,l}} \int_{(\frac{\Delta h_l}{\psi_l} \theta - \frac{\Delta h_l}{\psi_l} \theta_{2,l} + \Delta h_l)}^{h_{2,l}} B_r(\theta, z_l) r dz d\theta$$

where

$$\Phi = \sum_{l=1}^n \Phi_l \quad (B.4),$$

$$\Delta h_l = h_{2,l} - h_{1,l} \quad (B.5),$$

$$\psi_l = \frac{\Delta h_l}{h} \psi \quad (B.6),$$

$$\theta_{1,l+1} = \theta_{1,l} + \psi_l \quad (B.7),$$

$$\theta_{2,l+1} = \theta_{2,l} + \psi_l \quad (B.8),$$

and

$$h_{1,l+1} = h_{2,l} \dots \quad (B.9).$$

At this point we can introduce rotational motion by performing a change of variables. Let θ become $\theta + \omega t$, and $\phi = \theta + \omega t$. ϕ is the angular position with respect to the stator, and, since in my machine the fundamental component of the air gap field is stationary with respect to the stator, ϕ is also the angular position against which the air gap field is measured or computed. ωt is the steady state time varying angular position of the rotor, and in the case of my machine, it is also the time varying angular position of the armature conductors with respect to the air gap field. These values are shown in Figure B.2. After changing the integration variable and limits we get

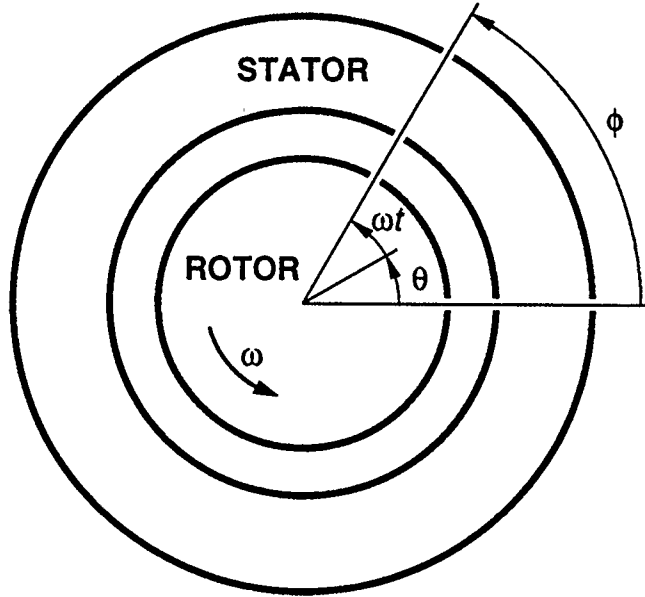


Figure B.2: Definition of Time Varying Angular Coordinates

$$\begin{aligned}
 \Phi_l(\omega t) = & \int_{(\theta_{1,l} + \omega t)}^{(\theta_{1,l} + \psi_l + \omega t)} \left[\frac{\Delta h_l}{\psi_l} (\phi - \omega t) - \frac{\Delta h_l}{\psi_l} \theta_{1,l} - h_{1,l} \right] B_r(\phi, z_l) r d\phi + \\
 & \int_{(\theta_{1,l} + \psi_l + \omega t)}^{(\theta_{2,l} - \psi_l + \omega t)} [h_{2,l} - h_{1,l}] B_r(\phi, z_l) r d\phi + \\
 & \int_{(\theta_{2,l} - \psi_l + \omega t)}^{(\theta_{2,l} + \omega t)} \left[h_{2,l} - \frac{\Delta h_l}{\psi_l} (\phi - \omega t) + \frac{\Delta h_l}{\psi_l} \theta_{2,l} - \Delta h_l \right] B_r(\phi, z_l) r d\phi
 \end{aligned} \tag{B.10}$$

As ϕ goes to zero (neglecting skewing), the first and third terms disappear and we have

$$\Phi_l(\omega t) = \int_{(\theta_1 + \omega t)}^{(\theta_2 + \omega t)} [h_{2,l} - h_{1,l}] B_r(\phi, z_l) r d\phi \tag{B.11}$$

In my research all of the slices are the same thickness, therefore

$$[h_{2,i} - h_{1,i}] = \frac{h}{n}, \text{ for } i = 1 \rightarrow n \quad (\text{B.12}),$$

where h is the total rotor height (length), and n is the number of contour intervals and is equal to 10 in my research. Using equations B.4, B.11, and B.12, the total time varying flux linkage in the coil can be expressed as

$$\begin{aligned} \Phi(\omega t) &= rh \int_{(\theta_1 + \omega t)}^{(\theta_2 + \omega t)} \left[\frac{1}{n} \sum_{i=1}^n B_r(\phi, z_i) \right] d\phi \\ &= rh \int_{(\theta_1 + \omega t)}^{(\theta_2 + \omega t)} [B_r(\phi)]_{\text{avg}} d\phi \end{aligned} \quad (\text{B.13}).$$

The approximations made in the process leading to equation B.13 were to neglect the skewing of the coil sides, and use a finite number of averages (these averages are taken vertically along the rotor height (length)).

As the harmonic order of the flux density distribution increases, the error in the computed flux linkages due to each harmonic increases if the effect of skewing is neglected. This error leads to the computed flux linkage due to each harmonic being higher than the actual value (see the worked example at the end of this appendix). In turn, the computed voltage and torque due to the higher harmonics is higher than the actual value. However, as shown in Chapter 3, the magnitudes of the higher harmonics of flux density also decrease as their orders increase (this is true for both averaged and unaveraged data). Since the error caused by neglecting skewing is greatest for the highest order harmonics, whose magnitudes are also the smallest, the resulting error in torque and voltage is minimized.

Results from the averaging process also point out the insignificance of the higher harmonics, as shown in Chapter 3. Compared to unaveraged data (data for any given contour), averaging dramatically reduces the magnitude (and therefore the importance) of the higher harmonics. In turn, the small higher harmonics will have little effect upon induced torque or voltage. Therefore, by averaging, we offset the error we have introduced by neglecting skewing (skewing and averaging amount to the same result as far as voltage and torque are concerned). Due to distributed, partial pitch windings, the effects of harmonics are reduced even more (as far as torque and voltage are concerned).

See Chapter 6.

A full study of the error introduced by neglecting skewing (computing the flux linkage using a vertically averaged flux density distribution (equation B.13) instead of the more exact sum of slices method (equations B.4 and B.10)) would determine the error incurred by using equation B.13. This would best be done by comparing the induced voltages and torques from the two methods. However, this would add significantly to the scope of my research, with little additional insight, so I will not pursue it further. Classic references such as Moullin [9] and Langsdorf [27] are quite satisfied with using the averaged flux distribution approach. This is because of the substantial smoothing in the voltage waveforms caused by skewing of the rotor teeth. This skewing substantially reduces the net effect of the higher order flux density harmonics (which are present in any given contour) upon the voltage.

Since the flux density distribution model will be developed from $[B_r(\phi)]_{\text{avg}}$ measurements, and will be used to predict $[B_r(\phi)]_{\text{avg}}$ as well, the actual skewed rotor should be (conceptually) replaced with an equivalent rotor of non-skewed construction. All coil positions should be those which would give an mmf distribution which is appropriate for the measured (or computed) $[B_r(\phi)]_{\text{avg}}$ and reluctance distributions (symmetry can be used to determine the exact location of the equivalent coils). Averaged (and therefore smooth) mmf distributions from these equivalent coil positions should be used rather than the stepped mmf distribution found at any particular contour along the rotor. The equivalent length of a coil side is the height (or length) of the rotor, h . The equivalent radius, r , is the air gap radius where $[B_r(\phi)]_{\text{avg}}$ is measured or computed. This is approximately the outside radius of the rotor.

INDUCED TORQUE

The torque induced on a coil can be found from equation 2.8. The coil torque, $T_{\text{coil}}(\omega t)$ is a position (or time) varying quantity as defined below:

$$T_{\text{coil}}(\omega t) = Ni(t) \frac{d\Phi(\omega t)}{d\phi} \quad (\text{B.14}),$$

where $i(t)$ is the current flowing in each conductor of the coil, N is the number of conductors in the coil, and $\Phi(\omega t)$ is the position or time varying flux linking the coil, as computed using equation B.13. Substituting equation B.13 into B.14 and applying the Fundamental Theorem of Integral Calculus (Swokowski [28, p.252], see Note 2) we get

$$T_{\text{coil}}(\omega t) = N r h i(t) ([B_r(\theta_2 + \omega t)]_{\text{avg}} - [B_r(\theta_1 + \omega t)]_{\text{avg}}) \quad (\text{B.15}).$$

A physical interpretation of equation B.15 is that the net change in flux in the coil consists of the flux lines cut by both the leading and the trailing sides of the coil. This is the origin of the "cutting of flux" equations for voltage ($e = B\dot{v}$) and torque ($T = B\dot{v}i$) used frequently in the literature. These equations are valid, when properly interpreted for a coil, even though the sides of the coil are embedded in slots and only see a very weak field. They are valid because they find their origin in the flux linkage equations for torque (equation 2.8) and voltage (equation 2.9) (Fitzgerald [7, p.152], Moullin [9, pp. 39, 302-311]). Equation B.15 (and its counterpart for voltage in the next section) allows us to compute the torque (and voltage) without computing the flux linkage. Therefore, no integrations need to be performed. The key information we need are the constants and a knowledge of the flux density distribution. Further, since none of the constants in equation B.15 change with the saturation conditions in the machine, the only way in which saturation will affect equation B.15 is through changes in the flux density distribution. By properly determining the flux density distribution under whatever operating conditions are present (even saturation) and feeding that density distribution into the portion of the computer model which computes the induced torque and voltage, we can develop the torque and voltage computation sections of the program independently by considering only the basic coil distributions in the rotor (armature), phase current variation with time (for torque computation), and rotating speed (for voltage computation). The factors affecting the flux distribution (field mmf distribution, armature reaction mmf distribution, and the reluctance distribution) are used to determine the flux density distribution at any point in time. Unlike methods such as inductance matrices or circuit models, this approach provides us with a very good picture of the actual physical mechanisms producing the electrical (terminal) and mechanical (shaft) behaviour of the machine.

Equation B.15 can be used to compute the total rotor torque by simply summing the individual contributions from each coil as follows

$$T_{\text{rotor}}(\omega t) = \sum_{k=1}^q i_k(t) N r h \sum_{j=1}^m [[B_r(\theta_{(2,j,k)} + \omega t)]_{\text{avg}} - [B_r(\theta_{(1,j,k)} + \omega t)]_{\text{avg}}] \quad (\text{B.16}),$$

where m is the number of coils in a phase winding, q is the number of phases in the machine, ωt is the displaced angular position of the rotor relative to the stator reference at time $t = 0$, $\theta_{(1,j,k)}$ is the angular position of side 1 of coil j of phase k at time $t = 0$ (the rotor angular reference ($\theta = 0$) is in line with the stator angular reference ($\phi = 0$) at time $t = 0$), and $\theta_{(2,j,k)}$ is the angular position of side 2 of the same coil.

By utilizing equation B.16 in the computer model, the distribution and pitch of the coils is automatically considered in determining torque and voltage. In the classical theory, breadth factors (accounting for the coils in the windings being distributed over some angular range in the armature slots) and pitch factors (accounting for fractional pitch windings) are used in the voltage and torque equations.

Under balanced steady state conditions, the sinusoidal, phase displaced currents, combine with the angular displacement and constant rotating speed of the phase windings to produce a constant torque (neglecting current time harmonics and winding space harmonics).

INDUCED VOLTAGE

Equation 2.9 can be used to determine the induced voltage in the phases by modifying it as follows:

$$e = N \frac{d\Phi}{dt} = N \frac{d\Phi}{d\phi} \frac{d\phi}{dt} = N \frac{d\Phi}{d\phi} \omega$$

where $d\phi/dt$ is the time rate of change of the rotor angular position with respect to the stator reference (to be used for transient analysis), and ω is the angular velocity of the rotor under steady state conditions. Proceeding similarly to the torque computation, the induced phase voltage for steady state conditions may be computed using

$$e_k(\omega t) = N r h \omega \sum_{j=1}^m [[B_r(\theta_{(2,j,k)} + \omega t)]_{\text{avg}} - [B_r(\theta_{(2,j,k)} + \omega t)]_{\text{avg}}], \text{ for } k = 1 \rightarrow q \quad (\text{B.17}).$$

GENERAL TORQUE AND VOLTAGE COMPUTATION ALGORITHM

The steps involved in computing the induced rotor torque and winding voltages can be summarized as follows:

- i) N (the number of conductors per coil), r (the rotor outside radius), h (the rotor or equivalent coil side length), P (the number of poles), and ω (the steady state angular velocity) are stored in memory. $\theta_{(1,j,k)}$ and $\theta_{(2,j,k)}$ are determined from the rotor constructional features, and are expressed with respect to the rotor angular reference ($\theta = 0$). These are stored in the first column of a two dimensional array. The direction of positive current flow can be indicated by a "+1" or "-1" in the second column. One side of a coil will have one sense, the other side will have the opposite sense. The phase rotation (a,b,c), the locations of the phase windings around the rotor (armature), and the positive mmf axis direction for each phase winding are known. Therefore the direction of rotor rotation and the direction of current flow in each coil side is known for some instant in time (say, the point in time when phase a current peaks). The torque sense on the coil can be found from $\mathbf{F} = i\mathbf{l} \times \mathbf{B}$, which tells us the force direction on the coil side. The torque sense will oppose rotation for generator action, and support rotation for motor action. Since power balance must exist in the coil, the product of instantaneous torque and instantaneous angular velocity must numerically equal the product of instantaneous induced voltage and instantaneous current (for all three phases). By defining the product of positive rotational direction and positive torque as producing positive mechanical power or motoring action, then since the current sense is also known in the coil, the induced voltage sense can be determined. When the machine is motoring the power flow is into the machine, therefore the instantaneous line voltage in phase a must be greater than the instantaneous phase a induced voltage in order to cause instantaneous phase

current to flow into the machine (neglecting leakage reactance). Therefore the senses of all of the machine variables are defined, and the proper sense of the induced winding voltage can be selected to satisfy air gap power balance and line terminal conventions by simply putting a positive or negative sign in front of equation B.17 (the induced voltage formula).

- ii) Read in the field current and rms phase current (for the fundamental only). If desired, harmonics can be introduced as well.
- iii) At time $t = 0$, the $\theta = 0$ reference for the rotor is in line with the $\phi = 0$ reference for the stator. The equations can be generalized if this is not the case by adding the angular difference between them at $t = 0$ to each argument in equations B.16 or B.17.
- iv) Compute the rotor position with respect to the stator for each time t . For steady state conditions this value is ωt (assuming the conditions of step iii are met).
- v) Compute the instantaneous phase currents at time t , with or without harmonics.
- vi) Using the rotor position, phase currents, and the field current, compute the average air gap flux density distribution, $[B_r(\phi)]_{\text{avg}}$, using the model.
- vii) Compute $T_{\text{rotor}}(\omega t)$ using equation B.16 and $e_k(\omega t)$ using equation B.17. In my research programs, I only computed $[B_r(\phi)]_{\text{avg}}$ for the point in time corresponding to the static measurement conditions in my experimental machine. $e_k(\omega t)$ was computed assuming the air gap field remained unchanged throughout the complete supply cycle. $e_k(\omega t)$ only needed to be calculated for phase a due to phase symmetry. Some error is introduced in this approach, since the space harmonics of the armature mmf wave are neglected, but as shown in Chapter 3, this error is very small since the harmonic distortion of the armature mmf wave over the course of a cycle is small relative to the armature mmf wave, and the armature mmf wave itself is quite small next to the dominating field mmf wave (under normal operating conditions).
- viii) Store the rotor torque and induced winding voltages as functions of t in an array.
- ix) Increment time, $t = t + \Delta t$ until a full AC power supply cycle is completed, or until adequate torque and voltage data has been computed.
- x) Return to step iv if more torque and voltage calculations are necessary, or else go to step xi.

- xi) Write rotor torque and induced phase voltages to output files.
- xii) End.

Under transient conditions, the field current, the phase currents, and ω are all time varying. Under steady state conditions, they can be treated as constants or analytically expressible quantities. However, in order to handle them under transient conditions, they need to be computed at each time step, using some iterative state variable procedure such as that used with the finite element solution method given in Krefta/Wasynczuk [6]. The torque will be affected by the rotor inertia, bearing friction, and windage. Eddy currents and hysteresis loss should also be included if possible. The mmf waves due to the induced currents in the damper windings will need to be added. Extension of this algorithm to the transient case will require a great deal more time and testing, but should be pursued as future work.

NOTE 1

This note shows that the flux linking a coil is equal to the net flux entering an angular portion of the cylindrical rotor surface bounded by the ends of the rotor and the intersection of the rotor cylindrical surface with the coil sides.

The flux lines entering the ends of the rotor are neglected here, because measurements show that they become very small relative to those normal to the cylindrical rotor surface. In Figure 2.4, the radial air gap flux density drops significantly within 10% of the rotor length at either end of the rotor. Also, the coil geometry for the end turns is very complex. Flux linkage in the end turns will be treated as part of the leakage flux in Appendix C.

Gauss's Law for a magnetic field,

$$\oint \mathbf{B} \cdot d\mathbf{S} = 0 \quad (\text{B.18})$$

(see Hayt [12, p.268]), states that all flux lines entering a closed surface must leave that closed surface. Consider the case of a coil of arbitrary pitch mounted in slots on a rotor, and whose sides are shown in plan view as points a and b in Figure B.3. Gauss's Law tells us that the net flux linking the coil (through surface 2) equals the net flux entering the rotor surface between points a and b (through surface 1) as shown below

$$\oint \mathbf{B} \cdot d\mathbf{S} = 0 = \int_{\text{surface 1}} \mathbf{B} \cdot d\mathbf{S} + \int_{\text{surface 2}} \mathbf{B} \cdot d\mathbf{S} \quad (\text{B.19}),$$

where surface 1 is over the rotor surface between points a and b (the locations of the coil sides) in Figure B.3, and surface 2 is the plane enclosed by the coil.

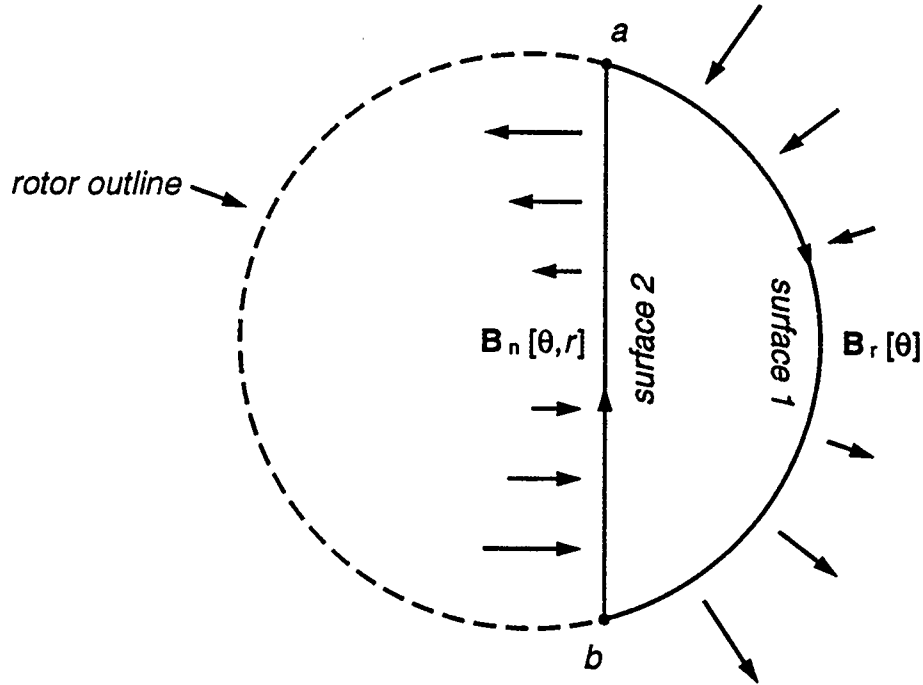


Figure B.3: Cross-Section of Rotor Surfaces Showing Integration Regions

Since the normal flux density distribution is known everywhere over the rotor's cylindrical surface (either through measurement or by computation), and the normal component is the only component (as proven in Chapter 2), the flux linking the coil through surface 2 can be computed by integrating the radial flux density over surface 1. By defining the integral over surface 1 in terms of cylindrical coordinates, and since we have defined the integral over surface 2 to be the net flux linking the coil, equation B.19 may be rearranged to give

$$\Phi_{\text{linking coil}} = \int_{\text{surface 2}} \mathbf{B}_n(\theta, r) \cdot d\mathbf{S} = \int_{\theta_a}^{\theta_b} \int_0^h B_r(\theta) r d\theta dz \quad (\text{B.20}),$$

where h is the height or length of the rotor, θ_a is the angular position of point a , θ_b is the angular position of point b , r is the rotor radius, $B_r(\theta)$ is the flux density distribution normal to the rotor surface, and $B_n(\theta, r)$ is the flux density distribution normal to the plane

enclosed by the coil sides (variation with z is neglected for simplicity). The difficult job of defining the limits of the first integral and $B_n(\theta, r)$ is avoided by using the second integral. It is important to note that $B_r(\theta)$ is defined as positive for flux entering surface 1, and $B_n(\theta, r)$ is positive for flux exiting surface 2 (in Figure B.3, this is the flux passing from right to left through surface 2).

NOTE 2

This note outlines the steps required to simplify the coil torque equation, B.14, to give equation B.15. Given equation B.14, the derivative of the coil flux linkage can be expressed as

$$\frac{d}{d\phi} (rh \int_{(\theta_1 + \omega t)}^{(\theta_2 + \omega t)} [B_r(\phi)]_{\text{avg}} d\phi) \quad (\text{B.21}),$$

by substituting B.13 into B.14. Ignoring the constants r and h (because they can simply be moved out of the derivative), B.21 can be expressed as

$$\frac{d}{d\phi} \left(\left(\int [B_r(\phi)]_{\text{avg}} d\phi \right) \Big|_{(\theta_2 + \omega t)} - \left(\int [B_r(\phi)]_{\text{avg}} d\phi \right) \Big|_{(\theta_1 + \omega t)} \right) \quad (\text{B.22}).$$

According to the Fundamental Theorem of Integral Calculus (Swokowski [28, p. 252]), the derivative of the integral of a function evaluated at a point is simply the value of that function at that point, therefore B.22 can be expressed as

$$[B_r(\theta_2 + \omega t)]_{\text{avg}} - [B_r(\theta_1 + \omega t)]_{\text{avg}} \quad (\text{B.23}).$$

This result agrees with Moullin [9, p. 9].

WORKED EXAMPLE

Consider using equation B.10, for a thin slice of the rotor length, to determine the total flux linked by a skewed coil. Coil skewing is considered in this example, but the variation of B_r with z is neglected (otherwise, an integration would have to be performed for every slice). Assume the flux distribution can be expressed in terms of stator angular position as $B_r(\phi) = B_{\text{max}} \cos(\phi)$. Consider the i^{th} slice as covering the entire rotor length, therefore $i = 1$ and $n = 1$. In my machine, $\psi = 7.5^\circ$ mechanical or $\pi/24$ mechanical radians. $\Delta h_1 = h$ (the rotor length) since $h_{1,1} = 0$ and $h_{2,1} = h$. The coil is full pitch, so $\theta_{1,1} = 0$ and $\theta_{2,1} = \pi$.

Substituting these values into equation B.10 we get

$$\begin{aligned} \Phi = r B_{\max} [& \left(\int_{\omega t}^{(\psi + \omega t)} \cos(\phi) \left[\frac{h}{\psi} (\phi - \omega t) \right] d\phi \right) + \\ & \left(\int_{(\psi + \omega t)}^{(\pi - \psi + \omega t)} \cos(\phi) [h] d\phi \right) + \\ & \left. \left(\int_{(\pi - \psi + \omega t)}^{(\pi + \omega t)} \cos(\phi) \left[\frac{h}{\psi} (\pi - \phi + \omega t) \right] d\phi \right) \right] \end{aligned} \quad (\text{B.24}).$$

When this integral is evaluated, the result is

$$\Phi(\omega t) = 2 r B_{\max} h \frac{\sin(\psi)}{\psi} \sin(\omega t) \quad (\text{B.25}).$$

In the limit, as ψ approaches 0, $\sin(\psi)/\psi$ approaches 1, the effect of skewing disappears, and equation B.25 reduces to

$$\Phi(\omega t) = 2 r B_{\max} h \sin(\omega t) \quad (\text{B.26}).$$

Using equation B.25, the term $\sin(\psi)/\psi$ is carried into both the induced torque and induced voltage equations as well:

$$T_{\text{coil}}(\omega t) = N i(t) 2 r B_{\max} h \frac{\sin(\psi)}{\psi} \cos(\omega t) \quad (\text{B.27}),$$

and

$$e_{\text{coil}}(\omega t) = N \omega 2 r B_{\max} h \frac{\sin(\psi)}{\psi} \cos(\omega t) \quad (\text{B.28}).$$

When ψ approaches 0, B.27 and B.28 reduce to classical textbook answers (see [7, p. 152]). Langsdorf [27, p. 194] describes the term $\sin(\psi)/\psi$ as a breadth factor which is used to account for skewing. He has determined this breadth factor for various harmonics of air gap flux density. For the n^{th} harmonic, $\sin(\psi)/\psi$ becomes $\sin(n\psi)/(n\psi)$. ψ is in mechanical radians. This breadth factor causes the harmonics of flux density to contribute less to the voltage or torque as their order increases. In essence, this results in a

substantial reduction of the tooth ripple in the coil voltage or torque waveform, since the higher harmonics of flux cause this ripple. This is desirable in order to reduce interference with telephone circuits. This smoothing helps justify the use of averaged flux density runs instead of developing a reluctance model for each contour. This effect is summarized below in Table B.1 for $\psi = 7.5^\circ$ mechanical.

Table B.1: Effect of Skewing on Flux Linkage	
Harmonic Order, n	$\sin(n\psi)/(n\psi)$
1	0.9972
3	0.9745
5	0.9301
7	0.8658
9	0.7842
11	0.6886
13	0.5826
15	0.4705
17	0.3565
19	0.2448
21	0.1392

Just how significant are the flux density distribution harmonics? In Table B.2, the harmonic content of the flux density distributions for three different cases are compared. All three cases are with the field windings excited with 0.5 p.u. (1 A). Case A is unaveraged (raw) data for a single contour at about the middle of the rotor (depth = 18.8 cm). Case B is averaged over 10 contours, with the first and last contours affected by end effects. Case C is averaged over 8 contours, with the first and last contours neglected. The reason why Case C is introduced is simply to show how the end effects

affect the averaged flux density distribution. The data for cases A and B are shown in Figure 3.1 in Chapter 3. When averaging is done, the effects of teeth and measurement noise are largely smoothed out.

From the Fourier analysis in Table B.2 we note the following features:

- i) The even harmonics are negligible (noise levels only).
- ii) The triplen is negligible.
- iii) End effects cause a reduction in the fundamental by about 6%. We are trying to represent a three dimensional field with a two dimensional averaged field. This work would be difficult to do even with finite element analysis. Experimental proof, through torque measurements, will serve as the best support for using averaging. By incorporating the end effects into the average, I expect we are getting a much closer estimate of the flux linkages than by neglecting them.
- iv) The main harmonics are the 5th and 7th. Anything past that is 1% or less of the fundamental.
- v) The higher harmonics remain negligible for all cases. There is no visible trend toward their reduction as averaging is introduced. Under highly saturated conditions (not shown here) some of the harmonics increase due to the effects of damper bar slots and pole saturation. The reason why the higher harmonics are so small is likely due to the smoothing done by the Hall effect crystal. Any detailed study of the effects of skewing and averaging would require finite element analysis. However, based on the results of Table B.1, their effects upon torque and voltage should be negligible.

Table B.2: Comparison of Measured Flux Density Harmonics

ORDER <i>n</i>	FLUX DENSITY MAGNITUDE, B_n (Wb/m ²)			NORMALIZED MAGNITUDE, B_n / B_1		
	CASE A	CASE B	CASE C	CASE A	CASE B	CASE C
1	0.3395	0.31962	0.3411	1.0	1.0	1.0
3	0.007617	0.008553	0.007904	0.0224	0.02675	0.02317
5	0.03602	0.03382	0.03646	0.1061	0.10579	0.1069
7	0.01236	0.011562	0.0124	0.0364	0.03617	0.0364
9	0.000458	0.000192	0.00027	0.00135	0.0006	0.000792
11	0.000146	0.000315	0.000175	0.00043	0.000985	0.000512
13	0.001583	0.001092	0.001422	0.00466	0.00342	0.00417
15	0.003219	0.003648	0.003595	0.009482	0.01141	0.01054
17	0.001624	0.000868	0.001153	0.004784	0.00272	0.00338
19	0.001353	0.001502	0.001566	0.003985	0.004698	0.00459
21	0.001261	0.000776	0.000914	0.003714	0.00243	0.00268

APPENDIX C

APPLICATION OF D-Q AXIS THEORY TO THE COMPUTER MODEL

CONVENTIONS AND PHYSICAL BEHAVIOUR IN STEADY STATE OPERATION

What are the conditions of the magnetic fields within a salient pole machine under different steady state conditions? For simplicity, consider phase *a* of the two pole machine shown in Figure C.1. The MMF axis of the field windings is indicated by the space vector F in Figure C.1a. F is fixed in space (centred on the field poles) and its magnitude is proportional to the field current. To avoid congestion, the distributed, partial pitch phase *a* winding (which sits in slots in the rotor) is represented by a concentrated, single turn, full pitch coil side on the outside of the rotor. The ends of the coil sides that are nearest to the reader are shown in the plane of the page. The ends of the coil sides that are farthest from the reader are not visible, but are located directly below the visible ends (below the plane of the page). The far ends of the diametrically opposed coil sides are connected via the end turns. For a generator, the near ends may be connected to a load, in which case the complex impedance of the load will determine the relationship between the terminal voltage and current. For a motor, the near ends are normally connected to a fixed bus voltage.

The polarity marks for current are shown inside the coil side cross-section. An "x" represents current going into the page and a dot represents current coming out of the page. For induced winding voltage a "+" polarity mark beside the coil side represents a higher voltage potential than a "-" which appears on the opposite coil side. When a "+" voltage polarity occurs beside a coil side with an "x" current polarity then, for that instant of time, the induced winding voltage opposes the current flow. This is the case (ignoring inductive effects) for the majority of a motoring cycle. If a "+" voltage polarity and a dot current polarity occur together then the induced winding voltage aids the current flow. This is the case for the majority of a generating cycle.

Induced voltage can exist when induced current does not. This is the open circuit condition for a generator.

The positive MMF axis of the phase *a* armature winding is indicated by the space

vector **A** in Figure C.1a. Its magnitude is proportional to the instantaneous phase *a* current. Its direction is defined opposite to the right hand rule in order to be consistent with my convention that the positive MMF axis produces flux that passes from the stator into the rotor. The stator (field winding) positive MMF direction is defined by the right hand rule, as normal.

Under balanced, steady state conditions (neglecting time and space harmonics) the MMF's of the three phases superimpose to give a constant magnitude resultant MMF which is fixed in space and whose axis is always in the direction indicated by **A**. See references [7, pp. 146-150] and [27, pp. 199-218]. For the point in time when the instantaneous current in phase *a* is a maximum, the phase *a* MMF axis coincides with **A**, and the axis of the sum of the phase *b* and *c* MMF's also coincides with **A**. The combined phase *a*, *b*, and *c* MMF waves are greater than for any one phase.

The angular position of **A** is determined by the internal power factor angle ψ . ψ is zero when **A** is on the +Q axis as shown in Figure C.1a. The reason why this convention is used will become apparent when we examine the two reaction phasor diagram (Figure C.1b).

The polarity of the induced voltage in a coil side may be determined from $\mathbf{u} \times \mathbf{B}$ where **u** is the velocity of the coil side and **B** is the flux density at the position of the coil (it is assumed constant over the entire length of the coil). See Hayt [12, pp. 350-352]. If the coil side is assumed to be moving sideways through the field (which, neglecting slot skewing, is always the case in a machine) then the resultant of $\mathbf{u} \times \mathbf{B}$ points towards the end of the coil side which is at the highest potential. For the conditions shown in Figure C.1a, the voltage in the coil side beneath the South pole will be higher at the end near the reader than at its far end. For the coil side beneath the North pole, the voltage at the near end is lower than at the far end. The total voltage in the coil is the sum of these two coil side voltages, and the contribution from the end turns is negligible. The coil voltage opposes the current flowing through it, so the machine is acting as a motor.

The torque sense is always such that **A** and **F** will try to align so as to minimize the reluctance (or maximize the stored energy) of the magnetic field system. In Figure C.1a, the torque direction is clockwise, which aids rotor rotation (motoring).

The induced voltage phasor in the phase *a* winding is E_a .

When there is no load, **A** is zero, and E_a equals E_f where E_f is the no load induced

voltage phasor. When a mechanical load is applied to the motor shaft (or a current is drawn from the generator terminals) the \mathbf{A} space vector is established (after a brief transient period) at an angle of ψ . The combination of \mathbf{A} and \mathbf{F} will produce a net air gap field (the axis of which is represented by the space vector \mathbf{B}_{net}) which satisfies the torque requirements of the shaft load (plus any friction, eddy current, and hysteresis losses).

\mathbf{B}_{net} will be situated somewhere between \mathbf{F} and \mathbf{A} . For a linear, cylindrical geometry machine \mathbf{F} and \mathbf{A} can be added vectorially to determine the direction of \mathbf{B}_{net} . For a salient pole machine, even under linear conditions, this cannot be done due to the widely varying air gap dimensions. However, the flux density model of Chapter 4 can provide us with this information, even under heavily saturated conditions. Once the flux density distribution is known then the direction of \mathbf{B}_{net} can also be found since it is the angular position of the peak of the fundamental of the net flux density distribution.

Fortunately, we do not have to go to all the trouble of determining the angular position of \mathbf{B}_{net} every time we wish to analyze the steady state operation of the machine. This is because the magnitude and phase angle of \mathbf{E}_a (which is critical for determining the electrical behaviour of the machine under load) can be determined directly from the net flux density distribution (see Appendix B and Chapter 6). Since the relation between the net flux density distribution and the induced winding voltage waveform under load (\mathbf{E}_a being the fundamental of this waveform) is linear (as defined by equation B.17), the magnitude of \mathbf{E}_a will be directly proportional to the fundamental of the net flux density distribution. Since the phase a winding is symmetric, the phase difference between \mathbf{E}_a and \mathbf{E}_f will equal (for a two pole machine) the space angular displacement of \mathbf{B}_{net} from \mathbf{F} .

In Figure C.1b, the fundamental phasors \mathbf{E}_f and \mathbf{E}_a are shown. The angle of displacement between them is δ , the internal torque or power angle. This angle is also shown in Figure C.1a, between \mathbf{F} and \mathbf{B}_{net} . For a loaded condition \mathbf{E}_f does not physically exist in the machine, but Blondel's Two Reaction method uses it as a reference for calculating \mathbf{E}_a .

For motoring conditions, \mathbf{E}_a opposes the constant terminal voltage, \mathbf{V}_a , thus limiting the phase current, \mathbf{I}_a , in the winding. The physical quantities which determine the current flow in the phase a winding are the winding resistance, R_a , and the winding leakage reactance, X_a . For my machine R_a is 0.542 Ω . This was determined by direct measurement, with temperature correction to 60°C. X_a was estimated to be 1.908 Ω , and is the sum of the

slot leakage reactance (computed using a formula in Langsdorf [27, pp. 45, 301-303]) and the end turn leakage (computed using a formula in Alger [32]). It is not critical that I use very accurate values in my simulations since I cannot compare the simulated data with measured data. However, I included them to demonstrate how to incorporate them into the simulations.

V_a , I_a , and E_a are related by

$$V_a = E_a + I_a(R_a + jX_a) \quad (C.1).$$

This phasor relationship is shown in the phasor diagram (Figure C.1b), and in the circuit diagram (Figure C.1c). Equation C.1 is the basis for my preprocessing program.

The external power factor angle, ϕ , is the phase angle between I_a and V_a , and can be measured at the machine terminals. It is an input to the preprocessing program, and is often constrained by the type of steady state operating curve which you are computing (for example, a constant power factor curve).

α , the phase angle between E_a and I_a , is output directly by the computer program. When *rotorg* (or ψ) is chosen, the position of **A** is set. Since the waveform of I_a peaks when the MMF axis of phase *a* is on **A**, all points on the time varying I_a waveform have a direct correspondence to the angular position of the rotor, and the positions of all of the coil sides throughout the AC cycle are known. Regardless of the magnitudes of the field or armature currents, for a fixed *rotorg* (or ψ) the phase of I_a (relative to rotor position) will not change. This makes I_a a good reference phasor. However, for a fixed *rotorg* (or ψ) the magnitude and phase of E_a changes depending upon the net flux density distribution. E_a can be computed throughout the AC cycle because the coil side positions are known throughout the AC cycle. Since these coil side positions also have a direct correspondence to the rotor position and to the phase of I_a , the phase shift of E_a from I_a , α , can be computed. In order to construct a meaningful phasor diagram for steady state conditions, such as that shown in Figure C.1b, *rotorg* (or ψ) must be held constant. This is not a problem since a fixed position for **A** is one of the fundamental assumptions in steady state analysis.

The internal torque or power angle, δ , is the phase angle between E_a and E_f . This is also the torque angle used in equation 5.4. δ for any steady state condition can be found from the computer model using the following steps:

- i) Find the desired magnitude and phase (α) of \mathbf{E}_a for this steady state operating condition using the preprocessing program (this computation is subject to the constraints of the type of operating curve you are trying to determine). \mathbf{V}_a , \mathbf{I}_a , and ϕ must be fixed in order to determine the desired \mathbf{E}_a . With the magnitude of \mathbf{I}_a fixed, the remaining free inputs to the computer model are the magnitude of the field current (I_f) and the position of \mathbf{A} (*rotorg* or ψ).
- ii) I_f and *rotorg* (or ψ) are selected on a trial and error basis in order to obtain a computer model output \mathbf{E}_a with the same magnitude and phase as the desired \mathbf{E}_a .
- iii) By letting the magnitude of \mathbf{I}_a go to zero and holding *rotorg* (or ψ) and I_f constant, \mathbf{E}_f can be found from the computer model. Under no load conditions, \mathbf{E}_a equals \mathbf{E}_f .

The assumed value of ψ can also be checked under no load conditions since α (output by the program) should equal ψ under no load. ψ , the internal power factor angle, is the angular position of \mathbf{A} and the phase angle between \mathbf{I}_a and \mathbf{E}_f . It is affected by the external power factor angle, ϕ , the torque angle, δ , and the $R_a + jX_a$ drop.

For motoring conditions, when ψ is positive (as shown in Figure C.1b) \mathbf{I}_a lags \mathbf{E}_f and \mathbf{A} helps the field pole MMF. When ψ is negative \mathbf{I}_a leads \mathbf{E}_f and \mathbf{A} opposes the field pole MMF. When ψ is zero, \mathbf{A} is on the +Q axis. See Langsdorf [27, pp. 194-199, 419-426].

\mathbf{A} , when ψ is zero, is fully directed into producing flux on the +Q axis. In this case, $\mathbf{I}_a = \mathbf{I}_q$, where \mathbf{I}_q is the quadrature axis magnetizing current. \mathbf{I}_q is defined to be in phase with \mathbf{E}_f for the following reason: if \mathbf{I}_q peaks when \mathbf{E}_f peaks, then, when they peak, the centre of the phase *a* winding will be under the centre of the field pole. The phase *a* MMF axis (in quadrature with the centre of the phase *a* winding) will be centred on the +Q axis. The relation between the magnitudes of \mathbf{I}_q and \mathbf{I}_a is $I_q = I_a \cos(\psi)$.

When ψ is 90° electrical, \mathbf{A} is in line with \mathbf{F} , and $\mathbf{I}_q = 0$. In this case $\mathbf{I}_a = \mathbf{I}_d$, where \mathbf{I}_d is the direct axis magnetizing current. \mathbf{I}_d is defined to be in phase quadrature with \mathbf{E}_f , and \mathbf{I}_d peaks when \mathbf{E}_f is zero. At this point in time, the centre of the phase *a* winding is located in quadrature to the field poles, and the phase *a* MMF is centred on the +D axis. The relation between the magnitudes of \mathbf{I}_d and \mathbf{I}_a is $I_d = I_a \sin(\psi)$.

The phasor sum of \mathbf{I}_d and \mathbf{I}_q is \mathbf{I}_a . \mathbf{I}_d and \mathbf{I}_q are shown in Figure C.1b.

When ψ is -90° electrical, \mathbf{A} opposes \mathbf{F} , and this corresponds to a purely leading internal power factor condition for a motor. When ψ is 90° electrical, \mathbf{A} adds to \mathbf{F} , and this

corresponds to a purely lagging internal power factor condition for a motor.

By the way in which I_d and I_q have been defined, I_d always represents the component of load current that produces direct axis magnetization. I_q always produces quadrature axis magnetization.

In two reaction theory, linear conditions are assumed. The quadrature (X_{rq}) and direct (X_{rd}) axis reactances, I_q , and I_d are used to determine the difference in E_a and E_f caused by armature reaction. The phasor equation expressing this is:

$$E_a = jI_q X_{rq} + jI_d X_{rd} + E_f \quad (C.2).$$

This equation is embodied in the phasor diagram, Figure C.1b. It formed the basis for my postprocessing program.

X_{rd} is greater than X_{rq} because of the higher inductance on the direct axis caused by the salient poles. The quadrature axis is dominated by the interpolar air gap. For linear conditions X_{rd} and X_{rq} can be computed based on machine construction, but this is a very laborious task (see Langsdorf [27, pp. 435-453]). Saturation conditions cannot be accounted for using this method.

My computer model determines E_a and E_f directly without using X_{rd} , X_{rq} , I_d , and I_q . However, I wrote the postprocessing program which computes these values (using known I_a , E_a , and E_f inputs) so that I could determine the effects of saturation upon X_{rq} and X_{rd} . Under saturated (and even linear) conditions both of them vary substantially. Over the course of the steady state conditions simulated in Figure 6.3, X_{rd} varied from 23.44 to 2.7 Ω , with lower values occurring under high direct axis MMF conditions. X_{rq} varied from 5.67 to 3.65 Ω . Often, when X_{rd} was low, so was X_{rq} . With this kind of variation in X_{rd} and X_{rq} , it is obvious why the linear theory, which assumes that both are constant, is inadequate for predicting saturated conditions.

Langsdorf [27, pp. 468-470] discusses the transition from generating to motoring action. When switching, the machine will go through a brief transient period where the rotor slows with respect to synchronous speed. The result is that slightly different steady state equations and conventions are used for a generator and a motor. Figure C.2 gives the magnetic field conditions for a generator. The equations for the phasor diagram, Figure C.2b, are:

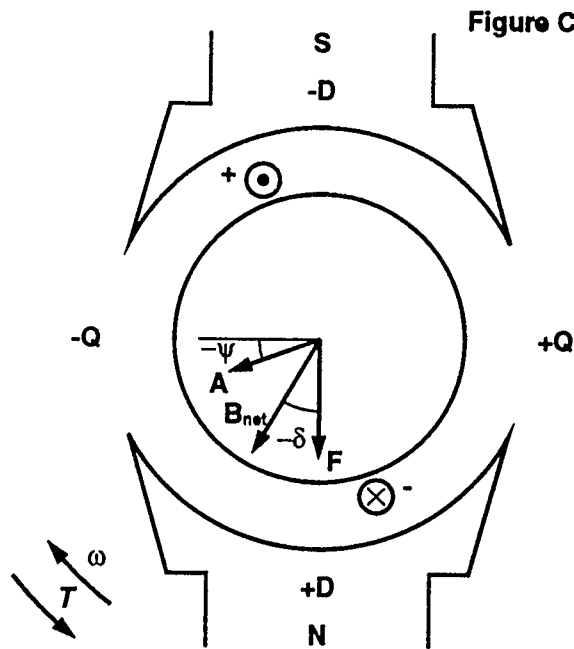


Figure C.2a: Magnetic Field Conditions
F = MMF axis of field windings, fixed in space
A = MMF axis of phase a winding
 ω = angular velocity, shown in + direction
T = torque, shown in - direction, for generating conditions
 δ = internal torque or power angle
B_{net} = axis of fundamental of net flux distribution under load
 ψ is positive for lagging internal power factor, demagnetizes +D axis
 ψ is negative for leading internal power factor, magnetizes +D axis

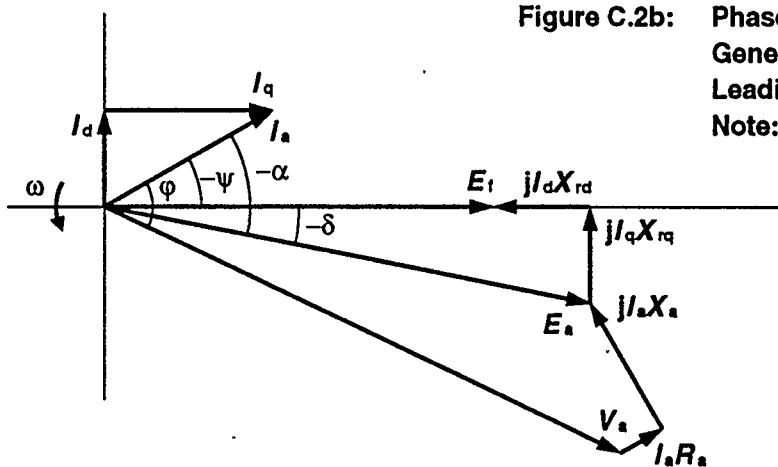


Figure C.2b: Phase a Phasor Diagram, Generating Conditions, Current Leading Induced No-Load Voltage
 Note: not to scale

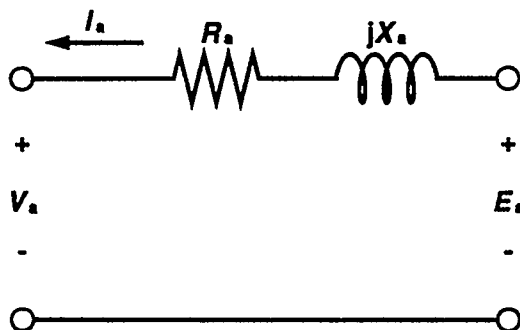


Figure C.2c: Circuit Diagram, Generating Conditions

Figure C.2: Magnetic Field Conditions, Phasor Diagram, and Circuit Diagram for a Two Pole, Salient Pole Generator

$$E_a = V_a + I_a(R_a + jX_a) \quad (C.3),$$

and

$$E_f = jI_qX_{rq} + jI_dX_{rd} + E_a \quad (C.4).$$

The conventions used in the circuit diagrams and the reference position of ψ have been changed. The flux density, torque, and voltage models were developed based on motoring conditions, however their programs were used successfully for generating conditions as well. Equations C.3 and C.4 are used for pre- and postprocessing. The output E_a (or E_f) must be phase shifted by 180° electrical for a generator, as does V_a . Because of the new convention for ψ , if ψ is negative (as shown in Figure C.2) A adds to F . This corresponds to a leading internal power factor condition. If ψ is positive, A opposes F . This corresponds to a lagging internal power factor condition (similar to a short circuit at the generator terminals). Also, the relation between ψ and *rotorg* is affected (see equation C.5 later).

COMPUTATION PROCEDURES FOR A NO LOAD V-CURVE

Details of the flux density, torque, and voltage computation models are given in Appendix B. Static conditions are assumed. Harmonics are neglected. E_a is computed by simulating rotor rotation through the static field. Two full AC cycles are computed for one mechanical revolution.

The computation procedures I will describe should be automated in the future. These were done by hand to identify any anomalies. None were found.

The procedure for obtaining a single steady state point on the no load V-curve shown in Figure 6.3 is as follows:

- i) All points on the V-curve are for constant V_a and output shaft power. Since rotational speed is constant, shaft torque is constant. The magnitude of V_a is 1.0 p.u (254 Volts rms). Output power and shaft torque are both zero. I_a , ϕ , ψ , and I_f all need to be defined for the one point in question. The V-curve is plotted with I_f as the independent variable and I_a as the dependent variable. For simplicity, the mechanical and core losses in the machine are assumed to be constant at 1.4 HP. This is the developed power at the air gap. Armature winding losses are neglected. I_a and ϕ are selected to give 1.4 HP with the given V_a (using air gap

power = $3V_a I_a \cos(\phi)$). The magnitude of I_a is selected at a convenient level to ensure that enough points are calculated to give a good V-curve. With V_a , I_a , ϕ , R_a , and X_a all known, the preprocessing program (based on equation C.1) is used to determine the desired E_a .

- ii) With the magnitude of I_a known, compute the instantaneous value of armature current corresponding to $\omega t = -\pi/6$ using equation 2.13. Through trial and error, select I_f and *rotorg* so that the computer model outputs a magnitude and phase for E_a that matches the desired E_a . *rotorg* (the rotor gauge reading on the experimental equipment in mechanical degrees) is related to ψ (in electrical degrees) through the following equation:

$$\psi = 2(\textit{rotorg} + 10) \quad (\text{C.5})$$

For the generator conventions of Figure C.2, you must subtract 180° electrical from equation C.5.

- iii) Once the I_f and *rotorg* are found which give the desired magnitude and phase of E_a , the armature current can be set equal to zero with I_f and *rotorg* held constant. Under these conditions, $E_a = E_f$. δ can be determined from their phase difference. ψ can be checked since it is the phase shift of E_f from I_a under no load conditions. The postprocessing program (based on equation C.2) can then be used to find I_d , I_q , X_{rd} , and X_{rq} . Computed torque and power from the computer model are usually in excellent agreement with the desired torque and power levels.

SAMPLE CALCULATION

Details of the calculations for one point on the no load V-curve are shown in Table C.1.

Table C.1: Sample Trial and Error Steady State Computation of a Point on the No Load V-Curve

Initial Conditions:

$V_a = 254 \angle 0^\circ$ V, $I_a = 21.75 \angle 83.7^\circ$ A, p.f. = 0.11 leading, $i_a = 26.6$ A

Desired $E_a = E_a \angle \alpha = 294.4 \angle -86.87^\circ$ V, Air gap torque = 5.57 N-m, Air gap power = 1.4 HP, 1800 RPM

TRIAL #	ψ (electrical degrees)	INPUTS TO THE COMPUTER MODEL			OUTPUTS FROM THE COMPUTER MODEL			COMMENT
		<i>rotorg</i> (mechanical degrees)	i_f (Amps)	i_a (Amps)	Air Gap Torque (N-m)	E_a (Volts)	α (electrical degrees)	
1	-86.0	-53.0	2.95	26.6	5.43	297.7	-87.10	In terms of phase reference: $E_a = 293.9 \angle -3.12^\circ$ $E_f = 421.8 \angle -4.26^\circ$
2	-85.8	-52.9	2.95	26.6	6.10	297.8	-86.84	
3	-85.8	-52.9	2.92	26.6	6.07	293.9	-86.82	
4	-85.8	-52.9	2.92	0	0	421.8	-87.96	

Notes on the sample calculation:

- i) Since this point was in the middle of a long series of points being calculated for the V-curve we started with a good first trial and convergence was fast. When starting fresh, up to 8 or 9 trials may be needed.
- ii) Changes in *rotorg* or ψ usually affect the phase of E_a most significantly.
- iii) Changes in I_f usually affect the magnitude of E_a most significantly.
- iv) The difference in the air gap torque is because the computer model takes into account the flux harmonics, but the torque from the electrical input power calculation only considers the fundamental of the induced winding voltage waveform.
- v) E_f is found after E_a has been found by simply dropping i_a to zero and holding everything else constant. Because this is a leading power factor condition in a motor, **A** and **F** largely oppose each other. When the armature reaction current (1.5 p.u.) is dropped, the no load voltage is very high since the field current is 1.46 p.u.. The internal torque angle, δ , is very small ($-86.82^\circ - (-87.96^\circ) = 1.14^\circ$ electrical). The small developed torque overcomes the 1.4 HP worth of core and friction losses to give 0 net shaft torque.
- vi) A small error (about 2° electrical) exists between ψ determined using equation C.5 and *rotorg*, and ψ determined from the computer model. This is likely due to experimental error in determining the reference axis of *rotorg*.
- vii) Equation C.2 (the postprocessing program) was used to compute the following D-Q axis parameters for the case shown in Table C.1:

$$I_d = 21.74 \angle 85.74^\circ \text{ A}$$

$$I_q = 0.77 \angle -4.26^\circ \text{ A}$$

$$X_{rd} = 5.89 \ \Omega$$

$$X_{rq} = 7.55 \ \Omega$$

Saturation on the direct axis has forced X_{rd} to be less than X_{rq} .